QST-M-39

QST Takasaki Annual Report 2021

Takasaki Advanced Radiation Research Institute

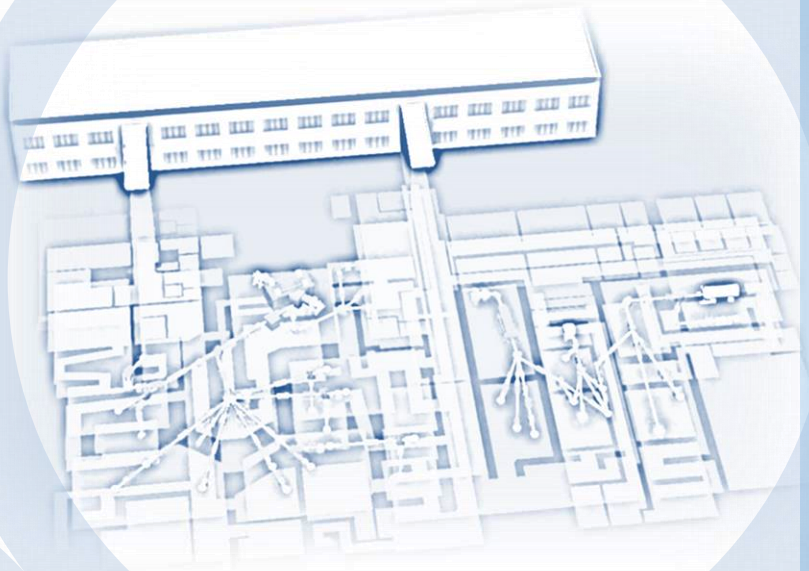

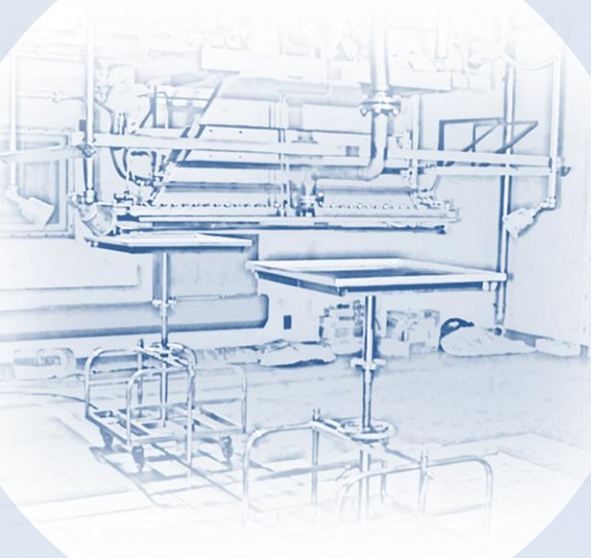

National Institutes for Quantum Science and Technology

Preface

MAEKAWA Yasunari

Director General
Takasaki Advanced Radiation Research Institute
Quantum Beam Science Research Directorate
National Institutes for Quantum Science and Technology

The National Institutes for Quantum Science and Technology (QST) was established in April 2016 by combining two research directorates, Quantum beam science and Nuclear fusion research in the Japan Atomic Energy Agency (JAEA), with the National Institute of Radiological Sciences (NIRS). Currently, QST has three research and development (R&D) directorates: Quantum Beam Science Research (QuBS), Quantum Life and Medical Science, and Fusion Energy. QuBS comprises Takasaki Advanced Radiation Research Institute (TARRI), Kansai Photon Science Institute (KPSI), and Institute for Advanced Synchrotron Light Source (IASLS). Using advanced beam facilities, we conduct intensive fundamental and applied research in fields such as materials science, life science, and quantum beam technology. TARRI has two research sites, Takasaki and Tokai, and manages three main radiation facilities at the Takasaki site: Takasaki Ion Accelerators for Advanced Radiation Application (TIARA), a 2-MeV electron accelerator, and ^{60}Co gamma-ray irradiation facilities.

At TARRI, we have 16 research projects and two research groups conducting quantum beam science R&Ds with the aforementioned three main radiation facilities to contribute to the progress of science and technology, as well as the promotion of industry. The Advanced Functional Polymer Materials Research Group was established in 2017 under QST's innovation hub program. Its purpose is to develop next-generation graft-polymer materials through the combined use of quantum beam processing, analysis techniques and material informatics. The Quantum Sensing and Information Materials Research Group was established in August 2018 to conduct fundamental and applied research for realizing quantum devices, such as quantum sensors, quantum bits, and spin transistors, based on wide-bandgap semiconductors including diamonds and 2D materials such as graphene. Furthermore, we conduct R&D on advanced ion beam technology at the Beam Engineering Section of the Department of Advanced Radiation Technology. Our beam facilities are available to industry, academia, and governmental research institutes, and beam time is allocated to users based on the evaluation of their R&D programs.

This annual report covers research activities at TARRI for the fiscal year 2021 (FY2021). This report is composed of two parts. Part I describes the recent activities of all research projects and groups, including the Beam Engineering Section. Part II presents recent R&D results obtained using the quantum beam facilities of TARRI. This part contains 74 research papers in the fields of materials science, life science and advanced quantum beam technology, and eight status reports on the operation and maintenance of the quantum beam facilities.

The following three topics are the research highlights of FY2021 in materials science, life science, and advanced quantum beam technology. The first topic is in the field of materials science. The 3D structures such as fold or protrusions are widely observed in human organs. However, on conventional cell culture dishes, epithelial cells only form a planar monolayer. In our study, unique structures like the human organs were built with a film-on-substrate cell culture system. This system mimics the in vivo layering of epithelium–basement membrane–mesenchyme by controlling the 3D distributions of scission/crosslinking regions of polylactic acid, which is a biocompatible and bioabsorbable polymer, using the ion beam nanofabrication technique. The second topic is in the field of life science. It has been difficult to detect genome-wide mutations from a mutagenized plant (the first generation) till now, because of the presence of cells with different mutation patterns. We developed a method to enrich progenitors originating from a single mutated cell in the mutagenized plant by using the loss of heterozygosity of genes for anthocyanin pigmentation in Arabidopsis and to detect genome-wide mutations occurring in the first-generation tissues. By taking advantage of the mutation characteristics in irradiated plants revealed through this research, it is expected that the mutation will be used for the early selection of promising strains in the improvement of trees and nutritionally reproductive plants, to select branches that bear good fruit even before maturity. The third topic is in the field of advanced quantum beam technology. The laser Compton scattering (LCS) gamma-ray distribution in the energy-angle phase space has been reconstructed from crystal diffraction data. Such diagnostics have been used for photon energies below 100 keV, but have not been realized for energies above 1 MeV. We demonstrated the reconstruction of the energy-angle phase space distribution of an LCS photon beam with an energy of 1.7 MeV by photon diffraction using silicon mosaic and comb crystals with improved integral reflectivity. This diagnostic technique is an efficient tool for LCS source development and is also beneficial for the use of existing LCS facilities.

An azimuthally varying field (AVF) cyclotron and three electrostatic ion beam accelerators in TIARA, as well as an MeV electron accelerator and ^{60}Co gamma-ray irradiation facilities have been continuously and safely operated. The key components of the accelerator system in TIARA are updated year by year to maintain its worldwide technological superiority. In this year (FY2021), control systems of three electrostatic accelerators and two microbeam apparatuses connected to both the single-ended and the tandem accelerators were replaced, and the stability of the beam current improved by 65 % under typical operating conditions. The new microbeam apparatus for quantum device fabrication enables to reduce the beam-spot size from the micrometer revel to tens of nanometers. The low-fluence gamma-ray irradiation conditions available in the food irradiation facility, which was closed in March 2022, were developed in irradiation room No. 3 of the first ^{60}Co gamma-ray irradiation facility.

Lastly, we would like to extend our gratitude to our domestic and foreign colleagues for their cooperation and support in our quantum beam science R&D, as well as technological advances in the facilities of TARRI.

Facilities

Charged particle beams and RI facilities

Takasaki Ion Accelerators for Advanced Radiation Application (TIARA) consisting of four ion accelerators, an electron accelerator, and gamma-ray irradiation facilities are available to researchers in QST and other organizations for R&D activities on new functional and environmentally friendly materials, biotechnology, radiation effects of materials, and quantum beam analysis. We are developing various shape area irradiation technique at the cyclotron. In addition, technical developments of elemental map imaging by C_{60} fullerene microbeam at the electrostatic accelerators are in progress.

Takasaki Ion Accelerators for Advanced Radiation Application: TIARA

TIARA facility

Cyclotron

Tandem accelerator

Single-ended accelerator

Ion implanter

Typical available ions

Accelerator	Ion	Energy (MeV)
AVF Cyclotron (K=110MeV)	H	10 80
	He	20 107
	C	75 320
	Ne	75 350
	Ar	150 520
	Fe	200 400
	Kr	210 520
	Xe	324 560
	Os	490
Tandem Accelerator (3 MV)	H	0.8 6.0
	C	0.8 18.0
	Ni	0.8 18.0
	Au	0.8 18.0
	C_{60}	0.8 9.0
Single-ended Accelerator (3 MV)	H	0.4 3.0
	D	0.4 3.0
	He	0.4 3.0
	e^-	0.4 3.0
Ion Implanter (400 kV)	H	0.02 0.38
	Ar	0.02 0.38
	Bi	0.02 0.37
	C_{60}	0.02 0.36

Energy-element range covered by the four accelerators

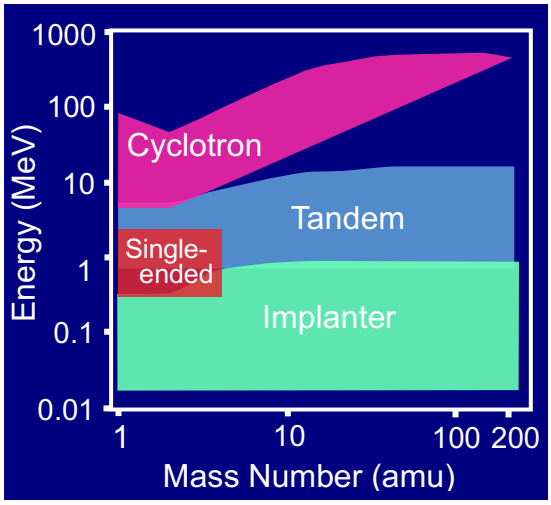

Cobalt-60 gamma-ray and electron beam irradiation facilities

Gamma-ray irradiation facility building

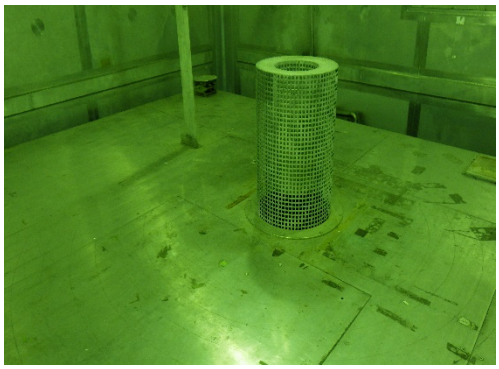

Gamma-ray irradiation room

Electron accelerator
(0.5～2.0 MeV, 0.1～30 mA)

Electron irradiation room with conveyor system

Specification

Apr. 2022

Name of facility	Cobalt-60 activity (PBq)	Number of rooms	Principal utilization
Co No.1 bld.	5.1	3	Radiation-resistance test, radiation effects on materials as polymers, semiconductors, and biological substances as bacteria, cell, plant
Co No.2 bld.	6.0	3	R & D on functional organic, inorganic materials and dosimetry
Food Irradiat. bld.	The third gamma-ray irradiation facility named 'food irradiation facility' has stopped operating as of March 1st, 2022. The lower dose rate-field of this facility was installed in the No.3 room of the Co No.1 building.		

Dose-rate range

Unit : kGy/h

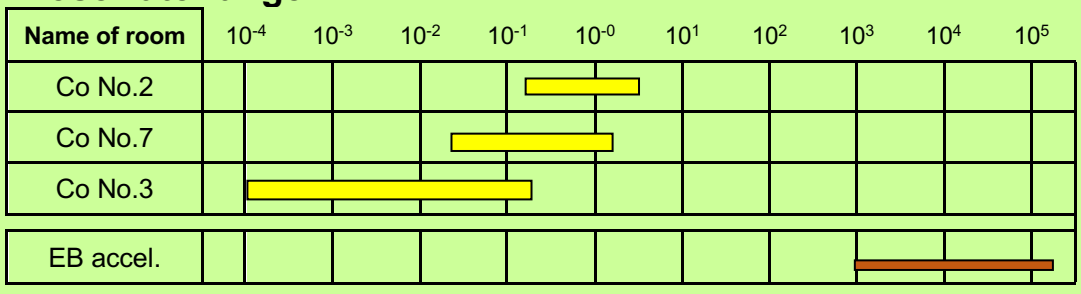

blank page

Contents

Part Ⅰ

1. Materials Science ····· 1

P1-1 Project “Functional Polymer” ····· 2
Leader : MAEKAWA Yasunari

P1-2 Project “Advanced Catalyst” ····· 3
Leader : YAMAKI Tetsuya

P1-3 Project “Positron Nanoscience” ····· 4
Leader : KAWASUSO Atsuo

P1-4 Project “Semiconductor Radiation Effects” ····· 5
Leader : OHSHIMA Takeshi

P1-5 Project “Environmental Polymer” ····· 6
Leader : SEKO Noriaki

P1-6 Project “Biocompatible Materials” ····· 7
Leader : TAGUCHI Mitsumasa

P1-7 Project “Spintronics in Two-dimensional Materials” ····· 8
Leader : SAKAI Seiji

P1-8 Project “EUV Ultra-fine Fabrication” ····· 9
Chief : YAMAOTO Hiroki

P1-9 Project “Element Separation and Analysis” ····· 10
Leader : OHBA Hironori

P1-10 Advanced Functional Polymer Materials Research Group ····· 11
Leader : MAEKAWA Yasunari

P1-11 Quantum Sensing and Information Materials Research Group ····· 12
Leader : OHSHIMA Takeshi

2. Life Science ····· 13

P2-1 Project “Microbeam Radiation Biology” ····· 14
Leader : FUNAYAMA Tomoo

P2-2 Project “Ion Beam Mutagenesis” ····· 15
Leader : OONO Yutaka

P2-3 Project “Medical Radioisotope Application” ····· 16
Leader : ISHIOKA Noriko S.

P2-4 Project “Radiotracer Imaging” ····· 17
Leader : KAWACHI Naoki

P2-5 Project “Generation of Radioisotopes with Accelerator Neutrons” ····· 18
Leader : HASHIMOTO Kazuyuki

3. Advanced Quantum-Beam Technology ····· 19

P3-1 Project “Single-ion Control with Laser-cooling” ····· 20
Leader : NARUMI Kazumasa

P3-2 Project “LCS Gamma-ray” ····· 21
Leader : HAJIMA Ryoichi
P3-3 Beam Engineering Section ····· 23
Section Manager : ISHII Yasuyuki

Part Ⅱ

1. Materials Science ····· 25

1-01 Direct observation of hierarchical structures in graft-type polymer electrolyte membranes using the AFM technique ····· 28
1-02 Synthesis and properties of polysubstituted anion conducting electrolyte membrane by radiation graft polymerization ····· 29
1-03 Development of gas permselective membranes by graft polymerization into ion-beam irradiated polymer films III ····· 30
1-04 Accelerated degradation of the irradiated electrode for vanadium redox flow battery ····· 31
1-05 Hydrogen in Al-Fe thin films prepared by sputtering ····· 32
1-06 Development of metal oxide-catalysts utilizing quantum beam irradiation technique (2) ····· 33
1-07 Modification of polymeric materials by quantum beam irradiation (2) ····· 34
1-08 Study on nitrogen-doping into carbon material by utilizing electron beam irradiation technique ····· 35
1-09 Preparation of ion-track membranes of polystyrene ····· 36
1-10 High-precision flat-plate reference infrared radiator with perfect blackbody composite made by high-energy ion track etching technique ····· 37
1-11 Proton and water selectivity of ion-track-grafted proton-exchange membranes for HI concentration ····· 38
1-12 Effect of 190 keV proton irradiation on superconducting properties in $FeSe_{0.5}Te_{0.5}$ thin films ····· 39
1-13 The origin of the weakened bonding of oxygen with the Pt catalyst on an ion-beam-irradiated carbon support ····· 40
1-14 Chemical state of platinum ions implanted into glassy carbon substrates ····· 41
1-15 Enhanced X-ray excited optical luminescence in MgO with Cr ion implantation ····· 42
1-16 Radiation resistance of diamond FeFET with inorganic ferroelectric gate ····· 43
1-17 Optical response of vacancy-induced magnetism in gallium nitride estimated by spin-polarized positron annihilation method ····· 44
1-18 Positron annihilation spectroscopy research on irradiation of a new fiber ····· 45
1-19 Local structure of high-energy implanted Ni into Si(100) ····· 46

1-20 Improvement of radiation resistance by hetero p/n junction in solar cells ····· 47

1-21 Characteristic sensitive area observed in FinFET SRAM ····· 48

1-22 Development of phthalocyanine ion beam for creation of multiple NV center in diamond ····· 49

1-23 Ensemble nitrogen vacancy centers in type-Ib diamond created by electron beam up to 8×10^{18} cm^{-2} ····· 50

1-24 Prediction of grafting yield by using machine learning ····· 51

1-25 A facile graft polymerization of biomass-based vinyl monomers from PE/PP substrates in a new generation safe organic solvent ····· 52

1-26 Simple evaluation method for distribution of graft chains by using thermogravimetric analysis ····· 53

1-27 Thin films produced by ion beam nanofabrication technique induced cell-driven 3D cell sheet formation ····· 54

1-28 Effect of radiolysis in gas phase on the corrosive environment in liquid phase ····· 55

1-29 Effect of outer diameter on the completely amorphized dose of silicon carbide nanotube by ion irradiation ····· 56

1-30 Radiation robustness of laser ceramics and single crystal for microchip laser remote analysis ····· 57

1-31 Gamma-ray irradiation experiment for ITER diagnostic systems in JADA IV ····· 58

1-32 Irradiation tests of radiation hard components and materials for ITER blanket remote handling system ····· 59

1-33 Evaluation of irradiation hardening for pure tungsten using micro tensile test ····· 60

1-34 Structural analysis of complex formed in adsorbent for gravity driven extraction chromatography ····· 61

1-35 Ion beam induced luminescence spectra of europium complexes in silica-based adsorbent ····· 62

1-36 Synthetic control of functional metal nanomaterials in SiO_2 by multiple particles irradiation ····· 63

1-37 Evaluation of radiation tolerance of COTS device for small satellite ····· 64

1-38 Thermodynamic study of $Ti_{1-x}Al_xN$ thin film growth on monocrystalline AlN by reactive CVD ····· 65

1-39 Color imaging of carbon ion ($^{12}C^{+5}$) beam by the 3D gel dosimeter based on phenothiazine-type color former ····· 66

1-40 Gamma-irradiation effect on radical centers derived from hydrothermally altered potassium feldspar and its application to fault dating ····· 67

2. Life Science ····· 69

2-01 Quality effects of carbon ion and proton beams and gamma-rays on reversion mutation in zebrafish embryos ····· 72

2-02 DNA damage foci formation after simulated-space radiation exposure ····· 73

2-03 Precise localized irradiation of individual organisms using focused heavy ion microbeams ·····74

2-04 New trial toward the precise identification of fluorescence dots originated from oxidative damage in DNA thin sheet perpendicularly irradiated with heavy ions····· 75

2-05 Development of depth-controlled irradiation methods for silkworm eggs – Determination of shielding range – ····· 76

2-06 Comparison between 190MeV $^{12}C^{6+}$ and 220MeV $^{12}C^{5+}$ ions in inducing *P-53* gene dependent bystander cell-killing effect in human tumor cell lines ····· 77

2-07 Basic study of immunoradiation therapy using anti-PD-L1 antibody ····· 78

2-08 Efficient dose of carbon ion beam irradiation for azalea seeds····· 79

2-09 Effect of carbon ion-beam irradiation on growth and mutation spectra of *Physcomitrium patens* ····· 80

2-10 Mutagenesis of the oil-producing algae by heavy ion irradiation····· 81

2-11 Genome analysis of the low cesium-accumulating mutants of *Rhodococcus qingshengii* CS98 generated by ion beam breeding ····· 82

2-12 Pilot-scale sake brewing tests using non-urea producing Gunma KAZE3 yeast bred by ion-beam mutagenesis ····· 83

2-13 Growth curve analysis of *Bacillus subtilis* spores to evaluate damage and growth inhibition by ion-beam and gamma Irradiations ····· 84

2-14 Gamma-ray resistance of the thermophilic *Rubrobacter* species ····· 85

2-15 Strategy for detecting genome-wide mutations in mutagenized Arabidopsis plants ····· 86

2-16 Elucidation of genes involved in camptothecin biosynthesis of *Ophiorrhiza pumila*····· 87

2-17 Enhancing the therapeutic effect of 2-^{211}At-astato-α-methyl-L-phenylalanine with probenecid loading····· 88

2-18 Rapid flow-based system for separation of radioactive metals by selective complex formation ····· 89

2-19 Preparation for single-cell RNA-sequence assay of PC12 pheochromocytoma cells····· 90

2-20 Spatial distributions of cesium and strontium in tea leaves evaluated by micro-PIXE analysis ····· 91

2-21 Identification of multi-element accumulation mechanism in legume····· 92

2-22 Visualization of zinc distribution in the root of oilseed rape plants by atmospheric micro-PIXE (Particle Induced X-ray Emission) analysis····· 93

2-23 Evaluation of photosynthate translocation dynamics to strawberry fruits in response to increasing daylight integrals at leaf surface····· 94

2-24 Elemental distribution into root dentin from pilot materials incorporating with titanium fluoride····· 95

2-25 Ion penetration of zinc-containing fluoride material into sound and demineralized dentin …… 96

2-26 Estimation of damage localization of ion beam-irradiated DNA in water by means of fluorescence anisotropy …… 97

2-27 Development of drug delivery system (DDS), through two repetitions of radiation …… 98

3. Advanced Quantum-Beam Technology …… 99

3-01 Measurement test of beam energy and position monitor system in the beam transport line for RI production …… 100

3-02 Cyclotron development study for the beam formation using the nonlinear magnetic field …… 101

3-03 Fabrication of mold for stamp by proton beam writing and transfer characteristics of printed a-IGZO TFT …… 102

3-04 Lithium concentration measurement in lithium-ion battery materials by nuclear reaction …… 103

3-05 Elemental analysis of silica/silicates accumulation in scleroderma lungs by in-air micro PIXE …… 104

3-06 Dentin remineralization enhances by trace-element …… 105

3-07 Au sputtering yield by C_{60-} and C_{70}-ion bombardment …… 106

4. Status of Quantum-Beam Facilities …… 107

4-01 Utilization status at the TIARA facility …… 108

4-02 Operation of the AVF cyclotron …… 109

4-03 Operation of electrostatic accelerators in TIARA …… 110

4-04 Operation status of the electron accelerator and the gamma-ray irradiation facilities …… 111

4-05 Utilization status of the electron accelerator and the gamma-ray irradiation facilities …… 112

4-06 Radiation monitoring in TIARA …… 113

4-07 Radioactive waste management in TIARA …… 114

4-08 Facility Use Program in Takasaki Advanced Radiation Research Institute …… 115

Appendices …… 117

Appendix 1 Publication List …… 118

Appendix 2 Type of Research Collaboration and Facilities Used for Research …… 134

Appendix 3 Abbreviated Name for National Organizations …… 136

Part I

Part Ⅰ

1. Materials Science

P1-1 Project “Functional Polymer” ……2
Leader : MAEKAWA Yasunari

P1-2 Project “Advanced Catalyst” ……3
Leader : YAMAKI Tetsuya

P1-3 Project “Positron Nanoscience” ……4
Leader : KAWASUSO Atsuo

P1-4 Project “Semiconductor Radiation Effects” ……5
Leader : OHSHIMA Takeshi

P1-5 Project “Environmental Polymer” ……6
Leader : SEKO Noriaki

P1-6 Project “Biocompatible Materials” ……7
Leader : TAGUCHI Mitsumasa

P1-7 Project “Spintronics in Two-dimensional Materials” ……8
Leader : SAKAI Seiji

P1-8 Project “EUV Ultra-fine Fabrication” ……9
Chief : YAMAMOTO Hiroki

P1-9 Project “Element Separation and Analysis” …… 10
Leader : OHBA Hironori

P1-10 Advanced Functional Polymer Materials Research Group …… 11
Leader : MAEKAWA Yasunari

P1-11 Quantum Sensing and Information Materials Research Group …… 12
Leader : OHSHIMA Takeshi

P1-1 Project “Functional Polymer”

Leader : MAEKAWA Yasunari

Project “Functional Polymer Research” has been developing the advanced functional polymer materials, such as polymer electrolyte materials and separation membranes for high performance fuel cells and hydrogen collection systems by using quantum beams. We have synthesized the proton- and anion-conducting electrolyte membranes (PEM and AEM) and the hydrogen permselective membranes using γ-rays and electron beams. We report herein two recent developments: new structural analysis on benchmark materials Nafion® and poly(ethylene-co-tetrafluoroethylene) (ETFE)-based AEMs for hydrogen- and alkaline hydrated hydrazine-fuel cells.

Three-component domains in the fully hydrated Nafion membrane characterized by partial scattering function analysis [1]

Nafion® is a benchmark PEM material that has been commercialized in residential and automobile fuel cells. Its properties are closely related to hierarchical structures upon hydration. The phase-separated morphology in the hydrated Nafion® has been extensively studied using the small-angle scattering technique. However, the detailed structure is still under debate because conventional intensity analysis fails to provide the concrete structure of individual components. This obstacle is for the first time solved by us using partial scattering function (PSF) analysis through the contrast variation small-angle neutron scattering (SANS) method.

Our results confirmed the validity of three-component domains of main-chain (MC), side-chain (SC) and water in Nafion®. The analysis of PSF self-terms revealed the detailed structure of each component, and that of the cross-terms gave the correlation between two components leading to the location determination. The whole structure pattern of Nafion® was constructed as shown in Fig. 1: MC forms bicontinuous-shaped template made of crystalline MC domains and amorphous domains composed of amorphous MC, SC and water. All components have a bicontinuous-like local structure. MC and SC show heterogeneity on the large-scale with a size of > 65 nm; however, water distributes homogeneously on the large-scale, indicating the formation of a well-connected network which is believed to be the key structural factor for high membrane conductivity.

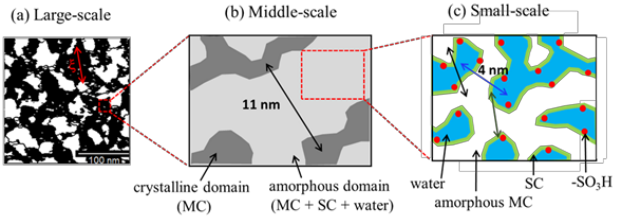

Fig. 1. Schematic of the hierarchical structure of the MC, SC and water domains in the fully hydrated Nafion®.

Synthesis and characterization of 4-vinylimidazolium/styrene-cografted anion-conducting electrolyte membranes [2]

Imidazolium(Im)-type AEMs exhibited lower water uptake and induced less damage to polymer backbone than ammonium-type AEMs, which recently attracted attention for AEM fuel cell applications. However, Im-AEM prepared from commercially available *N*-vinylimidazole as a graft monomer was subjected to severe β-elimination and ring-opening hydrolysis of imidazolium groups. We have found that these reactions can be suppressed by the copolymerization of hydrophobic styrene in the graft chain and by modifying imidazolium with protecting group at the C2 position of the imidazolium ring [2]. In this work, we synthesized a new imidazole monomer, 2-methyl-*N*-methyl-4(5)-vinylimidazole (2M4VIm), and then made AEMs by co-grafting 2M4VIm and styrene (St) to ETFE base films (denoted as 2M4VIm/St-AEM shown in Figure 2) to fully prevent β-elimination reaction and introduce methyl groups at the C1 and C2 positions to prevent hydroxide attack leading to ring-opening hydrolysis.

2M4VIm/St-AEM with a 6/4 molar ratio of 2M4VIm/St and 1.7 mmol/g ion exchange capacity (IEC) shows 75 mS/cm conductivity and 60% water uptake at room temperature in water, which are enhanced values compared to previously reported best AEM with 2-methyl-*N*-vinylimidazolium (2MNVIm/St-AEM) that have a similar comonomer ratio and IEC. SANS results on 2M4VIm/St-AEM revealed hydrophilic/hydrophobic two-phase separation, where hydrophilic layers consist of partially grafted polymers with water as ion channels. These AEMs exhibited higher alkaline stability in 1 M KOH at 80 °C at an early stage owing to the suppression of imidazolium β-elimination but lower long-term stability than that of 2MNVIm/St-AEM due to the ring-opening reaction of the imidazolium group for its outward orientation from the graft main chain. These findings provide new insight into imidazolium-based graft-type AEM, namely, further improvement of steric hindrance of the imidazole group will be desired.

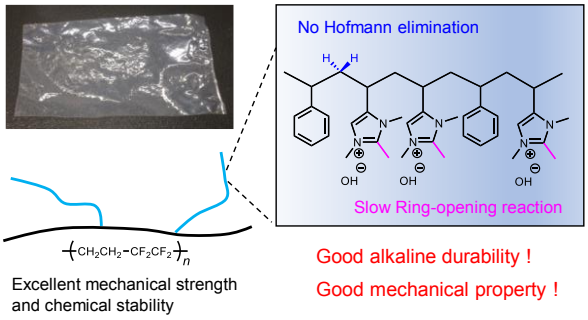

Fig. 2. Structure of β-elimination free 2M4Vim/St-AEM.

References

[1] Y. Zhao *et al*., Macromolecules **54**, 4128 (2021). DOI: 10.1021/acs.macromol.1c00587

[2] T. Hamada *et al*., Macromol. Chem. Phys. **222**, 2100028 (2021). DOI: 10.1002/macp.202100028

P1-2 Project “Advanced Catalyst”

Leader : YAMAKI Tetsuya

The main target of our project is development of catalytic materials for next-generation energy devices in future H_2 society by effective use of electron and ion beams. The advantage of our overarching strategy is that these quantum beams can lead to high-energy defect creation, active-site formation via non-equilibrium chemical reactions, and nano-to-micro fabrication. This report deals with R&Ds of nanomaterials for active electrocatalysts in polymer electrolyte fuel cells (PEFCs).

Development of highly-active platinum catalysts by ion beam-induced defects in carbon support [1]

Development of highly active catalysts for PEFCs is one of the urgent issues to promote the spread of fuel cell vehicles (FCVs). Platinum (Pt)/carbon catalysts are extensively used for an oxygen reduction reaction (ORR; $O_2 + 4H^+ + 4e^- \rightarrow 2H_2O$) in the cathode of PEFCs. However, the problem is that high loading of precious Pt increases the price of PEFCs and, therefore, hampers the expansion of the FCV market. We have been developing Pt/carbon with higher ORR activity utilizing ion beam-induced defects in the carbon support.

The Pt nanoparticles were deposited on a glassy carbon (GC) substrate irradiated with 380 keV Ar^+ at a fluence of 1×10^{16} ions/cm^2 in vacuum at room temperature. The ORR activity of the obtained Pt/irradiated GC catalyst was 2.2 times higher than that of Pt/non-irradiated GC catalyst. To elucidate the origin of the high ORR activity, the X-ray absorption fine structure (XAFS) for the Pt L_3-edge was measured at the synchrotron radiation facility, SPring-8.

As seen in XAFS spectra of Fig. 1, the peak intensity of Pt/irradiated GC at around 11567 eV was lower than that of Pt/non-irradiated GC, indicating the suppression of Pt oxidation probably due to a decrease in the bonding energy between Pt and oxygen (O). This would boost the desorption of O-containing intermediates during the ORR process. Density functional theory (DFT) calculations also suggested strengthening of the electronic interaction between Pt and carbon at the interface with electron transfer from Pt to defective carbon support. As a result, the introduction of defects in the carbon support by ion-beam irradiation was found to (i) modulate electronic interactions between Pt and the carbon support, (ii) decrease the bonding energy between Pt and O, and finally (iii) improve the ORR activity. Our results demonstrated the possibility of the reduction of Pt loading in PEFCs to contribute to the spread of FCVs.

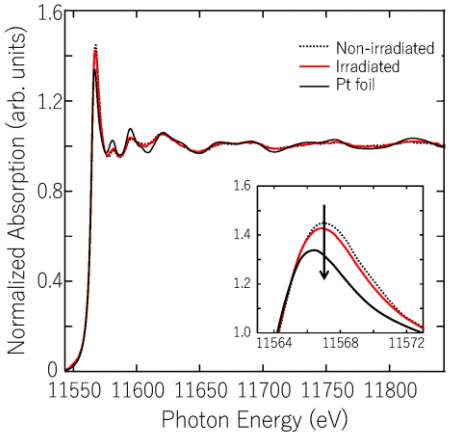

Fig. 1. Pt L_3-edge XAFS spectra of Pt nanoparticles deposited on the pristine and Ar^+-irradiated GC substrates. The result of a Pt foil is shown for reference.

Fabrication of free-standing nanowires with an ultra-high aspect ratio by utilizing high energy-charged particles [2]

High specific surface area is one of the most important properties for catalytic materials. We have succeeded in fabricating free-standing nanowires with diameters of single-nm and aspect ratios of > 100 by a so-called Single-Particle-Triggered Linear Polymerization (STLiP) method.

When a thin film of sublimable organic molecules (e.g. C_{60}-derivatives) was irradiated with charged particles at energies of several hundred eV (e.g. 350 MeV ^{129}Xe), polymerization of the organic molecules occurred in the latent tracks of charged particles. The irradiated film was heat-treated to sublimate the non-polymerized organic molecules outside the tracks.

Figure 2 (a) shows the SEM image of the isolated free-standing nanowires. The number, diameter, and length of nanowires are controllable by the number, species, and energy of charged particles. For comparison, Fig. 2 (b) indicates the nanowires fabricated by the conventional wet process involving the irradiation with charged particles and subsequent immersing into solvents. Apparently, the fabricated nanowires aggregated and lay onto the substrate, leading to their low specific surface area. Our new dry process gave free-standing nanowires with high specific surface area, which could be used for catalyst-supports or catalytic materials.

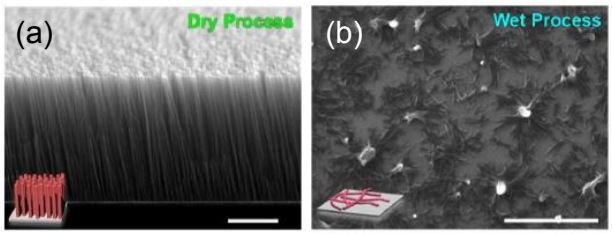

Fig. 2. SEM images of C_{60}-based nanowires fabricated by an STLiP method: a dry process with 350 MeV ^{129}Xe at 1×10^{11} ions/cm^2 and (b) the conventional wet process with 490 MeV ^{192}Os at 1×10^{11} ions/cm^2. A scale bar represents a length of 1 μm.

Acknowledgements

This work was supported in part by JSPS KAKENHI Grant Nos. 18H01923 and 21H04669.

References

[1] T. Kimata *et al.*, Phys. Rev. Mater. **6**, 035801 (2022). DOI: 10.1103/PhysRevMaterials.6.035801

[2] K. Kamiya *et al.*, Nat. Commun. **12**, 4025 (2021). DOI: 10.1038/s41467-021-24335-x

P1-3 Project “Positron Nanoscience”

Leader : KAWASUSO Atsuo

The aim of this project is to reveal the novel phenomena related to “spin” in solids using our original spin-polarized positron beam technologies. So far, we have been constructing the spin-polarized surface positronium spectroscopy that is substantially useful for detecting spin-polarization at the first surface layer and the spin-polarized positron annihilation spectroscopy in strong magnetic field for detecting vacancy-induced magnetism. To establish the foundation of the above spectroscopies, deep understanding of positron and positronium elementary processes is also important. We thus pursue such a basic aspect of positron physics, too. In this report, we pick up two topics in the last fiscal year (2021); one is the positronium formation process at GaN and AlN surfaces reveled by the positronium time-of-flight spectroscopy and one is the investigation of magnetic vacancies included in Co_2MnGa, which is expected as a ferromagnetic Weyl semimetal.

Positronium formation at GaN and AlN surface [1]

Positronium emission from wurtzite GaN(0001) and AlN(0001) surfaces was observed by positronium time-of-flight spectroscopy. The positronium energy spectra contained two positronium components distinguished by their energies. Through detailed analyses based on Monte Carlo simulations, these two components were attributed to positronium formed from valence and conduction electrons. The obtained results augment the previous arguments regarding the contribution of conduction electrons to positronium emission from 4H SiC(0001) and Si(111) surfaces.

Positronium, the bound state of an electron and a positron, has been extensively investigated in fundamental physics. Recently, some new challenges, such as positronium Bose–Einstein condensation and the development of positronium beams, are steadily being explored. In material physics, positronium spectroscopy plays an important role in probing spin-polarized surface electronic states. In these areas, obtaining a comprehensive understanding of the positronium emission process from solid surfaces is of fundamental importance.

Three positronium emission processes have been identified: (i) direct emission from the surface with a negative formation potential, (ii) combination between positrons confined in the surface mirror potential and surface electrons, and (iii) dynamical neutralization of energetic positrons during scattering at the surface. In some insulators, positronium Bloch states like Wannier–Mott-type exciton are known to be formed. Such bulk positronium is also thought to be directly emitted into vacuum when the positronium work function is negative.

Semiconductors are intermediate materials between metals and insulators. The dielectric constants of semiconductors lie between those of metals and insulators. The positronium binding energy in the bulk is expected to be small but finite (of the order of 10–100 meV), and hence bulk positronium emission cannot be dismissed in principle. Positronium emission from positrons in the surface mirror potential and surface dangling-bond states is also possible similar to metals.

To date, positronium emission from Ge, Si, and 4H SiC surfaces has been investigated. In contrast to the sharp rise in the energy spectrum at the negative of the positronium formation potential ($-\Phi_{Ps}$) observed for metals, the energy spectra of semiconductors exhibit high-energy tails above $-\Phi_{Ps}$, implying the contribution of electrons in the excited states to the positronium emission. In this work, we further investigated the positronium emission from GaN(0001) and AlN(0001) surfaces using positronium time of flight (PsTOF) spectroscopy. The high-energy positronium components were also observed here.

High-density magnetic vacancies in Co_2MnGa [2]

Co_2MnGa is a Weyl semimetal exhibiting giant anomalous Hall and Nernst effects. Using spin-polarized positron annihilation spectroscopy, we examined a Bridgman-grown Co_2MnGa single crystal with a nearly perfect $L2_1$-ordered structure and a reference Co_2MnAl polycrystal with a Mn–Al-disordered B2 structure. We found that a large amount of magnetic vacancies (more than 100 ppm) were included in the Co_2MnGa crystal but not the Co_2MnAl crystal. We discuss possible reasons for the inclusion of vacancies, the role of vacancies in the development of the ordered structure, and the electronic states associated with the vacancies. Toward the development of Co_2MnGa-based devices, the manners for reducing vacancies as well as the influence of vacancies on the electrical transport properties should be considered.

In 2016, Co_2MnGa and Co_2MnAl, which are two kinds of full Heusler alloys, were theoretically predicted to be ferromagnetic Weyl semimetals with potential applications in spintronic devices. The Weyl semimetallicity of Co_2MnGa has been experimentally confirmed through photoemission spectroscopy, the giant anomalous Hall effect, and the giant Nernst effect.

The crystallinity of Heusler alloy is always an important issue. Atomic swaps among the constituents result in disordered structures. Under non-stoichiometric conditions, excess antisite defects are formed. Furthermore, the inclusion of a large amount of vacancies was also found experimentally. Theoretical studies have suggested that the experimentally observed low half-metallicity and degraded electric performance may be explained by considering disorder and defects. The effects of crystal disorder and defects on the Weyl transport properties of Co_2MnGa may also be of some importance.

Positron annihilation spectroscopy is an established method for detecting atomic vacancies in crystalline solids. The spin-polarized version, spin-polarized positron annihilation spectroscopy, enables the investigation of magnetism associated with atomic vacancies. In this study, we applied this technique to a conventionally produced Co_2MnGa single crystal. The results show that the crystal contains a high-density of single vacancies and that ferromagnetism is maintained in the vicinity of the vacancies.

References

[1] A. Kawasuso *et al.*, J. Phys. B-At. Mol. Opt. **54**, 205202 (2021). DOI: 10.1088/1361-6455/ac32a0
[2] A. Miyashita *et al.*, J. Phys. Condens. Matter **34**, 045701 (2022). DOI: 10.1088/1361-648X/ac330

P1-4 Project “Semiconductor Radiation Effects”

Leader : OHSHIMA Takeshi

Quantum technologies, such as quantum computation, quantum cryptography information and quantum sensing, are regarded as indispensable technologies for our future life. Color centers, of which optical and spin properties can be manipulated with high fidelity, can be applied to quantum bits (qubits) and quantum sensors. We create color centers in wide bandgap semiconductors such as diamond and silicon carbide (SiC) using ion and electron beams. We study optical and spin properties of such color centers for qubits and quantum sensor applications. In addition, we investigate the radiation effects on semiconductor materials and devices to develop radiation resistant technologies for space and nuclear applications.

Creation of Nitrogen-Vacancy centers in diamond by electron irradiation

Negatively charged nitrogen-vacancy (NV) centers in diamond are known as a spin defect acting as a quantum sensor at room temperature [1]. To increase the sensitivity, high concentration NV centers are required. In such a case, electron irradiation into diamond with high nitrogen (N) concentration which is called as Ib diamond is a useful method [2]. However, the optimum conditions to create negatively charged NV centers by electron irradiation, especially a high NV concentration range has not yet been clarified. Here, we study the creation of NV centers by electron irradiation up to relatively high fluence regions (8×10^{18} /cm^2) [3].

Diamonds used in this study were type Ib diamonds grown by a high pressure and high temperature method. The P1 centers (substitutional neutral N atoms at the lattice sites of crystal) are contained from 46 to 80 ppm in the Ib diamonds. The concentration of P1 and negatively charged NV centers for diamonds were estimated by electron spin resonance (ESR) measurements. All samples were irradiated with 2 MeV electrons at room temperature and subsequently annealed at 1000°C for 2 hours in vacuum after electron irradiation.

Figures 1 (a) and (b) show P1 concentration and NV concentration as a function of 2 MeV electron fluence, respectively [3]. P1 concentration decreases with increasing electron fluence, and NV concentration increases with increasing electron fluence, as shown in Figs. 1 (a) and (b). This result indicates that N atoms capture vacancies which are created by electron irradiation during subsequent thermal annealing, as a result NV centers are created. In addition, it is concluded by photoluminescence measurements that no significant amounts of neutral NV centers, which do not act as quantum sensors, are observed in all samples even after electron irradiation at 8×10^{18} /cm^2. This suggests that enough amounts of P1 centers remain in all samples after irradiation, and residual P1 centers give charges to NV centers.

Ideally, two P1 centers are consumed when one NV center is created. Thus, one P1 is used to be for NV itself, and the other P1 works as a donor impurity. If this ideal relationship is correct, the amount of $([P1]+2[NV])/[P1]_{initial}$ should be unity. Where, $[P1]_{initial}$, [P1] and [NV] represent the amounts of P1 centers before irradiation, P1 centers after irradiation and negatively charged NV centers.

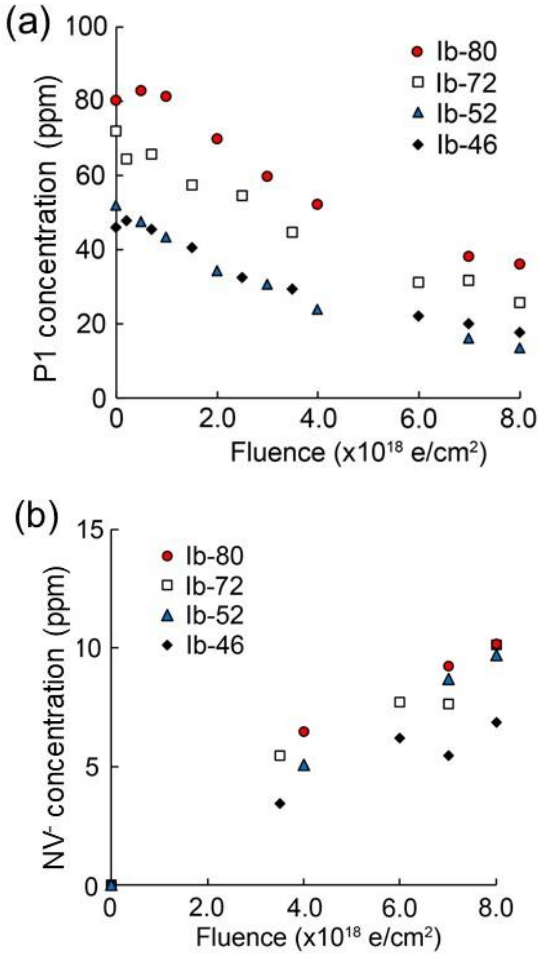

Fig. 1. (a) P1 concentration and (b) NV concentration as a function of 2 MeV electron fluence [3]. P1 and NV concentrations for each sample was measured using ESR. The concentration of P1 centers in ppm for each sample are described in the figures.

However, $([P1]+2[NV])/[P1]_{initial}$ decreases with increasing electron fluence, and the value becomes around 0.65 after irradiation at 8×10^{18} /cm^2. This result suggests that some P1 centers are used to create other defects but not NV centers. Since spin properties such as spin coherence time might be degraded by such residual defects, we need to improve the creation method for NV centers by electron irradiation. We are investigating the effects of annealing temperature and duration on the creation yield of NV centers and their spin properties.

References

[1] V. M. Acosta *et al*., Phys. Rev. B **80**, 115202 (2009). DOI: 10.1103/PhysRevB.80.115202
[2] S. Choi *et al*., Nature **543**, 221 (2017). DOI: 10.1038/nature21426
[3] S. Ishii *et al*., Quantum Beam Sci. **6**, 2 (2022). DOI: 10.3390/qubs6010002

P1-5 Project “Functional Polymer”

Leader : SEKO Noriaki

In the Project “Environmental Polymer Research”, we are developing functional polymer materials by radiation induced graft polymerization techniques using electron beams and γ-rays. Recently, we focus our reach on the metal-adsorption process of the functional materials, and the acceleration in the development of functional materials by the machine learning approach.

In situ observation of the chromium adsorption by X-ray absorption fine structure (XAFS) instrument [1]

To develop safe and simple methods for the reduction of toxic chromium (VI) to the less harmful chromium (III) in the industrial wastewater, we developed a functional adsorbent having amidoxime groups, namely AO-adsorbents, by the radiation induced graft polymerization of acrylonitrile onto a nonwoven fabric followed by conversion of the cyano groups into amidoxime groups. The resulted materials have a high chromium-adsorption capacity. In addition, we found that the toxic chromium (VI) was reduced to less harmful chromium (III) during the adsorption process.

To investigate the reduction process of the chromium (VI) to the chromium (III) in the AO-adsorbents, XAFS measurements were performed using the synchrotron radiation. The microstructures associated with the characteristic X-ray absorption edges were analyzed to obtain information regarding the local structure and the valence of the chromium adsorbed on the adsorbents. For this purpose, a flow cell system was designed for the in situ XAFS measurements under the chromium adsorption in the column-mode (Fig. 1).

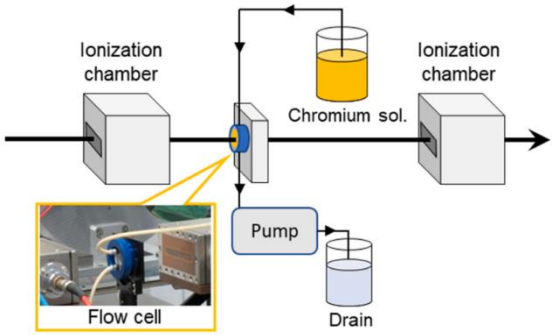

Fig. 1. Schematic diagram of the in situ XAFS adsorption system for studying the chromium reduction behavior in the AO-adsorbent.

We found that the chromium(III) exhibited a sharp edge and a very small pre-edge peak on the X-ray absorption near-edge structure (XANES) spectra while the chromium(VI) exhibited a characteristic pre-edge peak in the vicinity of 5980 eV. During the measurements, the spectra corresponding to the chromium (VI) and chromium (III) coexisted, but the former decreased while the latter increased gradually with increasing adsorption time, indicating that the chromium (VI) was reduced to the chromium (III) in the adsorbents. Furthermore, the desorption of the reduced chromium (III) from the adsorbents has not occurred during the measurement. The chromium(III) is adsorbed by the bidentate coordination of the AO groups in an octahedral structure, which is generally considered to have strong bonds and high stability. The reduction was due to the reaction of chromium (VI) with the AO groups on the adsorbents. Compared with coagulation sedimentation and electrochemical methods, the XAFS method is easy to operate and requires only circulation to complete the treatment. Thus, we believe that this method has the potential for further applications such as remediation of liquid waste from industrial processes.

Machine learning approach for prediction of the grafting yield in radiation induced graft polymerization [2]

In general, the development of new functional polymer materials is time-consuming and expensive, and the properties of the developed materials cannot fully meet the needs. In our project, the radiation-induced graft polymerization techniques have well been established for the development of functional polymer materials. In this study, we established a new, faster and more efficient method for material development using the machine learning approach. This study includes the strategy to find machine learning algorithms to establish polymerization prediction models.

A simple analytical flowchart from data collection to the evaluation of predictive modeling and testing of the predictive model is shown in Fig. 2. In total, 49 monomers were used, including 41 monomers as training data and the remaining 8 monomers as test data obtained from the experiments. The results indicate the extreme gradient boosting model showed higher prediction accuracy than the multiple linear regression model. From the machine learning approach, we can design new graft-type functional polymer materials having certainly functional capacity (grafting yield) and special structures/groups in future works.

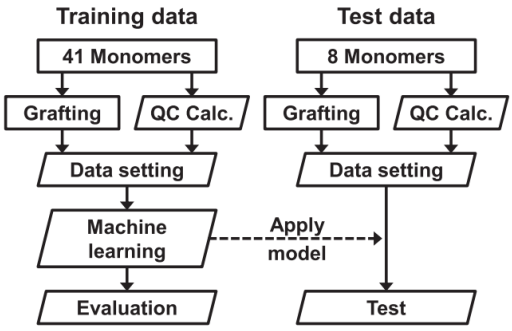

Fig. 2. Simple analytical flow chart from data collection to the evaluation of predictive modeling and testing of the predictive model.

References

[1] N. Hayashi *et al.*, Sep. Purif. Technol. **277**, 119536 (2021). DOI:10.1016/j.seppur.2021.119536

[2] Y. Ueki *et al.*, Appl. Mater. Today **25**, 101158 (2021). DOI:10.1016/j.apmt.2021.101158

P1-6 Project “Biocompatible Materials”

Leader : TAGUCHI Mitsumasa

Project “Biocompatible Materials” has been developing the functional biocompatible materials based on the radiation-induced crosslinking technique. The obtained materials can be utilized for bio-devices in diagnostic, treatment, and regenerative medicine.

Development of novel collagen hydrogels to regulate cellular processes

It has been found that cells cultured on conventional plastic dishes exhibit behaviors that differ from those observed *in vivo*. It is essential to use a culture substrate that mimics the key features of the native extracellular matrix (ECM), a hydrogel of proteins and polysaccharides with a wide range of elasticities (E = ~1 kPa to a few 100 kPa in soft tissue) and nanometer- to micrometer-topographies. Although we can obtain a collagen hydrogel via self-assembly, E is limited to ~1 kPa. Enhancing E values requires aldehydes or carbodiimide cross-likers, that damage cell-binding motifs such as arginine–glycine–aspartic acid (RGD). Thus, we developed a radiation-induced crosslinking method to produce the elasticity- and topography-controlled collagen hydrogels [1].

ECM-derived collagen type-I (porcine skin, Collagen BM, #639-30861; Nitta Gelatin), gelatin (porcine skin, Type A, G1890; Sigma-Aldrich), and collagen peptide (porcine skin, Type A; Nitta Gelatin) solutions were used. After pouring the solutions into cell culture dishes, micro-patterned flexible polydimethylsiloxane molds loaded onto a plastic cover were placed in the solution. The samples were irradiated with ^{60}Co γ-rays in the air at 15–20°C.

The irradiation of γ-rays successfully altered collagen I, gelatin, and collagen peptide solutions into micropatterned hydrogels without altering the amino acid composition ratio, cytocompatibility, and biodegradability. This is because the phenylalanine and tyrosine residues in these proteins become cross-linking points through a reaction with hydroxyl radicals generated in water [2]. The collagen hydrogels had tunable elastic moduli covering a broad range of soft tissues (E = 1–236 kPa) originating from the final collagen density in the hydrogels (0.3–14%) and precise micro-topographies (Fig. 1).

Using collagen hydrogels, we demonstrated various cell responses that could not be observed on conventional cell culture dishes (Fig. 2). The cells responded to elastic cues and changed their morphologies from a round to a flattened shape with increasing E. Depending on E, that is, the density of the collagen network, cells chose to stay on top of the collagen hydrogels or spontaneously migrate into them. HeLa cells became spindle-shaped with increasing E. Epithelial-mesenchymal transition would be induced on collagen hydrogels. We also demonstrated that microtopographies affected cell morphology, and the stiffer microgrooves aligned cells more effectively. Rat cardiomyocytes were aligned with aligned sarcomeres, which drive muscle contraction, and C2C12 myoblasts formed aligned myotubes. Collagen hydrogels can therefore be utilized to induce and control diverse cell behaviors *in vitro*.

In addition to reducing *in vivo* and *in vitro* behavioral disparity of cells, our collagen hydrogels may be useful for strategically inducing and controlling cell function and fate in tissue formation, maintenance, regeneration, and repair, and contribute to applications in tissue engineering and regenerative medicine.

As an example of applied research, we have developed functional postoperative anti-adhesion barriers using novel collagen hydrogels. By mixing or layering collagen gel, which has excellent cell adhesion, and non-adhesive materials such as carboxymethylcellulose and polyvinyl alcohol, we succeeded in achieving both wound healing and adhesion prevention [3, 4]. These materials could be used as highly functional barriers to prevent adhesions after abdominal and pelvic surgery that have severe clinical consequences and negative impact on patient quality of life.

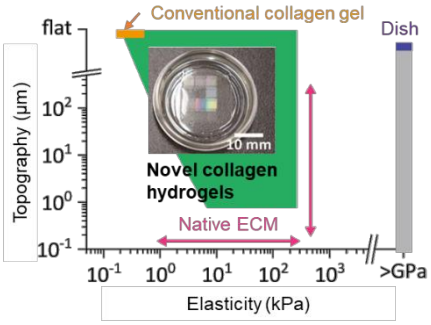

Fig. 1. Developed collagen hydrogel and its elasticity and topographic properties (green colored area) compared to conventional cell culture materials and *in vivo* soft tissue.

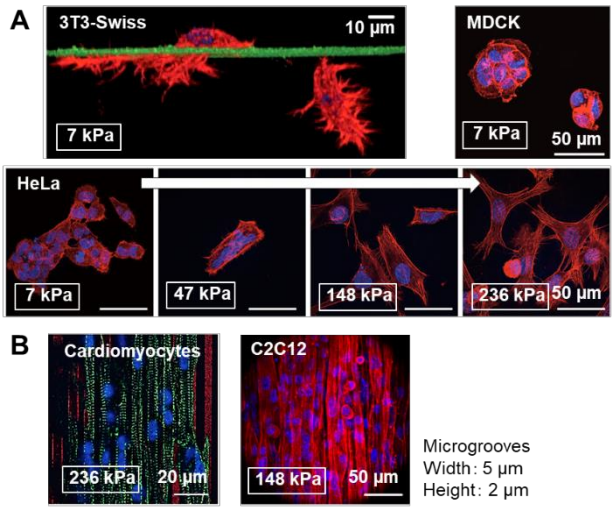

Fig. 2. Various cells cultured on the collagen hydrogels responded to both elasticity and microtopography.

References

[1] T. G. Oyama *et al.*, Biomed. Mater. **16**, 45037 (2021). DOI: 10.1088/1748-605X/ac0452
[2] A. Kimura *et al.*, Radiat. Phys. Chem. **180**, 109287 (2021). DOI: 10.1016/j.radphyschem.2020.109287
[3] A. E. Swilem *et al.*, Polym. Degrad. Stab. **197**, 109856 (2021). DOI: 10.1016/j.polymdegradstab.2022.109856
[4] B.J.D. Barba *et al.*, Polym. Adv. Technol. **32**, 4406 (2021). DOI: 10.1002/pat.5442

P1-7 Project “Spin Photonics in Two-dimensional Materials”

Leader : SAKAI Seiji

Our project aims to develop novel spintronic and spin-photonic devices for future information technology applications by taking advantages of the low dimensionality and quantum electronic properties of two-dimensional (2D) materials and related low-dimensional nanostructures. Advanced quantum beam techniques available at QST enable us to control and design the local atomic structures and spin-/photon-related properties in low-dimensional systems.

This fiscal year, we explored negative spin polarization materials, an emerging class of magnetic materials which provide a new operation principle of spintronic devices in collaboration with the NIMS group (H. Suto, Y. Sakuraba *et al.*) [1]. We focused on a disordered FeCr alloy as a possible candidate of negative spin polarization materials, and its spin-dependent transport properties and local atomic structures were investigated both theoretically and experimentally.

Study on FeCr thin film for a spintronic material with negative spin polarization

The injection of a spin current into magnetic materials to induce switching or precession of magnetization has been a subject of intensive research as the operating principle of spintronic devices such as magnetic tunnel junctions and spin-torque oscillators. In magnetic trilayer structures comprising such spintronic devices, a spin-polarized current generated in the fixed magnetic layer is transported to the free magnetic layer and exerts torque on the free layer magnetization. In most of magnetic materials for spin injection studied so far, the direction of the spin polarization of conduction electrons is “positive” and the same as the magnetization direction. On the other hand, there are also materials having “negative” spin polarization which generates spin current whose direction is opposite to the magnetization direction. Since the trilayer structures consisting of both positive and negative spin polarization magnetic layers show inverse magnetoresistance, i.e., a high (low) resistance for a parallel (antiparallel) magnetic configuration, opposite to normal magnetoresistance in those consist of only positive spin polarization magnetic layers, negative spin polarization materials are of technological importance for providing an additional degree of freedom in designing spintronic devices.

In the present study, we theoretically and experimentally investigated a disordered FeCr alloy which is a promising candidate for negative spin polarization materials [1].

First-principles calculations for the FeCr alloy predicted that despite the electronic density of states (DOS) at the Fermi level being positively spin-polarized, the conductivity of the minority-spin bands is markedly higher than that of the majority-spin bands, indicating nearly complete negative spin polarization of spin current generated therein. The large negative spin polarization in the conductance was attributed to the weak scattering of conduction electrons in the minority-spin bands due to the nearly identical partial DOS of Fe and Cr.

Magnetoresistance measurements conducted for giant magnetoresistive (GMR) device using a FeCr alloy thin film ($Fe_{0.7}Cr_{0.3}$) as one magnetic layer of the magnetic trilayer structure successfully provided the direct evidence of the negative spin polarization in the FeCr alloy. However, the amplitude of negative spin polarization (28%) estimated from the GMR measurements was much smaller than the theoretically predicted value (~100%).

To gain microscopic insight into the mechanism of the small negative spin polarization in the FeCr thin film, the local atomic structures of the films were analyzed by using the advanced synchrotron Mössbauer spectroscopy technique which was recently developed together in partnership with the Kansai Photon Science Institute [2, 3]. The Mössbauer spectroscopy indicated the presence of the atomic-scale inhomogeneity of the Fe and Cr composition even in the as-deposited FeCr thin film. Furthermore, Fe-rich regions were formed by annealing in the device fabrication process, owing to the phase separation nature of the Fe-Cr system. This inhomogeneity could be the origin of the small negative spin polarization estimated from the GMR device. This suggests that fabricating uniformly disordered FeCr thin films, for example by cooling the substrate to low temperatures during the film deposition, could improve the negative spin polarization.

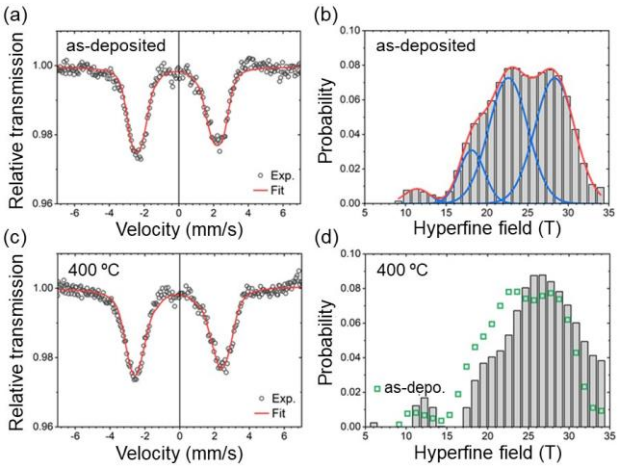

Fig. 1. (a) and (e) Mössbauer spectra of FeCr thin film ($Fe_{0.7}Cr_{0.3}$) in the as-deposited state and after annealing at 400 ºC. Fitting curves for the analysis of the hyperfine field distribution are also shown. (b) and (d) hyperfine field distribution calculated from (a) and (c), respectively [1]. Fitting by four Gaussian functions is depicted in (b), and the data in (b) are also plotted in (d) for comparison. The hyperfine field distributions in (b) and (d) are responsible for the number of Cr atoms neighboring the Fe atom. These results indicate short-range inhomogeneity in the as-deposited state and its development by annealing at 400 ºC.

References

[1] H. Suto *et al.*, J. Magn. Magn. Mater. **557**, 169474 (2022). DOI: 10.1016/j.jmmm.2022.169474
[2] T. Mitsui, *et al.*, Phys. Rev. Lett. **125**, 236806 (2020) (*Editors' Suggestion & Featured in Physics*). DOI: 10.1103/PhysRevLett.125.236806
[3] J. Okabayashi, *et al.*, Phys. Rev. B **103**, 104435 (2021). DOI: 10.1103/PhysRevB.103.104435

P1-8 Project “EUV Ultra-fine Fabrication”

Chief : YAMAMOTO Hiroki

Project “EUV Ultra-fine Fabrication” has been developing the functional polymer materials such as high-performance resist materials for extreme ultraviolet (EUV) and next generation EUV lithography. We have synthesized resist materials such as metal resist and block copolymer with chemical synthesis or by using quantum beams such as γ-rays and electron beam (EB). We aim to develop resist materials for EUV lithography and conduct fusion between top-down and bottom-up nanofabrication for next generation EUV lithography. We report herein two recent study: Comparison of photoresist sensitivity between KrF, EB, EUV exposure and Dependence of Dissolution Kinetics of Main-Chain Scission Type Resists on Molecular Weight.

Comparison of photoresist sensitivity between KrF, EB and EUV exposure [1]

It has been reported that the good correlation in sensitivity and resolution between EUV exposure and EB exposure because of the similar acid generation mechanism in resists during exposure. However, in the early stages of EUV resist development, there are problems on the points of the cost and time-consuming to evaluate all EUV resist materials by EB exposure. Therefore, we investigated the possibility of using KrF exposure as the initial screening of EUV resists.

Using various kind of photoresists, we measured sensitivity of photoresists by KrF, EB and EUV exposure, and calculated the correlation between each exposure. Fig.1 shows correlation among sensitivity in six kinds of photoresists between KrF, EB, EUV exposure. As a result, it was found that there was some correlation between KrF, EB and EUV exposure in resists except for the main chain scission type. Especially the correlation between KrF and EUV agree well with the number of acid generation calculated by the simulation.

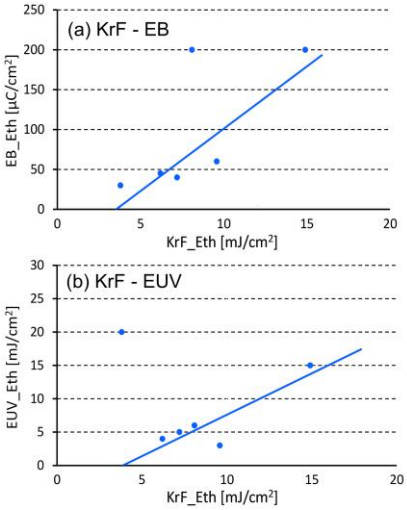

Fig. 1. Comparison of photoresist sensitivity curves of six kinds of photoresists between (a) KrF and EB, and (b) KrF-EUV).

Dependence of dissolution kinetics of main-chain scission type resists on molecular weight [2]

It is challenging to continue to implement EUV lithography for mass production because the demand for the EUV resist materials is very strict. Chemically amplified resist has been used for the purpose of both high sensitivity and high resolution. With the progress of miniaturization, the diffusion of acids used as a catalyst becomes an obstacle to the improvement of resist performance such as resolution. Therefore, it is difficult for chemically amplified resists to obtain sub-10 nm patterning.

Main chain scission type resists such as poly(methyl methacrylate) (PMMA) and ZEP520A induce main chain scissions after EB or EUV irradiation. it is thought they can improve resolution and LWR owing to the removing of resolution blur. Therefore, main-chain-scission-type resists have recently attracted much attention.

However, the details of the dissolution kinetics in main chain scission type resists remains unclear in organic solvent. In this study, the dissolution kinetics and molecular weight in main chain scission type resists such as PMMA and ZEP520A were investigated using a quartz crystal microbalance (QCM) method and a Gel Permeation Chromatography (GPC) to clarify the effects of the molecular weight after polymer degradation on the dissolution kinetics.

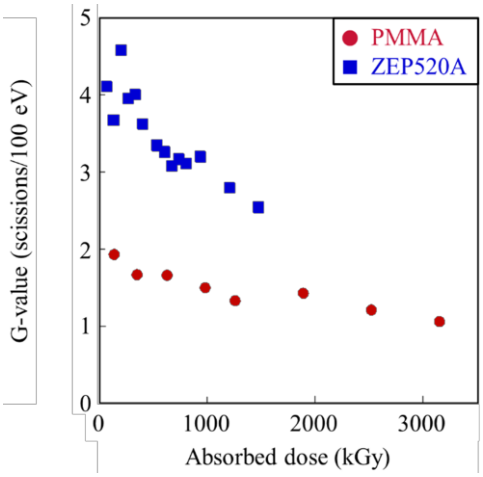

Fig. 2. Relationship between absorbed dose and G-values in PMMA and ZEP520A.

G-values of main chain scissions in PMMA and ZEP520A are estimated using GPC measurement. Figure 2 shows the relationship between absorbed dose and G-values in PMMA and ZEP520A. The G-value of ZEP520A showed higher G-values than that of PMMA. Also, dissolution behavior of PMMA and ZEP520A were investigated using QCM. There are three molecular weight regions in PMMA, whereas there are only two molecular weight regions in ZEP 520A. We couldn’t observe the middle molecular weight region, where swelling and dissolution occur simultaneously in PMMA. This region affects lithographic performance. These results indicate that ZEP520A is better to be better lithographic performance.

References

[1] Y. Ohta *et al.*, J. Photopolym. Sci. Technol. **35**, in press.
[2] A. Konda *et al.*, J. Photopolym. Sci. Technol. **35**, in press.

P1-9 Project "Element Separation and Analysis Research"

Leader: OHBA Hironori

Quantum beams are versatile sources for materials processing. Our project explores the basic process of the laser-matter interaction to separate elements from industrial waste liquid or analyze elements under harsh environments. We applied a new analytical method based on X-ray absorption fine structure (XAFS) and X-ray absorption near edge structure (XANES) as X-ray absorption spectroscopy for element separation to elucidate the laser-induced particle formation mechanism. For element analysis, we study the sensitive detection of element in an aqueous solution using laser-induced breakdown spectroscopy (LIBS). The recent results of our project are introduced as follows.

Dispersive XAFS study on the laser-Induced reduction of a Rh^{3+} ion complex: Presence of a Rh^{+} intermediate in direct photoreduction [1]

Photoreduction of precious metal (PM) ion complexes in aqueous and organic solvents has been studied as a method for preparing PM nanoparticles, recovering PMs from industrial waste, and modification of catalyst surfaces with PMs. Based on reaction mechanisms, photoreduction can be classified into (i) direct photoreduction, (ii) photocatalytic reduction, and (iii) photo activator reduction. This time, the reaction mechanism of the direct photo-reduction of a Rh^{3+} ion complex to a Rh^{0} species induced by pulsed ultraviolet laser irradiation was studied using dispersive XAFS. The time-resolved XANES showed the absence of isosbestic points and suggested that more than two Rh^{n+} species contribute toward the direct photoreduction of Rh^{3+}. Analysis of the time-resolved XANES data by singular value deposition showed that the direct photoreduction involves three Rh^{n+} species. Multivariate curve resolution by alternating least-squares analysis of the time-resolved XANES data gave pure spectra and the concentration profiles of the three Rh^{n+} species. The Rh^{n+} species were assigned to Rh^{3+}, Rh^{+}, and Rh^{0} based on the features of the pure XANES spectra. The concentration profiles suggested that the direct photoreduction proceeds in the order of $Rh^{3+} \rightarrow Rh^{+} \rightarrow Rh^{0}$. A reaction mechanism, which was proposed involving photoreductions of Rh^{3+} and Rh^{+}, photoinduced autocatalytic reductions of Rh^{3+} and Rh^{+}, and photooxidation of Rh^{+}, well reproduced the concentration profiles of three Rh^{n+} species. The direct photoreduction mechanism is schematically shown in Fig. 1.

Highly sensitive detection of sodium in aqueous solutions using laser-induced breakdown spectroscopy with liquid sheet jets [2]

Recently, ultrathin liquid sheet jets were applied to LIBS measurements [3]. The LIBS signal intensity depended largely on the sheet thickness; the 20 μm sheet jet yielded the highest optical emission among a range of 5–80 μm jets [3]. The presence of an optimal thickness was attributed to a compromise between minimizing splash and maximizing ablation volume. This stands in contrast to the conventional cylindrical jet (> 100 μm), for which a thicker jet is favorable for the sensitive detection of Na, indicating that a large ablation volume is advantageous for achieving high emission intensities in this range of thickness. Therefore, it is worth comparing the ultrathin sheet jet with the thick cylindrical jet in terms of the Na detection sensitivity of LIBS. In this study we examined the difference in Na detection sensitivity between LIBS with the sheet jet and LIBS with the cylindrical jet, combining both methods with conventional single-pulse ablation. The sensitivities of two types of liquid jets were compared: a liquid cylindrical jet with a diameter of 500 μm and a liquid sheet jet with a thickness of 20 μm. Compared with the cylindrical jet, the liquid sheet jet effectively reduced the splash from the laser-irradiated surface and produced long-lived luminous plasma. The limit of detection (LOD) of Na was determined to be 0.57 μg/L for the sheet jet and 10.5 μg/L for the cylindrical jet as shown in Fig. 2. The LOD obtained for the sheet jet was comparable to those obtained for commercially available inductively coupled plasma emission spectrometers. This method is expected to be applied to difficult-to-treat waste liquids containing precious metals in near future.

References

[1] M. Saeki, *et al.*, J. Phys. Chem. C **126**, 5607 (2022). DOI: 10.1021/acs.jpcc.1c10160

[2] R. Nakanishi, *et al.*, Opt. Express **29**, 5205 (2021). DOI: 10.1364/OE.415308

[3] H. Ohba, *et al.*, Opt. Express **22**, 24478 (2014). DOI: 10.1364/OE.22.024478

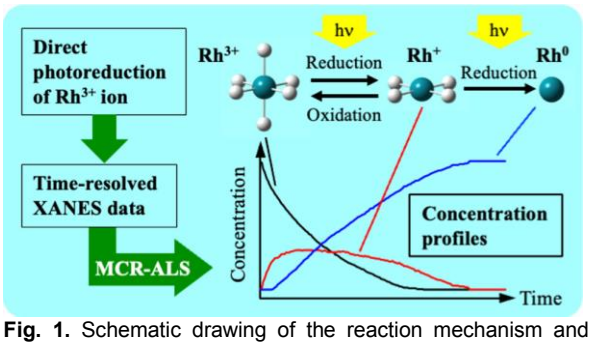

Fig. 1. Schematic drawing of the reaction mechanism and its analysis method.

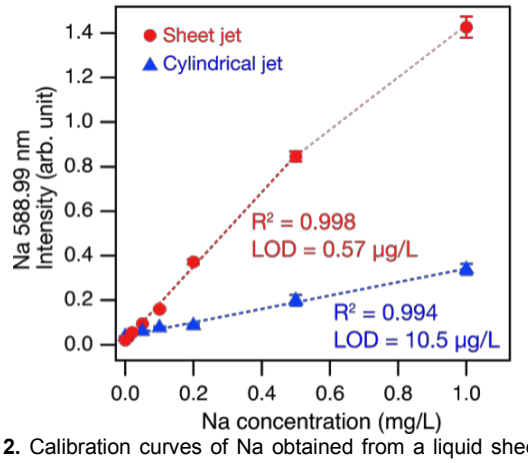

Fig. 2. Calibration curves of Na obtained from a liquid sheet jet and a liquid column jet.

P1-10 Advanced Functional Polymer Materials Research Group

Leader : MAEKAWA Yasunari

The research of "Advanced Functional Polymer Materials Group" has been focused on efficient development techniques for advanced functional polymer materials, which are widely used in advanced devices and construction materials. The technique includes materials informatics such as machine learning and neural network in addition to the established radiation techniques regarding the radiation-induced graft polymerization and X-ray/neutron structure analysis. This group has been conducting mainly the R&D for "Advanced functional polymer materials alliance" under QST innovation hub program in collaboration with participant companies.

Research results of "Advanced functional polymer materials alliance"

On the alliance project of the 5th year, the main achievements in four research subjects are as follows.

(1) Grafting yields prediction: To find quickly optimal experimental conditions, we constructed a GPBO model that combined Gaussian process (GP) and Bayesian optimization (BO) as the machine learning algorithms. The experimental conditions such as dose, grafting temperature, reaction time, and monomer concentration were optimized by using the GPBO model with only 62 experimental data, and we were able to predict the conditions that maximize the degree of grafting.

(2) Structural data accumulation: We analyzed the hierarchical structures of the proton-conducting electrolyte membranes (PEM) using an atomic force microscope and small angle X-ray/neutron scattering. The hydrophobic/hydrophilic domain structure in PEMs based on poly(ethylene-co-tetrafluoroethylene) (ETFE-PEM) was digitalized by dissipative particle dynamics simulation. It was found that the structure of ETFE-PEM can be well predicted by optimizing the terminal structure of monomer constituting the graft polymer.

(3) Property prediction: We evaluated the properties of the anion conducting electrolyte membranes (AEM), such as anion conductivity (AC) and water uptake (WU), using machine learning. In the random forest regression analysis, the AC, WU, and ionic conduction efficiency (AC/WU) were predicted and the importance of the explanatory variables was estimated. As a result of the evaluation, it was found that the ion exchange capacity showed a significant contribution to the explanatory variables.

(4) Database preparation: We continued the data migration work and increased the number of the data concerning the graft-type polymer materials. We improved the user interface for efficient utilization of the graft database.

Integrating the hydrophobic alcohol adding into radiation-induced emulsion graft polymerization method [1]

The emulsion graft polymerization method is an economical way to obtain higher reaction efficiency than the general organic solvent system. Upon immersing a polymer base material therein, the monomer micelles adhere to the polymer base material due to the action of the surfactant. As a result, the monomer concentration in the vicinity of the polymer base material surface becomes locally concentrated, and efficient migration occurs on the inside of the polymer base material to enhance the graft polymerization reaction. However, the drawback of this emulsion graft polymerization method is that at low monomer concentration the monomer dissolves in water and stable monomer micelles cannot be formed. For example, glycidyl methacrylate (GMA), which is a monomer comprising epoxy groups that facilitate the functionalization of a polymer material, is a typical monomer applied in emulsion graft polymerization. However, in an aqueous solvent, it dissolves at low concentrations (2 wt% or less), the stability of the formed monomer micelles is low, and the graft polymerization rate decreases. We focused on the hydrophobic alcohol such as 1-octanol. It is well known that hydrophobic alcohols work as a stabilizer for micelles. Therefore, we report that hydrophobic alcohol added emulsion graft polymerization method, in which by adding hydrophobic alcohol to a GMA monomer emulsion system, the graft polymerization rate was increased due to the stabilized GMA monomer micelles.

Fig. 1a and b show the degree of grafting at 0.5 and 0.25 wt% GMA monomer concentration, respectively. By adding 0.5 wt% of 1-octanol to the GMA monomer emulsion the degree of grafting was 4 times higher than in the case without addition at both 0.5 and 0.25 wt% GMA concentration. Surprisingly, even at the extremely low monomer concentration such as 0.25 wt%, the degree of grafting exceeded 80%. In emulsion graft polymerization, a rapid decrease in the grafting rate is often observed within a few hours. This is because the consumption of monomer destabilizes the monomer micelles. However, in the presence of 1-octanol, there was no sudden decrease in the grafting rate. This result suggests that the added 1-octanol strongly stabilizes the monomer micelles even after the monomer is consumed by the progress of the graft polymerization reaction. Thus, this method can be expected to be useful as an economic and eco-friendly graft polymerization method.

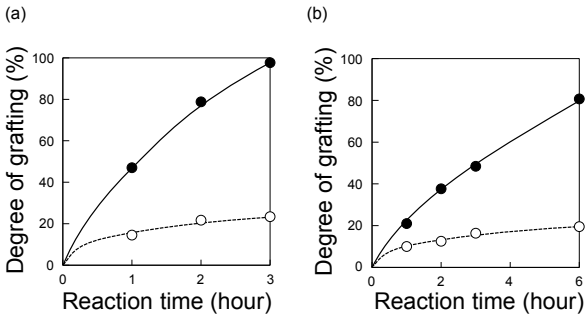

Fig. 1. Graft polymerization at the 0.5 (a) and 0.25 wt% (b) GMA monomer concentration with (●) and without 0.5 wt% 1-octanol (○).

Reference

[1] M. Omichi *et al.*, Radiat. Phys. Chem. **191**, 109867 (2022). DOI: 10.1016/j.radphyschem.2021.109867

P1-11 Quantum Sensing and Information Materials Research Group

Leader : OHSHIMA Takeshi

Quantum technologies such as quantum sensing, quantum information and quantum computing are required to realize Super Smart Society. Therefore, R&D for quantum technologies are intensively carried out all over the world now. We study quantum technologies together with domestic and international Universities and Research Institutes. We focus on color centers which act as spin defects and/or single photon emitters in wide bandgap semiconductors. In addition, we propose a new technology combining spintronics with photonics "spin-photonics". For color centers, we create such defects in wide bandgap semiconductors, *e.g.* diamond, silicon carbide (SiC) and gallium nitride using energetic particles. We investigate the optical and spin properties of color centers. In addition, we try to fabricate electronic devices with such spin defects/single photon emitters to realize quantum devices. For spin-photonics, we study technologies for new devices in which the interaction between spins and photons is applied to realize extremely low energy consumption devices. The research results that link to this group are also shown in the results obtained by the research projects "semiconductor radiation effects" and "spintronics in 2D materials"

Electrical detection of negatively charged silicon vacancy in silicon carbide

Negatively charged silicon vacancy (V_{Si}) in silicon carbide (SiC) is known as a quantum defect which act as a spin qubit and a quantum sensor at room temperature [1]. To manipulate and readout its spin states, the optically detected magnetic resonance (ODMR) technique is usually applied [2]. On the other hand, the electrical detection of V_{Si} is an interesting topic too since SiC is suitable for electric devices and quantum devices combined with electric devices are expected. However, the technique for electrically manipulation of V_{Si} properties has not yet been developed. In this study, we fabricate metal-oxide-semiconductor field effect transistors (MOSFETs) on hexagonal (4H) SiC, and detect V_{Si} in the MOSFETs using electrically detected magnetic resonance (EDMR) [3].

The MOSFETs used in this study were fabricated on an epitaxial layer grown on a Si-face 4H-SiC substrate by chemical vapor deposition. The gate oxide was formed using thermal oxidation followed by NO gas annealing. The thickness of the gate oxide was about 50 nm. V_{Si}s were introduced in 4H-SiC MOSFETs by irradiation of 80 keV-protons at 1×10^{13} /cm^2 at room temperature. The energy of protons was selected to create V_{Si} in the channel region of the MOSFETs by a Monte Carlo simulation code "SRIM". EDMR for 4H-SiC MOSFETs were measured at room temperature.

Figures 1 shows magnetic field angular dependence of EDMR spectra for MOSFETs before and after proton irradiation. As show in Fig. 1, peaks of EDMR signals (pointed out by red allows) are detected from MOSFETs irradiated with protons although no significant peaks are observed at the same positions for non-irradiated MOSFETs. Comparing with theoretical calculation, the peaks pointed out by red allows were concluded to be ODMR signals originated from V_{Si}.

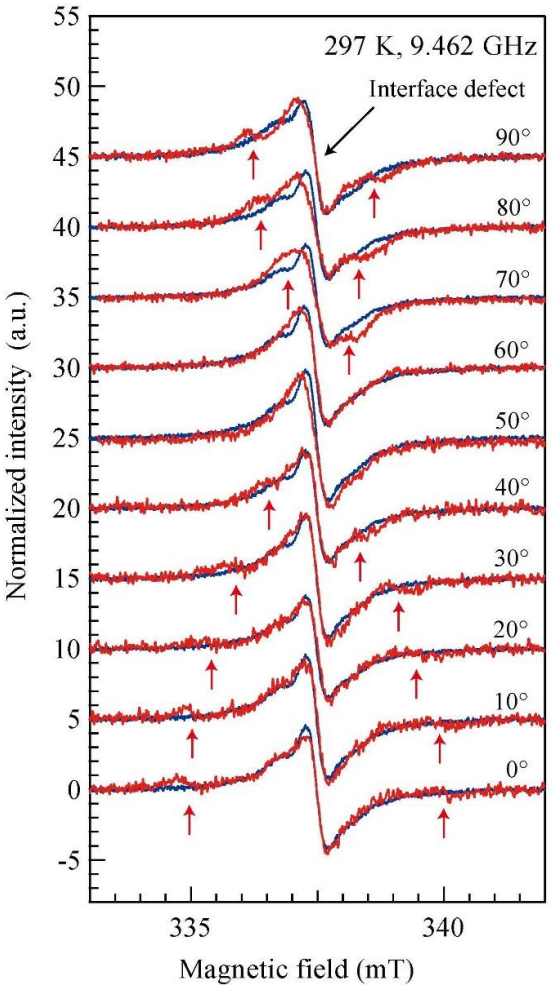

Fig. 1. Magnetic field angular dependence of EDMR spectra for proton irradiated 4H-SiC MOSFETs at room temperature [3]. Red and blue lines show EDMR spectra for MOSFETS after and before proton irradiation, respectively. The black arrow indicates the EDMR signal from the interface defects. Red arrows correspond to a spin defect of V_{Si}.

In addition, the intensity of EDMR signals for V_{Si} was measured under the different gate bias condition. As a result, the EDMR signals for V_{Si} increase around the gate bias between -2 and 1 V. This result can be explained in terms of the relationship between the Fermi level and the charge stability (thus -1 but not -2 nor 0) of V_{Si}.

References

[1] M. Widmann *et al.*, Nat. Mater. **14**, 164 (2015). DOI: 10.1038/nmat4145
[2] Y. Yamazaki *et al.*, J. Mater. Res. **33**, 3355 (2018). DOI: 10.1557/jmr.2018.302
[3] Y Abe *et al.*, Appl. Phys. Lett. **120**, 064001 (2022). DOI: 10.3390/qubs6010002

Part Ⅰ

2. Life Science

P2-1 Project “Microbeam Radiation Biology” ····· 14
Leader : FUNAYAMA Tomoo

P2-2 Project “Ion Beam Mutagenesis” ····· 15
Leader : OONO Yutaka

P2-3 Project “Medical Radioisotope Application” ····· 16
Leader : ISHIOKA Noriko S.

P2-4 Project “Radiotracer Imaging” ····· 17
Leader : KAWACHI Naoki

P2-5 Project “Generation of Radioisotopes with Accelerator Neutrons” ····· 18
Leader : HASHIMOTO Kazuyuki

P2-1 Project “Microbeam Radiation Biology”

Leader : FUNAYAMA Tomoo

The project "Microbeam Radiation Biology" promotes research for developing heavy-ion microbeam technology and for elucidating the radiation response mechanisms of livings using the developed technology.

Heavy ions with a high LET, which have higher biological effect, provide a concentrated energy deposition to the livings and cause severe damage on DNA. However, this concentrated energy deposition causes inhomogeneity of the spatial distribution of the energy deposition at the micrometer scale. To solve this problem, a technique for targeting cells under a microscope using a micrometer-scale beam spot, which is smaller than the cell, is required.

This microbeam irradiation technology allows to irradiate heavy ions only to a part of a cell or a cell population. Irradiating a specific part of an individual with microbeam enables to elucidate the mechanism of biological functions involving the irradiated region. Taking advantage of this feature, we are elucidating the response of individual organisms to local irradiation.

Induction of testis-ova with microbeam irradiation in p53-deficient medaka testis [1]

Teleost are sexually bipotential, and induction of testis-ova, in which spermatogonia differentiate into egg-like cells, can be observed. It was reported that gamma irradiation induces testis-ova differentiation in medaka testis lacking the p53 gene. Estrogen administration has also been reported to cause testis-ova differentiation in medaka testis. On the other hand, an increase in serum estrogen levels is known to be observed in irradiated mice. However, it is not clear whether radiation-induced differentiation of medaka testis-ova is mediated by increased serum estrogen levels. Thus, to clarify whether medaka testis-ova differentiation is mediated by increased estrogen levels in the blood, upregulated by radiation, we irradiated the testes of adult medaka fish locally with a microbeam and observed the formation of testis-ova after irradiation. In the testis of 7 days after irradiation, clusters of testis-ova cells were observed in the microbeam irradiated region. However, only normal spermatogonia were observed in the other surrounding spermatogonia cysts, as well as in the non-irradiated control testis. These results indicate that radiation-induced elevation of hormone signaling is not involved in the differentiation of testis-ova in medaka fish.

Autophagy is induced in *Caenorhabditis elegans* irradiated at very high doses [2]

Irradiation of adult *C. elegans* worms with 0.5 kGy of gamma or carbon radiation causes a decrease in whole-body locomotion. Our previous study showed that this reduced whole-body locomotion is recovered within a few hours after irradiation. These findings indicate that *C. elegans* has extremely high tolerance to radiation. However, the mechanism of this short-term recovery from the radiation effect remained unclear. Autophagy is an important biological homeostasis mechanism in eukaryotic cells. Autophagy degrades damaged proteins in injured cells and is involved in the recovery of cell function. Therefore, we investigated how autophagy works in irradiated *C. elegans* cells. Even in *C. elegans* irradiated with very high doses of radiation (3 kGy), we observed a certain recovery of whole-body locomotion, which was reduced by the irradiation. In this irradiated nematode, the induction of a gene involved in the function of autophagy in the cell was observed by fluorescence visualization. Autophagy plays a role in preventing the accumulation of abnormal proteins in cells, recycling proteins in response to changes in the cellular environment and eliminating pathogens. Our result supports that autophagy contributes to recovery from radiation damage, resulting in extremely high radioresistance in *C. elegans*.

Development of a novel assay method to detect response of *Caenorhabditis elegans* to extremely low concentration chemicals [3]

Our project has been studying the mechanism of chemotaxis of *C. elegans* using microbeam irradiation to understand the neural network function of the living organism. However, the changes induced by microbeam local irradiation were subtle enough not to be captured by conventional chemotaxis assay methods for *C. elegans*. The conventional chemotaxis assay for *C. elegans* has been widely used for more than 30 years. This method has some accuracy and efficiency issues in detecting slight changes in chemotaxis caused by irradiation, such as the influence of anesthetics that trap the attracted worms and the complexity of counting the number of worms on the agar plate. Therefore, we developed a novel test method, named Pond Assay for the Sensory Systems (PASS). In this method, a pore is made on the agar plate, filled with the test solution, and the olfactory and taste responses of the worms are examined. Worms that are attracted fall into the test solution pond and trapped without anesthesia because they cannot escape. The accuracy and efficiency of the assay has improved dramatically from the conventional method. This is because the response can only be evaluated by counting worms that have fallen into the pond of test solution. The performance of the PASS was evaluated by a chemotaxis test using diacetyl. The results showed that nematodes accurately sensed lower concentrations of diacetyl than previously reported. This test assay will greatly contribute to our future research on the mechanism of chemotaxis in *C. elegans* using microbeam irradiation.

References

[1] K. Nagata *et al.*, Cytologia **87** 1 (2022). DOI: 10.1508/cytologia.87.1
[2] A. Yamasaki *et al.*, Int. J. Mol. Sci. **22** 9810 (2021). DOI: 10.3390/ijms22189810
[3] M. Suzuki *et al.*, Biology **11** 335 (2022). DOI: 10.3390/biology11020335

P2-2 Project “Ion Beam Mutagenesis”

Leader : OONO Yutaka

Ion beams are useful mutagens to improve characteristics of plant and microbes because ion beams are thought to cause mutations via a mechanism distinct from those of chemical mutagens or gamma rays. Our project aims to understand feature of ion-beam-induced mutations and develop applications of ion beam mutagenesis in basic biology and applied biotechnology. We use a next generation sequencing technique to investigate the ion-beam- and gamma-ray-induced mutations at both genome wide and specific gene levels. In addition, we try to establish valuable mutants in various type of plants, algae, yeasts, fungi, and bacteria under collaborations with academic or industrial research organizations. Revealing biological basis of radiation response and resistance in molecular level is another major business in our project.

Analysis M1 genome reveals mutation-size-preferable sequence signatures [1]

Quantum beams such as ion beams and gamma rays induce various types of mutations in the genome DNA of organisms. Although most of mutations induced are single base substitutions (SBS)s and small-sized deletions or insertions, presence of relatively high ratio of rearrangements, which includes large DNA (≧100 bp) deletions (DEL)s, inversions, and chromosomal translocations are characteristic of mutation profile induced by quantum beams. The rearrangements usually have high impact on cell viability. Therefore, they are hardly transmitted to M2 generation (the second generation of mutagenized plants produced via self-pollination). Because an irradiated M1 plant is a chimera, which is consists of different cells having a different set of mutations, mutation profiles induced by quantum beams have been characterized using M2 plants or later generation. Therefore, not much information about the feature of the rearrangements induced by quantum beams is available. Nevertheless, characterization of mutation profile in a M1 plant (a mutagenized plant individual) is important because many crops and ornamental plants are reproduced through vegetative propagation and understanding genetic effects of quantum beams in M1 plants is necessary for effective breeding of these plants. To overcome difficulty of investigating mutation profile in M1 plants, we established triple heterozygous Arabidopsis plants of three anthocyanin biosynthetic genes (*TT4*, *TT3*, and *TT18*). If one of the *TT* genes is functionally disrupted by a mutation, a cell containing this mutation cannot produce anthocyanins and tissues originated from the mutated cell are deficient in red color pigments in the M1 plants. By extracting and analyzing genome DNA from these clonal tissues after gamma irradiation, mutation profile in the M1 plants were successfully revealed. The result showed that although mutation profile of the M1 tissues was comparable with that of M2 plants, proportion of rearrangements was higher in the genome of M1 tissues than M2 plants. Furthermore, analyzing a number of rearrangements and DELs reveals mutation-size-preferable sequence signatures in their rejoined sites (Fig.1). The frequency of insertions of nucleotides at the rejoined sites was significantly higher in the rearrangements than in the small (2~9 bp) and in the medium (10-99 bp) DELs, while the frequency of presence of micro homology (MH) sequences was highest in the medium DELs. Rejoined sites without an insertion and without MH were mostly found in the small DELs. These signatures implied that rearrangements, medium DELs, and small DELs tend to be formed by distinctive processes.

Microalgae biofuels: converting carbohydrates into oils [2,3]

Green microalgae have been expected as next generation biofuel producers that are able to synthesis lipids from CO_2 using sunlight as the energy source. However, in lipid-rich microalgae such as *Chlamydomonas* sp, lipid accumulation was decreased under light/dark cycling and under nitrate-replete conditions. To overcome these problems, by collaboration with Kobe University, we irradiated the *Chlamydomonas* strain JSC4 by carbon ion beams, cultured them under light/dark condition, and screened lipid-rich cells from the culture by using fluorescence activated cell sorting (FACS). The selected strain KOR1 has destructive mutations in the gene of starch debranching enzyme. The mutations are probably responsible for rapid carbohydrate degradation together with increased lipid and carotenoid contents in the strain KOR1. Next, we again irradiated the strain KOR1 by carbon ion beams and screened lipid-rich cells under nitrate-replate conditions. The obtained strains KAC1710 and KAC1801 showed 1.5-fold and 2.1-fold lipid content of the strain KOR1, respectively, in the abundant nitrate condition. Metabolome analysis revealed that the pool size of pyruvate was significantly increased in the both strains. We believe these improved strains could contribute to establish an effective process for practical microalgal biofuel production.

References

[1] S. Kitamura *et al*., PLoS Genet. **18**, e1009979 (2022). DOI:10.1371/journal.pgen.1009979
[2] Y. Kato *et al*., Commun. Biol. **4**, 450 (2021). DOI: 10.1038/s42003-021-01976-8
[3] T. Oyama *et al*., Algal. Res. **60**, 102544 (2021). DOI: 10.1016/j. algal.2021.102544

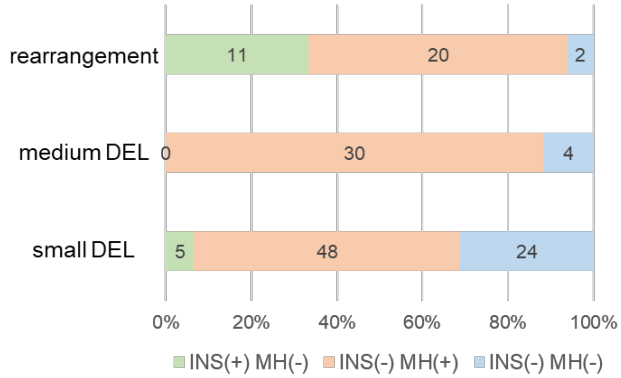

Fig. 1. Comparison of the characteristics among mutations; rearrangements, medium DELs, and small DELs. The ratio and number of rejoined sites with (+) and without (-) an insertion (INS) and/or MH are provided.

P2-3 Project “Medical Radioisotope Application”

Leader : ISHIOKA Noriko S.

The research objective of our project is to develop the radiopharmaceuticals labeled with useful radioisotopes (RI) for cancer theranostics. Our project focuses on the research of the RI drug delivery system (RI-DDS) using bioactive compounds such as antibodies and peptides in order to make the most of the ability of RI. To achieve our research objective, we also address effective RI production, the molecular mechanisms of radionuclide therapy, and dosimetry.

Dosimetry: a novel absorbed dose conversion method using pharmacokinetics of radiopharmaceuticals [1]

Radiopharmaceuticals deliver selectively RI to an organ or tumor tissue through physiological and metabolic processes. The distribution of RI can be traced by external measurement of emitted gamma-rays from RI themselves. Also, radiopharmaceuticals labelled with alpha or beta-emitting RI can destroy tumor cells because of their highly focused and deposited energy. Thus, radiopharmaceuticals have been used for both diagnostic and therapeutic purposes, and the unique duality is called “theranostics”.

Dosimetry for radiopharmaceutical therapy (RPT) is basically based on the schema recommended by the committee on Medical Internal Radiation Dose (MIRD). The MIRD method uses the pharmacokinetics of radiopharmaceuticals, calculates energy deposition of radiation from RI in the source organ to the target organ by Monte Carlo simulation, and determines the absorbed dose of the target organ. Recently, NRG-NCI-Workshop summarized that there were some challenging issues for RPT-dosimetry: optimizing imaging time points, alpha-dosimetry, and multi-scale dosimetry [2]. However, there has been no attempt to consider dosimetry from the viewpoint of theranostics.

Theranostics achieves diagnostic and therapeutic goals by changing the labeling RI. To take advantages of theranostics with diagnostic data available, we focused on the important pharmacokinetics in dosimetry. At first, we convert the pharmacokinetics of radiopharmaceuticals in diagnosis to that of therapeutic ones, and finally simulate the absorbed dose using converted pharmacokinetics of therapeutic ones. In particular, we aimed to simulate *in vivo* ^{211}At-labeled *meta*-benzylguanidine (^{211}At-MABG) absorbed doses by the dose conversion methods using ^{131}I-MIBG biodistribution data.

We used the framework of the Monte Carlo method to create several thousand virtual experimental data sets of activity concentrations (kBq/g) to get the statistical information. Virtual experiments showed that ^{211}At-MABG and ^{131}I-MIBG had similar properties of initial activity concentrations and biological pharmacokinetic parameters. Therefore, we firstly used the decay-corrected dose (pharmacokinetic) conversion that the half-life of ^{131}I was replaced with that of ^{211}At to evaluate the absorbed dose of ^{211}At-MABG. The decay-corrected dose conversion showed the relatively good simulation of true absorbed ^{211}At-MABG dose, but there were the differences from several to several tens of percent between them. We looked for the cause of the difference, and found out the ratio of the percent injected dose (%ID)/g as the cause. The trend of the ratios of the difference of simulated and true absorbed doses was almost perfectly matched to that of %ID/g observed 1 h after injection (Fig. 1). Next, we tried further correction by multiplying the decay-corrected absorbed doses of ^{211}At-MABG by the inverse of the ratio of %ID/g. This inverse ratio, we called the RAP (RAtio of Pharmacokinetics) coefficient, since we use the Ratio of Pharmacokinetics for dose conversion, showed a great improvement in the dose conversion (Fig. 2).

In conclusion, we challenged the hypothesis that the biodistribution data from diagnosis or previous treatments of ^{131}I-MIBG could be used to simulate approximate absorbed dose of ^{211}At-MABG. Using %ID/g, we found the novel dose conversion method, RAP.

Dosimetry: Optimal timing of a single biodistribution measurement for the RAP dose conversion method [3]

The RAP dose conversion displayed a good simulation of ^{211}At-MABG absorbed doses using a pharmacokinetics of ^{131}I-MIBG [1]. However, there were some mathematical ambiguities in determing the optimal timing of a single measurement of the %ID/g. Thus, we aimed to mathematically reconstruct the RAP method and to examine the optimal timing of a single measurement. We derived a new formalism of the RAP dose conversion method at time *t*. In addition, we acquired a formula to determine the optimal timing of a single measurement of the %ID/g, assuming the one-compartment model for biological clearance. The present formalism revealed optimizing imaging time points on absorbed dose conversion, RAP, between two radiopharmaceuticals.

References

[1] T. Sakashita *et al.*, Ann. Nucl. Med. **35**, 121 (2021). DOI: 10.1007/s12149-020-01548-67
[2] E. Roncali *et al.*, J. Nucl. Med. **62**, 1133 (2021). DOI: 10.2967/jnumed.120.255547
[3] T. Sakashita *et al.*, EJNMMI Phys. **8**, 80 (2021). DOI: 10.1186/s40658-021-00425-z

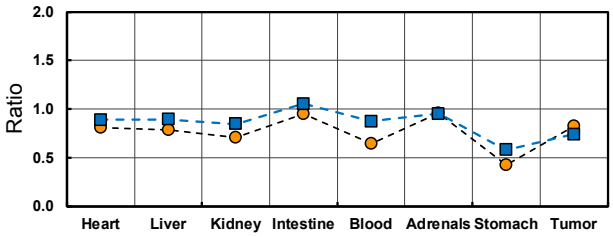

Fig. 1. The trend of the ratios of the difference of simulated and true absorbed doses (orange circles) and that of %ID/g observed 1 h after injection (blue squares) at organs and tumor tissues.

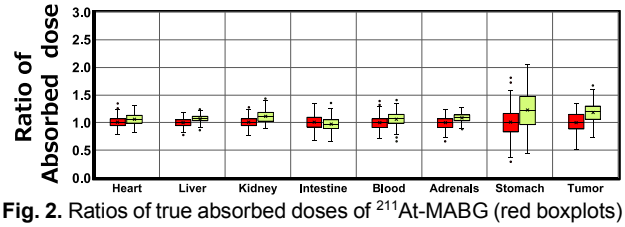

Fig. 2. Ratios of true absorbed doses of ^{211}At-MABG (red boxplots) and those approximately simulated from the RAP dose conversion method (green boxplots).

P2-4 Project “Radiotracer Imaging”

Leader : KAWACHI Naoki

The aim “Radiotracer Imaging Research” project is to measure, visualize the radiation sources quantitatively, and characterize the biological processes and functions, using radioisotopes and imaging devices such as positron emitting tracer imaging system (PETIS). We will establish systematized the most advanced techniques for live-imaging using radiotracers and these production methods, nuclear imaging apparatus, imaging techniques using each apparatus, and kinetic analytical methods for under-standing the elements and molecules transport functions related to agriculture, environmental problems and medicine within living systems.

Development of the positron-emitting ^{74}As tracer for non-invasive imaging of Arsenic dynamics in living plants

Arsenic (As) is a toxic element that is usually found in soils and groundwater as a result of natural and anthropogenic processes. Chronic exposure to inorganic As may lead to cancers of prostate, bladder and skin. *Pteris vittata* is known to have the ability to accumulate As at concentrations of up to 2%, making it a promising candidate for phytoremediation, the use of hyperaccumulator plants to clean As-contaminated soil and water. However, little is known in detail about the mechanism of As absorption in *P. vittata*, especially the role of the rhizome tissue. In this study, to visualize the movement of As in living plants, we utilized the positron-emitting ^{74}As tracer ($T_{1/2}$ = 17.7 d) and the positron-emitting tracer imaging system (PETIS). As a result, we succeeded in obtaining continuous images of hydroponically growing *P. vittata* absorbing ^{74}As from the roots and transporting it to the leaves while accumulating it in the rhizome (Fig.1). We also visualized As dynamics in a non-accumulator plant, *Arabidopsis thaliana*, as a control plant, and found that the ^{74}As was retained in the roots. Furthermore, we investigated the location and amount of As accumulated in *P. vittata* by autoradiography and inductively coupled plasma mass spectrometry, and obtained an overview of the As transport process in *P. vittata*. Under low As exposure, As was predominantly accumulated in young fronds and the midrib and rachis of mature fronds. In contrast, under high As exposure, most of the As finally accumulated in the periphery of the mature leaves, and tissue necrosis was observed in these areas. These results indicate that the rhizome of *P. vittata* plays a role in regulating the transient accumulation of As absorbed from the roots and the translocation of As to mature leaves to protect young leaves, especially under high As exposure. This study provides useful knowledge for the application of *P. vittata* in phytoremediation [1].

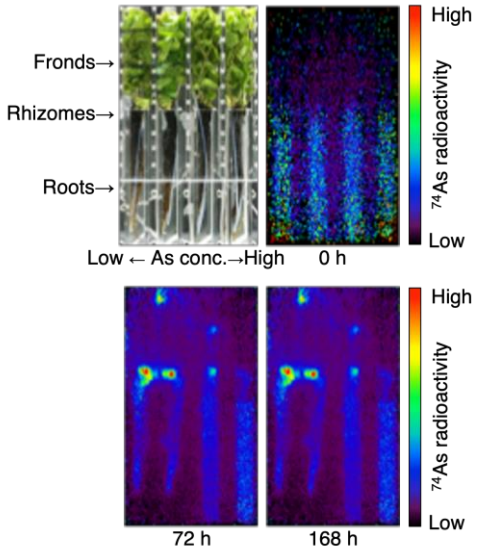

Fig. 1. Serial images of ^{74}As dynamics in *P. vittata*.

Development of new imaging method for therapeutic carbon-ion beams using imaging plates

Beam imaging methods for therapeutic carbon-ion beams is expected to eliminate deviations of the irradiation area and to improve treatment outcome. In this study, we proposed a new beam imaging method measuring secondary electron bremsstrahlung (SEB) with imaging plates (IP), which are widely used in the field of radiological diagnosis. An experimental study was performed at Gunma University Heavy Ion Medical Center. Figure 2(a) represents the experimental setup. Carbon-ion beams having ranges from 61 to 121 in 5-mm steps were injected into water target. A pinhole-type tungsten collimator was placed 30 cm under the beam axis. The diameter and length of the pinhole were 1 and 1 cm, respectively. The thickness of the collimator was 6 cm. The diameter of the beams was 3.5 of full width at half maximum. The number of the injected carbon ions for each measurement was 6×10^{10}. The acquired images for the carbon-ion beams having the range of 61, 91 and 121 mm are summarized in Fig. 2(b). As shown in this figure, we successfully acquired high-resolution beam images with the IP. It was found that the estimation of the carbon-beam range was possible with the accuracy of the standard deviation of 2.5 mm [2].

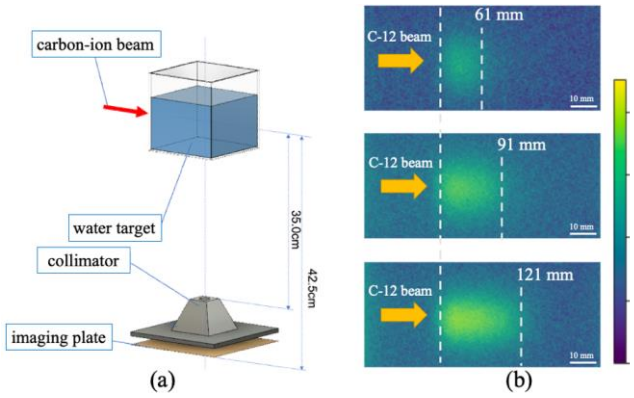

Fig. 2. (a) Experimental setup of the beam imaging. (b) Imaging result for the carbon-ion beams having the ranges of 61, 91 and 121 mm.

References

[1] Y. H.-T. Kohda *et al.*, Sci. Rep. **11**, 12149 (2021). DOI: 10.1038/s41598-021-91374-1
[2] M. Tsuda *et al.*, Radioisotopes **71**, 16155 (2020). DOI: 10.3769/radioisotopes.71.109

P2-5 Project "Generation of Radioisotopes with Accelerator Neutrons"

Leader : HASHIMOTO Kazuyuki

In our project, we have developed the production of medical radioisotopes (RI) for cancer diagnosis and therapy such as ^{99}Mo/^{99m}Tc, ^{90}Y, ^{47}Sc, ^{64}Cu, and ^{67}Cu using fast neutrons from a cyclotron accelerator. The neutrons were obtained by irradiating 40-50 MeV deuterons to beryllium or carbon. A separation and purification method of aimed radioisotope from the target materials and radioactive impurities has also been developed. We also investigate the production of medical RI such as ^{211}At and $^{95, 96}$Tc by the tandem accelerator in Tokai (Japan Atomic Energy Agency). Our final goal is to build a domestic production system of medical radioisotopes using accelerator driven neutrons.

Large scale production of ^{64}Cu and ^{67}Cu via the ^{64}Zn(n, p)^{64}Cu and ^{68}Zn(n, np/d)^{67}Cu reactions using accelerator neutrons [1]

Both ^{64}Cu and ^{67}Cu are promising radionuclides in nuclear medicine. Production yields of these radionuclides were quantified by irradiating 55.4 g of natural zinc with accelerator neutrons. The ^{64}Cu and ^{67}Cu yields using 100 g enriched Zn samples ^{64}Zn or ^{68}Zn, which is an attainable sample weight to be irradiated by accelerator neutrons, were estimated to be 940 GBq of ^{64}Cu in 13 hours and 56 GBq of ^{67}Cu in 24 hours irradiation. These results are based on the good agreement between the measured and calculated yields of ^{64}Cu, ^{67}Cu, and ^{65}Zn using a natural zinc sample of 55.401 g and 40 MeV deuterons.

In order to process a large amount of irradiated enriched zinc, a combined thermal- and resin-separation method was developed to isolate ^{64}Cu and ^{67}Cu in an acceptable separation timeframe. The zinc sample was separated by 99% in sublimation (apparatus shown in Fig. 1), out of which 97% was physically recovered to reuse. The enriched zinc can be recycled with the same methodology as well as purified before irradiation by pre-removal of copper to increase the specific activity of ^{64,67}Cu.

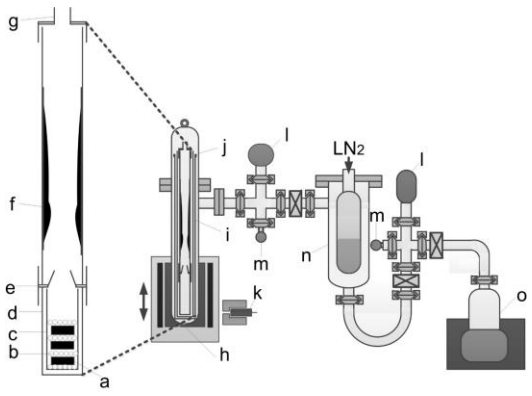

Fig. 1. Schematic diagram of thermal separation system showing an enlargement of the quartz tubes inserted within the stainless chamber.
[a] Zinc samples, [b] Quartz spheres placed in between, [c] Inner quartz tube, [d] Outer quartz tube, [e] Adaptor, [f] Quartz tube for zinc deposition, [g] Top lid, [h] Electric tubular furnace, [i] Stainless cylinder, [j] Sublimation chamber, [k] Lead-shielded CZT detector, [l] Pressure gauge, [m] Leak bulb, [n] Cold trap, [o] Turbo molecular pump.

Separation conditions can be optimized to minimize copper transport with zinc by monitoring radioactive zinc and copper in real time using CZT detector.

After the majority of zinc was removed with thermal separation, the residual zinc containing ^{67}Cu was on the order of mg, which was further purified using commercially available chromatographic resins followed by evaporation to dryness process giving 73% ^{67}Cu yield in total. The methods developed in this study can be a promising candidate for the clinical scale production of ^{64}Cu and ^{67}Cu.

Adsorption temperature of volatile astatine species formed via dry distillation in a glass tube [2]

The ^{211}At was produced via the ^{209}Bi(^{4}He, 2n)^{211}At reaction by irradiating a stack of a couple of bismuth targets with ^{4}He beams accelerated at 30 MeV and supplied from CYPRIS MP-30 cyclotron in the Advanced Clinical Research Center at Fukushima Medical University (FMU). Astatine atoms (~10^{11}) were isolated from bismuth targets irradiated with ^{4}He beams via dry-distillation. The dry distillation was conducted in a glass tube (4 mm inner diameter [i.d.] × 750 mm) filled with nitrogen gas by heating using an electric furnace for ~80 min at ~750 °C. The dry-distillation procedure was controlled by monitoring the astatine radioactivity using cadmium-zinc-tellurium (CZT) γ-ray spectrometers (GRSs). The reliability of the simultaneous measurements of temperatures and the astatine radioactivity with thermocouples and CZT GRSs in the present experimental setup was confirmed.

The adsorption temperature (T_{ads}) of astatine on glass was determined more precisely to be 42.2±2.5 °C than the results obtained in the previous studies [3,4]. The adsorption was observed in a narrow temperature range of 60–30 °C for the full width at half maximum (FWHM) of the radioactivity distributions, indicating that single volatile chemical species could be formed and adsorbed on the glass.

The present T_{ads} value of 42.2±2.5 °C was found to be different from the previously reported values of 16 °C, 272 °C, and 72 °C for At_2 [5], At, and AtO_2 [6], respectively, under the flowing gas measurement conditions. To understand the basic chemical nature of astatine and its volatile characteristics, further investigations need to be conducted to obtain comparable T_{ads} data.

References

[1] M. Kawabata *et al.*, J. Radioanal. Nucl. Chem. **330**, 913 (2021). DOI: 10.1007/s10967-021-07987-3
[2] I. Nishinaka *et al.*, J. Radioanal. Nucl. Chem. **329**, 1459 (2021). DOI: 10.1007/s10967-021-07879-6
[3] I. Nishinaka *et al.*, J. Radioanal. Nucl. Chem. **327**, 869 (2021). DOI: 10.1007/s10967-020-07546-2
[4] I. Nishinaka *et al.*, J. Radioanal. Nucl. Chem. **326**, 743 (2020). DOI: 10.1007/s10967-020-07308-0
[5] J. Merinis *et al.*, Radiochem. Radioanal. Lett. **11**, 59 (1972) (in French).
[6] A. Serov *et al.*, Radiochim. Acta **99**, 593 (2011). DOI: 10.1524/ract.2011.1850

Part Ⅰ

3. Advanced Quantum-Beam Technology

P3-1 Project “Single-ion Control with Laser-cooling” …… 20
Leader : NARUMI Kazumasa

P3-2 Project “LCS Gamma-ray” …… 21
Leader : HAJIMA Ryoichi

P3-3 Beam Engineering Section …… 23
Section Manager : ISHII Yasuyuki

P3-1 Project “Single-ion Control with Laser-cooling”

Leader: NARUMI Kazumasa

The objective of the project is to develop a high-precision single-ion-implantation system to create a nitrogen-vacancy (NV) center in diamond. NV centers play an important role in quantum technologies because they can be applied to quantum bits (qubits) and quantum sensors. For such purposes, it is necessary that one NV center exists within approximately 20 nm away from other ones. We are facing such a challenge with the single-ion implantation of nitrogen into diamond: The key techniques are ion trapping and laser cooling. These make it possible to provide extremely high-quality ion beams, whose emittance is close to zero. If an extremely low emittance is available, the beam size can be a nanometer scale with an appropriate focusing lens. Moreover, these techniques enable us to irradiate a target with single ions one by one.

Construction of a linear-Paul-trap system

As described above, ion trapping and laser cooling are key techniques for the project. We have developed a linear-Paul-trap system for calcium (Ca) ions. Figure 1 shows a photo of the inside of the trap chamber, which has a linear Paul trap, a Ca oven, an electron gun, and an ion detector. In addition, the system has two lasers for cooling and repumping with their optics and an electron-multiplying CCD camera for observation of laser-induced fluorescence. We have succeeded in detecting ions, which are generated in the trap and ejected from the trap. We are trying to trap ions in the trap at present, and then are going to observe laser-induced fluorescence. The immediate goal is the formation of a Ca^+ Coulomb crystal.

Examination of the choice of an electrostatic focusing lens for the single-ion-implantation system

In the single-ion-implantation system, a linear Paul trap is combined with an appropriate focusing lens in order to have a nanobeam. We have examined the choice of a focusing lens: two kinds of electrostatic focusing lenses, Einzel and acceleration lenses, have been compared. Figure 2 shows schematic figures of both the lenses. An Einzel lens consists of three electrodes. An ion is decelerated between the first and the second electrodes at first, and then accelerated between the second and the third electrodes: The energy of an ion does not change before and after the lens. On the other hand, an acceleration lens, which has been developed at QST/Takasaki, is composed of two electrodes. An ion is accelerated between the two electrodes. In both the lenses, an ion beam can be focused with the acceleration or the deceleration. In order to compare both the lenses, the magnification was calculated with numerical simulations based on the MUNRO code [1]. The results are shown in Fig. 3 as a function of the N value, which is defined as the energy ratio E_1/E_2. It is obvious in Fig. 3 that the magnification of both the lenses decreases monotonously with the N value and that the acceleration lens takes smaller N values than the Einzel lens for the same magnification. Smaller N values leads to lower voltage required to focus a beam. Therefore, we have selected the acceleration lens as the focusing lens of the single-ion implantation system.

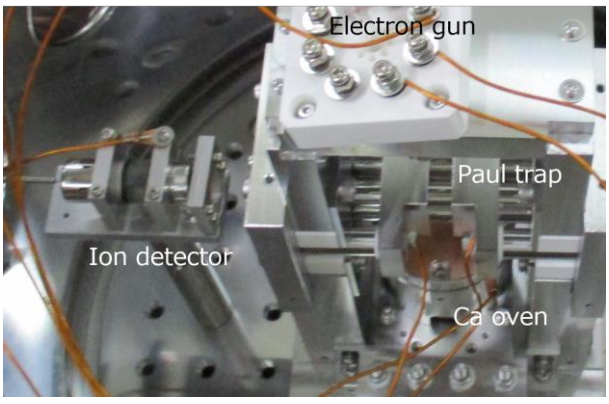

Fig. 1. Photo of the linear Paul trap system.

Reference

[1] E. Munro, “A set of computer programs for calculating the properties of electron lenses”, University of Cambridge, Engineering Department, 1975.

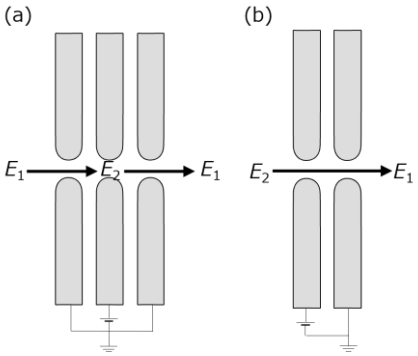

Fig. 2. Schematic figures of (a) an Einzel lens and (b) an acceleration lens. E_1 and E_2 are the energy of an ion.

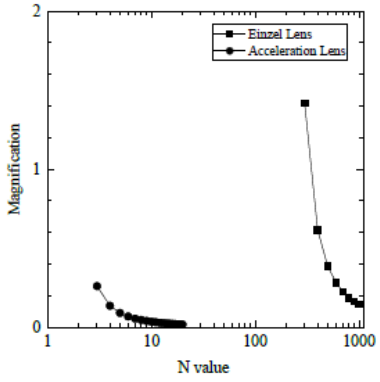

Fig. 3. Dependence of the magnification on the N value for an Einzel lens and an acceleration lens. For the N value, see the text.

P3-2 Project “LCS Gamma-ray”

Leader : HAJIMA Ryoichi

The research objective of LCS Gamma-ray Research Project is developing the technologies of high-brilliance γ -ray generation and exploring its scientific and industrial applications such as nuclear physics, nuclear astrophysics and non-destructive measurement of nuclear material. The γ-ray source is based on laser Compton scattering (LCS), which enables one to generate energy-tunable mono-energetic γ-rays. In the research project, we are developing critical components for electron accelerators to achieve small-emittance and high-average current beams, γ-ray optics and a Monte Carlo simulation code.

Reconstruction of the LCS γ-ray Distribution in the Energy-Angle Phase Space from Crystal Diffraction Data [1]

The distribution of LCS photons in energy-angle phase space reflects the parameters of the laser and electron beams at the collision point and provides the spectral density and bandwidth available for LCS sources. Therefore, diagnostics of the energy-angle phase space are important for the development of high-flux, narrow-bandwidth LCS sources. Such diagnostics have been used for photon energies below 100 keV, but have not been realized for photon energies above 1 MeV. In this study, we demonstrated the reconstruction of energy-angle phase space distribution of an LCS photon beam with energy of 1.7 MeV by photon diffraction using silicon mosaic crystal and silicon comb crystal with improved integral reflectivity. The reconstructed photon distribution is well reproduced by numerical simulations. This diagnostic technique is an efficient tool for LCS source development and is also beneficial for the use of existing LCS facilities.

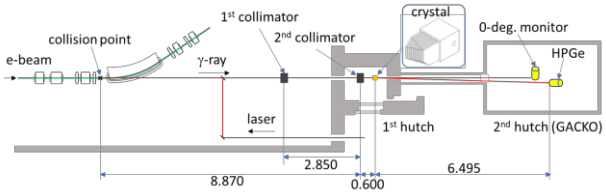

Fig. 1. The LCS beamline of the storage ring NewSUBARU.

The experiment was carried out at the LCS beamline of the storage ring NewSUBARU as shown in Fig. 1. The diffraction crystal was installed just after the second collimator and a high-purity Germanium detector at the second hutch was used to measure the diffracted γ-ray with rotating the crystal. From the measured γ-ray spectrum, we can reconstruct the γ-ray distribution at the energy-angle phase space.

Figure 2 shows the measured γ-ray spectra with rotating a mosaic crystal. We can identify diffraction from the (440) plane around 1700 keV and diffraction from (220) plane around 850 keV in addition to the natural background at 1461.7 keV. The energy-angle phase space can be reconstructed by back-projection of the γ-ray spectra as shown in Fig. 3. We show a result of Monte Carlo simulation with the experimental parameters for comparison. From the figure, we can confirm that the reconstructed distribution is

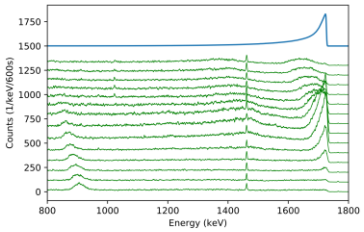

Fig. 2. Diffracted γ-ray spectra with rotating a mosaic crystal. The top line is the incident γ-ray spectrum.

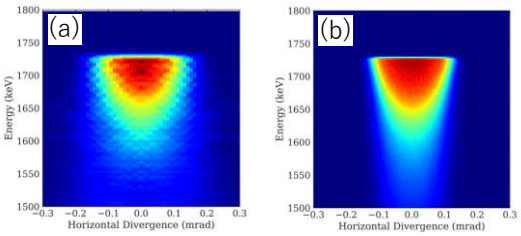

Fig. 3. Energy-angle phase space in the horizontal plane: (a) reconstructed from the diffraction data and (b) obtained from Monte Carlo simulation.

well reproduced by numerical simulations. The demonstrated method provides an efficient diagnostic technique for evaluating the parameter of the electron and laser beams at the collision point and optimizing the collimator geometry to shape the energy spectrum.

Low-lying electric and magnetic dipole strengths in ^{207}Pb [2]

The low-lying electric (E1) and magnetic (M1) dipole excitations in atomic nuclei have attracted interest during the past decades. The observation of such excitations provides valuable information on collective and single-particle motions. Previously, the low-lying dipole strength distribution in ^{207}Pb was studied by using nuclear resonance fluorescence (NRF). While the spins and parities of the states at 5490, 5598, and 5611 keV are known from previous work, those of the higher-lying states remain to be revealed. In this study, we conducted a NRF measurement of ^{207}Pb using a quasi monochromatic, linearly polarized photon beam generated by laser Compton scattering (LCS). The experimental results were compared with predictions from the particle-vibration coupling with the quasi particle random-phase approximation model (PVC+QRPA) using Skyrme effective forces.

The experiment was performed at the NewSUBARU storage ring facility where the LCS photons with maximum energies of 5.8, 6.3, and 6.8 MeV were produced. Figure 4 presents parts of the photon-scattering spectra observed at a polar angle of $\theta = 90^\circ$ relative to the incident photon beam with E^{max} = 5.8 MeV. The spectrum was obtained at azimuthal angles of $\varphi = 0^\circ$ and 90° relative to the polarization plane.

To determine the spins and parities of the observed states, we used the azimuthal intensity ratio defined by $R' = N_\perp / N_\parallel$

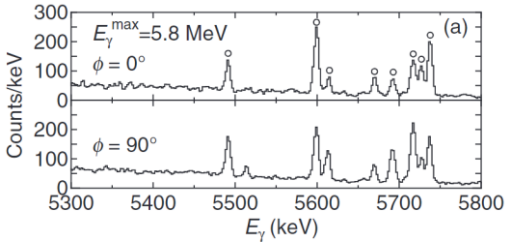

Fig. 4. Photon-scattering spectra observed at a polar angle of θ = 90° relative to the incident photon beam and azimuthal angles of φ = 0° (top) and 90° (bottom) relative to the polarization plane of the

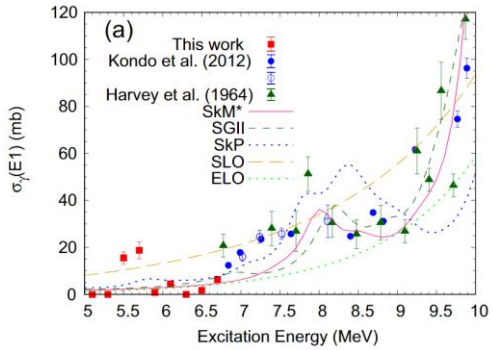

Fig. 5. E1 photoabsorption cross sections obtained from the experiment are compared with previous experiments and calculations based on the PVC+QRPA.

where $N_\perp$($N_\parallel$) represents the intensity of resonant photons detected in the plane perpendicular (parallel) to the polarization plane at θ = 90°. The E1 photoabsorption cross sections deduced from the present (γ, γ') experiment are shown with those obtained from previous experiments of (γ, n) and calculations based on the PVC+QRPA. The predicted photoabsorption cross sections in the energy region from 5 to 10 MeV are shown in Fig. 5. The PVC+QRPA calculations are in reasonable agreement with the experimental data above ≈ 6 MeV. A small bump observed around 8 MeV is reproduced for all three Skyrme forces.

Isomer production ratio of the ^{112}Cd(n, γ)^{113}Cd reaction in an s-process branching point

A β-decay unstable isomer with a half-life of 14.1 yr at 264 keV in^{113}Cd is a branching point in the s-process, from which a weak branch reaches to a rare tin isotope^{115}Sn whose astrophysical origin has been an open problem. We have measured γ-rays decaying to the ground state or the isomer in the^{112}Cd(n, γ)^{113}Cd reaction using high-energy resolution detectors in conjunction with a time-of-flight method.

The ratio at thermal energy was measured using neutrons at the JRR-3 nuclear reactor. To explore the ratio in an energy region of keV, we measured γ-rays from neutron capture reactions on an enriched ^{112}Cd target with intense neutron pulses provided by the Accurate Neutron-Nucleus Reaction measurement Instrument (ANNRI) in the Materials and Life Science Experimental Facility (MLF) at the Japan Proton Accelerator Research Complex (J-PARC) The isomer production ratios were evaluated from the intensity ratios of γ-rays populating the isomer to γ-rays decaying to the total of the ground state and the isomer. In the previous experiment, we measured the ratios of resonances with energies of up to 5 keV. In the present study, we conducted resonance measurements up to 30 keV, the energy region relevant to the s-process in the core

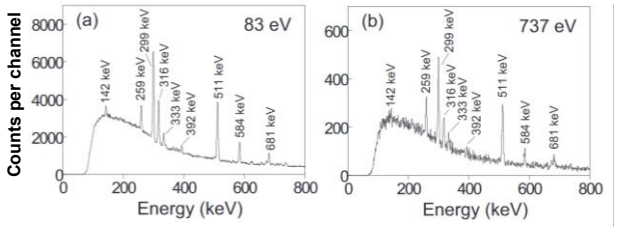

Fig. 6. Energy spectra gated on 83 eV (a) and 737 eV resonances(b). γ–rays radiated from neutron capture reactions on ^{112}Cd are clearly observed.

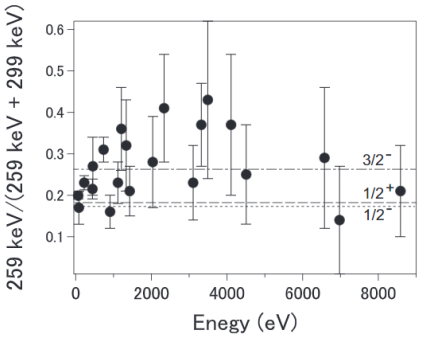

Fig. 7. γ-ray intensity ratios of 259 keV decaying to the isomer to the sum of 259 and 298 keV decaying to the ground state. These values are expected to be approximately proportional to the isomer production ratios. The dashed line represents the expected ratio of resonances with a spin and a parity of $J_\pi = 1/2^+$ calculated using a statistical model. The dotted line and dot-dashed lines represent those of $J_\pi = 1/2^-$ and $J_\pi = 3/2^-$ resonances, respectively.

He burning of massive stars and shell He burning of low mass stars.

Figure 6 shows typical γ-ray energy spectra with a gate on 83 or 737 eV neutron energy in the TOF. Most γ-rays in these spectra originate from excited states in ^{113}Cd. Although the 333-keV γ-ray is observed in some spectra with gates on neutron resonances in ^{112}Cd we cannot assign its origin. A γ-ray with an energy of 259 keV that decays to the ^{113}Cd isomer is observed and γ-rays decaying to the ground state with energies of 299 and 316 keV are also observed in both spectra.

To evaluate the isomer production ratios as a function of neutron energy, we evaluate the γ-ray intensity ratios of 259 keV to the sum of 259 and 299 keV, R = 259 keV/(259+299 keV), obtained from individual γ-ray spectra with a gate on a neutron resonance energy in Fig. 7. These ratios are expected to be approximately proportional to the isomer production ratios.

The result shows that the isomer production ratio does not increase drastically in the energy region of E < 9 keV, supporting the previous results that the s-process contribution from the ^{113}Cd isomer to the solar abundance of ^{115}Sn is relatively minor. However, because the ratios in the energy higher than 9 keV have not been measured, the s-process origin of ^{115}Sn is still an unresolved problem.

References

[1] R. Hajima *et al.*, Appl. Phys. Express. **14**, 104004 (2021). DOI:10.35848/1882-0786/ac2631
[2] T. Shizuma *et al.*, Phys. Rev. C **103**, 024309 (2021). DOI: 10.1103/PhysRevC.103.024309
[3] T. Hayakawa *et al.*, Phys. Rev. C **103**, 045801 (2021). DOI: 10.1103/PhysRevC.103.045801

P3-3 Beam Engineering Section

Section Manager : ISHII Yasuyuki

The research objectives in our section are development of various accelerator-related-techniques including ion-beam-irradiation-techniques and ion-beam-analyses. Each member has been engaged in individual research more than one. Recent remarkable studies are shown as follows; the first article is progression of idiopathic pulmonary fibrosis Is associated with silica/silicate Inhalation, and the second one is absolute local quantification of Li as function of state-of-charge in all-solid-state Li batteries via 2D MeV Ion-Beam Analysis.

Progression of idiopathic pulmonary fibrosis is associated with silica/silicate inhalation [1]

Recently, environmental dust exposure has emerged as a possible risk factor for interstitial pneumonia. Inhaled silica/silicates and titanium are associated with the progression of rapidly progressive pneumoconiosis. However, the relationship between inhaled elements and idiopathic pulmonary fibrosis (IPF) remains unclear. In this study, we focused on IPF presenting with histological usual interstitial pneumonia and investigated the relationship between inhaled elements and IPF progression. We examined the elements in the lungs using in-air micro-particle induced X-ray emission analysis (PIXE). Lung tissue samples with IPF were analyzed and compared with control lung samples as shown in Fig. 1. There was a significant difference between IPF and the control lungs in terms of silicon, assumed to form silica/silicates. Inhaled silicon in the lungs significantly correlated with the annual decline in forced vital capacity in patients with IPF. Furthermore, IPF patients with higher accumulation of silicon showed a significantly poorer prognosis than those with lower accumulation of silicon in the lungs. These significant differences were also seen in multivariate analyses, including smoking history, IPF severity, and/or antifibrotic treatment. In-air micro-PIXE can be beneficial for detecting inhaled elements in the lung. These results indicate that inhaled silica/silicates in the lung may be partly involved in the progression of IPF.

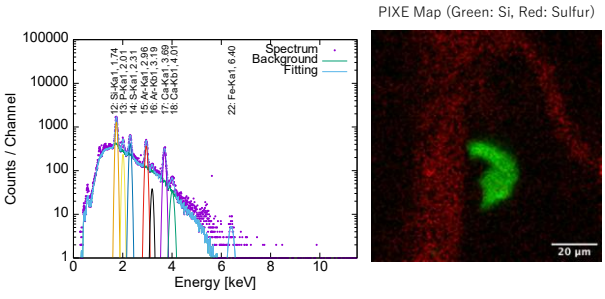

Fig. 1. A PIXE spectrum and an elemental map of control lung tissue samples. Red: sulfur distribution and lung tissue form, Green: the distribution of silicon.

Absolute local quantification of Li as function of state-of-charge in all-solid-State Li batteries via 2D MeV ion-beam analysis

Direct observation of the lithiation and de-lithiation in lithium batteries on the component and microstructural scale is still difficult. This work presents recent advances in MeV ion-beam analysis, enabling quantitative contact-free analysis of the spatially-resolved lithium content and state-of-charge (SoC) in all-solid-state lithium batteries via 3 MeV proton-based characteristic x-ray and gamma-ray emission analysis. The analysis is demonstrated on cross-sections of ceramic and polymer all-solid-state cells with LLZO and MEEP/LIBOB solid electrolytes. Different SoCs are measured in ex-situ and one polymer-based operando cell is charged at 333 K during analysis. The data obtained in reference [2] unambiguously show the migration of lithium upon charging. Quantitative lithium concentrations are obtained by taking the physical and material aspects of the mixed cathodes into account. This quantitative lithium determination as a function of SoC gives insight into irreversible degradation phenomena of all-solid-state batteries during the first cycles and locations of immobile lithium. The determined SoC matches the electrochemical characterization within uncertainties. The presented analysis method thus opens up a completely new access to the state-of-charge of battery cells not depending on electrochemical measurements. Automated beam scanning and data-analysis algorithms enable a 2D quantitative Li and SoC mapping on the µm-scale, not accessible with other methods as shown in Fig. 2.

Fig. 1. Camera image of the 4.2 V charged LLZO-based cells as seen through the beam window (center) with a schematic of the cell setup (right) including approximate thicknesses. The red rectangle marks the analysis region of 50 × 300 µm^2 and the resulting Co mapping by PIXE and Li mapping by PIGE (left).

References

[1] Y. Koga *et al.*, Environ. Sci. Technol. Lett. **8**, 903-910 (2021). DOI: 10.1021/acs.estlett.1c00659

[2] S. Möller *et al.*, Batteries **7**, 41 (2021). DOI: 10.3390/batteries7020041.

blank page

Part Ⅱ

Part Ⅱ

1. Materials Science

1-01 Direct observation of hierarchical structures in graft-type polymer electrolyte membranes using the AFM technique ····· 28
T. Motegi, K. Yoshimura, Y. Zhao, A. Hiroki and Y. Maekawa

1-02 Synthesis and properties of polysubstituted anion conducting electrolyte membrane by radiation graft polymerization ····· 29
K. Yoshimura, Y. Kaneshiro, A. Hiroki, Y. Zhao, M. Kinoshita and Y. Maekawa

1-03 Development of gas permselective membranes by graft polymerization into ion-beam irradiated polymer films III ····· 30
S. Hasegawa, A. Hiroki, S. Sawada and Y. Maekawa

1-04 Accelerated degradation of the irradiated electrode for vanadium redox flow battery ····· 31
H. Ishitobi, R. Obata, T. Ide, H. Okazaki, T. Yamaki, H. Koshikawa, S. Yamamoto and N. Nakagawa

1-05 Hydrogen in Al-Fe thin films prepared by sputtering ····· 32
S. Yamamoto, H. Saitoh, T. Taguchi and T. Yamaki

1-06 Development of metal oxide-catalysts utilizing quantum beam irradiation technique (2) ····· 33
A. Idesaki and S. Yamamoto

1-07 Modification of polymeric materials by quantum beam irradiation (2) ····· 34
A. Idesaki, A. Hiroki, S. Hasegawa and Y. Maekawa

1-08 Study on nitrogen-doping into carbon material by utilizing electron beam irradiation technique ····· 35
A. Idesaki, H. Koshikawa, H. Okazaki, S. Yamamoto and T. Yamaki

1-09 Preparation of ion-track membranes of polystyrene ····· 36
H. Koshikawa, S. Yamamoto, M. Sugimoto, S. Sawada and T. Yamakii

1-10 High-precision flat-plate reference infrared radiator with perfect blackbody composite made by high-energy ion track etching technique ····· 37
Y. Shimizu, M. Imbe, K. Godo, N. Sasajima, H. Koshikawa, T. Yamaki and K. Amemiya

1-11 Proton and water selectivity of ion-track-grafted proton-exchange membranes for HI concentration ····· 38
N. Tanaka, S. Sawada, C. Sugimoto and T. Yamaki

1-12 Effect of 190 keV proton irradiation on superconducting properties in $FeSe_{0.5}Te_{0.5}$ thin films ····· 39
T. Ozaki, H. Okazaki, H. Koshikawa, S. Yamamoto and T. Yamaki

1-13 The origin of the weakened bonding of oxygen with the Pt catalyst on an ion-beam-irradiated carbon support ····· 40
H. Okazaki, T. Ikeda, A. Idesaki, H. Koshikawa, D. Matsumura, S. Yamamoto and T. Yamaki

1-14 Chemical state of platinum ions implanted into glassy carbon substrates ····· 41
T. Kimata, S. Kato, T. Kobayashi, S. Yamamoto, T. Yamaki and T. Terai

1-15 Enhanced X-ray excited optical luminescence in MgO with Cr ion implantation ····· 42
T. Ueno, H. Okazaki, S. Li, S. Sakai, T. Yamaki, T. Watanuki,Y. Takeichi,
M. Mizuguchi, H. Iwasawa and Y. Ohtsubo

1-16 Radiation resistance of diamond FeFET with inorganic ferroelectric gate ····· 43
T. Kawae, H. Okazaki and T. Yamaki

1-17 Optical response of vacancy-induced magnetism in gallium nitride estimated
by spin-polarized positron annihilation method ····· 44
M. Maekawa, A. Miyashita and A. Kawasuso

1-18 Positron annihilation spectroscopy research on irradiation of a new fiber ····· 45
H. Fukazawa, M. Yamaguchi, M. Maekawa and A. Kawasuso

1-19 Local structure of high-energy implanted Ni into Si(100) ····· 46
S. Entani, S.-I. Sato, M. Honda and T. Ohshima

1-20 Improvement of radiation resistance by hetero p/n junction in solar cells ····· 47
T. Nakamura, M. Imaizumi, S.-I. Sato and T. Ohshima

1-21 Characteristic sensitive area observed in FinFET SRAM ····· 48
K. Takeuchi, K. Sakamoto, K. Yukumatsu T. Kato, H. Matsuyama, A. Takeyama,
T. Ohshima and H. Shindo

1-22 Development of phthalocyanine ion beam for creation of multiple NV center in diamond ····· 49
S. Onoda, K. Kimura, N. Kosuge, T. Baba, W. Kada, K. Yamada, T. Teraji,
J. Isoya, O. Hanaizumi and T. Ohshima

1-23 Ensemble nitrogen vacancy centers in type-Ib diamond created
by electron beam up to 8×10^{18} cm^{-2} ····· 50
S. Ishii, S. Saiki, S. Onoda, Y. Masuyama, H. Abe and T. Ohshima

1-24 Prediction of grafting yield by using machine learning ····· 51
Y. Ueki, N. Seko and Y. Maekawa

1-25 A facile graft polymerization of biomass-based vinyl monomers from PE/PP substrates
in a new generation safe organic solvent ····· 52
T. Nirazuka, K. Matsubara, R. Kakuchi, M. Omichi and N. Seko

1-26 Simple evaluation method for distribution of graft chains
by using thermogravimetric analysis ····· 53
M. Omichi and N. Seko

1-27 Thin films produced by ion beam nanofabrication technique
induced cell-driven 3D cell sheet formation ····· 54
T. G. Oyama, K. Oyama, H. Miyoshi and M. Taguchi

1-28 Effect of radiolysis in gas phase on the corrosive environment in liquid phase ····· 55
K. Hata, A. Kimura, T. Sato, C. Kato and M. Taguchi

1-29 Effect of outer diameter on the completely amorphized dose
of silicon carbide nanotube by ion irradiation ····· 56
T. Taguchi, S. Yamamoto and H. Ohba

1-30 Radiation robustness of laser ceramics and single crystal for microchip laser remote analysis ····· 57
K. Tamura, R. Nakanishi, H. Ohba, T. Taira and I. Wakaida

1-31 Gamma-ray irradiation experiment for ITER diagnostic systems in JADA IV ····· 58
S. Kitazawa, T. Hatae, M. Ishikawa, T. Oikawa, R. Imazawa, E. Yatsuka, K. Nojiri, T. Ushiki, S. Kono, K. Torimoto, M. Inamine, T. Kikuchi, T. Yokozuka, H. Murakami, K. Shimizu and T. Sugie

1-32 Irradiation tests of radiation hard components and materials for ITER blanket remote handling system ····· 59
M. Saito, Y. Kawai, K. Nakata, Y. Noguchi and N. Takeda

1-33 Evaluation of irradiation hardening for pure tungsten using micro tensile test ····· 60
T. Nozawa, Ju-Hyeon Yu, T. Miyazawa, M. Ando, S. Nogami, A. Hasegawa and H. Tanigawa

1-34 Structural analysis of complex formed in adsorbent for gravity driven extraction chromatography ····· 61
S. Watanabe, Y. Sano and H. Matsuura

1-35 Ion beam induced luminescence spectra of europium complexes in silica-based adsorbent ····· 62
M. Nakahara, S. Watanabe, Y. Ishii, R. Yamagata, N. Yamada, M. Koka, T. Yuyama, T. Ishizaka, W. Kada and N. Hagura

1-36 Synthetic control of functional metal nanomaterials in SiO_2 by multiple particles irradiation ····· 63
F. Hori, T. Yamada, H. Obayashi, T. Matsui, A. Iwase, S. Semboshi, N. Taguchi and S. Tanaka

1-37 Evaluation of radiation tolerance of COTS device for small satellite ····· 64
K. Tomita, K. Toda, K. Akashi, J. Harada, T. Ohshima and S. Satoh

1-38 Thermodynamic study of $Ti_{1-x}Al_xN$ thin film growth on monocrystalline AlN by reactive CVD ····· 65
Y. Kasukabe, H. Shimoda and S. Yamamoto

1-39 Color imaging of carbon ion ($^{12}C^{+5}$) beam by the 3D gel dosimeter based on phenothiazine-type color former ····· 66
T. Tachikawa and K. Yamada

1-40 Gamma-irradiation effect on radical centers derived from hydrothermally altered potassium feldspar and its application to fault dating ····· 67
T. Fukuchi

1 - 01 Direct observation of hierarchical structures in graft-type polymer electrolyte membranes using the AFM technique

T. Motegi, K. Yoshimura, Y. Zhao, A. Hiroki and Y. Maekawa

Department of Advanced Functional Materials Research, TARRI, QST

Introduction

Polymer electrolyte membrane (PEM) is key material for next-generation energy devices such as metal-air batteries and fuel cells, and are desired to have both high mechanical strength and high ion conductivity. However, the fact that not only the chemical composition (molecular design) but also the polymer association state (hierarchical structure) in the micron to nano range affects the material properties and functions has hindered the progress of material creation. In addition, structural evaluation by X-ray and neutron scattering techniques requires microscopic image models for scattering profile analysis [1]. In this study, we performed structural measurements by atomic force microscopy (AFM) on PEMs prepared by radiation-induced graft polymerization, which does not require a film-forming process that affects the hierarchical structure.

Experimental

A 50 μm thick ethylene tetrafluoroethylene (ETFE) substrate film was irradiated with 15 kGy of γ-rays under an Ar atmosphere. After immersion in a 40 vol% styrene /toluene solution, the membrane was immersed in 0.2 M chlorosulfonic acid/1,2-dichloroethane solution followed by pure water at 50°C to obtain a PEM grafted with polystyrene sulfonic acid (PSSA) (Scheme 1). The water uptake (WU [%]) of the PEM was calculated using following equation:

$$\mathrm{WU}\ (\%) = (W_{\mathrm{s,wet}} - W_{\mathrm{s,dry}}) / W_{\mathrm{s,dry}} \times 100$$

where $W_{\mathrm{s,wet}}$ and $W_{\mathrm{s,dry}}$ are the masses of water-swollen and dried PEM, respectively.

The AFM measurements were performed by AFM5300E (Hitachi, Tokyo, Japan) equipped with an open-loop scanner. The PEMs were embedded in epoxy resin and sectioned by an ultramicrotome for cross-sectional imaging. All AFM measurements were performed at room temperature with a relative humidity range of 20%–30%.

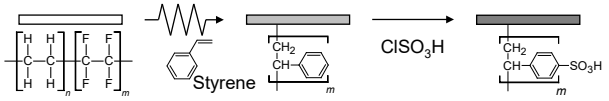

Scheme 1. Process of PS grafting and sulfonation with ETFE base film.

Results and discussion

In the AFM phase images of cross-sections of ETFE-PEM with different grafting degree (GD), the structure derived from hard PSSA graft chains was observed in the area of small phase shift, and the area increased with increasing GD (Fig. 1a, b, black area). The area ratio of the PSSA-derived structure and the volume ratio calculated from the membrane weight measurement showed good agreement, indicating that quantitative evaluation is possible (Fig. 1c).

The size (radius from the center of mass) of the PSSA-derived structures contributing to ionic conduction was calculated from image analysis, and it monotonically increases up to 39% GD to about 12 nm, whereas it significantly increases at 46% GD (Fig. 2a, ■). As shown in Fig. 2b, this result indicates that above the GD threshold (here about 40%), adjacent PSSA-derived structures fuse, affecting, for example, the connectivity of ion conduction paths (Fig. 2a, ○). The structural properties of PEMs can be visualized and semi-quantitatively characterized by AFM [2]. The unnoticed hydrophilic domains of a few tens of nm are expected to enable the design of the functions of PEM.

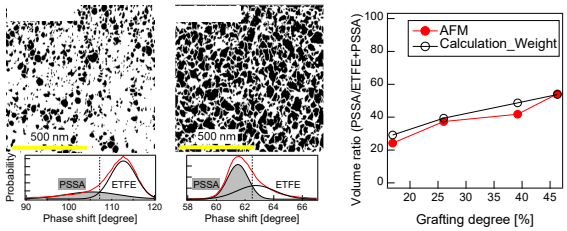

Fig. 1. (a,b) Binarized phase images for the cross-section of ETFE-PEM with a GD of (a) 16% and (b) 46%. The phase shift distribution was also shown with a threshold point (dashed line). (c) Plot of the area fraction obtained from AFM (●) and the volume fraction of PSSA to total PEM volume (○).

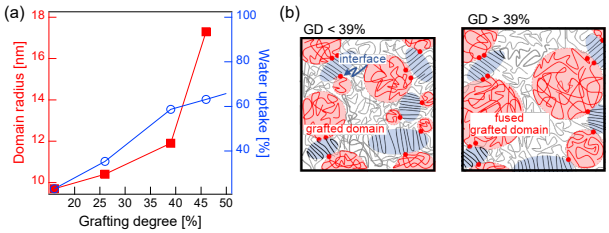

Fig. 2. (a) Plot of size of PSSA-derived structures (■, left axis) and water content of PEM (○, right axis) against GD. (b) Schematic diagram of ETFE-PEM at low GD ~ 39% where each grafted domain is separate from the others, and ETFE-PEM at high GD where several domains are grown and fused together to create a larger domain.

Acknowledgments

This work was supported by JSPS KAKENHI Grant Nos. 18H03850 and 19K15407 and partially supported by QST President's Strategic Grant (Exploratory Research).

References

[1] Y. Zhao *et al.*, Macromolecules **54**, 4128 (2021). DOI: 10.1021/acs.macromol.1c00587

[2] T. Motegi *et al.*, Langmuir **38**, 9992 (2022). DOI: 10.1021/acs.langmuir.2c01398

1 - 02 Synthesis and properties of polysubstituted anion conducting electrolyte membrane by radiation graft polymerization

K. Yoshimura[a)], Y. Kaneshiro[b)], A. Hiroki[a)], Y. Zhao[a)], M. Kinoshita[b)] and Y. Maekawa[a)]

[a)]Department of Advanced Functional Materials Research, TARRI, QST
[b)]Department of Applied Chemistry, Saitama Institute of Technology

Anion conducting electrolyte membrane (AEM) fuel cells (AEMFCs) have recently received a widespread attention because of their promising power density and cost advantage in utilization of platinum group metal (PGM)-free catalysts [1]. These properties suggest them as candidates to replace proton conducting electrolyte membrane (PEM) fuel cells (PEMFCs). However, several issues associated with AEMFCs have not been well resolved so far, particularly in terms of alkaline durability and ion conductivity. Recently, our group developed a new series of imidazolium-type AEMs (**StIm-AEM**) by radiation-induced grafting method, where 2-(4-ethenylphenyl)-1-propyl-1*H*-imidazole monomers were grafted into poly(ethylene-co-tetrafluoroethylene) (ETFE) base films [2]. These AEMs exhibit well-balanced properties of high ion conductivity and moderate alkaline stability; the AEMs degraded via the initial ring opening reactions and following oxidation reaction of the imidazolium unit.

In this study, we aimed to improve the durability of **StIm-AEM**. AEMs were synthesized by grafting poly(2-(4-ethenylphenyl)-1,4,5-trimethyl-*N*-alkyl-imidazolium), which have methyl substituents on 4,5-position of imidazolium unit. The effect of the number of the carbon atoms on alkyl substituents was investigated.

2-(4-ethenylphenyl)-1,4,5-trimethyl-1*H*-imidazole (Me-StIm) as a graft monomer was synthesized using 4-vinylbenzaldehyde and 2,3-butanedione with the ammonia. The ETFE films were irradiated with a ^{60}Co γ-ray source (QST Takasaki) at room temperature in argon atmosphere with an absorption dose of 50 kGy. The pre-irradiated ETFE films were immersed into the argon-purged monomer solution of Me-StIm in 1,4-dioxane (50 vol%). The imidazole groups in the grafted-ETFE were *N*-alkylated by alkyl iodide. The resultant AEMs were immersed in 1 M HCl, followed by 1 M KOH at room temperature for 16 h to give the OH^- forms of the AEMs, as shown in Fig. 1.

The ionic conductivity was measured by two-point probe AC impedance spectroscopy at 100% relative humidity in N_2-purged deionized water. The alkaline stability of AEMs was evaluated by monitoring the change in conductivity of AEMs in 1 M KOH at 80 °C.

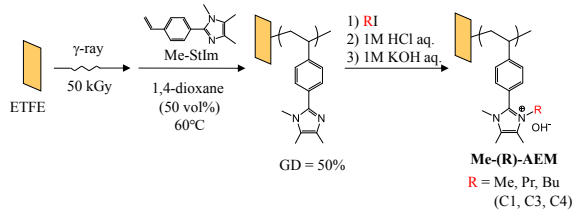

Fig. 1. Reaction scheme, grafting-degree (GD), and a number of the carbon atoms on alkyl substituents for prepared AEMs.

The poly(Me-StIm)-grafted ETFE films with grafting degrees of 50% were successfully prepared and the *N*-alkylation reaction proceeded quantitatively. **Me-Me-AEM**, **Me-Pr-AEM**, and **Me-Bu-AEM** with calculated IECs of 1.55, 1.42 and 1.39 mmol g^{-1} showed ionic conductivities of 91, 46, and 13 mS cm^{-1} at 60°C, respectively. The conductivities were decreased drastically with increasing the hydrophobicity of alkyl substituents. The water uptake of these AEMs were 72, 49, and 7%, respectively.

Figure 2 shows the normalized conductivities of the AEMs on the basis of the initial conductance as a function of immersion time. The **Me-Me-AEM** become a gel and lose their strength within 50 h immersion and the **Me-Bu-AEM** showed sudden loss of conductivity. On the other hand, the **Me-Pr-AEM** showed good alkaline stability even though compared with 4,5-unsubstituted **StIm-AEM**. The conductivity loss of the **Me-Bu-AEM** probably due to the loss of ion channel connection. The gradual loss of conductivity was mainly caused by imidazolium ring opening degradation reaction, which triggered by the attack of hydroxide ion at the 2-position of imidazolium ring. Thus, these results indicated that the importance to take a balance between steric protection and membrane properties. Accordingly, the Me-StIm-graft-ETFE with appropriate *N*-alkyl substituents would be promising AEM for alkaline durable AEMFCs.

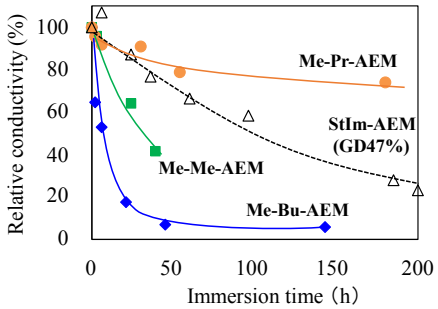

Fig. 2. The AEM conductivities after being immersed in 1 M KOH at 80 °C.

References

[1] N. Chen *et al.*, Angew. Chem. Int. Ed. **60**, 7710 (2021). DOI: 10.1002/anie.202013395
[2] Y. Zhao *et al.*, Soft Matter **16**, 8128 (2020). DOI: 10.1039/D0SM00947D

1 - 03 Development of gas permselective membranes by graft polymerization into ion-beam irradiated polymer films III

S. Hasegawa, A. Hiroki, S. Sawada and Y. Maekawa

Department of Advanced Functional Material Research, TARRI, QST

Separation and purification of gas molecules with similar physical and chemical properties are an important matter in industry. In the present system for the gas separation and purification, however, it is accompanied by a large energy loss [1]. The permselective membranes are required to reduce the energy loss.

Radiation-induced graft polymerization is a useful technique for introducing new functional polymers into polymer substrates. We previously reported that the hydrogen permselective membranes were prepared by the graft polymerization with γ-irradiated polyvinylidene fluoride films [2]. On the other hand, when polymer films are irradiated with heavy ion beam instead of γ-rays, radicals are produced in the latent track. The graft polymerization of vinyl monomers proceeds from the radicals, generated in the latent track to produce perpendicularly aligned cylindrical graft-polymer region with several hundred nm diameter. In this work, we propose a development of gas permselective membranes by the combination of the ion-beam irradiation and the graft polymerization (Fig. 1) and summed up of graft-type permselective gas membranes using nuclear tracks by ion beam irradiation.

Substrates with graft-type gas permselective membrane was used ethylene tetrafluoroethylene copolymer (ETFE) films (AGC Inc.) and poly(vinylidene chloride) (PVDC, ASAHI-KASEI Corp.) with 25 μm thickness were irradiated with 560 MeV Xe ions ($^{129}Xe^{26+}$) or 310 MeV Kr ions ($^{87}Kr^{20+}$) at TIARA, respectively. The irradiated films were immersed into various monomer solutions containing of p-trimethoxysilyl styrene (TMSS), vinylethoxysilane (VESI) or 3-methacryloxypropylmethyl diethoxysilane (3-MPMDS) (TMSS, VESI or 3-MPMDS/toluene = 50:50 vol.%) at 60 °C to obtain these-grafted films. Permeabilities of hydrogen (H_2), oxygen (O_2), nitrogen (N_2), and methane gas (CH_4) through the grafted films were conducted by a differential pressure method.

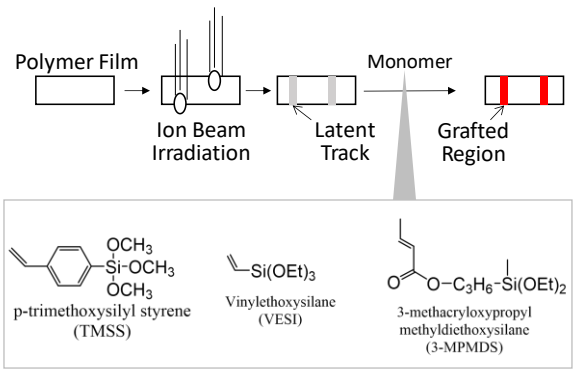

Fig. 1. Synthetic illustration of gas permselective films prepared by the combination of ion beam irradiation and graft polymerization.

Grafting degree (GD), gas permeability, and gas permeation ratio with the obtained films are summarized in Table 1. The H_2, O_2, N_2, and CH_4 permeation through the original PVDC and ETFE films were quite low, in which each gas permeability exhibited below 0.8×10^{-11} mol/sec·m^2·Pa. These gas permeabilities of the ion-beam irradiated (non-grafted) PVDC films showed 4.5 - 5.0 × 10^4 times higher than original film, and the permeability through ion-beam irradiated ETFE film showed 1.3 to 9 times higher than original one.

PVDC-*g*-TMSS film (GD:12%) showed higher H_2 gas permeation (6.4×10^{-11} mol/sec·m^2·Pa). The highest permeation ratio (H_2/N_2, H_2/N_2) was 5.8 and 6.0, respectively. The H_2 and CH_4 permeabilities of the ETFE-*g*-TMSS film (GD:1.9%) were 119×10^{-9} and 53×10^{-9} mol/sec·m^2·Pa, respectively, and the H_2/CH_4 was 0.3. On the other hand, The H_2 permeability of the ETFE-*g*-VESI, and 3-MPMDS (GD:0.9 and 2.7%) were 978 and 25780 times larger than through ETFE-*g*-TMSS films, and H_2/CH_4 was 4.5 and 2.2, respectively. It was found that the appropriate selection of the substrate membrane and the graft chains could selectively extract the target gas by the method of filling the nuclear tracks with graft chains.

Table 1
GD, gas permeability, and gas permeation ratio with films obtained by the combination of ion beam irradiation and graft polymerization.

Substrate	Treatment*	Graft Chains	GD (%)	Gas permeability ($\times 10^{-11}$ mol/sec · m^2 · Pa)				H_2/O_2	H_2/N_2	H_2/CH_4
				H_2	O_2	N_2	CH_4			
PVDC	-	-	-	0.2	0.1	0.1	-	1.1	1.2	
PVDC	1	-	-	7700	5600	5900	-	1.3	1.4	
PVDC	1+3	TMSS	12	6.4	1.1	1.1	-	5.8	6.0	
PVDC	2+3	TMSS	19	83	160	340	-	2.5	0.5	
ETFE	-	-	-	0.8	-	-	0.1	-	-	8.0
ETFE	1	-	-	1	-	-	0.9	-	-	1.1
ETFE	1+3	TMSS	1.9	0.46	-	-	1.6	-	-	0.3
ETFE	1+3	VESI	0.9	45	-	-	1000	-	-	0.045
ETFE	1+3	3-MPMDS	2.7	11900	-	-	5300	-	-	2.25

*1:Ion beam irradiation, 2:γ-rays irradiation, 3:Graft polymerization

Acknowledgments

This work was supported by the Japan Society for the Promotion of Science (JSPS) KAKENHI Grant Number 16K06785.

References

[1] R.W. Baker *et al.*, Ind. Eng. Chem. Res. **41**, 1393 (2002).DOI: 10.1021/ie0108088

[2] S. Hasegawa *et al.*, Quantum Beam Sci. **4**, 23 (2020). DOI: 10.3390/qubs4020023

1 - 04 Accelerated degradation of the irradiated electrode for vanadium redox flow battery

H. Ishitobi[a)], R. Obata[a,b)], T. Ide[a)], H. Okazaki[b)], T. Yamaki[b)], H. Koshikawa[b)], S. Yamamoto[b)] and N. Nakagawa[a)]

[a)] Graduate School of Science and Technology, Gunma University
[b)] Department of Advanced Functional Materials Research, TARRI, QST

Introduction

Vanadium redox flow battery (VRFB) is the key device to store and/or level the intermittent renewable energy output. The degradation of the electrode of VRFB is a technical issue because VRFB frequently repeats charge/discharge operations. The previous studies insisted the reason for degradation is not explained by the changes of surface oxygen groups at the negative electrode [1], and explained by the corrosion of the graphite felt [2]. However, the detail of the degradation is still under discussion because some starting materials for the electrodes initially contain surface oxygen species. In this study, we employed a single-walled carbon nanotube (SWCNT) without surface oxygen groups as the starting material for the electrode. SWCNT was activated by the electron beam irradiation, and then repetitively charged and discharged under accelerated degradation conditions (1.8 V). X-ray photoelectron spectroscopy was performed for each electrode.

Experimental section

SWCNT electrode sheet was prepared by vacuum filtration [3]. SWCNT powder (Zeon Corporation) was dispersed in methanol by sonication. The SWCNT suspension was then filtered under vacuum and dried at 100 °C with evacuation. Then SWCNT sheet (75 μm-thick) was irradiated by 29.7 MGy of the electron beam in the air at TARRI. A custom-built single-cell setup made of a carbon block with an interdigitated flow field was used for charge-discharge measurement (cutoff at 1.8 V/0.6 V). The irradiated SWCNT sheet was sandwiched by a carbon paper (MFK, Mitsubishi Chemical Corp.) and these were placed on both the negative and the positive sides used as electrodes, and Nafion 117 membrane was used as the separator. The concentration of vanadium active materials was 1 M, which was dissolved in sulfuric acid aqueous solution. The surface elements of the electrodes were analyzed by an X-ray photoelectron spectrometer (PHI5000Versaprobe II, ULVAC-PHI) at TARRI.

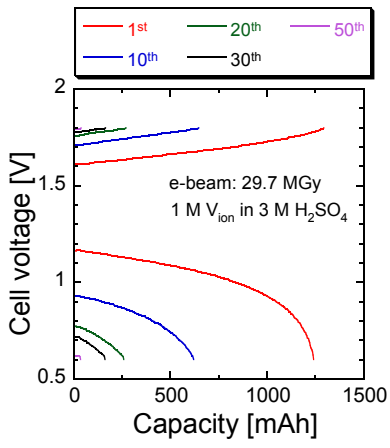

Fig. 1. Charge/discharge profiles during the accelerated degradation test.

Results and discussion

The surface oxygen species was not found for the pristine SWCNT (Table 1), thus the effect of original oxygen species can be neglected. Figure 1 shows the data of the accelerated degradation test by charge/discharge. The charging voltage increased, the discharging voltage decreased, and the discharge capacity decreased during the repetitive operation. Table 1 shows the surface elemental fraction of each electrode by XPS analysis. The surface oxygen at the negative electrode decreased after the accelerated degradation test. Relatively high voltage (1.8 V) should decrease the potential at the negative electrode. The surface oxygen is considered to be reduced due to the low potential. Since the surface oxygen groups are believed to be active sites for the reaction at the negative half-cell [4], the decomposition of the surface oxygen at the negative half-cell is attributed to the main reason for the degradation.

Acknowledgments

This research was supported by JSPS KAKENHI Grant Number JP18K14048.

References

[1] A. M. Pezenshki *et al.*, J. Electrochem. Soc. **163**, A5202 (2016). DOI: 10.1149/2.0251601jes
[2] P. Trogadas *et al.*, Electrochem. Commun. **48**, 155 (2014). DOI: 10.1016/j.elecom.2014.09.010
[3] Y. Hatakeyama *et al.*, J. Electroanal. Chem. **878**, 114603 (2020). DOI: 10.1016/j.jelechem.2020.114603
[4] H. Ishitobi *et al.*, J. Electrochem. Energy Convers. Storage **17**, 031001 (2020). DOI: 10.1115/1.4044959

Table 1.
The surface elemental fraction of each electrode by XPS analysis.

		Surface elemental fraction		
		C	O	N
Pristine		100	N.D.	N.D.
Before the test		81	18	0.4
After the test	Negative	89	10	1.1
	Positive	83	17	0.4

*N.D.: Not detected.

1 - 05 Hydrogen in Al-Fe thin films prepared by sputtering

S. Yamamoto[a)], H. Saitoh[b)], T. Taguchi[c)] and T. Yamaki[a)]

[a)]Department of Advanced Functional Materials Research, TARRI, QST
[b)]Synchrotron Radiation Research Center, KPSI, QST
[c)]Tokai Quantum Beam Science Center, TARRI, QST

Hydrogen storage materials composed of low-cost and environmentally friendly metals such as Al, Fe promote realizing a hydrogen society. Although Al and Fe demonstrate almost no hydrogen storage at ordinary temperature and pressure, it has recently been investigated that Al-Fe alloy (Al_3FeH_4) store hydrogen under high temperature and high-pressure conditions [1]. This Al-Fe alloy is thermodynamically predicted to store hydrogen even under normal temperature and pressure, and if it can be realized, an inexpensive and lightweight hydrogen storage materials can be provided. In this study, Al-Fe thin films were prepared by sputtering method, and the hydrogen distribution in the films was investigated by ion beam analysis techniques. As a result, we found that hydrogen is uniformly distributed in the amorphous Al-Fe thin film.

The Al-Fe films was deposited on Si (100) substrates in an Ar gas atmosphere (0.18 Pa) by using an rf magnetron sputtering with a sintered target (atomic ratio of Al: Fe = 76: 24). The hydrogen distribution in the films was measured by ERD (elastic recoil detection) and the composition of the films was measured by RBS (Rutherford backscattering spectroscopy) using 3 MV single-ended accelerator at QST Takasaki. For the ERD measurement, an analyzing beam of 2.8 MeV $^4He^+$ was incident on the sample at an angle of 75° to the surface normal and the recoiled hydrogen atoms were detected at an angle of 30° with respect to the analyzing beam. An Al foil (12 μm thickness) was placed in front of the detector to stop the forward scattered He ions. For the RBS measurement, an analyzing beam of 2.0 MeV $^4He^+$ was incident on the sample and the backscattered particles were detected at an angle of 165° with respect to the analyzing beam. The thickness of the films was confirmed by cross sectional TEM observation. The structure of films was characterized by XRD (X-ray Diffraction) with CuK_a radiation.

Figure 1 shows the XRD patterns from the Al-Fe and Al films deposited on Si (100) substrates at room temperature. It can be confirmed that the Al film has a polycrystalline structure from diffraction peaks of Al 111 and Al 200, and the Al-Fe film has an amorphous structure from single broad peak around 35 degrees. The Al-Fe films features an amorphous structure in spite of metal. The results of RBS measurements confirmed that the composition of the Al-Fe films was almost same as that of the Al-Fe sputtering target. The results of ERD measurements of the Al-Fe (247 nm thickness) and Al (160 nm thickness) films are shown in Figure 2. The ERD spectra in Fig.2 corresponds to the hydrogen distribution in the Al-Fe film (a) and the Al film (b), the hydrogen in the Al-Fe film is more abundant than in the Al film, and the hydrogen is uniformly distributed from the surface to the Si substrate interface. The amount of hydrogen in the Al-Fe film is estimated to be about 18 at%. Our measurements indicate the amorphous Al-Fe film has hydrogen-storage properties at ordinary temperature and pressure. It is not clear at this time how hydrogen in the Al-Fe film was incorporated in the film. Therefore, we plan to clarify the mechanism of incorporation of hydrogen into the film.

Acknowledgments
This work was financially supported by JSPS KAKENHI Grant Number 18K04739. The authors thank Ms. C. Suzuki for her help with the TEM observations.

Reference

[1] H. Saitoh *et al*., Mater. Des. **208**, 109953, (2021). DOI: 10.1016/j.matdes.2021.109953

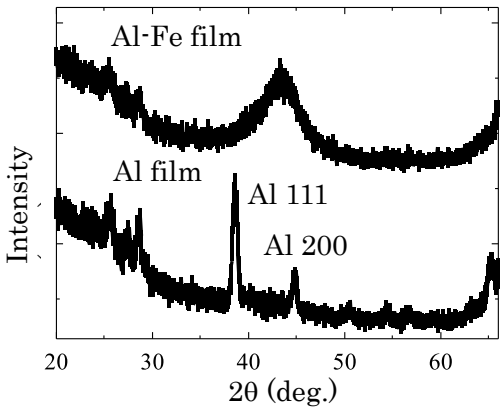

Fig. 1. X-ray diffraction patterns for the Al-Fe film and the Al film.

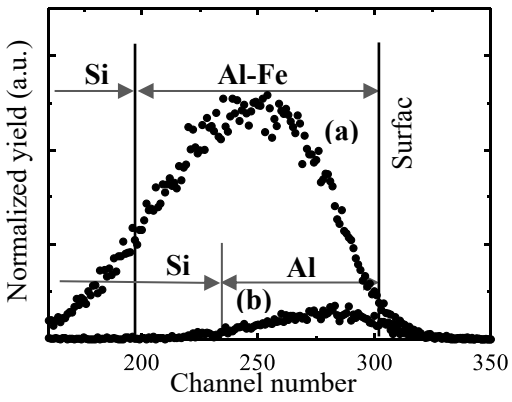

Fig. 2. ERD spectra for the Al-Fe film (a) and the Al film (b).

1 - 06 Development of metal oxide-catalysts utilizing quantum beam irradiation technique (2)

A. Idesaki and S. Yamamoto

Department of Advanced Functional Materials Research, TARRI, QST

According to the Basic Hydrogen Strategy formulated in March 2019, efforts for popularization of 800,000 fuel cell vehicles (FCVs) by 2030 are declared as one of the goals in the field of mobilities in Japan. To achieve this goal, the cost of polymer electrolyte fuel cells (PEFCs) for the FCVs should be reduced; the cost of about 20,000 yen/kW for the current PEFCs is required to be reduced to about 5,000 yen/kW. In the PEFCs, platinum of several tens grams is used as a catalyst to enhance the reaction at the cathode as shown in Fig. 1. Therefore, non-precious metal catalysts have been desired to reduce the cost of the PEFCs. An oxygen reduction reaction (ORR; $O_2 + 4H^+ + 4e^- \rightarrow 2H_2O$) occurs at the cathode in the PEFC. This ORR proceeds through production of some intermediates (*OOH, *O, *OH) as shown in Fig.1. The adsorption energy of the intermediates on the catalyst surface dominates the performance of the catalysts, therefore, appropriate adsorption energy of each intermediate should be controlled to realize the highest performance. However, theoretical calculation has revealed that the equilibrium potential ($E^0 = 1.23$ V vs. RHE) cannot be achieved in the case of platinum catalysts because the adsorption energy of the intermediates is independently uncontrollable on the platinum catalysts [1]. On the other hand, another theoretical calculation has predicted that titanium oxide (TiO_2) with oxygen defects and/or doped heteroatoms exhibit the possibility to realize the equilibrium potential of 1.23 V vs. RHE [2]. Here, we propose the quantum beam irradiation technique as a method to form ideal catalytic sites and electron conductive paths for TiO_2. In this work, a mixture of TiO_2 powder/polyacrylonitrile/carbon nanotube was irradiated by 2 MeV electron beam with dose of 5 MGy under N_2 atmosphere and pyrolyzed at 1000 °C under N_2 atmosphere. Comparing with the unirradiated sample, the EB-irradiated sample showed higher ORR activity: enhanced current density and onset potential for the ORR (Fig. 2). This result indicated that the treatments of EB-irradiation and subsequent pyrolysis are effective to form catalytic sites and electron conductive path for TiO_2 powder.

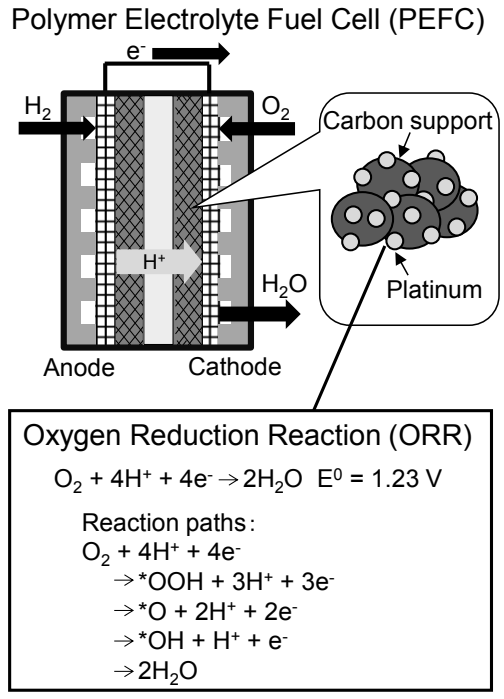

Fig. 1. Scheme of the polymer electrolyte fuel cell (PEFC) and oxygen reduction reaction (ORR) at the cathode.

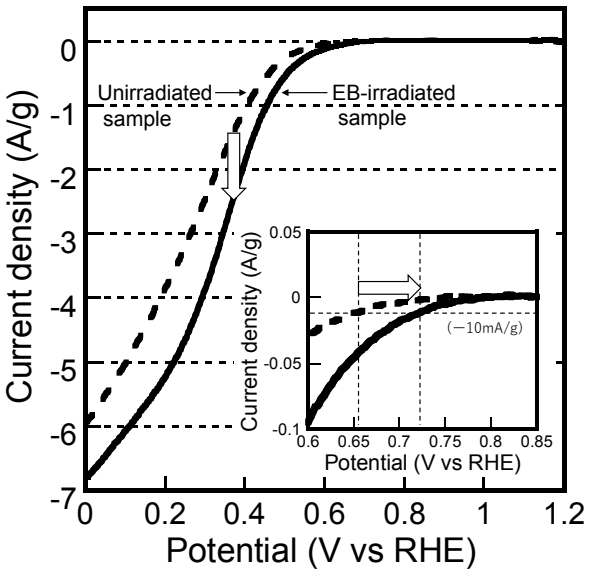

Fig. 2. ORR activity of TiO_2 catalyst synthesized by utilizing EB-irradiation technique.

Acknowledgments

This work is based on results obtained from a project, JPNP20003, commissioned by the New Energy and Industrial Technology Development Organization (NEDO). This is a collaboration work with Fukuoka University, Chiba University, Osaka University, Kyushu University, Oita University, Kochi University of Technology, and Utsunomiya University.

References

[1] A. Kulkarni *et al.*, Chem. Rev. **118**, 2302 (2018). DOI: 10.1021/acs.chemrev.7b00488

[2] Y. Yamamoto *et al.*, J. Phys. Chem. C **123**, 19486 (2019). DOI: 10.1021/acs.jpcc.9b03398

1 - 07 Modification of polymeric materials by quantum beam irradiation (2)

A. Idesaki, A. Hiroki, S. Hasegawa and Y. Maekawa

Department of Advanced Functional Materials Research, TARRI, QST

The Basic Hydrogen Strategy was formulated by Hydrogen and Fuel Cell Strategy Council in March 2019. In the Basic Hydrogen Strategy, efforts for popularization of fuel cell vehicles (FCVs) and hydrogen station (HRSs) are declared as one of the most important issues in the field of mobilities. The main components installed in the FCVs are fuel cells and high pressure-hydrogen tanks so that the costs of them should be reduced in order to realize the popularization of FCVs and HRSs. In the case of the high pressure-hydrogen tanks, the cost of ¥700,000 for one current tank is required to be reduced to around ¥300,000. The common high pressure-hydrogen tank for FCVs, type IV tank, is composed of plastic liners and carbon fiber reinforced plastics (CFRPs). It is effective to reduce the amount of expensive carbon fiber in order to realize the low cost-tank, therefore, novel high performance-polymeric materials which can be alternative to the CFRPs have been strongly desired.

The materials in the type IV tank are exposed repeatedly to severe conditions such as high pressure of 70 MPa, wide temperature range of -40 °C to 85 °C. Especially, the materials must retain sufficient durability against the high pressure-hydrogen; the materials with low hydrogen gas permeability and high mechanical properties are desirable. Professor Nishimura at Kyushu University has summarized relationship between hydrogen gas permeability and elongation at break for various polymeric materials as shown in Fig. 1. Although the polymeric materials should maintain the capability of elastic deformation against the repetitive loading and unloading in the practical use, the elongation can be one of the indicators for the screening of materials. Hard polyamides, which exhibit low hydrogen gas permeability and low elongation at break, cannot afford large deformation. Polyethylenes, which exhibit high elongation at break, can afford large deformation, however, cannot suppress the hydrogen gas permeation. According to the relationship as shown in Fig. 1, our goal for development of polymeric materials with low hydrogen gas permeability and high mechanical properties is to achieve the “TARGET ZONE”. We have examined introduction of crosslinking structure into the polymeric materials, which is expected to reduce the hydrogen gas permeability and enhance the mechanical properties, utilizing quantum beam irradiation technique. In this work, four kinds of polyamides were irradiated by ^{60}Co gamma-rays up to dose of 2500 kGy under vacuum at ambient temperature. After the irradiation, the samples were immersed into formic acid/chloroform for 48h at room temperature and dried at 80°C for 16h under decompression to measure the gel fraction. The gel fraction was calculated by the following equation:

$$\text{Gel fraction (\%)} = W_1 / W_0 \times 100$$

where W_0 is the initial weight (g) and W_1, the final weight (g) of dried sample. It was found that the gel fraction increased in the dose range of several hundred kGy due to the crosslinking to produce insoluble component. Other measurements such as tensile tests, exposure tests for high pressure-hydrogen gas, and so on, have been under conducting. These data will be summarized as a database for discussion of the guideline for development of high pressure-hydrogen-resistant polymeric materials.

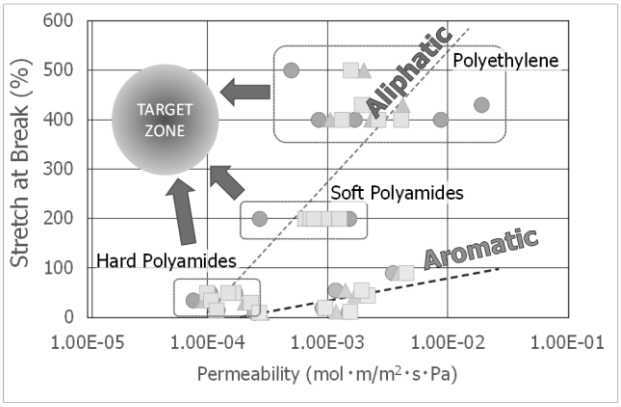

Fig. 1. Relationship between H_2 permeability and tensile property for various polymeric materials.

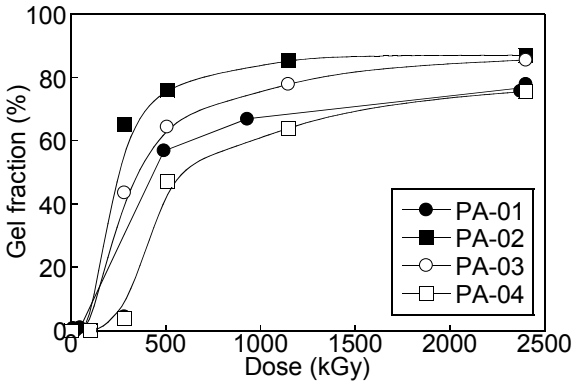

Fig. 2. Change of gel fraction of polyamides after gamma-ray irradiation under vacuum at ambient temperature.

Acknowledgments

This work is based on results obtained from a project, JPNP20003, commissioned by the New Energy and Industrial Technology Development Organization (NEDO). This is a collaboration work with Prof. Shin Nishimura at Kyushu University and Prof. Katsuhisa Tokumitsu at The University of Shiga Prefecture.

1 - 08 Study on nitrogen-doping into carbon material by utilizing electron beam irradiation technique

A. Idesaki, H. Koshikawa, H. Okazaki, S. Yamamoto and T. Yamaki

Department of Advanced Functional Materials Research, TARRI, QST

Nitrogen-doped (N-doped) carbon materials which exhibit the catalytic activity for an oxygen reduction reaction (ORR; $O_2 + 4H^+ + 4e^- \rightarrow 2H_2O$) have been expected as a platinum-alternative catalyst in the cathode of proton exchange membrane fuel cells. As shown in Fig. 1, nitrogen is doped into carbon structure as several chemical structures: pyridinic nitrogen, graphitic nitrogen, pyrrolic nitrogen and oxidized nitrogen. It has been reported that the requirements for catalytic activity of N-doped carbon are the formation of a graphite structure and the incorporation of N into carbon as the pyridinic nitrogen structure [1], therefore, it is important to develop a method to fabricate N-doped carbon in high efficiency. In many cases, the N-doped carbons have been fabricated by pyrolysis of blends of precursor polymers and/or metal-compounds. However, the catalytic activity of obtained N-doped carbons is not sufficient because of their low N content (N/C ~ 0.02). In this work, N-doping into carbon materials was examined by utilizing electron beam (EB) irradiation technique.

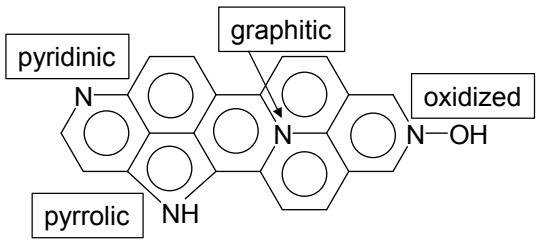

Fig. 1. Chemical structure of N-doped carbon.

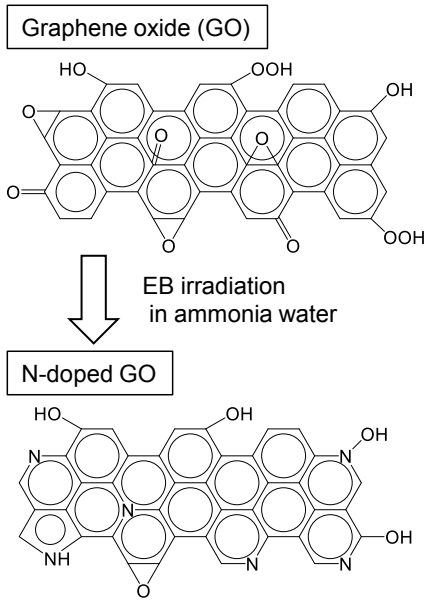

Fig. 2. Scheme of N-doping into graphene oxide by EB irradiation.

Graphene oxide (GO) powder was irradiated by 2 MeV electron beam (EB) with dose of 100 kGy in 28% ammonia water at room temperature. After the irradiation, the chemical states of nitrogen (N) in the carbon materials were investigated by X-ray photoelectron spectroscopy (XPS). The N/C of about 0.08 was obtained GO sample which is four times higher than that of conventional N-doped carbon. It was found that the main chemical structure of N was pyridinic N in the GO sample; the incorporated N was consisted of 49% of pyridinic N, 35% of pyrrolic N, 14% of graphitic N and 2% of oxidized N. The XPS measurement revealed that the decreasing in the oxygen species such as C=O, COOH and C=O. This result suggests that N incorporation into the GO structure was achieved through the decomposition of C=O, COOH and C=O bonds, as illustrated in Fig. 2. The ORR catalytic activity of obtained N-doped GO was evaluated by a rotating disk method in the oxygen-saturated 0.5 M H_2SO_4 (Fig. 3). Comparing with the as-received GO sample, the obtained N-doped GO sample showed higher negative current density at higher potential, indicating that higher performance for the ORR. As a conclusion, the N-doping into carbon materials by utilizing EB irradiation technique is useful to fabricate carbon material with the ORR activity.

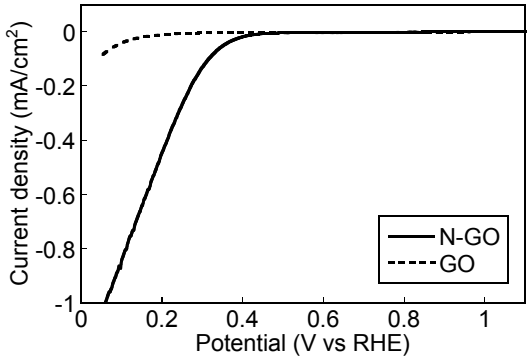

Fig. 3. ORR activity of N-doped GO obtained by EB irradiation technique.

Acknowledgments

This work was partly supported by JSPS KAKENHI Grant Number 21H04669.

Reference

[1] N. Kannari *et al.*, Carbon **50**, 2941 (2012).
DOI: 10.1016/j.carbon.2012.02.063

1 - 09 Preparation of ion-track membranes of polystyrene

H. Koshikawa, S. Yamamoto, M. Sugimoto, S. Sawada and T. Yamaki

Department of Advanced Functional Materials Research, TARRI, QST.

A polymer film is irradiated with MeV-GeV heavy ions, and the damaged regions in a cylindrical shape, referred to as latent tracks, are susceptible to a proper etchant. There have been numerous studies on the resulting ion-track membranes for poly(ethylene terephthalate) and polycarbonate because the tracks of these materials are easily dissolved in an alkaline solution. However, very few studies have been reported for ion-track membranes of radiation-resistant polystyrene (PS); to our knowledge, only one proceeding report [1] was published by J. Kaewsaenee *et al*. They reported the conditions of irradiation and the subsequent chemical etching, but they did not mention the information regarding the depth direction of the prepared pores, *i.e.*, whether or not the pores penetrated through the PS film. We discuss the morphology of the pores to demonstrate their cone structure using surface and cross-sectional scanning electron microscope (SEM) images toward developing the first example of PS ion-track membranes with through-pores.

Experimental

Commercially-available 50-μm-thick PS films were irradiated with 560 MeV ^{129}Xe ions at a fluence of 3.0×10^6 ions/cm^2 from the TIARA cyclotron of the QST. The irradiated PS films were etched in a mixture of 40% H_2SO_4 and 1.2 mol/L $K_2Cr_2O_7$ at 80 °C without stirring. The etched samples were washed with a large amount of water and dried for 4 h in air. The surface and cross-section of the membranes were observed with an SEM after their Au coating. To prepare cross-sections without any distortion, we tried two sectioning methods; one was commonly used freeze fracturing and the other was new electron-beam irradiation fracturing.

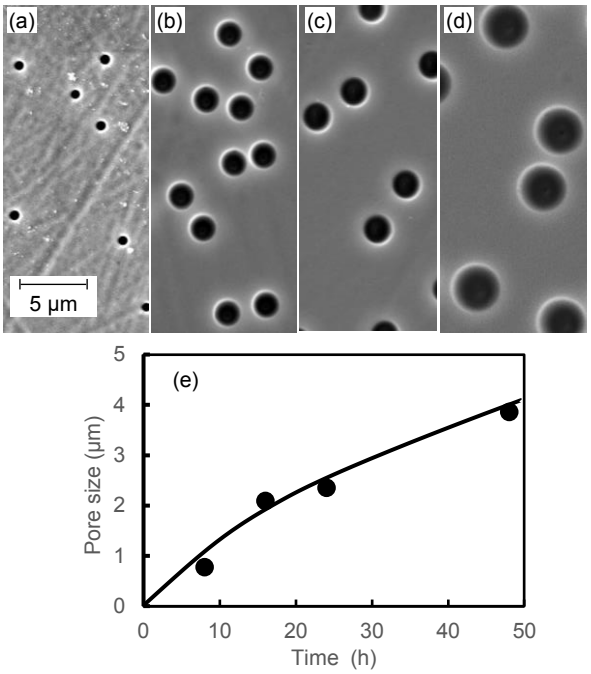

Fig. 1. The SEM images (a)-(d) of the surface of the membranes, which were obtained by the 8, 16, 24 and 48-h etching. **(**e) was the relationship between etching time and the diameter of ion-track PS membranes.

Results and discussion

Figures 1 (a)-(d) show the SEM images of the surface of the membranes prepared by etching for 8, 16, 24 and 48 h. The pores with surface diameters of 0.78, 2.1, 2.4 and 3.9 μm were obtained. Figure 1 (e) shows a plot of etching time and the pore diameter. The longer the time was, the larger the pore size became, confirming the validity of the results.

In order to investigate the pore morphology, cross-sectional specimens were prepared. As shown in Fig. 2 (a), the cut surfaces obtained by the freeze fracturing seemed not to be flat and were far from ideal; such the large distortion made it impossible to observe the cross-section of the pores clearly. On the other hand, the ion-track membrane was irradiated in air with 2 MeV electron beams at a dose of 355 MGy, leading to embrittlement as a consequence of radiation effects. Thus, the sample was easily broken to give cut surfaces with much lower distortion and to increase the image resolution as seen in Fig. 2 (b). Figure 2 (c) shows an enlarged view of the cross-section near the surface, confirming non-penetrating cones with a depth of 6.2 μm and aspect ratio of 2.6.

Reference

[1] J. Kaewsaenee *et al.*, 31st Congress on Sci. and Technology of Thailand at Suranaree University of Technology, 18-20 (2005)

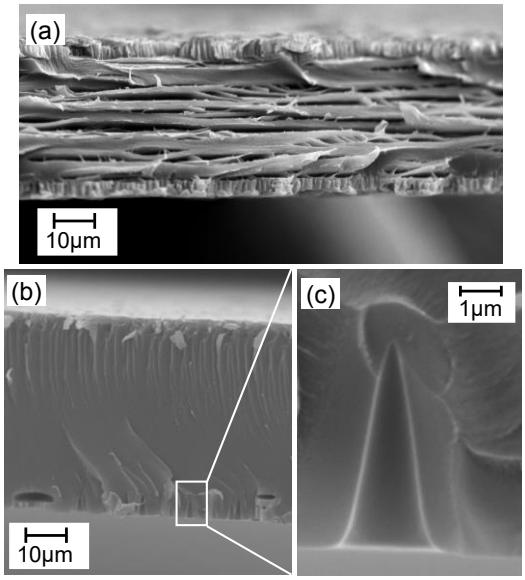

Fig. 2. The cross-sectional SEM images of ion-track PS membranes. The specimens were prepared by using (a) freeze fracturing and (b, c) and electron-beam irradiation fracturing.

1 - 10 High-precision flat-plate reference infrared radiator with perfect blackbody composite made by high-energy ion track etching technique

Y. Shimizu[a)], M. Imbe[a)], K. Godo[a)], N. Sasajima[a)],
H. Koshikawa[b)], T. Yamaki[b)] and K. Amemiya[a)]

[a)]National Metrology Institute of Japan, AIST
[b)]Department of Advanced Functional Materials Research, TARRI, QST

Thermal imagers visualize real-time surface temperature distribution without contact based on infrared imaging. The accuracy of thermal imaging has become increasingly important with the widespread use of a thermal imager as a fever screening tool to prevent the spread of infectious diseases. Flat-plate blackbody infrared radiators are temperature references that correct the measurement errors of the thermal imagers at the screening sites, enabling more accurate onsite measurements. High-precision reference radiators should have a high emissivity ε (close to 1). However, conventional high-emissivity materials have insufficient mechanical durability, making it difficult to employ them for onsite reference radiators. We have developed durable perfect blackbody sheets with numerous micro conical pit structures (antireflection (AR) structures) formed by high-energy ion track etching technique and demonstrated high emissivity and in-plane uniformity of the sheet [1, 2]. In this study, we fabricated a blackbody plate by applying the blackbody sheet technology, and developed a high-precision flat-plate reference radiator equipped with the blackbody plate.

The blackbody plate consists of the light absorption layer of a carbon-based paint on an aluminum substrate and the AR layer of a UV-curable resin (Fig. 1(a)). A Poly allyl diglycol carbonate (CR-39 in trade name) substrate was etched after being irradiated with energetic heavy ion beam from an azimuthally varying field cyclotron at the Takasaki Ion Accelerators for Advanced Radiation Application (TIARA). A Polydimethylsiloxane (PDMS) replica mold was made by tracing the AR structure on the CR-39 substrate after etching. The AR structure of the UV-curable resin on the blackbody plate was successfully formed using the PDMS replica mold (Fig. 1(b)). The reflectance (= 1 − ε) of the blackbody plate should be ultralow in the measurement wavelength range of thermal imagers (typically from 7 μm to 14 μm). Our blackbody plate exhibited sufficiently low reflectance < 0.001 (ε > 0.999) over the target wavelength range (Fig. 1(c)) [3].

A prototype of flat-plate reference infrared radiator was fabricated by mounting the blackbody plate on a Peltier unit to control temperature (Fig. 2). The reference radiator achieved an unprecedentedly small expanded uncertainty (95 % level of confidence) of ~0.1 °C for the radiance temperature [4] (The emissivity of the conventional reference radiator product is typically 0.96 ± 0.02, resulting in an expanded uncertainty of ~0.4 °C). The AR structure fabricated by high-energy ion track etching played a pivotal role in the high emissivity of our reference blackbody radiator. The high-precision reference blackbody radiator will contribute to improving the reliability of non-contact fever screening by thermal imagers.

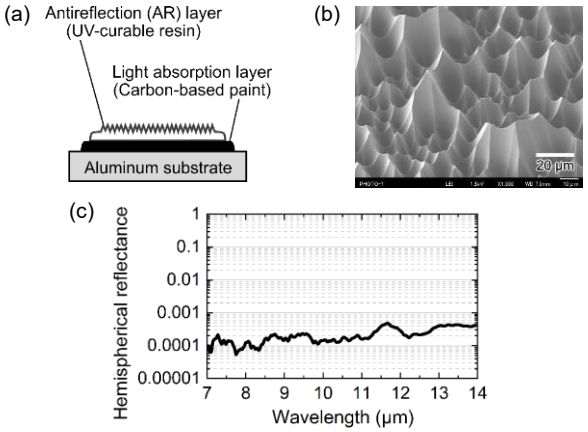

Fig. 1. (a) Schematic cross section, (b) scanning electron microscopy image of AR surface, and (c) hemispherical reflectance of the blackbody plate for reference radiator.

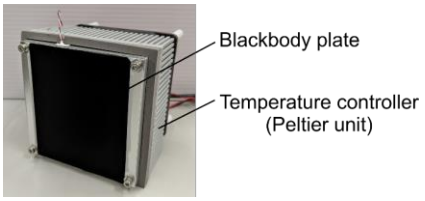

Fig. 2. Prototype of flat-plate reference infrared radiator.

Acknowledgments

This work was partially supported by KAKENHI JP21H03753 and AMED JP20he0822011.

The ion beam irradiation experiment was conducted at TIARA of QST, which was supported by the Inter-University Program for the Joint Use of JAEA/QST Facilities.

References

[1] K. Amemiya *et al.*, J. Mater. Chem. C **7**, 5418 (2019). DOI:10.1039/c8tc06593d
[2] Y. Shimizu *et al.*, Opt. Express **28**, 22606 (2020). DOI:10.1364/OE.397136
[3] Y. Shimizu *et al.*, Opt. Lett. **46**, 4871 (2021). DOI:10.1364/OL.433028
[4] Y. Shimizu *et al.*, Appl. Opt. **61**, 517 (2022). DOI:10.1364/AO.446426

1 - 11 Proton and water selectivity of ion-track-grafted proton-exchange membranes for HI concentration

N. Tanaka[a)], S. Sawada[b)], C. Sugimoto[a)] and T. Yamaki[b)]

[a)]HTGR Research and Development Center, JAEA
[b)]Department of Advanced Functional Materials Research, TARRI, QST

The thermochemical water-splitting hydrogen production method, called iodine–sulfur (IS) process, has been developed to reduce CO_2 emission. In the IS process, a new proton-exchange membrane (PEM) [1] prepared by the radiation-induced graft polymerization has been applied to the electro-electrodialysis (EED), which can enrich hydrogen iodide (HI) in an HI-I_2-H_2O mixture (HIx solution). We developed the PEMs by a radiation grafting method [1], which involves the irradiation of the base polymer film with γ-rays and graft polymerization for introduction of the cation exchange groups. The prepared PEMs with the high ion exchange capacity (IEC) were found to show the H^+ conductivity higher than that of the conventional PEM. Unfortunately, however, these highly-conductive PEMs showed lower selectivity (H^+ and H_2O): they unexpectedly permeated the other chemical species such as I^- and H_2O because the ion channels composed of the hydrophilic graft chains and absorbed water would swell excessively.

Quite recently, we have started to develop the PEMs by an ion-track grafting technique using MeV-GeV heavy ions, instead of γ-rays. Such a high-energy ion beam can create the one-dimensional cylindrical ion channels. The resulting cylindrical ion channels can efficiently transport H^+, while the surrounding unmodified regions can restrict the excess swelling of the ion channels. So far, it was confirmed that the ion-track grafted PEM could have the practical applicability to EED [2]. In this study, the effect of ion species on the H^+ and H_2O selectivity was investigated.

In order to verify the effect of bombarding ions, the base poly(ethylene-*co*-tetrafluoroethylene) film irradiated with 560 MeV ^{129}Xe and 520 MeV ^{40}Ar at 3.0×10^8 and 1.0×10^9 ions/cm^2, respectively. For the PEM preparation, this was followed by graft polymerization of styrene into the ion tracks and sulfonation of the grafted styrene units (referred to as ^{129}Xe and ^{40}Ar PEMs). The ^{129}Xe and ^{40}Ar PEMs had IECs of 1.0-2.3 mmol/g while the PEMs prepared by the conventional γ-ray-induced grafting (referred to as a γ-ray PEM) exhibited 1.1-2.4 mmol/g [1]. For the HI concentration test, the EED cell with an effective area of 5 cm^2 was used. An aqueous HI/I_2 solution at the molality of [HI] = [I_2] = 10 mol/kg was supplied to both the cathode and anode sides. The EED was conducted at 40°C by applying a constant current of 200 mA/cm^2. The transport number (t_+) and water permeation factor (β) as H^+ and H_2O selectivity were calculated by measuring the time course of the solution concentrations during the EED operation.

Figure 1 shows the t_+ values of the tested PEMs as a function of IEC. The measured values decreased with an increase of IEC, and there was no difference between the ^{129}Xe and ^{40}Ar PEMs. At lower than 1.5 mmol/g of IEC, the t_+ values of the ^{129}Xe and ^{40}Ar PEMs were higher than those of γ-ray PEM, suggesting that H^+ selectivity was improved by the ion-track grafting technique.

Figure 2 shows the IEC dependence of β. The values of ^{129}Xe and γ-ray PEMs seemed to exhibit a similar trend in that they represented the maximum in the vicinity of IEC = 1.5 mmol/g. On the other hand, the β value of the ^{40}Ar PEM was almost independent of IEC; especially, this was not enhanced around IEC = 1.5 mmol/g. These results suggest that the grafting with the lighter ions would give us PEMs with suppressed H_2O permeation for the HI concentration.

Acknowledgments

This work was supported by JSPS KAKENHI Grant Number JP20K05203.

References

[1] N. Tanaka *et al.*, Chem. Eng. Sci. **237**, 116575 (2021). DOI: 10.1016/j.ces.2021.116575
[2] N. Tanaka *et al.*, MRM 2021, H5-PR17-05 (2021).

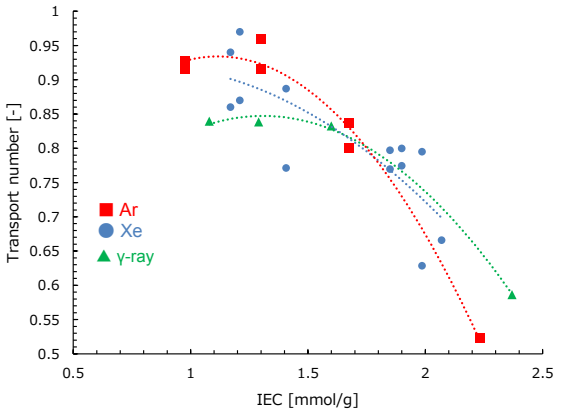

Fig. 1. IEC dependence of transport numbers (●:^{129}Xe, ■:^{40}Ar, ▲:γ-ray).

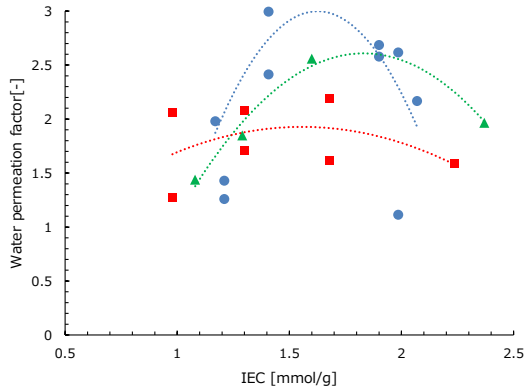

Fig. 2. IEC dependence of water permeation factors (●:^{129}Xe, ■:^{40}Ar, ▲:γ-ray).

1 - 12 Effect of 190 keV proton irradiation on superconducting properties in $FeSe_{0.5}Te_{0.5}$ thin films

T. Ozaki[a)], H. Okazaki[b)], H. Koshikawa[b)], S. Yamamoto[b)] and T. Yamaki[b)]

[a)]School of Engineering, Kwansei Gakuin University
[b)]Department of Advanced Functional Materials Research, TARRI, QST

Introduction

Iron-based superconductors have some fascinating properties for applications, such as reasonably high superconducting transition temperature T_c, a quite smaller anisotropy γ and larger critical grain boundary angle than high-T_c cuprate superconductors. In order to employ superconductors in the practical application, it is crucial to raise the critical current density J_c in magnetic fields. The high in-field J_c performance could be obtained by introducing nano-sized precipitates and defects, which can pin the vortices. The desirable vortex-pinning defects could be afforded by ion irradiation, which basically enables the creation of various defects, such as points, clusters and tracks, by choosing appropriate ion species and energy. We have introduced pinning defects in iron-chalcogenide $FeSe_{0.5}Te_{0.5}$ (FST) superconducting films to enhance J_c in magnetic field by ion irradiation.[1,2)] In this study, we report the effect of the irradiation fluence with 190 keV proton on superconducting properties in FST thin films.

Experiment

All FST films with ~100 nm thickness were fabricated by the pulsed laser deposition (PLD) method using a Nd:YAG laser (λ = 266 nm). The same FST film was characterized before and after irradiation to eliminate the influence of sample variations. A beam of 190 keV proton at fluences of 5×10^{14} to 1×10^{16} ions/cm^2 was directed to the film surface at normal incidence. Superconducting transport properties were measured using the conventional four-probe method in a physical property measurement system (PPMS DynaCool, Quantum Design).

Results and Discussion

Figure 1 shows T_c as a function of fluence for FST films before and after 190 keV irradiation at (a) 0 T and (b) 10 T with $H//c$. Interestingly, the FST film irradiated at a 5×10^{14} ions/cm^2 dose exhibited an increase of T_c at 0 T by ~0.3 K. The enhancement of T_c could arise from the nanoscale compressive strain produced by the proton irradiation.[1)] However, T_c decreased after the irradiation at over 1×10^{15} ions/cm^2 doses. We also found that the T_c enhancement at 10 T for the FST films irradiated at a 5×10^{14} ions/cm^2 dose is larger than that at 0 T. In addition, the increase of T_c at 10 T was observed in the FST film irradiated at a 1×10^{16} ions/cm^2 dose, which shows a decrease of T_c at 0 T after the irradiation. This could be attributed to the vortex pinning defects produced by 190 keV proton irradiation.

Figure 2 shows magnetic field dependence of J_c enhancement, $(J_c^{after} - J_c^{before})/J_c^{before}$, for FST films irradiated with 190 keV protons. Upon irradiation at fluences from 1×10^{15} to 1×10^{16} ions/cm^2, systematic J_c

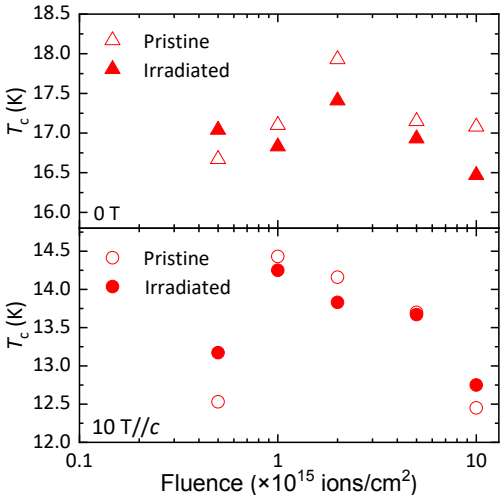

Fig. 1. Fluence dependence of T_c at (a) 0 T and (b) 10 T for FST films before and after the 190 keV irradiation.

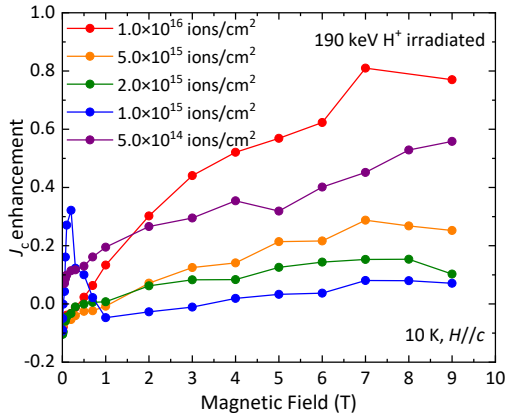

Fig. 2. J_c enhancement as a function of magnetic field for FST films irradiated with 190 keV protons.

enhancement was observed in the magnetic field, reaching ~80% enhancement over 7 T. This indicates that the structural defects produced by 190 keV proton irradiation can be highly effective pinning centres.

Our studies show that 190 keV proton irradiation is sufficient in order to provide a strong pinning defect landscape in iron-chalcogenide $FeSe_{0.5}Se_{0.5}$ superconducting films.

References

[1] T. Ozaki *et al.*, Nat. Commun. **7**, 13036 (2016). DOI: 10.1038/ncomms13036
[2] T. Ozaki *et al.*, Supercond. Sci. Technol. **33**, 094008 (2020). DOI: 10.1088/1361-6668/ab9f66

1 - 13 The origin of the weakened bonding of oxygen with the Pt catalyst on an ion-beam-irradiated carbon support

H. Okazaki[a)], T. Ikeda[a)], A. Idesaki[a)], H. Koshikawa[a)], D. Matsumura[b)], S. Yamamoto[a)] and T. Yamaki[a)]

[a)]Department of Advanced Functional Materials Research, TARRI, QST
[b)]Materials Sciences Research Center, JAEA

Our previous study demonstrated that the Pt nanoparticles (NPs) on an Ar^+-irradiated glassy carbon (GC) substrate exhibited a higher oxygen reduction reaction (ORR) activity than those on the non-irradiated GC substrate [1]. From the x-ray absorption fine structure (XAFS) measurements, we found that the vacancy introduction increased the Pt-C interaction [2], which would change the electronic structure of the Pt NPs. We also performed the *in situ* XAFS measurements in an O_2 atmosphere to elucidate the electronic states of the Pt NPs upon O_2 adsorption, which is the first step of the ORR process. We demonstrated that the Pt-O* antibonding level due to oxygen adsorption were lowered in energy. The observed shift suggests that electrons could easily be filled in the antibonding level because its level gets close to the Fermi level, leadings to a weaker Pt-O* bond. Since Pt binds oxygen too strongly and thus the ORR rate is limited by the removal of surface oxide [3], the weak Pt-O* bond results in higher ORR activity. In order to elucidate the origin of the weakened Pt-O* bond, we simulated the oxygen adsorption to a Pt cluster supported by graphene with vacancies.

We simulated oxygen adsorption to Pt_4 cluster supported on the pristine graphene (PG) and the graphene sheet with the double vacancies (DV), which has the smallest formation energy for the sheet with vacancies until six, in water by the molecular dynamics calculation using the Car-Parrinello MD approach [4] within a planewave pseudopotential scheme. The total energies were converted to Gibbs free energies.

We found that the oxygen adsorption and the supported form of Pt_4 cluster by graphene sheet for DV are different from that for PG, as shown in Fig. 1. For the oxygen adsorption, the oxygen binds to the Pt atom with Pt-C bond for DV whilst adsorbs to the Pt atom without Pt-C bond for PG. For the supported form, two Pt atoms have two Pt-C bonds in DV. On the other hand, one Pt in the interface has only one Pt-C bond in PG. Thus, these results suggest that the vacancies affect to the oxygen adsorption through the Pt-C bond. The changes of free energy before and after oxygen adsorption for both cases are estimated to be -0.385 eV for DV and -1.113 eV for PG. This indicates that the oxygen adsorption was weakened by the vacancies because the gain of free energy before and after oxygen adsorption was small. Therefore, we could assume the model with the weakened Pt-O* bond by the vacancy introduction, which is consistent with our previous XAFS research.

We estimated the hybridization of electron orbital between Pt cluster, the adsorbed oxygen, and graphene sheet. The orbital overlap populations between Pt 5*d* and O 2*p* orbitals were estimated to be 0.07 for DV, and 0.13 for PG, respectively. The small hybridization between Pt 5*d* and O 2*p* orbitals for DV compared to that for PG means that the Pt-O* bond is weakened by the vacancies. We also found that the hybridization between Pt $5d_{z^2}$ and C 2*p* orbitals very increases by the vacancy introduction. This implies the increase of Pt-C interaction by the vacancy introduction, which is consistent with the result in our previous XAFS study [2]. The origin of the strong hybridization between Pt $5d_{z^2}$ and C 2*p* orbitals is that the covalent bond electrons of the carbon atom next to the vacancies due to the vacancy introduction are deficient and then are compensated from the Pt 5*d* electrons. Therefore, we found that the strong hybridization between Pt $5d_{z^2}$ and C 2*p* leads to the reduction of the overlap populations between Pt $5d_{z^2}$ and O 2*p* orbitals. In the study, we demonstrated that the origin of the weakened Pt-O* bond is the increase of Pt-C interaction by the vacancy introduction into carbon support in Pt catalysts and the vacancy can change the bond strength between Pt and adsorbates in ORR process.

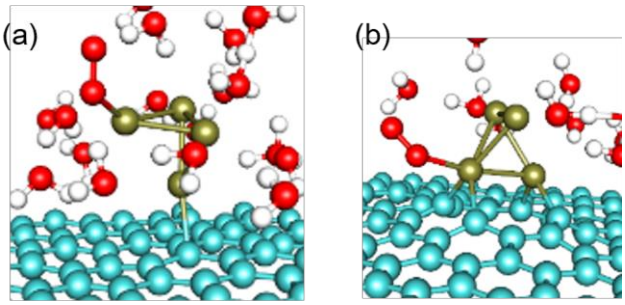

Fig. 1. The structure of Pt_4 cluster with adsorbed oxygen molecule on (a) the PG and (b) the DV in water. Yellow, blue, red, and white balls are Pt, carbon, oxygen, and hydrogen atoms, respectively.

Acknowledgments

This work is partially supported by a Grant-in-Aid for Scientific Research (KAKENHI) Grant Numbers 18H01923 and 21H04669.

References

[1] T. Kimata *et al.*, Phys. Rev. Mater. **6**, 035801 (2022). DOI: 10.1103/PhysRevMaterials.6.035801
[2] H. Okazaki *et al.*, J. Chem. Phys. **152**, 124708 (2020). DOI: 10.1063/1.5144568
[3] F. W. Lytle *et al.*, J. Chem. Phys. **70**, 4849 (1979). DOI: 10.1063/1.437376
[4] R. Car and M. Parrinello, Phys. Rev. Lett. **55**, 2471 (1985). DOI: 10.1103/PhysRevLett.55.2471

1 - 14 Chemical state of platinum ions implanted into glassy carbon substrates

T. Kimata[a,b], S. Kato[b], T. Kobayashi[c], S. Yamamoto[a], T. Yamaki[a] and T. Terai[b]

[a]Department of Advanced Functional Materials Research, TARRI, QST
[b]Department of Nuclear Engineering and Management, The University of Tokyo
[c]Neutron Beam Technology Team, RIKEN

Glassy carbon (GC) has been widely used as an electrode material, owing to its graphite-like properties and excellent chemical and electrochemical stability. We investigated the effect of tungsten (W)-ion implantation on GC substrates in terms of the W depth distribution and the chemical and morphological properties of the implanted layer. Unfortunately, nanoparticles of W carbide and W semicarbide that appeared in the implanted GC layer had intrinsically low electrochemical activity[1]. We have recently prepared electrochemically active platinum (Pt) nanoparticles on Ar^+-implanted GC substrates, where the Pt-C bonding promoted by ion-beam-induced lattice defects would be the origin of the higher activity[2]. Here, the GC substrates were implanted with Pt ions to efficiently express Pt/C interfacial interactions, and then the chemical states of the constituent elements in the Pt-ion-implanted GC substrate were investigated[3].

The GC substrates were implanted with 100 keV Pt ions in an IA chamber at the TIARA ion implanter. Sample analysis was performed by X-ray photoelectron spectroscopy (XPS); a 2 keV Ar-ion sputtering gun was used for destructive in-depth analysis of the Pt-ion-implanted layer.

Figures 1 (a) and (b) show Pt 4f and C 1s spectra obtained for the samples after the Ar-ion sputtering for different durations, respectively. As shown by the blue line in Fig. 1 (c), for sputtering longer than 120 s, the intensity of the Pt 4f peak gradually increased as the Pt-ion-implanted layer was exposed on the surface and the Pt concentration increased. At depths greater than 30 nm, the Pt 4f peak shifted toward lower energies (red line in Fig. 1 (c)), suggesting that the chemical shift also has an effect. Since the chemical shift is expected to be due to the formation of Pt-C bonds, we also examined the C 1s XPS spectra. The green line in Fig. 1 (c) indicated that the peak position of C 1s shifted to lower energy as the sputtering time increased and the measured layer became deeper. Comparing the C 1s shift with the Pt concentration distribution, the peak shifted toward lower energies as the Pt concentration increased. However, the difference between the binding energy for this peak and that for the Pt carbide was approximately 0.7 eV, suggesting that this peak shift was not owing to the formation of Pt carbide molecules, but owing to the interaction between Pt and C, as observed in our previous studies[2].

Acknowledgments

This work was partly supported by JSPS KAKENHI Grant Numbers 20760600, 22760678, 24561047, 18H01923, and 21H04669.

References

[1] T. Kimata *et al*. (2022). In T. Yatsuhashi et al. (Eds.) High-energy chemistry and processing in liquid. Springer Nature, Singapore, pp. 311. DOI: 10.1007/978-981-16-7798-4_16
[2] T. Kimata *et al*., Phys. Rev. Mater. **6**, 035801 (2022). DOI: 10.1103/PhysRevMaterials.6.035801
[3] T. Kimata *et al*., J. Appl. Phys. under editorial process.

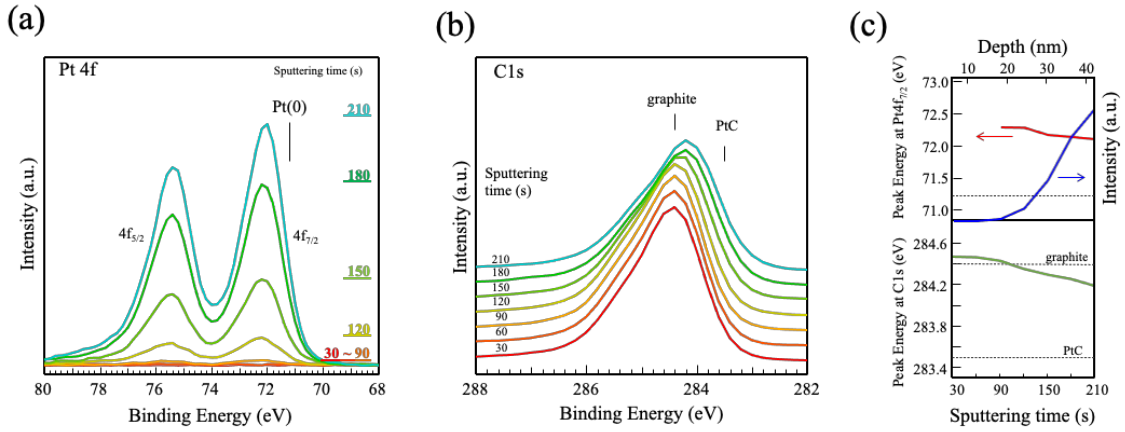

Fig. 1. (a) Pt 4f XPS and (b) C 1s XPS spectra of the GC sample implanted with 100 keV Pt ions at a fluence of 1.7×10^{16} ions/cm^2. Sputtering time indicates the irradiation time by an Ar-ion sputtering gun. (c) The peak energies at Pt $4f_{7/2}$ (red line) and C 1s (green line), and peak intensity (blue line) at Pt $4f_{7/2}$, against the sputtering time.

1 - 15 Enhanced X-ray excited optical luminescence in MgO with Cr ion implantation

T. Ueno[a,b], H. Okazaki[c], S. Li[b,d], S. Sakai[b,d], T. Yamaki[c], T. Watanuki[a,b], Y. Takeichi[e], M. Mizuguchi[f], H. Iwasawa[a,b,g] and Y. Ohtsubo[b,g]

[a]Synchrotron Radiation Research Center, KPSI, QST
[b]QST Advanced Study Laboratory, QST
[c]Department of Advanced Functional Materials Research, TARRI, QST
[d]Quantum Materials and Applications Research Center, TARRI, QST
[e]Department of Applied Physics, Graduate School of Engineering, Osaka University
[f]Division of Materials Research, IMaSS, Nagoya University
[g]Department of Advanced Synchrotron Radiation Research and Development, IASLS, QST

X-ray excited optical luminescence (XEOL) is photoluminescence induced by X-ray illumination on materials. X-ray absorption spectrum (XAS) of thin film fabricated on a transparent substrate such as MgO can be obtained by measuring XEOL emitted inside the substrate because its intensity is basically proportional to X-ray absorption of a film [1].X-ray magnetic circular dichroism (XMCD), a difference in XAS for right- and left-handed circularly polarized X-rays, can be used as a microscopic probe of magnetism. X-ray-detected ferromagnetic resonance (XFMR) is a technique to investigate magnetization dynamics in ferromagnetic films or multilayers which requires to detect very small XMCD signal associated with spin precession [2]. Such signal is obtained by measureing XEOL from substrates. In case of MgO, XEOL is mainly attributed to Cr^{3+} impurities.

In the research and development of quantum and spintronic materials, it is important to expand applicability of XFMR to diverse class of matter. In this study, we tried to enhance the intensity of XEOL from MgO substrate by increasing density of Cr^{3+} with ion implantation to facilitate the XFMR experiment.

Cr ion implantation was performed using an ion implanter at TIARA. Prior to ion implantation, MgO(001) substrates (about 10 × 10 mm^2 with 0.5 mm thick) are processed by ultrasonic cleansing in acetone and isopropanol, and subsequent UV ozone irradiation to prepare a clean surface. 190-keV accelerated Cr^+ ion beam was irradiated on MgO substrates at room temperature with varying fluences from 10^{14} to 10^{16} ions/cm^2). Ion beam energy was set to maximize the amount of Cr ions at around 100 nm from a surface. Irradiated MgO substrates are annealed at 900 °C for 1 h, and their surface roughness was evaluated by atomic force microscopy.

XEOL measurement was performed at BL-19B at the Photon Factory, KEK. Linearly polarized X-ray with an energy of 720 eV was used. Samples were kept at room temperature during the experiment. XEOL spectra were measured using a FLAME-S-VIS-NIR-ES spectrometer (Ocean Insight, Inc., USA).

Figure 1 shows the XEOL spectra of MgO. XEOL intensity is enhanced for samples with the fluence of 10^{15} /cm^2 and 10^{16} /cm^2 as compared to that of pristine MgO. On the other hand, a slightly smaller XEOL intensity was observed for the 10^{14} /cm^2 fluence sample than that of pristine MgO. Black bars in Fig. 1 represent peaks originating from the Cr^{3+} ion. This result indicates that Cr^{3+} impurity as XEOL color center in MgO was successfully increased by Cr ion implantation. However, XEOL intensity was not proportional to the Cr ion fluence. This may come from the difference in surface roughness between different fluence. We need further investigation to determine optimal fluence and post-annealing process to maximize XEOL intensity.

In conclusion, Cr ion implantation successfully increased XEOL intensity from MgO. Ion implantation to substrate materials is expected to be a viable method to enhance the efficiency of the XEOL-XAS experiment.

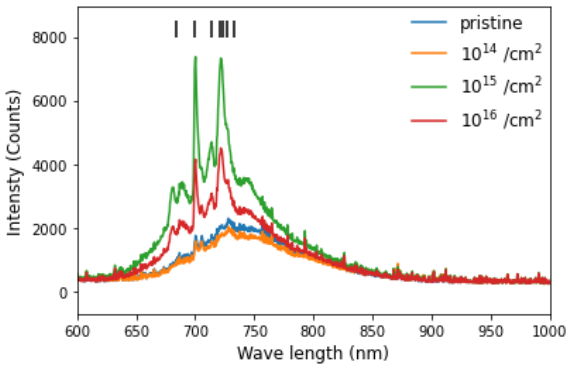

Fig. 1. X-ray excited optical luminescence (XEOL) spectra of MgO. Black bars represent peak positions of Cr^{3+} derived luminescence.

Acknowledgments

This work was supported by QST President's Strategic Grant (QST Advanced Study Laboratory). Synchrotron radiation experiment was performed at Photon Factory under the approval of the Photon Factory Program Advisory Committee (Proposal No. 2021PF-G020).

References

[1] C. A. F. Vaz *et al.*, J. Electron Spectrosc. Relat. Phenom. **189,** 1 (2013). DOI:10.1016/j.elspec.2012.12.012
[2] C. Klewe *et al.*, Synchrotron Radiat. News **33**, 12 (2020). DOI:10.1080/08940886.2020.1725796

1 - 16 Radiation resistance of diamond FeFET with inorganic ferroelectric gate

T. Kawae[a)], H. Okazaki[b)] and T. Yamaki[b)]

[a)]College of Science & Engineering, Kanazawa University
[b)]Department of Advanced Functional Materials Research, TARRI, QST

Introduction

It is well known that the power devices exploit the limited power source efficiently for electrical equipment. For outer space development in near future, it is required to create the power devices with excellent resistance to radiation and heat rays. Widegap semiconductor diamond is known to be a promising candidate as a next-generation power device material with excellent radiation resistance. Then, in order to enhance the efficient operation of power FET devices, we proposed the ferroelectric gate diamond FET (FeFET), and demonstrated its typical properties such as an efficient carrier inducing [1]. In addition, inorganic ferroelectrics also have superior radiation resistance [2]. Thus, the ability to operate the diamond FeFET with inorganic ferroelectric gate in extremely harsh environments exposed to radiation and heat rays is required for further expansion of application areas of the outer space industry.

From our preliminary study of FeFET with widegap semiconductor ZnO and inorganic ferroelectric $Pb(Zr,Ti)O_3$ (PZT) in γ-ray environments, we found that elemental diffusion at the channel-ferroelectric gate interface is the most serious problem caused by γ-ray irradiation [3]. Based on the above results, we have prepared Metal Ferroelectric Insulator Semiconductor (MFIS)-type gate [4] and selective grown channel structures that compose diamond FeFET, and investigated electrical properties of prepared structures to high-energy γ-ray irradiation.

Experimental procedure

The p^+-diamond layer was deposited on the (111) diamond substrate by a microwave plasma chemical vapor deposition method. To prepare the MFIS gate, Au, PZT and Al_2O_3 films were deposited on the p^+-diamond coated substrate by thermal evaporation, chemical solution deposition and atomic layer deposition methods, respectively. The p^--diamond channel and p^+-diamond source/drain electrode were selectively grown on the (111) diamond substrate using patterned Ni hard-mask film.

The prepared MFIS gate and diamond channel structures were irradiated with γ-rays at Co-60 irradiation facility of TARRI, under the conditions of a dose rate of 3.85 kGy/h and of an irradiation time of 4 h. Their electrical properties were compared before and after the irradiation.

Results and discussion

The prepared MFIS gate exhibited clear ferroelectricity. Figure 1 (a) shows P-V curves of the prepared MFIS gate before/after γ-ray irradiation with a total dose of 15.4 kGy. After the γ-ray irradiation, no degradation in the ferroelectricity and insulating properties were observed. Observed excellent radiation resistance of electrical properties were mainly caused by barrier function of the Al_2O_3 insulating layer for interdiffusion between PZT and diamond layer. Figure 1 (b) shows I-V curves of the selectively grown p^--diamond channel before/after γ-ray irradiation with a total dose of 15.4 kGy. No degradation of channel conductivity was observed for γ-ray irradiation. Also, it is considered that deterioration of the p^+/p^- homoepitaxial diamond interface did not occur since non-linear I-V curves (due to the creation of the Schottky barrier) were not observed after the irradiation.

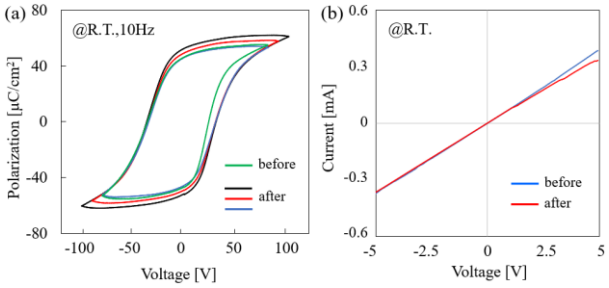

Fig. 1. (a) P-V curves of MFIS gate and (b) I-V curves of the selectively grown channel before/after the γ-ray irradiation.

These observed results demonstrate excellent radiation resistance of the fundamental electrical properties of the MFIS gate and selectively grown channel structures which constitute a proposed diamond FeFET. In order to realize the advanced power FeFET for harsh environments, it is necessary to systematically study the device properties of proposed diamond FeFET to high-energy γ-ray irradiation, such as on-resistance, threshold voltage shift, and channel mobility. Preparation of FeFET using ferroelectric $BiFeO_3$ which has the higher Curie temperature and polarization value than those of PZT is also useful to obtain the excellent device performance [5].

Acknowledgments

This work was supported by JSPS KAKENHI Grant Number JP20K04595, and Kanazawa Univ., CHOZEN project 2022.

References

[1] T. Kawae *et al.*, Appl. Phys. Lett. **108**, 242101 (2016). DOI: 10.1063/1.4953777
[2] S. J. Brewer *et al.*, J. Appl. Phys. **120**, 024101 (2016). DOI: 10.1063/1.4955424
[3] T. Kawae *et al.*, QST Takasaki Annu. Rep. 2020, **QST-M-33** 35 (2021).
[4] T. Kawae *et al.*, Jpn, J. Appl. Phys. **52**, 04CH03 (2013). DOI: 10.7567/JJAP.52.04CH03
[5] T. Kawae *et al.*, Phys. Status Solidi B **252**, 833 (2015). DOI: 10.1002/pssb.201451553

1 - 17 Optical response of vacancy-induced magnetism in gallium nitride estimated by spin-polarized positron annihilation method

M. Maekawa, A. Miyashita and A. Kawasuso

Department of Advanced Radiation Technology, TARRI, QST

The vacancy-induced magnetism has attracted attention as a new method for fabricating ferromagnetic semiconductor materials without the doping of magnetic elements. At cation vacancies in semiconductors, the magnetization is normally cancelled out because the same number of electrons with spin up and down are arranged. If these vacancies are adjacent, the degenerate energy levels of cation vacancies are exchange-splitted due to the interaction among unpaired electrons [1]. As a result, one electrically-neutral cation vacancy in metal nitride can possess the magnetization of 3 μB (μB: Bohr magneton). This is the theoretically proposed origin of vacancy-induced magnetism. Gallium nitride (GaN) introducing cation vacancy (gallium vacancy, V_{Ga}) by N ion implantation is expected to exhibit the magnetization. However, although the positron annihilation measurements clearly show the introduction of $V_{Ga,}$ only a very weak magnetization has been detected [2]. In addition, the intensity of the magnetic Doppler broadening (MDB) measured by the spin-polarized positron annihilation (SP-PAS) method, which will increase by the vacancy-induced magnetism, is not increased in the ion implantation region. This disappearance of vacancy-induced magnetism might be caused by the cancelling out of induced spins by the extra electrons trapped to the V_{Ga} defects. In this study, we have investigated whether the magnetism is enhanced by light illumination that flick off the extra electrons at the vacancies.

Sample was prepared by irradiation of 100 keV nitrogen ions (10^{15} cm^{-2}) onto a GaN epitaxial film (undoped, 2 μm thick) grown on a sapphire substrate using the TIARA ion implanter. The MDB spectra were measured by the SP-PAS method under ultraviolet (UV) light (360 nm LED irradiation, 3 W) illumination under the magnetic fields of 0.91T at the temperature of 20 K.

Figure 1 shows the MDB spectra of GaN sample irradiated with nitrogen ions. The positron incident energy was set to 6 keV (equivalent to the N ion implantation depth). In the dark condition (UV off), the MDB spectrum is almost flat same as reported before [2]. As positrons are known to preferentially trapped to V_{Ga} in GaN [3], this result indicates that vacancy-induced magnetism have not appeared. When the vacancy-induced magnetism is recovered, the finite intensity will appear on the MDB spectrum. However, even under UV irradiation condition, the MDB intensity have not increased. Figure 2 shows the energy dependence of the MDB intensity for UV illumination or dark condition. Not only in the ion implantation depth (5~7 keV) but also in all depth regions, clear systematic changes are not detected.

In our experiment, the enhancement of the vacancy-induced magnetism of GaN by UV light irradiation was not observed, suggesting that the magnetism is not suppressed by the electron compensation at the cation vacancies. The vacancy-induced magnetism in GaN might be caused not by single cation vacancies as predicted theoretically, but by other defect structures, such as vacancy clusters[4].

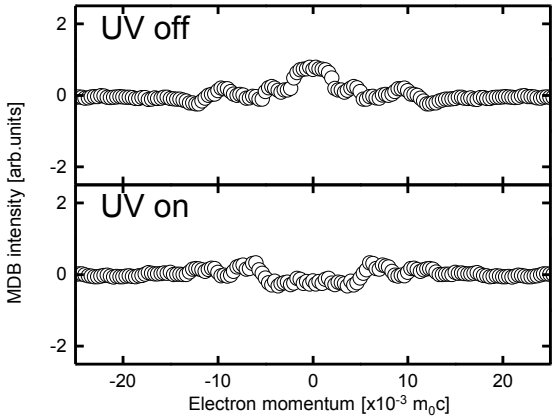

Fig. 1. UV irradiation effect of MDB spectra of N-ion irradiated GaN measured at the incident positron energy of E=6keV.

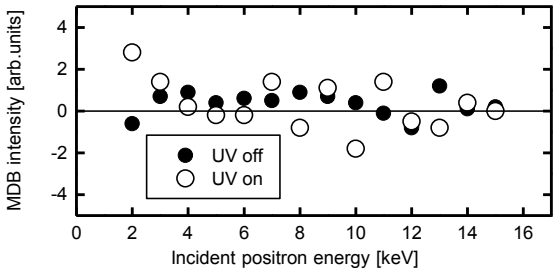

Fig. 2. The positron energy dependence of the MDB intensity.

Acknowledgments

This work was supported by JSPS KAKENHI Grant Number 18K04931.

References

[1] O. Volnianska *et. al*, Phys. Rev. B **83**, 205205(2011). DOI: 10.1103/PhysRevB.83.205205

[2] M. Maekawa *et al.*, e-J. Surf. Sci. Nanotechnol. **16,** 347(2018). DOI: 10.1380/ejssnt.2018.347

[3] K. Saarinen *et. al.*, Physica B **273–274**, 33 (1999). DOI: 10.1016/S0921-4526(99)00400-7

[4] M. Maekawa *et al*., Phys. Rev. B **102**, 054427 (2020). DOI: 10.1103/PhysRevB.102.054427

1 - 18 Positron annihilation spectroscopy research on irradiation of a new fiber

H. Fukazawa[a)], M. Yamaguchi[a)], M. Maekawa[b)] and A. Kawasuso[b)]

[a)]Nippon Fiber Co.
[b)]Department of Advanced Radiation Technology, TARRI, QST

Fly Ash (FA, Fig. 1(a)) is an industrial byproduct generated during coal combustion at coal-burning thermal power plants. To date, its industrial utilization has been limited primarily to the construction industry despite its potential versatility. However, this abundantly available byproduct can be put to better use now that it can be turned into a continuous long fiber, named as BASHFIBER® (Fig. 1(c)).

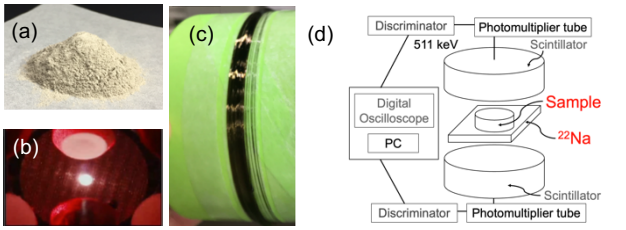

Fig. 1. (a) Fly ash (FA). (b) Thermal test in ISS. (c) Mono-filament of BASHFIBER®. (d) The experimental overview about PAS.

Made of a mixture of FA, slag and metallic elements, the fiber has great resistance to alkali to industrial Kevlar® or carbon-fiber which would be used to reinforce such materials as concrete. Unlike asbestos, BASHFIBER® is a continuous and perfect mono-filament with even diameter distribution all the way through and has no fuzz or branches. This reinforcing fiber is hugely versatile for industrial use, showing potential for a variety of applications. NEDO (New Energy and Industrial Technology Development Organization, Japan) has supported a civil engineering application and METI (Ministry of Economy, Trade and Industry, Japan) authorized the project as the Zero-Emission Challenge in 2021 [1].

Resistance fibers for space

Exposure to the space environment and thermal properties had tested the durability of BASHFIBER® on the exterior and inside of the International Space Station (ISS) [2], and it showed its resistance to cosmic rays. BASHFIBER® could provide an alternative to industrial glass or carbon fibers used to reinforce materials, contributing to more durable materials for use in space.

The returned samples have been studied on the ground more academically by the PAS (Positron Annihilation Spectroscopy, Fig. 1(d)) dedicated to it. Furthermore, to understand the exposure effects with atomic levels on the fiber in space, we started the irradiation test in 2021.

Positron annihilation spectroscopy

Figure 2(a) shows the spectra of ordinally glass fibers. Blue color curve in Fig. 2(a) is the spectrum of ordinally glass fiber. Red color curve in Fig. 2(a) is the spectrum of irradiated that by the electric beam in TARRI. Total dose is about 1.45 GGy. Clear difference exists between non-irradiated and irradiated fibers. The similar result implying the structural changes with irradiation was also reported by Ref. 3.

Figure 2(b) shows the spectra of BASHFIBER®. Any differences between non-irradiated and irradiated fibers are not observed. We also measured XRD, Raman, TG-DTA, SEM and so on, but a difference between those has not been observed. To understand the phenomena, we have planned other irradiation experiments including proton and gamma. High-energy proton beam experiments are especially important for the space communication application because the development of resistance materials for solar cosmic ray is now urgent challenges.

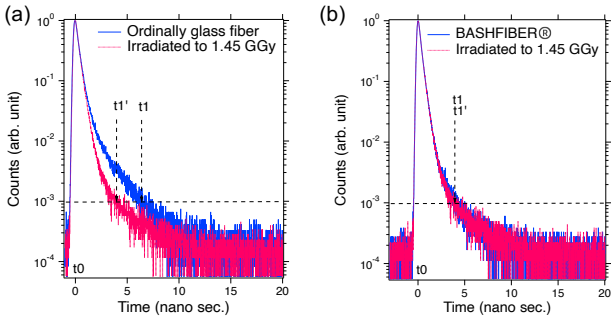

Fig. 2. Spectra of lifetime obtained for irradiated fibers in our system.

Acknowledgments

This work had been partially supported by Space Exploration Innovation Hub Center, JAXA, and the grant-in-aid of public interest foundation corporation, Himawari-Venture. We would like to thank to J-POWER (Electric Power Development Co., Ltd.), The Kansai Electric Power Company Incorporated, ITOCHU Corporation and SUMITOMO CORPORATION for providing us raw materials.

References

[1] List of Companies Taking on the Zero-Emission Challenge, https://www.meti.go.jp/english/press/2021/1005_002.html

[2] Measurement of Thermophysical Properties of Bash Fiber, https://www.nasa.gov/mission_pages/station/research/experiments/explorer/Investigation.html?#id=8304

[3] M. Hasegawa *et al.*, Nucl. Instrum. Methods Phys. Res. B **116**, 347 (1996). DOI: 10.1016/0168-583X(96)00070-5

1 - 19 Local structure of high-energy implanted Ni into Si(100)

S. Entani[a)], S.-I. Sato[a)], M. Honda[b)] and T. Ohshima[a)]

[a)]Quantum Materials and Applications Research Center, TARRI, QST
[b)]Materials Science Research Center, JAEA

Ni silicide synthesis by Ni ion beam irradiation into Si attracts attention due to its advantages including the ability of formation of local structures, the controllability of ion beams, the formability of silicide without heat treatment and the high reproducibility of the resulting specimen.

In this work, we investigate the evolution of the $NiSi_2$ synthesis during 3.0 MeV Ni^+ ions irradiation ranging from 10^{13} to 10^{16} ions·cm^{-2}. The local atomic structure of Ni implanted in Si is clarified by analyzing Ni *K*-edge fluorescent XAFS. Si(100) specimens were irradiated with 3.0 MeV Ni^+ ions at room temperature. The irradiation experiments were carried out at Takasaki Ion accelerators for Advanced Radiation Application (TIARA), National Institutes for Quantum Science and Technology (QST). The Ni *K*-edge XAFS spectra were collected in the fluorescence mode at BL-27B hard X-ray beamline at the Photon Factory of High Energy Research Organization (KEK-PF).

Figure 1 shows Ni *K*-edge EXAFS spectra of Ni^+-irradiated Si. Difference arose in the fine structure of the spectra between the ion fluence below 10^{14} ions·cm^{-2} and above 10^{15} ions·cm^{-2}. In the Fourier transforms (FTs) of the EXAFS spectra with the ion fluence lower than 10^{14} ions·cm^{-2}, two prominent structures are observed at around 1.7 and 2.2 Å, which are attributed to the Ni-Si bond in $NiSi_2$ and the Ni-Ni bond in metallic face-centered cubic Ni, respectively [1]. It can be considered that the high diffusivity of Ni in crystalline Si causes segregation of implanted Ni atoms as well as the formation of $NiSi_2$ phase. The peak from the Ni-Ni bond disappears after the Ni irradiation at the fluence above 10^{15} ions·cm^{-2}. Table 1 summarized the Ni-Si and Ni-Ni bond length in the Ni-implanted Si obtained by EXAFS analysis. In the case of 10^{13} and 10^{14} ions·cm^{-2}, the FTs can be fitted with two single-scattering paths (Ni-Si in $NiSi_2$ and Ni-Ni in fcc Ni). The difference of the Ni-Si bond length in Ni-irradiated Si from the bulk crystal is larger for the

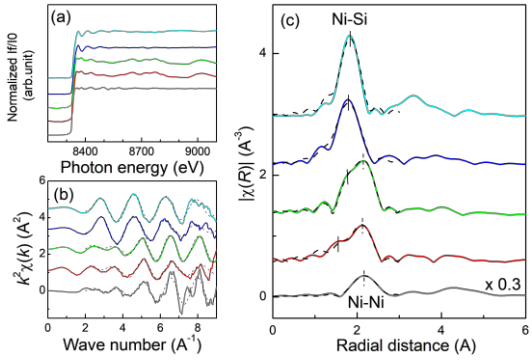

Fig. 1. (a) EXAFS spectra, (b) k^2-weighted $\chi(k)$ spectra and (c) Fourier transformations (FTs) of the EXAFS spectra. Grey, red, green, blue and sky blue lines in (a,b,c) are spectra of Ni foil, 10^{13}, 10^{14}, 10^{15}, 10^{16} ions·cm^{-2}-irradiated Si, respectively. The simulated fitting curves (dotted line) are also indicated.

10^{14} ions·cm^{-2} irradiation than that of the 10^{13} ions·cm^{-2}. This is thought to be originated from the increase in lattice strains due to the accumulation of radiation induced damage and implanted Ni atoms. In contrast, the FT spectrum can be fitted with a Ni-Si single-scattering path in the case of 10^{15} and 10^{16} ions·cm^{-2}. These results indicate that at the fluence above 10^{15} ions·cm^{-2} the $NiSi_2$ phase is dominantly formed, and the Ni-Ni bond formation is less dominant.

It is found that the increase in the concentration of Ni did not lead to the increase in the formation of the Ni-Ni bond. Ion beams lose their energy in the material and causes displacements of the lattice atoms via the nuclear energy depositions. As the ion fluence increases to a critical value, the accumulated damage produces a continuous amorphous region in the crystal. According to the Kinchin-Pease model, the displacements per atom is calculated by considering kinetic energy transfers above a threshold of the displacement energy; $T_d/2E_d$, where T_d is the damage energy (the nuclear energy deposition) and E_d is the displacement energy of lattice atoms [3]. Thus, the critical fluence D_c for Si-amorphization is expressed as $D_c = 2E_dN_{Si}/T_d$, where N_{Si} is density of silicon atoms. With using E_d = 15 eV, $T_d = 2.1 \times 10^9$ eV·cm^{-1} and $N_{Si} = 5.0 \times 10^{22}$ atoms·cm^{-3}, D_c is calculated to be 7.1×10^{14} ions·cm^{-2}. This suggests that the amorphization of Si begins to appear at the fluence above 10^{15} ions·cm^{-2}. It is considered that the amorphization of Si due to the accumulation of irradiation induced damage is key to obtain the $NiSi_2$ phase in Ni^+-irradiated Si.

Table 1
Ni-Si and Ni-Ni bond lengths of Ni atoms implanted in Si.

Fluence (ions·cm^{-2})	Ni-Si length (Å)	Ni-Ni length (Å)
10^{13}	2.27 ± 0.03	2.45 ± 0.02
10^{14}	2.65 ± 0.02	2.50 ± 0.01
10^{15}	2.33 ± 0.02	–
10^{16}	2.31 ± 0.01	–
	2.36 ($NiSi_2$ on Si(111)) [2]	2.48 ± 0.02 (Ni foil)

Acknowledgments

XAFS experiments were performed as part of the projects accepted by the Photon Factory Program Advisory Committee (PF-PAC Nos. 2018G518, 2020G589).

References

[1] S. J. Naftel *et al.*, Phys. Rev. B **57**, 9179 (1998). DOI:10.1103/PhysRevB.57.9179
[2] D. Cherns *et al.,* Philos. Mag. A. **46**, 849 (1982). DOI: 10.1080/01418618208236936
[3] G. H. Kinchin and R. S. Pease, Rep. Prog. Phys. **18**, 1 (1955). DOI: 10.1088/0034-4885/18/1/301

1 - 20 Improvement of radiation resistance by hetero p/n junction in solar cells

T. Nakamura[a)], M. Imaizumi[a)], S.-I. Sato[b)] and T. Ohshima[b)]

[a)]Research and Development Directorate, JAXA,
[b)]Quantum Materials and Applications Research Center, TARRI, QST

The conversion efficiency of a solar cell corresponds to the amount of non-radiative recombination via defect levels. For space solar cells, it is difficult to suppress the defect density after exposure of high-energy electrons and protons since the particles create radiation-induced defects in solar cells. In this study, we investigated the device structure that can reduce the effect of non-radiative recombination centers, namely, extend the effective minority-carrier lifetime with the same defect density. We focused on the solar cell that employs a hetero p/n junction structure [1] instead of a homo p/n one to reduce radiation damage in the depletion region and show the differences in radiation resistance of carrier lifetime between the two structures.

First, we show the simulation results of the radiation damage coefficient for the carrier lifetime in the depletion region (K_τ^{dep}) [2] of a GaAs p/n homojunction (HOJ) and an n-InGaP(emitter)/p-GaAs(base) heterojunction (HEJ) using the solar cell simulation software PC1D [3]. Figure 1 plots K_τ^{dep} of HOJ and HEJ solar cells as a function of the doping concentration in the emitter layer ($n^{emitter}$). In the case of high $n^{emitter}$, there is almost no difference in K_τ^{dep} between HOJ and HEJ structures. However, in the case of low $n^{emitter}$, the result indicates that K_τ^{dep} of the HEJ is lower than that of the HOJ, that is, a suitable HEJ structure can be improved the radiation resistance of the solar cells.

Then, K_τ^{dep} of HEJ structures were obtained from experiment. We employed a GaAs p/n HOJ design as reference and three different n-InGaP/p-GaAs HEJ designs. The doping (sulfur) concentration of the InGaP emitter layer were varied for the HEJ structures. The solar cells were irradiated with 1 MeV electrons at National Institutes for Quantum and Radiological Science and Technology (QST), Takasaki. The fluence was 1×10^{14} cm^{-2}.

Figure 2 shows the dependence of K_τ^{dep} on the sulfur concentration in the InGaP emitter layer. The actual sulfur concentration depth profiles were measured by secondary ion mass spectrometer. K_τ^{dep} of the HOJ solar cell agreed with the simulation result. K_τ^{dep} of the HEJ solar cells were lower than that of the HOJ solar cell. Furthermore, the lower the sulfur concentration in InGaP emitter layer, the lower K_τ^{dep}. This tendency also agreed with the simulation. We consider that the radiation resistance of HEJ structure can be improved by decreasing $n^{emitter}$ and forming a significant region of the depletion region in the emitter layer which has a lower intrinsic carrier density. We believe that further improvement of radiation resistance of HEJ solar cell is possible by optimizing the doping concentration profiles in a p/n junction.

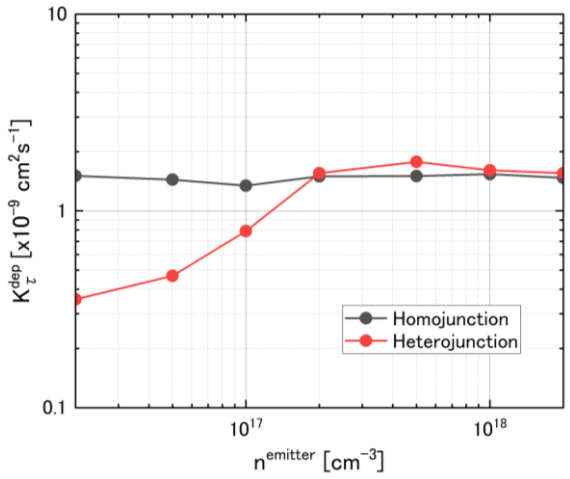

Fig. 1. Simulation results of the $n^{emitter}$ dependence of K_τ^{dep} of homojunction and heterojunction.

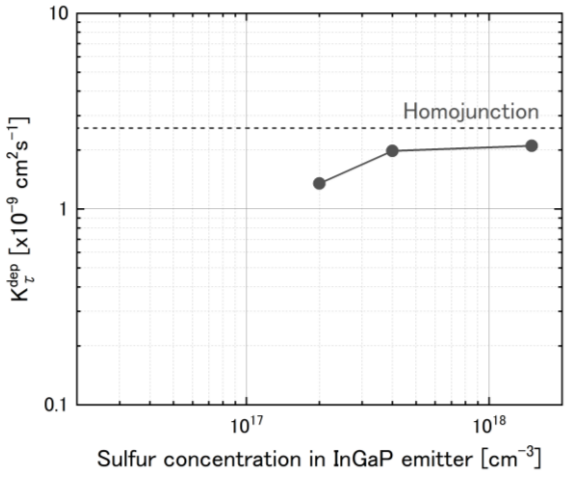

Fig. 2. Experimental results of the dependence of K_τ^{dep} on the sulfur concentration in InGaP layer.

Acknowledgments

The authors thank the kind assistance of M. Sugai and M. Kohsaka of the AES Corporation.

References

[1] T. Nakamura *et al.*, J. Appl. Phys. **130**,153102 (2021). DOI: 10.1063/5.0060158
[2] T. Nakamura *et al.*, J. Appl. Phys. **132**, 115701 (2022). DOI: 10.1063/5.0099106
[3] See https://www.engineering.unsw.edu.au/energy-engineering/research/software-data-links/pc1d-software-for-modelling-a-solar-cell

1 - 21 Characteristic sensitive area observed in FinFET SRAM

K. Takeuchi[a)], K. Sakamoto[a)], K. Yukumatsu[a)] T. Kato[b)],
H. Matsuyama[b)], A. Takeyama[c)], T. Ohshima[c)] and H. Shindo[a)]

[a)]Research and Development Directrate, JAXA
[b)]Socionext Inc.
[c)]Quantum Materials and Applications Research Center, TARRI, QST

Introduction

FinFET, which has three-dimensional gate structure field effect transistor (FET), is widely utilized in modern commercial electronics. Static random-access memories (SRAMs) are key circuits occupying over the half of the area in integrated circuits. Single bit upsets (SBUs) and multiple-cell upsets (MCUs) caused by an energetic particle hitting on FinFET SRAMs are major concern in not only space but also terrestrial environment.

Experimental setup

The device under test (DUT) is fabricated in a commercial 16-nm bulk FinFET process. DUTs were irradiated by a mono-energetic heavy-ion beam using Takasaki Ion Accelerators for Advanced Radiation Application (TIARA) at QST. Details are described in [1]

Results and Discussions

SBUs and 2-bit MCUs were observed under Neon (56 MeV) and Nitrogen (75 MeV) irradiation. Fig. 1 shows the cross-section (CS) of 2-bit MCUs under N and Ne irradiation. 2-bit MCUs were consist of four types of vertical 2-bit MCUs (as shown in the x-axis label in Fig. 1), which depends on the voltage distribution condition of the FinFET SRAM bit cell. In Fig. 2, the estimated sensitive areas (SA) under N and Ne irradiation are illustrated based on the experimental results. In the case of N irradiation, the SA is supposed to be separated along two fins comprising an n-type FinFET, because the estimated width was narrower to cover the two-fin FinFET.

Simulation

The technology computer aided design (TCAD) simulation, which is Hyper Environment for Exploration of Semiconductor Simulation (HyENEXSS) [2], is used to analyze the along-fin characteristic charge collection of FinFET SRAM bit cell. Details including simulation conditions are described in [3]. By integrating the drain current, the collected charge (Q_{col}) was obtained. Fig. 3 illustrates simulation results, showing a good agreement with experimental results.

Conclusion

The CS of SBUs and MCUs on commercial 16-nm FinFET SRAM induced by heavy ion irradiation were investigated. The estimated SA of SBU and 2-bit MCUs were proposed, which implies the along-fin effects of FinFET in SRAM under heavy ion irradiation.

Acknowledgments

The authors would like to thank the Ryoei Technica Corporation for their technical support and members of the accelerator operation group at TIARA in the experiments.

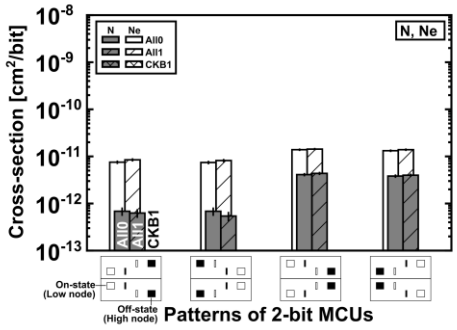

Fig. 1. 2-bit MCUs CS bar plots for each MCU pattern. The x-axis labels show patterns of each MCU in the case of All0/All1 pattern. The error bars represent the standard deviation. Note that there were few 2-bit MCUs in the case of CKB1 pattern.

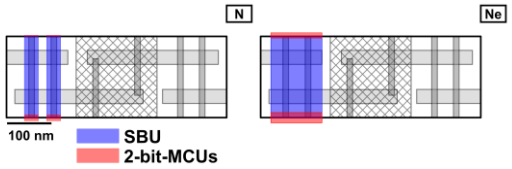

Fig. 2. Illustrations of estimated SA under N and Ne irradiation. The blue and red areas are estimated SA of SBU and 2-bit MCUs, respectively.

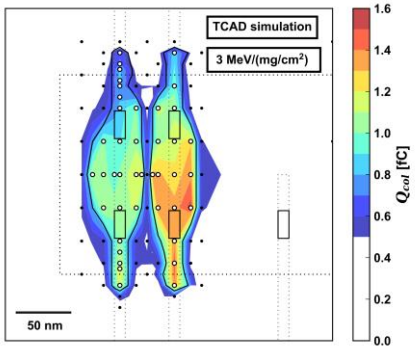

Fig. 3. Q_{col} map of nFinFETs plotted on the top view of the TCAD model. The contour area plot represents the Q_{col} at each point, which interpolated linearly, where the area is colored by the color scale shown in the color bar. The black contour plot is overlaid on the map, which shows the area over the 50% upset probability. The white and black plots show upset and no upset position, respectively, when the e-h pair deposits. The black squares, gray and black dotted lines are gates, fins and the estimated SRAM bit cell border, respectively. The scale bar represents 50 nm.

References

[1] K. Takeuchi *et al.*, IEEE Trans. Nucl. Sci. **69**, 1833 (2022). DOI: 10.1109/TNS.2022.3188993.
[2] N. Kotani, SISPAD'98, (1998).
[3] K. Takeuchi *et al.*, Proc. of RADECS, (2020)

1 - 22 Development of phthalocyanine ion beam for creation of multiple NV center in diamond

S. Onoda[a)], K. Kimura[a, b)], N. Kosuge[a,b)], T. Baba[a,b)], W. Kada[a,b)], K. Yamada[c)], T. Teraji[d)], J. Isoya[e)], O. Hanaizumi[b)] and T. Ohshima[a)]

[a)]Quantum Materials and Applications Research Center, TARRI, QST
[b)]Faculty of Science and Technology, Gunma University
[c)]Department of Advanced Radiation Technology, TARRI, QST
[d)]Research Center for Functional Materials, NIMS
[e)]Faculty of Pure and Applied Sciences, University of Tsukuba

A nitrogen vacancy (NV) center in diamond is known as a solid-state spin quantum bit (qubit) at room temperature. The fabrication of scalable quantum registers based on NV center is a long-standing issue. In 2005, NV-N pair was successfully fabricated by N_2 ion implantation [1]. In 2010, an entanglement between two electron-spin qubits was demonstrated by using an NV-NV [2]. Later, strongly dipolar coupled NV-NV was realized by $^{14}N^+$-30 keV implantation via nanoholes in PMMA resist mask [3]. By utilizing nanohole technique, the creation yields of NV-NV dramatically improved. However, the scaling of NV centers is stagnant up to two for several years. The problem of the technique is the finite size of nanohole. While the distribution of nitrogen atoms is determined by both ion straggling and nanohole diameter. In 2019, our previous research gave a ground-breaking idea of multiple NVs by introducing molecular ion ($C_5N_4H_n$) implantation [4]. We successfully create three NV centers. This is no doubt that further incrementation of NV center complex is capable to be accomplished by developing new beams of molecular ions which contain higher number of nitrogen atoms. In this study, we newly develop phthalocyanine ($C_{32}N_8H_{18}$) ion beam [5].

Phthalocyanine powder was used as the ion source. The power was vaporized and ionized by a heater at 336 °C in the support Ar gas ambient. The positive ions were electrically extracted by an acceleration voltage of 3 kV. The extracted beam contained a variety of fragments. Fig. 1 shows the mass spectrum of ions from the phthalocyanine ion source. The horizontal axis shows the mass number, and the vertical axis shows the beam current. A wide variety of fragments and Ar were detected in mass numbers ranging from 0 to 250. The $C_{32}N_8H_{18}$ ion was detected at approximately a mass number of 505. The $C_{32}N_8H_{18}$ ion beam passing through the slits after the mass spectrometry magnet was accelerated at an energy of 281 keV and implanted into diamond samples. After ion implantation, the samples were annealed at 1000 °C for 2 hours in a vacuum to combine nitrogen atom with vacancy and also to recover the diamond lattice structure. Multiple NV centers were found as bright spots in laboratory built confocal microscopy observation. We successfully found one, two, three, four and five NV centers in confocal spots. Since the distance between nitrogen atoms introduced by molecular ion implantation is calculated to be 9±4 nm, they are expected to have a strong dipolar coupling. In addition to CFM observation, we measured the optically detected magnetic resonance (ODMR) spectra. ODMR enable to identify the number of NV centers up to four, when all NV centers have different orientation axes. We clearly found four NV centers in a confocal spot, which shows eight dips in ODMR spectrum. Unfortunately, five NV centers cannot be identified, but this would soon be justified by introducing a local magnetic field gradient to ODMR, where NV centers with the same orientation can be identified.

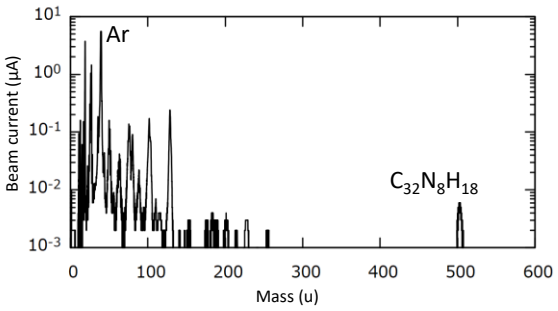

Fig. 1. Mass spectrum of ions from phthalocyanine ion source.

Acknowledgments

This work was supported by JSPS KAKENHI (No. 21H04646), JST Moonshot R&D Grant Number JPMJMS2062 and MEXT Q-LEAP Grant Number JPMXS0118067395. W.K. acknowledges the support of Gunma University for the promotion of scientific research. T.T. acknowledges the support of MEXT Q-LEAP (JPMXS0118068379), JST CREST (JPMJCR1773), MIC R&D for construction of a global quantum cryptography network (JPMI00316), JSPS KAKENHI (No. 20H02187 and 20H05661).

References

[1] R. J. Epstein *et al.*, Nat. Phys. **1**, 94 (2005). DOI: 10.1038/nphys141
[2] P. Neumann *et al.*, Nat. Phys. **6**, 249 (2010). DOI: 10.1038/nphys1536
[3] I. Jakobi *et al.*, J. Phys. **752**, 012001 (2016). DOI: 10.1088/1742-6596/752/1/012001
[4] M. Haruyama *et al.*, Nat. Commun. **10**, 2664 (2019). DOI: 10.1038/s41467-019-10529-x
[5] K. Kimura *et al.*, APEX **15**, 066501 (2022). DOI: 10.35848/1882-0786/ac7030

1 - 23 Ensemble nitrogen vacancy centers in type-Ib diamond created by electron beam up to 8×10^{18} cm^{-2}

S. Ishii, S. Saiki, S. Onoda, Y. Masuyama, H. Abe and T. Ohshima

Quantum Materials and Applications Research Center, TARRI, QST

The negatively charged nitrogen-vacancy (NV^-) center in diamond is a lattice defect consisting of one nitrogen atom adjacent to one atomic vacancy. The NV^- center has been in the center of attention as a quantum sensor for detection of magnetic field, electric field, temperature, strain and so on [1]. For quantum sensing with high-sensitivity, high concentration of ensemble NV^- centers is required. For example, the magnetic sensitivity is proportional to the reciprocal of $(NT_2)^{1/2}$, where N is the number of NV centers and T_2 is the spin coherence time. Thus, the dense NV^- centers with long T_2 increases the sensitivity. In this study, we investigate irradiation fluence dependence of the density of NV centers and P1 centers (which are subsequent Nitrogen atoms) in type-Ib diamonds by using electron spin resonance (ESR) [2].

Commercially available type-Ib diamonds synthesized by high-pressure-high-temperature (HPHT) method (Sumitomo Electric Industries, Osaka, Japan) were used in this study. Nitrogen atom at a lattice site is called as P1 center, and the initial concentrations ($[P1]_{initial}$) were measured by ESR and referred to as Ib-80, Ib-72, Ib-52, Ib-46 depending on $[P1]_{initial}$ of 80, 72, 52, and 46 ppm, respectively. Electron beam irradiation in atmosphere at an energy of 2 MeV was carried out with irradiation fluence up to 8.0×10^{18} electrons (e)/cm^2 at TARRI, QST. Subsequently, irradiated samples were annealed in furnace at 1000 °C for 2 h in vacuum at each fluence step.

Figure 1(a) and Fig. 2(a) show ESR signals of P1 and NV^-centers before and after irradiations at fluences of 3.5, 6.0 and 8.0×10^{18} e/cm^2. The P1 concentration decreases with increase in fluence as shown in Fig. 1(b). In contrast, the NV^- concentration increases with increase in fluence as shown in Fig. 2(b). Figure 3(a) summarizes the change in P1 centers. The decrease rate of P1 centers shows similar tendencies for all type-Ib diamond samples, regardless of $[P1]_{initial}$ (40–80 ppm) in the low fluence range (~4.0×10^{18} e/cm^2). The reduction rate of P1 centers suggests that P1 centers are consumed by recombination with introduced vacancies. However, the decrease rate of P1 centers became lower in the high fluence ranges from 6.0×10^{18} e/cm^2 to 8.0×10^{18} e/cm^2, especially when $[P1]_{initial}$ is smaller, in spite that [P1] still exists even after irradiation at 8.0×10^{18} e/cm^2. The process of P1 center consumption seems to shift depending on the residual P1 centers. Furthermore, as shown in Fig. 3(b), the P1 center consumption and NV^- center creation were compared and as a result, it is concluded that some amounts of the P1 centers were consumed by other defects. The conversion efficiency from $[P1]_{initial}$ to the $[NV^-]$ reached ~19% at 8.0×10^{18} e/cm^2 and the value confirms the usefulness of electron beam irradiation for high concentration of NV^- centers in type-Ib diamonds, whereas results in this study suggest that not all P1 centers converted to NV^- center.

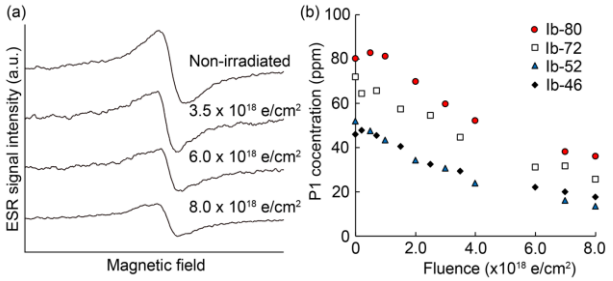

Fig. 1. (a) The center peaks of ESR spectra from P1 center of Ib-46 when the external magnetic field is parallel to [100] axis. (b) Irradiation fluence dependence of [P1].

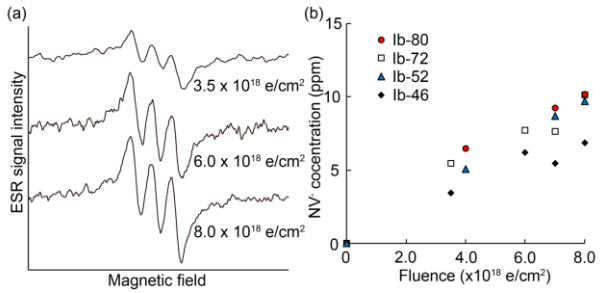

Fig. 2. (a) The left most peaks of ESR spectra from NV center of Ib-46 when the external magnetic field is parallel to [111] axis. (b) Irradiation fluence dependence of [NV^-].

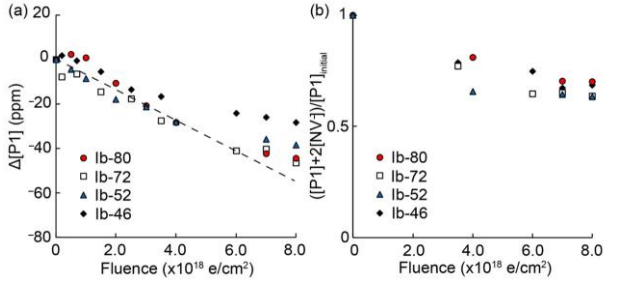

Fig. 3. (a) Irradiation fluence dependence of Δ[P1] (changes from the $[P1]_{initial}$). Broken line is for visual guide. (b) Irradiation fluence dependence of value of ([P1] + 2[NV^-])/$[P1]_{initial}$.

Acknowledgments

This work was supported by Quantum Leap Flagship Program (Q-LEAP; JPMXS 0118067395) of MEXT.

Reference

[1] J. F. Barry *et al.*, Rev. Mod. Phys. **92**, 015004 (2020). DOI: 10.1103/RevModPhys.92.015004A

[2] S. Ishii *et al.*, Quantum Beam Sci. **6**, 2 (2022). DOI: 10.3390/qubs6010002

1 - 24 Prediction of grafting yield by using machine learning

Y. Ueki, N. Seko and Y. Maekawa

Department of Advanced Functional Materials Research, TARRI, QST

Radiation-induced grafting can impart desired functions without degrading the physical and chemical properties of the trunk polymer. However, in the conventional grafting method, the researchers make hypotheses based on experience and intuition, and repeatedly verify the hypotheses through experiments to obtain a new material. Therefore, the research period with the conventional method was long, and as a result, a great deal of labor and expense was required to commercialize the new material. To solve the above problems, we believe it is necessary to renew the conventional inefficient process based on precedent, experience, and intuition into a highly efficient process that integrates experimental science and data science. The objective of this study is to use machine learning to predict grafting yields and further quantify the importance of explanatory variables on grafting yields.

Of the 49 methacrylate ester monomers, 41 monomers were selected as training data, and the remaining eight monomers were used in experiments as test data. The grafting yield, which is the objective variable, obtained by actual grafting experiments. The explanatory variables for building the machine learning dataset were calculated by quantum chemical (QC) calculations using Spartan'18 software. 28 explanatory variables were employed based on the monomer structure information, natural bond orbital (NBO) charges of the methacrylate group, NMR chemical shifts of the methacrylate group, and FT-IR vibrational frequencies and intensities. Multiple linear regression (MLR) and extreme gradient boosting (XGBoost), which is one of the ensemble learning methods, were adopted as the machine learning method to construct the grafting yield prediction model, and R-Studio was used for its calculation. Two machine learning algorithms were used: the "glmnet" algorithm for MLR and the "xgbTree" algorithm for XGBoost, as implemented in the caret package. The prediction accuracy of the grafting yield prediction model was evaluated through the coefficient of determination (R^2) and the root mean square error (RMSE).

It is known that the prediction accuracy of a prediction model varies greatly depending on the type of machine learning algorithm. Figure 1 shows the results of MLR and XGBoost models. The prediction results of the XGBoost model, which is an ensemble learning method, showed smaller prediction errors and higher accuracy in predicting grafting yields compared to the MLR model. The XGBoost model succeeded in instantly predicting the grafting yields of unknown monomers with high accuracy by simply inputting information on its physical properties (Test data: R^2 = 0.71, RMSE = 41.51). The RMSE value for the unknown monomer was about half that of the MLR model, which greatly improved the generalization performance of the prediction model. This result may be attributed to the characteristics of ensemble learning, which is less susceptible to outliers and noise and can make stable predictions. In other words, since this study is a small data analysis with only 41 monomers used in the training data, data bias and outliers are likely to occur. Therefore, it is inferred that the XGBoost model, which is an ensemble learning with higher outlier resistance, was selected as a better machine learning method than the MLR model, which is susceptible to the influence of outliers.

By analyzing the prediction model, it is possible to objectively evaluate which explanatory variables are important response factors governing the grafting yield. As a result of analyzing the XGBoost model, we found that "polarizability of monomer" and "NMR chemical shift of oxygen atom near the substituent in monomer" are the important explanatory variables for the graft polymerization among the 28 explanatory variables that make up the prediction model. Especially, we assume that the "NMR shift of oxygen atom" was selected as an important explanatory variable because of the following reason. This oxygen atom is more susceptible to the influence of substituents than other atoms, and it is assumed that this is because the difference in substituent structure manifested a change in the physical and chemical properties of the oxygen atom. This "NMR chemical shift of oxygen atom" is a useful scientific discovery that researchers had previously overlooked and could not have discovered without the use of machine learning. The use of machine learning is expected to lead to the "creation of new knowledge" and the "deepening and development of basic research".

Reference

[1] Y. Ueki *et al*., Appl. Mater. Today, **25**, 101158 (2021). DOI:10.1016/j.apmt.2021.101158

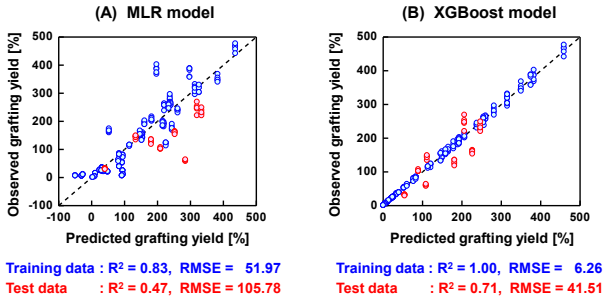

Fig. 1. Predicted versus observed grafting yields plot. (A) MLR model and (B) XGBoost model.

1 - 25 A facile graft polymerization of biomass-based vinyl monomers from PE/PP substrates in a new generation safe organic solvent

T. Nirazuka[a)], K. Matsubara[a)], R. Kakuchi[a)], M. Omichi[b)] and N. Seko[b)]

[a)]Division of Molecular Science, Faculty of Science and Technology, Gunma University
[b)]Department of Advanced Functional Materials Research, TARRI, QST

Introduction

Surface modification of polymeric materials is one of the most important research topics in the synthesis of functional polymeric materials. Among various surface modification methods, radiation-induced graft polymerization (RIGP) has been as a unique chemical method that can install new material properties to out-of-the-box materials without harming their physical properties. In this regard, we have achieved RIGP of methacrylated vanillin (MV), which can be synthesized from the lignin derivative vanillin, from the surfaces of materials such as polyethylene-coated polypropylene (PE/PP) and cellulose.[1, 2] Of note here, the graft polymerization of MV needed to be carried out in classical organic solvents, including DMSO in order to secure the homogeneity during the graft polymerization conditions. Although the use of DMSO as a solvent led to satisfactory graft polymerization results, it must be emphasized here that the use of DMSO as a solvent unnecessarily increased the operational cost because of the high boiling point of the DMSO. In addition, the unnecessary contact to DMSO solution containing reactants would be potentially dangerous due to the skin penetration of the DMSO solutions in general.

Considering the above backgrounds, we turned our attentions to the use of a new generation solvent instead of conventional solvents. In this study, PE/PP substrate was subjected to the graft polymerization of MV in a safer and newer organic solvent featuring easy-to-use properties compared to conventional solvents (Fig.1).

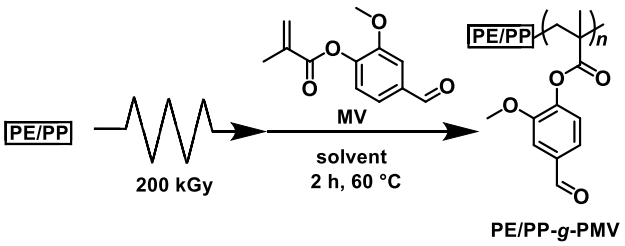

Fig. 1. Radiation-induced Graft polymerization of MV from PE/PP substrates.

Results and Discussion

As mentioned in the introduction, radiation-induced graft polymerization of MV was targeted in a new generation safe solvent. For this, we turned our attention to the use of cyclopentyl methyl ether (CPME) as a new solvent (Fig. 1). This is because CPME is a hydrophobic ether-based organic solvent with a boiling point of 106 °C. Unlike conventional ether-based solvents such THF or diethyl ether, CPME shows limited tendency to form peroxides and high tolerance to acidic and basic conditions. In addition, CPME can be easily removed via azeotropic distillation with water. As such, CPME renders the ideal solvent properties for the use in graft polymerization of MV. The MV graft polymerization is briefly documented here. MV (0.60 g) was dissolved in a CPME (3.6 mL) and the resulting reaction solution was degassed with argon gas. PE/PP substrate irradiated with 200 kGy electron beam was immersed in the CPME solution and allowed to react for 2 hours at 60 ºC. After the reaction completion, the resulting PE/PP substrate was washed with CPME and methanol to afford MV-grafted PE/PP substrate (PE/PP-*g*-PMV). Though CPME is known as a good organic solvent for a range of organic molecules, its penetration to PE/PP was sufficiently suppressed so that only the surface graft polymerization was reazlied. As a result, CPME showed higher grafting efficiency than the conventional DMSO solution system. Specifically, the grafting degree (GD), corresponding to the weight gain via the graft polymerization, was above 400 % in CPME while GD in DMSO remained only around 150 %. This result rendered that the use of a new generation safe solvent of CPME led to not only replace the high-boiling point DMSO but also increase the grafting efficiency concurrently.

Conclusions

In this work, we have succeeded in performing graft polymerization of MV in the state-of-the-art organic solvent, CPME, which should lead to the decrease in difficulties during the graft polymerizations and concurrently increase the efficiency of the graft polymerization process. We believe that the use of CPME should increase the overall greenness for the graft-polymerization processes.

Acknowledgments

R. K. gratefully acknowledges the Leading Initiative for Excellent Young Researchers (LEADER) for the financial support. R. K. also acknowledge the S-Membrane Project and the F-Materials Project at Gunma University for the financial support.

References

[1] R. Kakuchi *et al*., Polym. J. **53**, 523 (2021). DOI:10.1038/s41428-020-00448-w
[2] T. Hamada *et al*., ACS Sustainable Chem. Eng. **7**, 7795 (2019). DOI:10.1021/acssuschemeng.8b06812.

1 - 26 Simple evaluation method for distribution of graft chains by using thermogravimetric analysis

M. Omichi and N. Seko

Department of Advanced Functional Materials Research, TARRI, QST

Radiation graft polymerization is widely used in the development of functional polymer materials. To synthesize the grafting materials, the grafting rate is an important factor because the amount of functional groups directly affects the functionality. However, it is known that the adsorption performance of radiation graft materials varies greatly depending on the graft polymerization conditions even at the same grafting rate. The reason is that the grafted chains are not uniformly propagated in the base polymer material. The grafted chains could be distributed at the surface and its depth parts of the base polymer material. Therefore, it is important how to control this distribution uniform as well as grafting rate. In this study, we report the simple evaluation method for the distribution of grafted chains by taking advantage of the difference in pyrolysis behavior of radiation grafting materials caused by the distribution of grafted chains.

The polyethylene (PE) nonwoven fabrics (size: 1.2 × 2.5 cm, average weight: 18 mg) were packed into a gas barrier bag. After that, the bag was sealed under a nitrogen atmosphere, and the PE fabrics in the bag was irradiated with an electron beam of 250 keV energy and 3.9 mA current at room temperature for a total dose of 50 kGy. The irradiated PE fabrics were then stored in −80 °C freezer until use. The PE film was immersed in the 7.5-100 wt% GMA monomer solution (Dimethyl sulfoxide solvent) and heated at 40 °C. Reaction time was adjusted to achieve a grafting rate of 100%. After the reaction, the PE fabrics were washed three times with methanol and vacuum-dried overnight to obtain the GMA-grafted PE (GMA-*g*-PE) with the same 100% grafting rate and different grafted chain's distributions. The thermogravimetric analysis (TG) was performed with the GMA-*g*-PE, a heating rate of 10 °C/min, and flowing nitrogen (50 mL/min).

Figure 1 shows cross-sectional scanning electron microscope (SEM) images of GMA-*g*-PE fibers (GMA monomer concentration:7.5 and 100 wt%) after conversion reaction with an iminodiacetic acid disodium salt (IDA-Na). For both 7.5 and 100 wt% GMA concentration, sodium element detected only in the outer layer, which contains GMA grafted chains, by using energy dispersive X-ray spectroscopy. At low GMA concentration, it takes a long time for the grafting rate to reach 100% and the grafted chains form to the inside of the PE substrate. On the other hand, at high GMA concentration, grafted chains form on localized surface of the PE substrate. These results indicate that the distribution of grafted chains can be controlled by adjusting the monomer concentration and reaction time.

Figure 2 shows derivative thermogravimetry (DTG) curves of GMA-*g*-PE fabrics with the same 100% grafting rate and the different distribution of grafted chains. At the DTG peak at around 350 °C, it was confirmed that the peak intensity increases as the GMA monomer concentration decreases. This peak is mainly attributed to the GMA grafted chains. These results suggested that at low GMA monomer concentrations, the PE substrate was also pyrolyzed at around 350 °C simultaneously with the GMA-grafted chains. The PE area, which the graft chains have formed, is likely to be pyrolyzed. This implied that the DTG peaks can be used to estimate approximate the PE area containing the grafted chains.

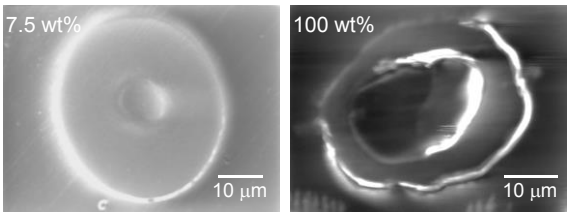

Fig. 1. Cross-sectional SEM images of GMA-*g*-PE fibers (GMA monomer concentration:7.5 and 100 wt%) with the grafting rate of 100% after conversion reaction with an IDA-Na.

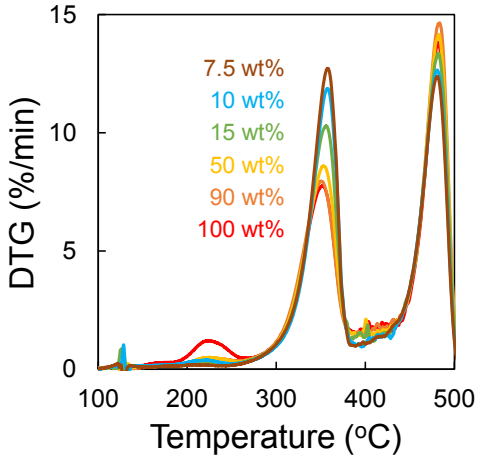

Fig. 2. DTG curves of GMA-*g*-PE fabrics with the same 100% grafting rate and the different distribution of graft chains (GMA monomer concentration:7.5, 10, 15, 50, 90 and 100 wt%).

In conclusion, we have succeeded in evaluation of the distribution of grafted chains as the pyrolysis behavior of radiation grafting materials. This evaluation method is expected to make it possible to optimize graft polymerization conditions for the expression of functionality, considering not only the graft rate but also the distribution of grafted chains.

1 - 27 Thin films produced by ion beam nanofabrication technique induced cell-driven 3D cell sheet formation

T. G. Oyama[a)], K. Oyama[a)], H. Miyoshi[b)] and M. Taguchi[a)]

[a)]Department of Advanced Functional Materials Research, TARRI, QST
[b)]Graduate School of Systems Design, Tokyo Metropolitan University

Folds and protrusions are widely observed in human organs such as the brain, airways, and gut, and they play key roles in the tissue/organ functions. These 3D structures are formed during embryonic development from simple flat epithelial cell sheets through morphogenesis. However, on conventional cell culture dishes, the epithelial cells only form a planar monolayer. One of the most widely accepted theories is that epithelial pattern formation is triggered by mechanical instabilities between the epithelial sheet and the mesenchyme foundation, similar to that observed in non-living film-on-substrate structures. Thus, we developed a film-on-substrate cell culture system (FoSS) that mimics the *in vivo* layered systems of epithelium–basement membrane–mesenchyme [1].

FoSS was realized by controlling the 3D distributions of scission/crosslinking probabilities in polylactic acid (PLA), a biocompatible and bioabsorbable polymer, by the ion beam nanofabrication technique. PLA substrates were prepared by hot-pressing the pellets (Eco-Plastic U'z S-12; optical purity of L-lactic acid = 99.6%; M_W = 112,000; Toyota Motor Corporation) at 15 MPa and 190 °C. A 50 keV N^+ ion beam at a flux of 2.5–6.7 × 10^{11} ions/cm^2/s was irradiated under vacuum (~3.0 × 10^{-4} Pa). Stainless-steel masks were used for the pattern irradiation. The obtained FoSS surfaces were investigated using micro-area X-ray photoelectron spectroscopy (XPS) (PHI5000 VersaProbe II, ULVAC-PHI), atomic force microscope (AFM) (AFM5300E, Hitachi High-Technologies Corporation), and static water contact angle (WCA) meter (FACE, CA-V, Kyowa Interface Science). MDCK cells (RCB0995) were cultured on FoSS.

The XPS analyses revealed that FoSS is composed of three layers: a crosslinked/carbonized surface layer, a decomposed middle layer, and a foundation of non-irradiated PLA (Fig. 1). The chemically modified FoSS surface was found to be cytocompatible and exhibited high cell adhesion property. The decomposed middle layer was locally decomposed and underwent solation under the cell culture conditions, due to the lowered glass-transition and melting temperatures.

The improved surface properties of FoSS allowed cells to start adhesion approximately 30 min after seeding. When the fluence was 7.1 × 10^{13}, 1.0 × 10^{14}, and 1.4 × 10^{14} ions/cm^2, the cultured cells caused the surface layer to wrinkle and delaminate as thin films within 1 day of culture. The thickness of the surface layer peeled after irradiation at 1.0 × 10^{14} ions/cm^2 was 165 ± 13 nm (n = 3). The wrinkles gradually extended and then connected the cells, even though the cells were separated by several hundred micrometers. Interestingly, the cells affected each other's migration through the wrinkles formed between them. Specifically, the cells tended to migrate along the wrinkles due to the topographical effects, moving to each other's places by the shortest cut.

On patterned FoSS, the cells started delaminating the surface layer in the irradiated areas about 1 h after seeding and formed 3D structures by aggregating the delaminated films within 48 h (Fig. 2). The peeled thin films were crumpled by and enclosed in the MDCK monolayer, and they became the cores of the 3D architectures. As a result, we successfully obtained 3D epithelial sheets with millimeter-length folds and submillimeter protrusions using the FoSS.

FoSS can form 3D cell sheets simply and effectively using a traction force provided by the cell population. FoSS will facilitate the production of not only *in vitro* models of 3D morphogenesis, but also 3D cell sheets that are currently in demand in biology, drug development, tissue engineering, and regenerative medicine.

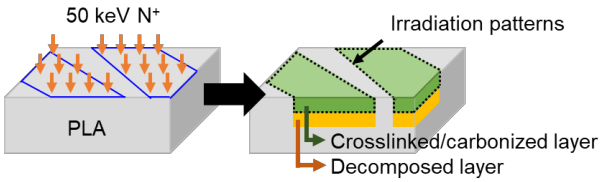

Fig. 1. Developed film-on-substrate cell culture system (FoSS).

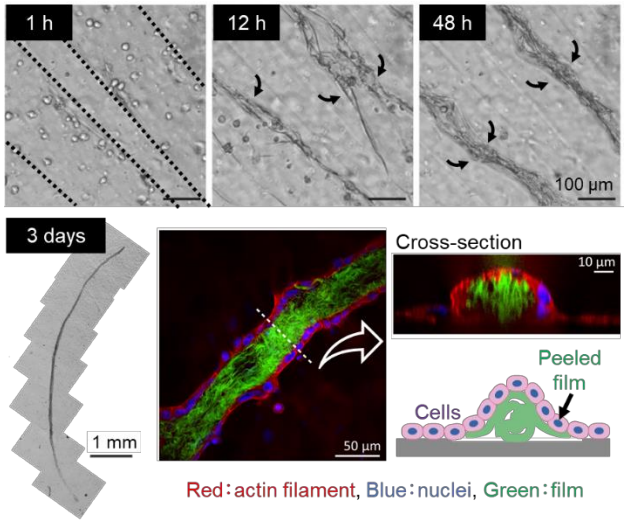

Fig. 2. Cell-induced buckling-delamination of FoSS and 3D cell sheets formation.

Reference

[1] T. G. Oyama *et al.*, Mater. Des. **208**, 109975 (2021). DOI: 10.1016/j.matdes.2021.109975

1 - 28 Effect of radiolysis in gas phase on the corrosive environment in liquid phase

K. Hata[a)], A. Kimura[b)], T. Sato[a)], C. Kato[a)] and M. Taguchi[b)]

[a)]Nuclear Safety Research Center, JAEA
[b)]Department of Advanced Functional Materials Research, TARRI, QST

Radiolysis of contaminated water of the Fukushima Daiichi Nuclear Power Station (1F) is a critical issue to evaluate the corrosion behavior of structural components in the containment vessel. A large volume of gas phase space exists in the 1F containment vessel and is constantly exposed to ionizing radiation. Although the gas phase is less sensitive to ionizing radiation than the liquid phase, the effect of radiolysis of chemical species in the gas phase may not be negligible under the large volume and the long irradiation time. Especially, nitrogen oxides (NO_x), which are dominant species produced from gas-phase radiolysis, are known as strong oxidants. These nitrogen oxides are mainly produced by the reaction of excited nitrogen and oxygen in the air. In this study, the effect of radiolysis of the gas phase in the 1F containment vessel on chemical species in the contaminated water was evaluated. γ-ray irradiation experiments under gas-liquid coexistence conditions were conducted to quantify the products from radiolysis of the gas and liquid phase, respectively.

The ^{60}Co γ -ray irradiation facility, TARRI, QST was used for the irradiation. Glass vials of 20 ml containing 5 - 20 ml of pure water were sealed with a cap and a butyl rubber septum. The samples were saturated with air or N_2 containing 5-10 % O_2. The liquid phase of some samples was shielded with a 100 mm lead block for some experiments to focus on radiation effects in the gas phase (Fig. 1). The dose rate in the liquid phase was attenuated by a factor of about 100. The concentration of nitrate ion (NO_3^-) in the liquid phase was measured by an ion chromatograph. The pH and H_2O_2 concentration were measured by pH meter and HPLC with an electrochemical detector.

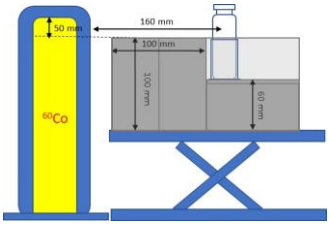

Fig. 1. Layout of the sample vial, shielding lead block for the ^{60}Co γ-ray irradiation.

Samples with a liquid phase volume of 10 ml (gas-liquid ratio: 50/50) saturated with N_2 containing 0 to 20% O_2 were irradiated by γ-rays (Fig. 2a). Samples changing the gas-liquid ratio under air-saturated conditions were irradiated by γ-rays as shown in Fig. 2b. The NO_3^- concentration increased with the oxygen concentration or the gas phase portion, indicating that NO_3^- is mainly formed in the gas phase. In addition, O_2 was necessary for NO_3^- formation in the gas phase.

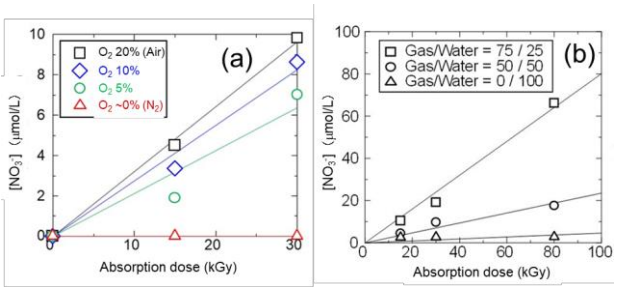

Fig. 2. NO_3^- production in gas-liquid coexistent samples under γ-ray irradiation. (a) The effect of O_2 in N_2 and (b) the effect of gas-liquid ratio.

To investigate the effect of NO_3^- formation in the gas phase on the corrosive environment of the liquid phase, gas-liquid coexistent samples (gas/liquid = 75/25) were irradiated with γ-rays under conditions in which the liquid phase was shielded with the lead block. Fig. 3 shows (a) concentration of H_2O_2 and (b) pH in the gas-liquid coexistent samples as a function of absorbed dose under aerated condition. The absorbed dose rate of water was 0.016 kGy/h, and the longest irradiation period was about 300 h. A slight decrease in pH and formation of H_2O_2 was confirmed. The solid lines in Fig. 3 were the simulation results of pure water radiolysis under the same conditions. The simulation, which did not take into account the effect of NO_3^-, was equivalent to the experimental results. It can be considered that the effect of radiolysis in the gas phase on the liquid phase is small.

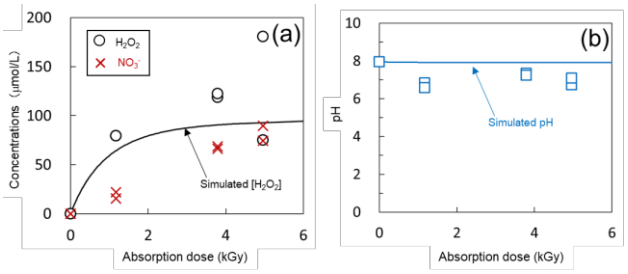

Fig. 3. (a) Concentrations of H_2O_2 and NO_3^- and (b) pH in partially shielded gas-liquid coexistent samples (gas/liquid = 75/25) under γ-ray irradiation.

In the future, we continue to investigate the effects of products from the gas-phase radiolysis such as NO_3^- on the liquid phase.

Acknowledgments

This research was supported by the Nuclear Energy Science & Technology and Human Resource Development Project JPJA20P20333127.

1 - 29 Effect of outer diameter on the completely amorphized dose of silicon carbide nanotube by ion irradiation

T. Taguchi[a)], S. Yamamoto[b)] and H. Ohba[a)]

[a)]Tokai Quantum Beam Science Center, TARRI, QST
[b)]Department of Advanced Functional Materials Research, TARRI, QST

Silicon carbide (SiC) is a promising non-oxide ceramic material used in a wide range of applications. SiC has been utilized as a wide-bandgap semiconducting material and structural material under high temperatures, owing to its attractive chemical, physical, and mechanical properties. Conversely, nanomaterials may possess excellent and novel properties that differ from those of their bulk materials. In particular, we succeeded in synthesizing nanometer-sized polycrystalline SiC nanotubes with engrossing geometries [1]. Photoluminescence energy peaks were observed for these SiC nanotubes, which were higher than in the case of bulk SiC; indicating bioactivity for the first time and demonstrating a novel microstructural change by ion irradiation that differed from bulk SiC materials [2, 3]. Recently, we have reported that the completely amorphized dose of SiC nanotube was much higher than those of bulk SiC materials [3]. However, the size effect of a completely amorphized dose of SiC nanotube has not been investigated. Therefore, the effect of outer diameter on the complete amorphization dose of SiC nanotube by ion irradiation at room temperature was investigated in this study.

The multi-walled carbon nanotubes (MWCNTs: GSI Creos Corporation, Tokyo, Japan) were heated with Si powder (The Nilaco Corporation, Tokyo, Japan) at 1,200 °C for 30 h in a vacuum. The samples were then heated at 800 °C for 4 h in the air to remove unreacted MWCNTs and carbon layers. The samples heated in the air were immersed in 5 M NaOH and then a 0.2 M HCl solutions to eliminate the thin SiO_2 layers. The molybdenum grid holder, which deposited the polycrystalline SiC nanotubes, was irradiated with 200 keV Si^+ ions from a 400 kV ion implanter at room temperature in TEM (Model JEM-4000FX, JEOL Ltd., Japan) operating at 400 kV. The in-situ TEM observation under ion irradiation was performed at the Takasaki Ion Accelerators for Advanced Radiation Application (TIARA) facility at the National Institutes for Quantum Science and Technology. The ion fluence was up to 1.2×10^{20} ions/m^2, and the corresponding irradiation damage (in terms of displacement per atom; dpa) for the SiC was estimated by SRIM 2008 to be 3.2 dpa. The circumstantial microstructural developments to the SiC nanotubes before and after ion irradiation were observed by TEM (Model 2100F, JEOL Ltd., Akishima, Japan) operating at 200 kV. Electron energy-loss spectroscopy (EELS, Enfinium spectrometer, Nippon Gatan, Nishi-Tokyo, Japan) was carried out to evaluate the plasmon energies of SiC nanotubes before and after the ion irradiation.

The SiC nanotubes formed in this study have heterogeneous inner and outer diameters because as-received MWCNTs also have heterogeneous inner and outer diameters and wall thickness. Five kinds of SiC nanotubes with different outer diameters were irradiated. The irradiated SiC nanotubes in this study have an outer diameter in the range of 106 ± 6 to 236 ± 22 nm. Figure 1 shows the effect of outer diameter on the complete amorphization dose of SiC nanotube by ion irradiation at room temperature. This result reveals that Most SiC nanotube with smaller outer diameter has a higher resistance to completely amorphization by ion irradiation. However, the complete amorphization dose in the SiC nanotubes with an outer diameter of 111±14 nm (hereinafter named SiC nanotube A) was hardly high compared to that with a large outer diameter. According to the EELS evaluations of several SiC nanotubes, the plasmon energy in the SiC nanotube A was high compared to that with a high completely amorphization dose. This result exhibits that the SiC nanotube A has smaller amounts of point defects such as interstitials, vacancies and stacking faults compared to that with a high completely amorphization dose. From these results, the complete amorphization dose of SiC nanotube by ion irradiation is dependent on its outer diameter and the number of intrinsic defects.

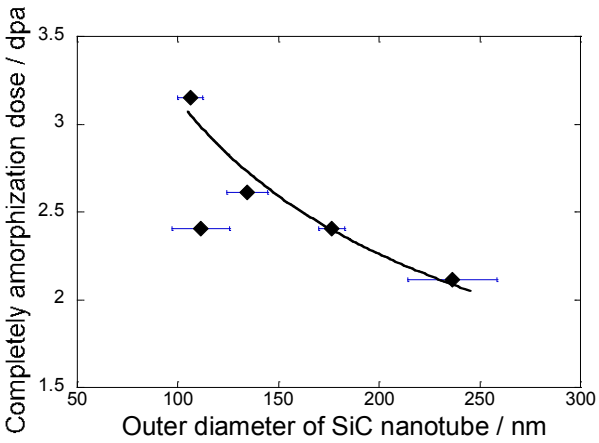

Fig. 1. Effect of outer diameter on completely amorphization dose of SiC nanotube by ion irradiation at room temperature.

References

[1] T. Taguchi *et al*., J. Am. Ceram. Soc. **88**, 459 (2005). DOI:10.1111/j.1551-2916.2005.00066.x
[2] T. Taguchi *et al*., Appl. Surf. Sci. **403**, 308 (2017). DOI:10.1016/j.apsusc.2017.01.176
[3] T. Taguchi *et al*., Acta Mater. **154**, 90 (2018). DOI:10.1016/j.actamat.2018.05.030

1 - 30 Radiation robustness of laser ceramics and single crystal for microchip laser remote analysis

K. Tamura[a)], R. Nakanishi[a)], H. Ohba[a)], T. Taira[b,c)] and I. Wakaida[d)]

[a)]Tokai Quantum Beam Science Center, TARRI, QST
[b)]Institute for Molecular Science, NINS
[c)]RIKEN Spring-8 center, RIKEN
[d)]Collaborative Laboratories for Advanced Decommissioning Science, JAEA

Decommissioning of TEPCO Fukushima Daiichi nuclear power plant (F1-NPP) is needed, where molten fuel debris might be submerged in water. To obtain information inside the reactor core, remote inspection technique in narrow space is required. A fiber-optic probe laser-induced breakdown spectroscopy (LIBS) is considered one of the promising methods for remote inspection [1]. Giant-pulse microchip laser (MCL) is compact with high peak power of MW level, and since the feature is suitable for LIBS application, it was applied to remote LIBS system, where MCL is set close to the target and bright plasma is generated by direct laser irradiation. Based on the developed system, effective remote inspection is expected [2, 3]. However, radiation effects to the system needs to be investigated considering its operation in the radiation environment. In the previous annual report, we reported that the laser output decreased by the increase of radiation dose rate of gamma ray. In this work, the radiation effects on the properties of a laser remote inspection system using ceramics (Cer) and single crystal (SC) microchips laser composite were measured. Instead of comparing properties at different dose rates, the temporal changes of the properties at fixed low dose rate of gamma-ray for a relatively long period of time were observed. Owing to their successive utilization at relatively low dose rate, radiation-sensitive methods need to be explored to evaluate small radiation influence.

The radiation dose rate effects were measured using a ^{60}Co gamma-ray source. Two sets of the same laser system were placed each in a radiation area irradiated at the dose rate of approximately 150 Gy/h and in a non-radiation area (0 Gy/h) behind a wall as a reference. Both were operated similarly, and their laser properties were measured. Another apparatus was positioned outside the wall a few meters from the specimen. Monolithic Nd:YAG/Cr:YAG composites ($3 \times 3 \times 10$ mm^3) were used as specimens and placed in a holder. A Cer composite (Konoshima Chemical/Baikowski-Japan, Japan) and an SC composite (Cryslaser Inc., Chengdu, P. R. China) were examined. Laser output energy from the composite was measured with an energy detector and an oscilloscope.

Figure 1 shows the single pulse energy as a function of dose (Gy) from the radiation start for ceramics and SC with (150) and without (0) irradiation. The plot was normalized at the initial time. During measurements, the pump laser was operated at an LD current of 150 A at 5 Hz. LD pump 61temporal duration was adjusted (45–60 μs) to generate a single pulse. Under no irradiation (0), energy reduction is negligible for ceramics (Cer 0) and SC (SC 0). For ceramics with irradiation (Cer 150), the energy decreased with time and reached 78% of the initial value. This phenomenon may be ascribed to the increase in optical loss in the ceramics during irradiation. Significant energy decrease was also measured for SC (SC 150). Although the intensity was fluctuating, a comparison of relative intensity at the almost saturated region (>1500 Gy) revealed that the reduction rate for SC was smaller (~6%) than that for ceramics. This result indicates that the radiation effect on SC specimen was smaller than that on ceramics, and SC is more robust against radiation than ceramics [4].

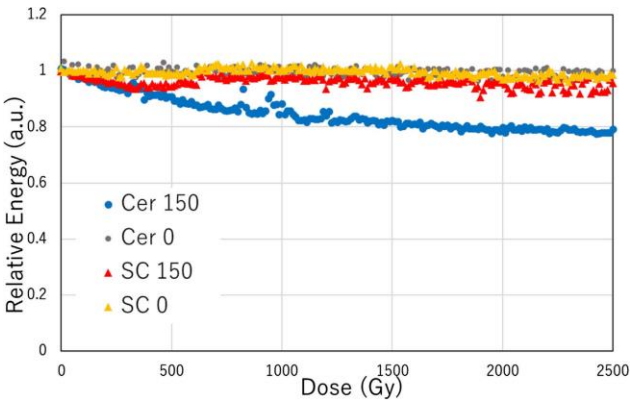

Fig. 1. Relative pulse energy as a function of dose (Gy) for ceramics (Cer) and single crystal (SC) specimens with (150) and

Acknowledgements

This work includes a part of the results of “Advanced study on remote and in-situ elemental analysis of molten fuel debris in damaged core by innovative optical spectroscopy”, the Center of World Intelligence Project for Nuclear S&T and Human Resource Development, the Ministry of Education, Culture, Sports, Science and Technology (MEXT), Japan.

References

[1] M. Saeki *et al.*, J. Nucl. Sci. Technol. **51**, 930 (2014). DOI: 10.1080/00223131.2014.917996
[2] K. Tamura *et al.*, J. Nucl. Sci. Technol. **57**, 1189 (2020). DOI: 10.1080/00223131.2020.1776648
[3] K. Tamura *et al.*, J. Nucl. Sci. Technol. **58**, 405 (2021). DOI: 10.1080/00223131.2020.1854880
[4] K. Tamura *et al.*, Jpn. J. Appl. Phys. **61**, 032003(2022). DOI: 10.35848/1347-4065/ac4dd1

1 - 31 Gamma-ray irradiation experiment for ITER diagnostic systems in JADA IV

S. Kitazawa, T. Hatae, M. Ishikawa, T. Oikawa, R. Imazawa, E. Yatsuka, K. Nojiri, T. Ushiki, S. Kono, K. Torimoto, M. Inamine, T. Kikuchi, T. Yokozuka, H. Murakami, K. Shimizu and T. Sugie

Department of ITER Project, NFI, QST

JADA (ITER project Japan Domestic Agency) is developing to procure five diagnostic systems, microfission chamber (MFC), poloidal polarimeter (PoPola), Edge Thomson Scattering (ETS), divertor impurity monitor (DIM) and divertor infrared thermography (IRTh).

The reliability under the ITER radiation conditions of relevant equipment to be installed in the vacuum vessel, in the interspaces (IS) between the vacuum boundary and the biological shield and in the port cells (PC) outside the biological shields should be evaluated. In this project, we launched gamma-ray irradiation experiments in QST Takasaki Advanced Radiation Research Institute from 2018. The results obtained in the experiments are used important basses for showing that components can maintain its their performances under the ITER radiation environment in the design review for each diagnostic system.

For MFC, two prototype preamplifiers for ITER were tested in 3rd cell at Co-60 1st Building. The gamma-ray irradiation was performed up to 100 Gy at a dose rate of 10-25 Gy/h. We investigated the effects of gamma rays on the pulse amplification factor, frequency characteristics and signal stability (noise level) of the preamplifiers in situ during irradiation. A function generator created programed pattern signals and those signals were input into the preamplifiers through attenuator which had a gain inverse of that of the amplifier. The output signals from the amplifier were continuously monitored and periodically recorded by an oscilloscope and compared with the generated signals. As a result of analyzing the obtained data, it was confirmed that no abnormality occurred.

For PoPola, an endurance test on the piezoelectric element to be used in ITER was performed in 2nd cell at Co-60 1st Building. The gamma-ray irradiation was performed up to 1 MGy at a dose rate of 6.3 kGy/h. The sample was fixed during irradiation in a stainless-steel cage with the height adjusted by a laboratory jack. After the irradiation, the soundness of the piezo element was tested, and no degradation of performance of stroke length and stroke force was confirmed, proving that it can be used for the actual ITER machine.

For ETS, continuing previous results [1], optical elements were irradiated in 6th Cell at Co-60 2nd Building. The glass materials and optical fibers were irradiated by gamma rays up to 10 MGy and investigated before and after irradiation in spectral transmittance at 590-1070 nm.

For DIM, optical fibers were irradiated eventually up to 200 kGy in 1st cell at Food irradiation Building and 2nd Cell at Co-60 1st Building. The candidate optical fiber from the previous experimental results [2] were examined for more detailed optical property verification. The gamma-ray irradiation tests were performed observing the spectral transmittance after irradiations for the fibers; solarization-resistant silica fibers for measurement in the UV region (200-450 nm) and silica fibers with low OH content in the VIS/NIR region (400-1,000 nm). In addition to the conventional NA = 0.22 optical fibers, the radiation resistance of the NA = 0.12 optical fibers were also confirmed in the tests. Further experimental trial-and-error is required to contribute to the decision of availability.

For IRTh, experiments by XPS at TARRI were performed on ZnSe and ZnS lens specimen irradiated with gamma-ray up to 5.6 MGy in the previous year. It was found that transmittance deterioration around the light wavelength of 3 μm occurred near the surface, and it was found that it was not the effect of the color center caused by gamma-ray irradiation, and it was found that it does not hinder use in a gamma ray environment [3].

The details of each experiment are summarized in elsewhere [4].

Acknowledgments

We would like to thank Naotsugu Nagasawa, Hajime Seito, Hiroyuki Okazaki, Shunya Yamamoto and Hiroshi Koshikawa (TARRI) for their cooperation in the irradiation and observation.

References

[1] E. Yatsuka *et al.*, Fusion Eng. Des. **160**, 111846 (2020). DOI: 10.1016/j.fusengdes.2020.111846
[2] S. Kitazawa *et al.*, Plasma Fusion Res. **14** 3405089 (2019). DOI: 10.1585/pfr.14.3405089
[3] T. Ushiki *et al.*, Rev. Sci. Instrum. **93**, 84905 (2022). DOI: 10.1063/5.0089269
[4] S. Kitazawa *et al.*, Plasma Fusion Res., *submitted*.

1 - 32 Irradiation tests of radiation hard components and materials for ITER blanket remote handling system

M. Saito, Y. Kawai, K. Nakata, Y. Noguchi and N. Takeda

Department of ITER Project, NFI, QST

The ITER blanket remote handling system (BRHS) will replace the first walls in a gamma radiation environment having a dose rate of 250 Gy/h to 500 Gy/h. BRHS components have a radiation hardness requirement of 1 MGy, however, we set a radiation hardness target value of 5 MGy to increase the availability of the system. In this study, we investigated the radiation hardness of part of frame ground on the AC servo motors. Our AC servo motors are designed to fix the shield wire frame ground (FG) onto the inside of the motor by crimped terminal for conduction [1]. However, this design requires additional space for fixing the shield wire FG, which will increase the length of the motors. Instead, the shield wire FG will be fixed onto the outside of the rear bracket. However, fixing the shield wire FG on the outside of the motor will leave the screw exposed, so we need to verify whether screws loosen, or electrical resistance increases due to irradiation by conducting irradiation tests.

Test methods

Test pieces (100 mm x 100 mm x 3 mm) were made using various materials, surface-treated A 6063 and SUS303, as shown in Table 1. Test pieces were set on a stand (Figure 1) and irradiated up to 3 MGy at 2 kGy/h and then from 3 MGy up to 5 MGy at 4 kGy/h. After irradiation, the surface of the materials and the screws were observed, and conduction resistance (requirement is 500 m Ω or less) was measured.

Table 1
Candidate materials for motor.

Material	Surface treatment	Size [mm]
A6063	Black colored alumite	100 x 100 x 3
A6063	Chromate	100 x 100 x 3
SUS303	No treatment	100 x 100 x 3

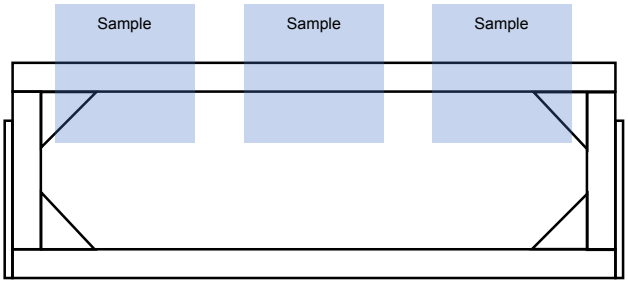

Fig. 1. Test pieces were set on the stand for irradiation.

Test results

Screw: None of the screws became loose.

Conduction resistance: Conduction resistance satisfied the requirement up to 5 MGy in A6063 (Chromate) and SUS303. However, in the case of A6063 (Black colored alumite), conduction resistance exceeded the requirement value before irradiation up to 5 MGy.

Surface observation: Surfaces of A6063 (Black colored alumite) and SUS303 did not change owing to irradiation. White dots were observed on the surface of A6063 (Chromate) in 1 MGy irradiation, however, these dots did not flake off.

Irradiation tests have narrowed down the choice of candidates to either A6063 (Chromate) or SUS303. For our future work, we will compare the manufacturability of the materials and in-body temperatures.

Table 2
Surface of candidate materials after irradiation.

Before irradiation	1 MGy	5 MGy
A6063 (Black colored alumite)		
		
A6063 (Chromate)		
		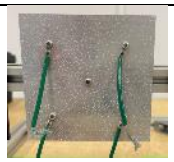
SUS303		
		

Acknowledgments

The authors would like to acknowledge K. Mizuhashi, K. Takeuchi, K. Saga, and E. Nakamura of Beam Operation Co., Ltd.; and H. Seito and Y. Nagao from the Takasaki Advanced Radiation Research Institute who supported the irradiation experiments.

Reference

[1] M. Saito *et al*., QST Takasaki Annu. Rep. 2016 **QST-M-8**, 66 (2017).

1 - 33 Evaluation of irradiation hardening for pure tungsten using micro tensile test

T. Nozawa[a)], Ju-Hyeon Yu[a)], T. Miyazawa[b)], M. Ando[a)], S. Nogami[b)], A. Hasegawa[b)] and H. Tanigawa[a)]

[a)]Department of Fusion Reactor Materials Research, RFI, QST
[b)]Department of Quantum Science and Energy Engineering, Graduate School of Engineering, Tohoku University

Tungsten materials are one of the leading candidates as divertor materials for DEMO reactors. However, since the divertor material in DEMO reactors is exposed to up to 10 dpa neutron irradiation, must evaluate the irradiation effect, and a self-ion irradiation experiment that can remove unnecessary phenomena (transmutation, precipitation, etc.) during the irradiation is significant. However, in the case of tungsten ion irradiation, since the irradiation area is very limited to about 2 μm from the irradiation surface, a method for evaluating the irradiation effect on mechanical properties is limited. The micro tensile test is a new method that could evaluate the tensile properties using a specimen of micro level and it is thought to be effective for assessing ion irradiation materials with a minimal irradiation area. Therefore, this study investigates the effects of self-ion irradiation (specifically, irradiation hardening) on tungsten materials using micro tensile tests. In addition, verification tests were also conducted to examine the validity of the irradiation hardening results obtained through the micro tensile test.

Evaluated the effect of irradiation hardening for ITER-grade pure tungsten (IGW) [1]. 18 MeV W^{6+} ions were irradiated to 18 dpa at 500 °C and 800 °C. Figure 1 shows the results of the micro tensile verification tests [2].

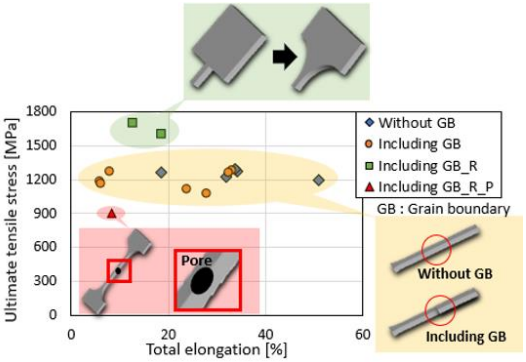

Fig. 1. Results of the micro tensile test for unirradiated specimens with consideration of the effects of the specimen shape and the presence of the grain boundary and pores inside the specimen.

The green data apply a round shoulder to the specimens and can confirm the effect of the shape of the specimen on the test result because it shows higher UTS (ultimate tensile stress) compared to data without a round shoulder (yellow and blue data). Next on, the yellow data includes a grain boundary in the specimen gauge, and the blue data does not include a grain boundary. These data indicate that the grain boundary does not affect the test results because it shows a constant UTS regardless of the presence or absence of a grain boundary. Finally, the red data indicate the result of the defect (pore) included in the specimen gauge. This data shows a significantly lower UTS compared to other data, even though it adopts a round shoulder. Since the tungsten material used in this study was manufactured through powder metallurgy, it contains numerous pores, and the specimen is likely to contain pores. Therefore, in this study, a round shoulder specimen was adopted, and it was manufactured not to include pores and ignored the existence of a grain boundary.

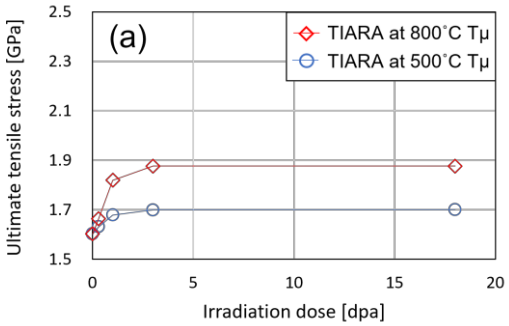

Fig. 2. Results of the irradiation hardening by the micro tensile test.

Figure 2 shows the trend of irradiation hardening using a micro tensile test [2]. In the irradiation at 500 °C, UTS was increased with the irradiation dose, and when the irradiation dose exceeded 1.0 dpa, the UTS was constant at about 1.7 GPa. On the other hand, when irradiated at 800 °C, the UTS increased until the irradiated dose reached 3.0 dpa, and UTS was constant at about 1.9 GPa. These results suggest that the saturation of irradiation hardening depends on temperature. In addition, this trend was the same as irradiation hardening saturation using nanoindentation in the 2020 annual report. Therefore, as a result of careful consideration, we have concluded that the micro tensile test method is very effective for evaluating the tensile properties and hardening of ion irradiation materials. However, the total elongation did not depend on the irradiation temperature or the irradiation dose, which is thought to be affected by the crystal direction. Therefore, in the future, single crystal pure tungsten will be used to evaluate the effect of the crystal direction and the irradiation hardening using identical crystal direction specimens.

References

[1] Ju-Hyeon Yu *et al.*, Fusion Eng. Des. **157**, 111679 (2020). DOI:10.1016/j.fusengdes.2020.111679
[2] Ju-Hyeon Yu *et al.*, Nucl. Mater. Energy. **30**, 101145 (2022). DOI:10.1016/j.nme.2022.101145

1 - 34 Structural analysis of complex formed in adsorbent for gravity driven extraction chromatography

S. Watanabe[a)], Y. Sano[a)] and H. Matsuura[b)]

[a)]Nuclear Fuel Cycle Engineering Laboratories, JAEA
[b)]Atomic Energy Research Laboratory, Tokyo City University

Introduction

Trivalent minor actinides (MA(III): Am and Cm) contained in high level liquid waste (HLLW) generated from reprocessing of spent nuclear fuel possess radiotoxicity, and partitioning and transmutation of those elements are important strategy for sustainable nuclear energy [1]. In order to recover MA(III) from HLLW with practical process, our group is proposing a hybrid process consist of solvent extraction and extraction chromatography which is expected to reduce amount of secondary wastes and to have advantages in safety and economy over the processes of only the solvent extraction or the extraction chromatography. In this technology, MA(III) and lanthanides (Ln(III)) are recovered from high level liquid waste by the solvent extraction with centrifugal contactors, and MA(III) is separated from Ln(III) by gravity driven extraction chromatography. Existing extraction chromatography utilize porous silica support made by sol-gel method, and small pore and particle size generate large pressure drop of packed columns. The gravity driven extraction chromatography requires a new support for adsorbents, and we are conducting optimization in structure of the support to achieve efficient flow of mobile phase in columns and separation performance. In this study, influence of co-existing elements on local structure of complexes around Eu (III) formed in the adsorbent is investigated by Ion beam induced luminescence (IBIL) and Extended X-ray absorption fine structure (EXAFS) techniques to give beneficial information to the optimization study.

Experimental

Silica based porous supports were prepared by liquid column cutting method. N,N,N',N',N'',N''-hexaoctylnitrilotriacetamide (HONTA) was impregnated into styrene-divinyl benzene copolymer coating around the particles, and Eu(III) with co-existing elements (Re(VII), Pd(II), Zr(IV) or Mo(VI)) were loaded into the adsorbents from 0.1 M nitric acid solution.

Eu-L_{III} edge (6.98 keV) EXAFS measurements were carried out at the BL5S1 beamline of Aichi Synchrotron Radiation Facility, Japan. The adsorbent was put in a SUS flat washer with 1 mm thickness and 10 mm inner diameter, and then sealed by two Kapton films.

The IBIL measurements were performed using the ILUMIS system equipped in the light-ion microbeam line connected to a 3-MV single-ended accelerator in TIARA [2]. A few particles of the adsorbent were put on a Kapton film attached to a sample holder, and sealed by a Kapton film. The samples were irradiated by 3 MeV proton beam with a beam current of about 100 pA. The IBIL Spectra were observed by an UV-vis spectrometer (Solid Lambda CCD, Spectra CO., Ltd.).

Results and discussion

EXAFS analysis revealed that the number of the nearest coordinating O atom around Eu(III) slightly depends on elements co-existing in the adsorbents. IBIL spectra of Eu(III) loaded in the adsorbents with various elements are shown in Fig. 1. These characteristic peaks are assigned to be $^5D_0 \rightarrow {}^7F$ transitions of 4f electron in Eu(III) [3]. Influence of the co-existing elements on the peak profile at around 700 nm which corresponds to the $^5D_0 \rightarrow {}^7F_4$ transition was observed. The $^5D_0 \rightarrow {}^7F_4$ transition profile is known to be sensitive to symmetry of atoms around Eu(III), therefore change in symmetry of the complex must be observed by the IBIL measurement. Quantum chemical calculation on Eu(III)-HONTA complex showed that difference in orientation of nitrate ions in the complex caused the difference in EXAFS and IBIL. These results contributed to design of an appropriate MA(III) recovery process flow.

Acknowledgments

This work is supported by the Innovative Nuclear Research and Development Program from the Ministry of Education, Culture, Sports, Science and Technology of Japan.

References

[1] IAEA, Technical Reports Series No. 435, IAEA, Vienna (2004).
[2] W. Kada, *et al.*, Nucl. Instrum. Methods Phys. Res. B **332**, 42 (2014). DOI: 10.1016/j.nimb.2014.02.026
[3] K. Binnemans, Coord. Chem. Rev. **295**, 1 (2015). DOI: 10.1016/j.ccr.2015.02.015

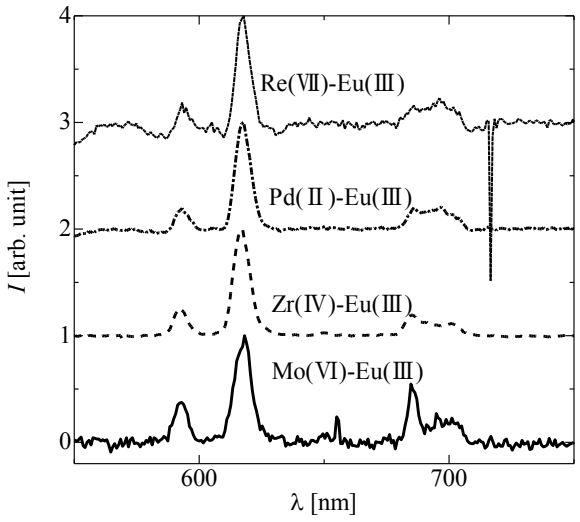

Fig. 1. IBIL spectra of Eu(III) loaded into the adsorbents.

1 - 35 Ion beam induced luminescence spectra of europium complexes in silica-based adsorbent

M. Nakahara[a)], S. Watanabe[a)], Y. Ishii[b)], R. Yamagata[b)], N. Yamada[c)], M. Koka[c)], T. Yuyama[b)], T. Ishizaka[b)], W. Kada[d)] and N. Hagura[e)]

[a)]Nuclear Fuel Cycle Engineering Laboratories, JAEA
[b)]Department of Advanced Radiation Technology, TARRI, QST
[c)]Beam Operation Co., Ltd.
[d)]Faculty of Science and Technology, Gunma University
[e)]Faculty of Science and Engineering, Tokyo City University

Introduction

In a nuclear fuel reprocessing, it is desirable to recover not only U and Pu but also minor actinides (MA) such as Np, Am, Cm to reduce radiotoxicity and the volume of vitrified wastes [1]. An extraction chromatography process has been studied to recover MA from high-level liquid wastes generated in reprocessing of spent nuclear fuels. Porous SiO_2 particles impregnated with an extractant for MA are used as an adsorbent for the extraction chromatography process. The adsorbent was packed into a column, and high-level liquid waste was flowed through the column to separate MA. It is important to evaluate the structure of complexes for efficient MA recovery because the structure of complexes such as symmetry would affect the ease of elution for MA. In the previous studies [2,3], Eu was used instead of MA, and ion beam induced luminescence (IBIL) spectra of Eu were measured by H^+ ion irradiation to evaluate the structure of Eu complexes. However, there is few studies about of the IBIL analysis of complexes in the adsorbent, and collecting a lot of IBIL data is needed to evaluate the structure of complexes. Linear energy transfer (LET) is possible to affect the IBIL spectrum of complexes. Therefore, the influence of ion beams on the IBIL spectra of Eu was evaluated in this study.

Experimental

Styrene-divinylbenzene copolymer was coated on the surface of porous SiO_2 particles (SiO_2-P), which were impregnated with extractant. In this study, *n*-octyl(phenyl)-*N*,*N*-diisobutylcarbamoylmethylphosphine oxide (CMPO) was used as an extractant. Eu was used as simulated material for MA because Eu^{3+} has similar extraction behavior to trivalent MA. Eu nitrate solution was mixed with CMPO-impregnated SiO_2-P particles, which was separated from Eu nitrate solution. The recovered adsorbent was put in a Kapton case and was used for the IBIL measurement.

In the experiments, two ion beams, a 3 MeV H^+ in the light-ion microbeam line connected to a 3-MV single-ended accelerator [4] and 107 MeV Ar^{8+} with the beam line for large-area uniform irradiation at an azimuthally varying field (AVF) cyclotron in TIARA were used. The exposure times were 6.5 s and 1 s for H^+ and Ar^{8+} ions irradiation, respectively.

Results and discussion

Figure 1 shows the IBIL spectra of Eu complexes in the CMPO/SiO_2 adsorbent by H^+ and Ar^{8+} irradiation. The spectrum obtained by Ar^{8+} ion irradiation was similar to that by H^+ ion irradiation. However, intensity of luminescence of Eu complexes irradiated by A^{8+} ion was larger than that irradiated by H^+ ion. Therefore, the IBIL spectra of a tiny amount of Eu complexes could be measured by Ar^{8+} ion irradiation. It is known that Eu^{3+} ion which has 54 electrons in the closed shells and 6 electrons in the 4f shell and exhibits strong luminescence in the transition of 4f electrons [5]. The $^5D_0 \rightarrow {}^7F_J$ (J = 0–6) transitions in the luminescence spectrum are observed. The peak was observed at 592 nm due to the $^5D_0 \rightarrow {}^7F_1$ transition, and the dominant peak was at 617 nm assigns the $^5D_0 \rightarrow {}^7F_2$ transition. Very close two peaks were confirmed at 689 and 696 nm in the $^5D_0 \rightarrow {}^7F_4$ transition. Among these transitions, the $^5D_0 \rightarrow {}^7F_2$ transition is known as hypersensitive transition and the intensity strongly depends on the environment. The $^5D_0 \rightarrow {}^7F_2$ transition is used as a measure for the asymmetry of Eu^{3+} site. The evaluation of the symmetry of Eu complexes in the adsorbent would be useful for ease of elution for Eu, and it contributes the MA recovery in the extraction chromatography process.

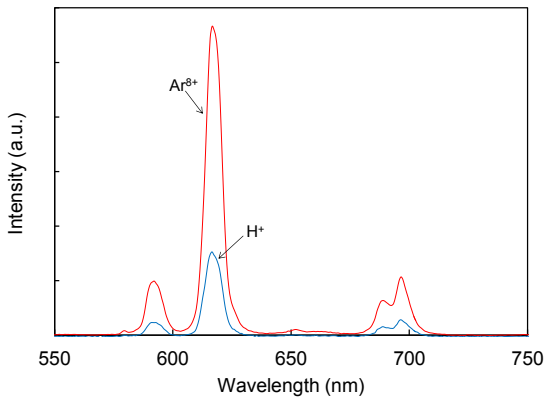

Fig. 1. IBIL spectra of Eu complexes in the CMPO adsorbent.

References

[1] Y.-Z. Wei *et al.*, Nucl. Technol. **132**, 413 (2000). DOI: 10.13182/NT00-A3154
[2] S. Watanabe *et al.*, Nucl. Instrum. Methods Phys. Res. B **450**, 61 (2019). DOI: 10.1016/j.nimb.2018.08.029
[3] S. Watanabe *et al.*, Nucl. Instrum. Methods Phys. Res. B **477**, 60 (2020). DOI: 10.1016/j.nimb.2019.10.004
[4] W. Kada *et al.*, Nucl. Instrum. Methods Phys. Res. B **332**, 42 (2014). DOI: 10.1016/j.nimb.2014.02.026
[5] K. Binnemans, Coord. Chem. Rev. **295**, 1 (2015). DOI: 10.1016/j.ccr.2015.02.015

1 - 36 Synthetic control of functional metal nanomaterials in SiO_2 by multiple particles irradiation

F. Hori[a)], T. Yamada[a)], H. Obayashi[a)], T. Matsui[a)] A. Iwase[a,b)], S. Semboshi[c)], N. Taguchi[d)] and S. Tanaka[d)]

[a)]Deptment of Quantum and Radiation Engineering, Osaka Metropolitan University
[b)]The Wakasa Wan Energy Research Center
[c)]Institute for Materials Research, Tohoku University
[d)]Research Institute of Electrochemical Energy, AIST

Metallic nanomaterials have attracted tremendous attention due to their unique properties, such as luminescence, absorption, magnetic property, catalytic activity and hydrogen absorption. These properties come from their size, shape, alloy system and complex electronic state which is not appear in bulk materials. Ion irradiation to solid target is one of a method to synthesis of nanostructured materials (precipitations) that is highly controlled impurity injection with high density of energy into solid followed by thermal annealing. In some cases, metal nanoparticles are formed in silica glass without annealing by ion implantation. We suppose this method is useful to synthesize the new functional nanomaterials with control of alloy structures and phases. So far, we have successfully synthesized new functional nanoparticles in glassy solid by using this method [1, 2]. In this study, amorphous SiO_2 was alternately irradiated with Ni and Ag ions at room temperature to investigate the effects of multi-ion irradiation and changing their irradiation order on the formation of nanoparticles in solid. We found that it is possible to form metal nano-composite and also the irradiation sequence affects the formation of Ag-Ni metal nano-composite. The structure of these nanoparticles synthesized by Ag and Ni ions irradiation in SiO_2 has only discussed with X-ray diffraction results in our previous report [3].

Experimental

Transparent amorphous silica glass (SiO_2: $5 \times 5 \times 1$ mm^3) was prepared as an irradiation target. The target was irradiated with 380 keV Ag ions and 200 keV Ni ions at room temperature by using ion implanter at TIARA, National Institutes for Quantum and Radiological Science and Technology (QST-Takasaki). Dual irradiation with Ag and Ni ions has done by changing irradiation order (AN: is irradiated firstly with Ag ions and followed by Ni ions, NA: is vice versa). The irradiation fluence of Ag ion is 5×10^{15} to 7×10^{16} /cm^2 and that of Ni ions was 1×10^{15} to 1×10^{17} /cm^2. After each ion irradiation, these samples were examined by fine structure by using X-ray at KEK, UV-vis, Grazing Incidence X-ray Diffraction (GIXD) and Scanning TEM with Energy dispersive X-ray spectroscopy (EDX) analysis. Figure1 shows the depth profiles of implanted ions of 380 keV Ag and 200 keV Ni calculated by TRIM. By changing the ion energy, it is possible to deposit ions to the same depth.

Results and Discission

Our previous data of light absorption for synthesized nanoparticles AN and NA showed clearly different [3]. The lattice structure of these nanoparticles is defined as face centered cubic by GIXD, but their brag peaks of NA is slightly shifted to low angle compare with that of AN. This result is considered to be due to the lattice expansion of the NA nanoparticles caused by the alloying of Ag and Ni atoms. Figure 2 shows cross-sectional photographs of NA and AN sequential irradiation formed nanoparticles by using STEM-EDX. From this figure, it was found that ions are deposited at almost the same depth as expected in any order of irradiation and composite nanoparticles were generated, but there were clear differences in particle size distribution and state. That is, in case of NA, core-shell particles having a uniform particle size are formed centering on Ni and covered with Ag. In the case of AN, the particle size is dispersive and they look like an alloy of Ni and Ag. This result is also consistent with the XRD results.

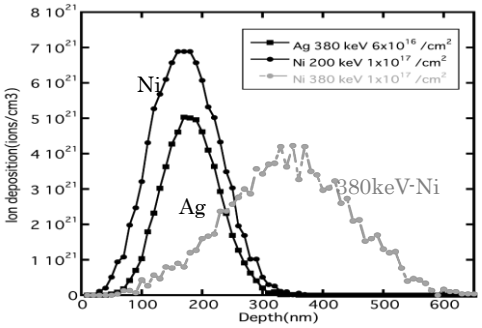

Fig. 1. TRIM simulation of 380keV-Ag and 200keV-Ni into SiO_2.

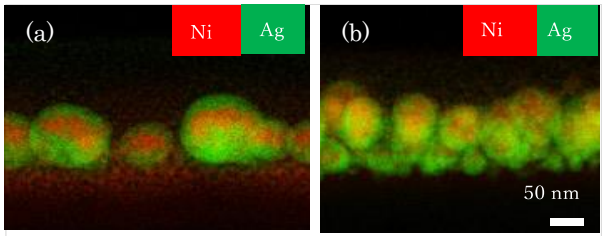

Fig. 2. TEM-EDX observation of nanoparticles in SiO_2 synthesized by ion implantation. (a) Irradiation sequence NA and (b) AN.

Acknowledgments

We would like to thank to TIARA staff for their help to ions irradiation experiment.

References

[1] T.Yamada *et al.*, Nanotechnology **31**, 455706 (2020). DOI: 10.1088/1361-6528/abaadf
[2] T. Yamada *et al.*, Trans. Mater. Res. Soc. Jpn. **45**, 127 (2020). DOI: 10.14723/tmrsj.45.127
[3] F.Hori *et al.*, QST Takasaki Ann. Rep. 2020 **QST-M-33**, 41 (2021).

1 - 37 Evaluation of radiation tolerance of COTS device for small satellite

K. Tomita[a)], K. Toda[a)], K. Akashi[a)], J. Harada[a)],
T. Ohshima[b)] and S. Satoh[b)]

[a)]Advanced Engineering Services Co., Ltd. (AES)
[b)]Quantum Materials and Applications Research Center, TARRI, QST

In recent years, the development of small satellites has become more active and has been requiring lower cost, smaller size, and higher functionality of onboard components. To meet these requirements, the use of COTS devices is desired. However, in general, COTS devices are not designed for use in space environments, and their radiation tolerance is unknown. Therefore, it is necessary to confirm the operation and degradation status of COTS devices in the space environment by radiation tests.

The effects of radiation on electronic devices can be divided into two major patterns: Total Ionization Dose (TID) and Single Event Effect (SEE). TID is the performance degradation of electronic devices caused by β, γ, and proton beams. SEE is a functional failure caused by incoming heavy particles. In this research, small satellite which is assumed to use COTS devices is less affected by TID because of its low orbit and short operation period of one year. On the other hand, even a single occurrence of SEE can destroy the electronic device itself and the surrounding circuits. The purpose of this research is to evaluate radiation tolerance in the space environment by testing various COTS devices and observing the occurrence of SEE.

This research utilized the Shared Use Program of QST. The AVF cyclotron and real-time beam monitor irradiation chamber at Takasaki Advanced Radiation Research Institute was used for the evaluation.

Only Kr beam was used as the irradiation source due to machine time constraints. The SEE probability was calculated from the cross-section area obtained from the test, the LET (Linear Energy Transfer) threshold, and the orbital radiation distribution calculated using CREME96 [Cosmic Ray Effects on Micro-Electronics (1996 Revision)].

The orbital characteristics of the small satellite for which the COTS devices are to be used in this research, are as follows; altitude of 700 km, orbital inclination of 98 degrees, satellite structure using aluminum of 2 mm thickness, and operational period of one year.

The radiation tolerance of COTS device was evaluated by comparing the calculated frequency of SEE occurrence with the expected operation period.

In FY2021, we selected FPGA (Field Programmable Gate Array) as the sample. The FPGA is an SOI (Silicon On Insulator) process product that is expected to have radiation tolerance and is a device with built-in RAM (Random Access Memory) and IO (Input Output) peripherals in addition to general-purpose logic cells (39K scale). It is applicable to signal processing units in small satellite components.

Table 1 shows the evaluation items, test results, and calculated probability of SEE occurrence under the assumed orbit characteristics for the samples.

The test included the following evaluation items.

- SEL (Single Event Latch-up)
- SEFI (Single Event Functional Interrupt)
- SEU (Single Event Upset)

For SEL, when the current consumption of a sample increases above SEL threshold (twice the current consumption during normal operation), it was judged to be a SEL, and the number of occurrences was counted. In addition, a power reset was performed to confirm the method to restore the sample to normal operation after the SEE occurred.

For SEFI, the number of occurrences was counted when a sample malfunction was detected.

For the SEU, bit errors were counted for the SRAM (Static Random Access Memory) area and gate section in the FPGA.

Test results showed that Kr irradiation did not cause SEL, SEFI and SEU. Therefore, the probability of SEE occurrence was calculated assuming that one event of SEE occurred by Kr as a worst-case scenario. The Single Event Probability values shown in Table 1 indicate that the frequency of SEE occurrences is low for the expected one-year operation period, thus the sufficient radiation tolerance was confirmed.

Finally, since the sample COTS devices were not made for use in a space environment, the results of this test do not indicate superiority or inferiority of the performance or function of the device itself.

Table 1
Single event probability of FPGA.

Evaluation Item	LET Threshold (MeV-cm^2/mg)	Cross-sectional area (cm^2)	Integral Flux (#/cm^2/year)	Single Event Probability (event/year)
SEL	>34.0	8.29E-07	7.30E-03	<6.05E-09
SEFI		8.29E-07		<6.05E-09
SEU (SRAM)		1.58E-12 (cm^2/bit)		<1.15E-14 (event/bit/year)
SEU (Gate)		2.63E-10 (cm^2/bit)		<1.92E-12 (event/bit/year)

1 - 38 Thermodynamic study of $Ti_{1-x}Al_xN$ thin film growth on monocrystalline AlN by reactive CVD

Y. Kasukabe[a), b)], H. Shimoda[b)] and S. Yamamoto[c)]

[a)]Global Learning Center, Tohoku University
[b)]Department of Metallurgy, Tohoku University
[c)]Department of Advanced Functional Materials Research, TARRI, QST

Films of $Ti_{1-x}Al_xN$ have been known as the material which exhibits superior mechanical and thermal properties, and those are widely used as coatings for industrial applications such as cutting tools. Irrespective of those attracting performance, little is studied on the growth mechanism as well as the chemical process. In this work, $Ti_{1-x}Al_xN$ thin films have been prepared by reactive Chemical Vapor Deposition (CVD) and analyzed by Field Emission Gun Scanning Electron Microscopy (FEG-SEM), Transmitting Electron Microscope (TEM) [1], and X-ray Diffraction (XRD).

Recently, it has been reported that $Ti_{1-x}Al_xN$ films have been grown by use of the titanium tetra chloride, $TiCl_4$, and c-plane (0001) monocrystalline hexagonal aluminum nitride, AlN, precursors [2]. The AlN has been prepared at 1500 °C with the gas mixture of NH_3 and $AlCl_3$ on c-plane (0001) monocrystalline hexagonal sapphire. During the $Ti_{1-x}Al_xN$ growth, hydrogen (H_2) gas is used as carrier gas of $TiCl_4$. The growth has been performed on the 100-nm-thick monocrystalline AlN on sapphire.

In order to characterize the effect of H_2 carrier gas flux on the crystallinity and composition of $Ti_{1-x}Al_xN$ films, X-ray diffraction patterns of the films deposited at 1200 °C for 15 minutes with H_2 carrier gas flux fixed (a) at 100 sccm (Standard Cubic Centimeter per Minute), (b) at 1000 sccm and (c) 2000 sccm on monocrystalline AlN substrates, were observed as shown in Fig. 1. The shift of the position of the peak $Ti_{1-x}Al_xN$ (222) marked by * can be found according to the Vegard's law. Moreover, it can be recognized that H_2 carrier gas promotes the growth of $Ti_{1-x}Al_xN$ film which leads to the increase in the intensity of $Ti_{1-x}Al_xN$ (222) peak. These indicate that more H_2 carrier gas leads to the growth of of Ti-rich $Ti_{1-x}Al_xN$ films.

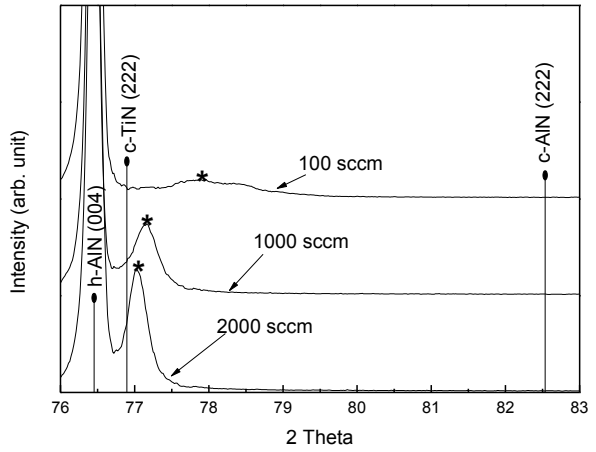

Fig. 1. X-ray diffraction patterns of the layers fabricated on monocrystalline AlN at 1200 °C with H_2 gas fixed at (a) 100 sccm, (b) 1000 sccm, (c)2000 sccm. The marks of * indicate the position of the peak of $Ti_{1-x}Al_xN$ (222).

In order to evaluate the composition of the $Ti_{1-x}Al_xN$ non-stoichiometric compound grown by introducing $TiCl_4$ gas using H_2 carrier gas onto a monocrystalline AlN substrate at 1200 °C, a thermodynamically phase diagram was simulated at 0.01 atm and 1200 °C for the AlN-$TiCl_4$-H_2 ternary system as shown in Fig. 2. This simulation was calculated in a closed equilibrium state, and the actual experiment was performed in an open system with a gas flow rate. Therefore, it is considered that there is a large amount of H_2 in the vicinity of the AlN substrate surface compared to $TiCl_4$ and AlN, and the H_2-rich state shown in Fig. 2 is realized, which leads to the growth of $Ti_{1-x}Al_xN$ films. The affinity of nitrogen for titanium is stronger than that of nitrogen for aluminum, and in the initial stage of the reaction, TiN non-stoichiometric compounds are preferentially formed on the AlN substrate, and then Al is incorporated into the TiN non-stoichiometric compounds by the diffusion. Therefore, Al atoms of the AlN substrate are classified into those that eventually become $Ti_{1-x}Al_xN$ and those that become gases such as aluminum chlorides ($AlCl_3$, $AlCl_2$, AlCl) and leave the substrate. Therefore, the more H_2 carrier gas flux, the more aluminum chloride evaporates and the less the amount of Al (x) in the resulting $Ti_{1-x}Al_xN$ non-stoichiometric compound.

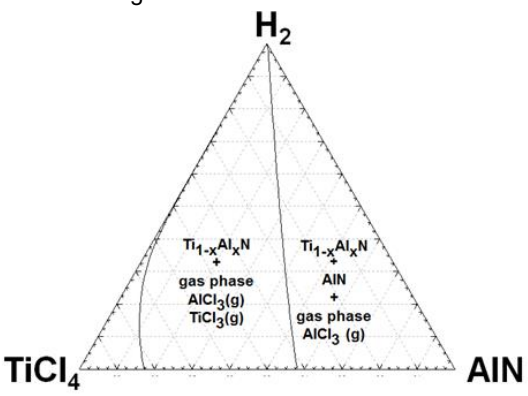

Fig. 2. AlN-$TiCl_4$-H_2 ternary phase diagram simulated at 1200 °C at 0.01 atm. Note that Ti_{1-x}AlxN lattice structure is cubic system, and AlN is hexagonal system. Main compounds existing in the gas phase are noted.

Therefore, it can be concluded that the H_2 carrier gas promotes the growth of Ti-rich $Ti_{1-x}Al_xN$ films.

References

[1] H. Abe *et al.*, JAERI-Research **96-047**, 1 (1996). DOI: 10.11484/jaeri-research-96-047
[2] R. Boichot *et al.*, Surf. Coat. Technol. **205**, 1294 (2010). DOI: 10.1016/j.surfcoat.2010.08.049

1 - 39 Color imaging of carbon ion ($^{12}C^{+5}$) beam by the 3D gel dosimeter based on phenothiazine-type color former

T. Tachikawa and K. Yamada

Faculty of Engineering, Graduate School of Science and Engineering, Saitama University

Introduction

The color formers have been developed [1-2] to visually detect radiation that is harmful to the human body but cannot be detected by the human senses. Gel dosimeters based on the color formers [3] will be useful for the visually detection of the area irradiated with heavy particle beams, which are used for cancer treatment. In our previous studies on γ ray detective color formers, the phenothiazine-type color former 1, which has water-solubility by introducing a water-soluble substituent into the protecting

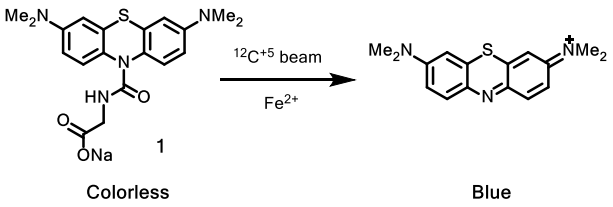

Scheme 1. Coloration of phenothiazine-type color former 1

group, showed the color development by 10 Gy of γ irradiation in aqueous solution with the addition of iron(II) sulfate heptahydrate [4]. This paper presents the color development characteristics by carbon ion beam irradiation of the hydrogel dye dosimeters, which are prepared with phenothiazine-type color former 1 and gelatin or κ-carrageenan as gelling agents. Gelatin and κ-carrageenan are familiar gelling agents for water.

Results and discussion

The hydrogel dye dosimeters were prepared as follows. The color former solution containing iron(II) sulfate heptahydrate was prepared so that the concentrations were $[\mathbf{1}]_0$=0.13 mM and $[Fe^{2+}]_0$=0.125 mM. 120 mg of gelatin was added to 1 mL of the solution and the solution was heated to 60°C and then cooled in a freezer for 10 minutes. For the κ-carrageenan gel, 15 mg of k-carrageenan was used instead of 120 mg of gelatin.

Irradiation of carbon ion beam to the hydrogel dye dosimeter was carried out at TIARA. 220 MeV carbon ions ($^{12}C^{+5}$) were irradiated to the dosimeters at 4 nA for the exposure times of 30 s and 60 s, or at 2 nA for 120 s with scanning the beam over the area of 7.5 cm x 7.5 cm under normal temperature and ambient pressure.

The images of the hydrogel dye dosimeters using gelatin as a gelling agent or κ-carrageenan before and after carbon ion beam irradiation are shown in Fig. 1 and Fig. 2, respectively. From the images, the coloration of the color former due to carbon ion beam irradiation was confirmed, and the gelatin gel developed a green color, while the κ-carrageenan gel developed a blue color.

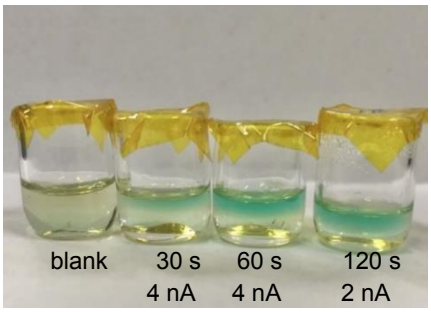

Fig. 1. Color changing image of **1** in gelatin gel dosimeter after $^{12}C^{+5}$ beam irradiation ($[\mathbf{1}]_0$ = 0.13 mM, $[Fe^{2+}]_0$ = 0.125 mM).

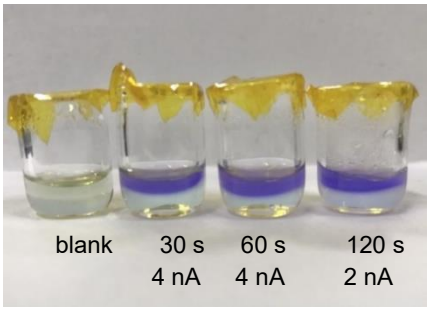

Fig. 2. Color changing image of **1** in κ-carrageenan gel dosimeter after $^{12}C^{+5}$ beam irradiation ($[\mathbf{1}]_0$ = 0.13 mM, $[Fe^{2+}]_0$ = 0.125 mM).

The colored gel after irradiation was dissolved in water and the UV-VIS spectra were measured. The longest wavelength absorption band was observed at 650 nm for the gelatin gel, and the absorption band at 650 nm was not observed in the κ-carrageenan gel, but the absorption band was observed at 560 nm.

The, hydrogel dye dosimeters not containing iron (II) sulfate heptahydrate were prepared and irradiated with carbon ion beam. The gelatin gel and the k-carrageenan gel dosimeters did not develop any color by the irradiation. The sensitizing effect of iron (II) sulfate heptahydrate is important also for the coloration by carbon ion beam.

References

[1] H. Itoi, *et. al.,* Chem. Lett. **38**, 1002 (2009). DOI: 10.1246/cl.2009.1002
[2] T. Tachikawa, *et. al.,* Isotope News **731**, 7 (2015).
[3] T. Tachikawa, *et. al.,* Material Stage **14**, 1 (2014).
[4] T. Tachikawa and S Ishibashi, QST Takasaki Annu. Rep. 2019 **QST-M-29**,76 (2020).

1 - 40 Gamma-irradiation effect on radical centers derived from hydrothermally altered potassium feldspar and its application to fault dating

T. Fukuchi

Faculty of Education, Graduate Faculty of Interdisciplinary Research, Univeristy of Yamanashi

It is important for the purpose of earthquake disaster prevention to date the absolute age of unrecognized active faults distributed in the regions without clear tectonic landform or Quaternary overlying sediments. At present, we have no available dating technique except for ESR (electron spin resonance), TL (thermo-luminescence) or OSL (optically stimulated luminescence) dating method.

In the ESR method, we use fault rock formed by fault shearing at the time of fault movement and estimate the absolute age of fault rock using radical centers detected from fault-rock-forming minerals [1]. The fault-rock-forming minerals are often subjected to frictional heat and hydrothermal alteration by fault shearing. Therefore, the radical centers derived from hydrothermally altered minerals may give the absolute age of fault movement.

In this study, I carried out hydrothermal reaction experiments for 2 weeks at 250 ℃ under an aqueous solution of 10%NaOH using the powder sample of potassium feldspar extracted from the Hoo-type granite distributed along the Hakushu fault belonging to the Itoigawa-Shizuoka Tectonic Line (ISTL) Active Fault System.

Figure 1 shows the X-ray diffraction (XRD) patterns obtained from the natural and hydrothermally altered samples. The XRD analysis indicates that the XRD peaks of potassium feldspar (orthoclase) disappear and those of plagioclase (albite) extremely decease, while those of kaolinite, a kind of clay mineral, newly appear after the hydrothermal reaction under an aqueous solution of 10%NaOH.

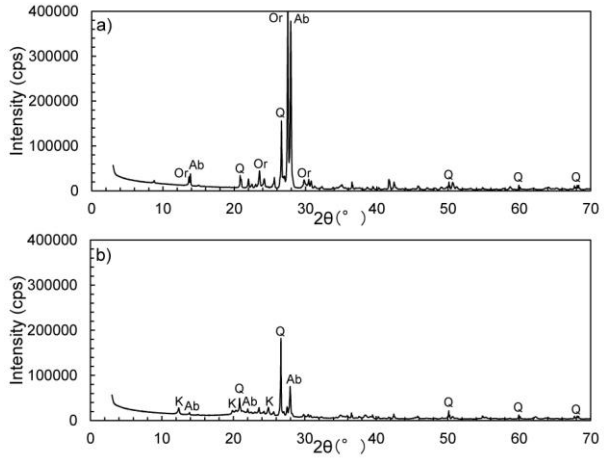

Fig. 1. X-ray diffraction patterns obtained from the natural and hydrothermally altered samples of potassium feldspar. The heating temperature and duration are 250 °C and 2 weeks. a) natural sample consisting mainly of potasium feldspar (orthoclase) in the fresh Hoo-type granite, b) hydrothermally altered sample under an aqueous solution of 10%NaOH.Q: quartz, Ab: albite, Or: orthoclase, K: kaolinite.

Figure 2 shows ESR spectra obtained from the natural and hydrothermally altered samples. The abscissa is represented by the g-value, spectroscopic splitting factor. The ESR analysis reveals that unknown multiple radical centers except the signal at g = 1.997 come to appear from the hydrothermally altered sample under an aqueous solution of 10%NaOH after gamma-irradiation. The signal at g = 1.997 is the Ge center derived from germanium ions in quartz [1].

The unknown multiple radical centers regularly increase with increasing radiation dose, and then they may be applicable to the dating of hydrothermal alteration in faulting, that is, the absolute dating of fault movement. It is unclear whether the unknown multiple radical centers are derived from kaolinite since the intrinsic signal derived from kaolinite has a large linewidth and increases by gamma-irradiation with a high radiation dose of 10 kGy or more [2].

References

[1] T. Fukuchi, Radioisotopes **70**, 131 (2021).
DOI: 10.3769/radioisotopes.70.131

[2] T. Fukuchi, Jpn. J. Appl. Phys. **35**, 1977 (1996).
DOI: 10.1143/JJAP.35.1977

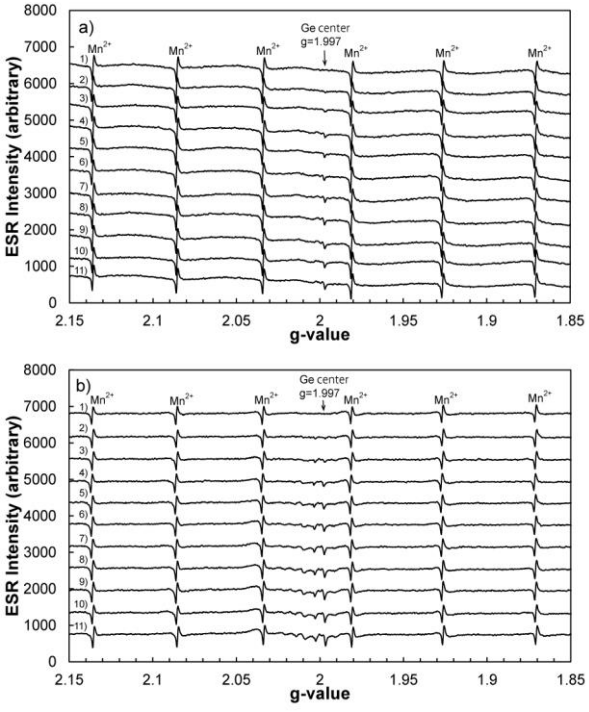

Fig. 2. Gamma-irradiation effect on radical centers detected from the natural and hydrothermally altered samples. a) natural sample, b) hydrothermally altered sample. The ESR spectra were measured at a microwave power of 1 mW under RT. The irradiation dose rate is 317.3 Gy/h. Irradiation time: 1) 0h, 2) 1h, 3) 2h, 4) 3h, 5) 4h, 6) 5h, 7) 6h, 8) 7h, 9) 8h, 10) 9h, 11) 10h.

blank page

Part Ⅱ

2. Life Science

2-01 Quality effects of carbon ion and proton beams and gamma-rays on reversion mutation in zebrafish embryos ····· 72
S. Oda, D. Li, E. Sha, Y. Shen, B. Ma, M. Suzuki and T. Funayama

2-02 DNA damage foci formation after simulated-space radiation exposure ····· 73
T. Oizumi, T. Suzuki, T. Funayama, and AJ. Nakamura

2-03 Precise localized irradiation of individual organisms using focused heavy ion microbeams ···· 74
T. Funayama and M. Suzuki

2-04 New trial toward the precise identification of fluorescence dots originated from oxidative damage in DNA thin sheet perpendicularly irradiated with heavy ions ····· 75
A. Ito, K. Urano, A. Sudo, B. Daisi, S. Yoshida, R. Hirayama, Y. Furusawa, Y. Yokota and T. Funayama

2-05 Development of depth-controlled irradiation methods for silkworm eggs – Determination of shielding range – ····· 76
N. Miyasaka, Y. Soma, T. Funayama, M. Suzuki and K. Shirai

2-06 Comparison between 190MeV $^{12}C^{6+}$ and 220MeV $^{12}C^{5+}$ ions in inducing *P-53* gene dependent bystander cell-killing effect in human tumor cell lines ····· 77
M. Suzuki, T. Funayama and M. Suzuki

2-07 Basic study of immunoradiation therapy using anti-PD-L1 antibody ····· 78
T. Hara, T. Funayama, H. Sato, Y. Nakagami, Y. Suzuki and T. Ohno

2-08 Efficient dose of carbon ion beam irradiation for azalea seeds ····· 79
K. Ureshino, K. Satoh and Y. Oono

2-09 Effect of carbon ion-beam irradiation on growth and mutation spectra of *Physcomitrium patens* ····· 80
Y. Yokota, K. Satoh and A. N. Sakamoto

2-10 Mutagenesis of the oil-producing algae by heavy ion irradiation ····· 81
H. Araie, Y. Hase, Y. Iwata, Y. Oono and I. Suzuki

2-11 Genome analysis of the low cesium-accumulating mutants of *Rhodococcus qingshengii* CS98 generated by ion beam breeding ····· 82
K. Satoh, S. Ozawa, H. Hayashi and Y. Oono

2-12 Pilot-scale sake brewing tests using non-urea producing Gunma KAZE3 yeast bred by ion-beam mutagenesis ····· 83
T. Watanabe, M. Yanagisawa, K. Satoh and Y. Oono

2-13 Growth curve analysis of *Bacillus subtilis* spores to evaluate damage and growth inhibition by ion-beam and gamma Irradiations ····· 84
K. Tatsumoto, R. Asada, J. J. Sakamoto, T. Tsuchido, M. Furuta, K. Satoh and Y. Oono

2-14 Gamma-ray resistance of the thermophilic *Rubrobacter* species ····· 85
K. Katsumata, K. Satoh, Y. Oono, K. Miyazaki and I. Narumi

2-15 Strategy for detecting genome-wide mutations in mutagenized Arabidopsis plants ····· 86
S. Kitamura, K. Satoh and Y. Oono

2-16 Elucidation of genes involved in camptothecin biosynthesis of *Ophiorrhiza pumila* ····· 87
A. Takamatsu, N. Tsujimoto, S. Kitamura, Y. Oono and M. Yamazaki

2-17 Enhancing the therapeutic effect of 2-^{211}At-astato-α-methyl-L-phenylalanine with probenecid loading ····· 88
H. Hanaoka, Y. Ohshima, H. Suzuki, I. Sasaki, T. Watabe, K. Ooe, S. Watanabe and N. S. Ishioka

2-18 Rapid flow-based system for separation of radioactive metals by selective complex formation ····· 89
Y. Sugo, S. Obata, R. Miyachi, H. Manabe, M. Mori, S. Ohira and N. S. Ishioka

2-19 Preparation for single-cell RNA-sequence assay of PC12 pheochromocytoma cells ····· 90
T. Sakashita, Y. Ohshima, Y. Yokota and N. S. Ishioka

2-20 Spatial distributions of cesium and strontium in tea leaves evaluated by micro-PIXE analysis ····· 91
A. Terakawa, K. Momokita, Y. Hattori, M. Sato, K. Ishii, M. Koka, N. Yamada, R. Yamagata, Y. Ishii, N. Suzui, T. Satoh and N. Kawachi

2-21 Identification of multi-element accumulation mechanism in legume ····· 92
J. Furukawa, Y. Noda, N. Suzui, Y.-G. Yin, M. Koka, N. Yamada, R. Yamagata, Y. Ishii, N. Kawachi and T. Satoh

2-22 Visualization of zinc distribution in the root of oilseed rape plants by atmospheric micro-PIXE (Particle Induced X-ray Emission) analysis ····· 93
S. Nakamura, Y. Imaizumi, K. Suda, A. Shinozawa, K. Sato-Izawa, N. Yamada, R. Yamagata, Y. Ishii, T. Satoh, Y.-G. Yin, N. Suzui and N. Kawachi

2-23 Evaluation of photosynthate translocation dynamics to strawberry fruits in response to increasing daylight integrals at leaf surface ····· 94
Y. Miyoshi, K. Hidaka, Y.-G. Yin, N. Suzui, K. Kurita and N. Kawachi

2-24 Elemental distribution into root dentin from pilot materials incorporating with titanium fluoride ····· 95
K. Okuyama, Y. Matsuda, H. Yamamoto, M. Sakurai, K. Naito, H. Kanda, T. Saito, M. Hayashi, Y. Tamaki, T. Satoh, N. Yamada, R. Yamagata and Y. Ishii

2-25 Ion penetration of zinc-containing fluoride material into sound and demineralized dentin ····· 96
H. Yamamoto, K. Okuyama, Y. Matsuda, K. Naito, H. Kanda, M. Sakurai, M. Hayashi, T. Satoh, N. Yamada, R. Yamagata and Y. Ishii

2-26 Estimation of damage localization of ion beam-irradiated DNA in water by means of fluorescence anisotropy ····· 97
K. Akamatsu, N. Shikazono and K. Satoh

2-27 Development of drug delivery system (DDS), through two repetitions of radiation ····· 98
S. Harada and T. Satoh

blank page

2 - 01 Quality effects of carbon ion and proton beams and gamma-rays on reversion mutation in zebrafish embryos

S. Oda[a)], D. Li[a)], E. Sha[a)], Y. Shen[a)], B. Ma[a)], M. Suzuki[b)] and T. Funayama[b)]

[a)]Department of Integrated Biosciences, The University of Tokyo
[b)]Department of Radiation-Applied Biology Research, TARRI, QST

Cells have a variety of machineries to repair DNA damaged by various environmental factors such as ionizing radiation and ultraviolet light and it is essentially important to elucidate the crosstalk between these damage repair machineries to understand genome stability. Recently, transgenic mouse and medaka have been developed to visualize reversion mutation *in vivo*, that regain the lost phenotype of a mutated gene [1, 2] and occurrence of reversion mutation can be detected by expression of GFP in place of mCherry in the transgenic medaka with a partially duplicated β-actin promoter [2]. In this study, we generated a transgenic zebrafish line with the construct to visualize reversion mutations in medaka, and reversion mutations induced by irradiation with three types of radiation (carbon ion and proton beams, gamma-rays) were observed in zebrafish embryos.

The construct, in which the 3' portion of the medaka β-actin promoter and GFP gene were inserted downstream of the mCherry gene driven by the medaka β-actin promoter [2], was microinjected into fertilized eggs of zebrafish and a transgenic zebrafish line was generated, which expresses mCherry in cells throughout the whole body with red fluorescence when without reversion mutations.

Irradiation of carbon ion beam ($^{12}C^{5+}$, 26.7 MeV/u, 5 or 10 Gy) to the transgenic zebrafish embryos at 9 hour-post-fertilization (hpf) induced severe malformations such as short and/or curved tail, swelling of pericardium cavity, and all of the irradiated embryos died within 4 days after the irradiation. In addition, induction of GFP expression was observed in all of the embryos irradiated with 5 or 10 Gy of carbon ion beam (Fig. 1). In the transgenic zebrafish embryos generated in this study, reversion mutations were detected only after lethal doses of irradiation of carbon ion beam.

Irradiation of proton beam (H^+, 15 MeV/u, 10 Gy) to the transgenic zebrafish embryos (9 hpf) also induced the severe developmental malformations such as short and/or curved tail, swelling of pericardium cavity, however, some embryos were still alive 6 days after the irradiation. We observed GFP expression in 12 embryos among the irradiated 18 embryos (Fig. 1). In this study, we found that proton beam induced less severe malformations and a higher survival rate than carbon ion beam of the same dose. This result suggests that proton beam irradiation might be more suitable to induce and study reversion mutations *in vivo* in zebrafish embryos.

All (20 of 20) of the transgenic zebrafish embryos (9 hpf) irradiated with 30 Gy of gamma-rays showed severe developmental malformations (short and/or curved tail, swelling of pericardium cavity, head dysplasia, etc.) and expressed GFP but died within 3 days after the irradiation. Irradiation of 20 Gy of gamma-rays also induced similar malformations in all of the embryos but some of them survived 3 days after the irradiation and a half of the irradiated embryos (10 of 21) expressed GFP 2 days after the irradiation. More embryos survived after 10 Gy of gamma-ray irradiation and some embryos showed malformations (curved tail, swelling of pericardium cavity) only after hatching, however, none of them expressed GFP.

The obtained results suggest that higher (and lethal) dose of gamma-ray irradiation is required to induce reversion mutation in zebrafish embryos and proton beam is more suitable to induce reversion mutation in zebrafish embryos *in vivo* than carbon ion beam and gamma-rays.

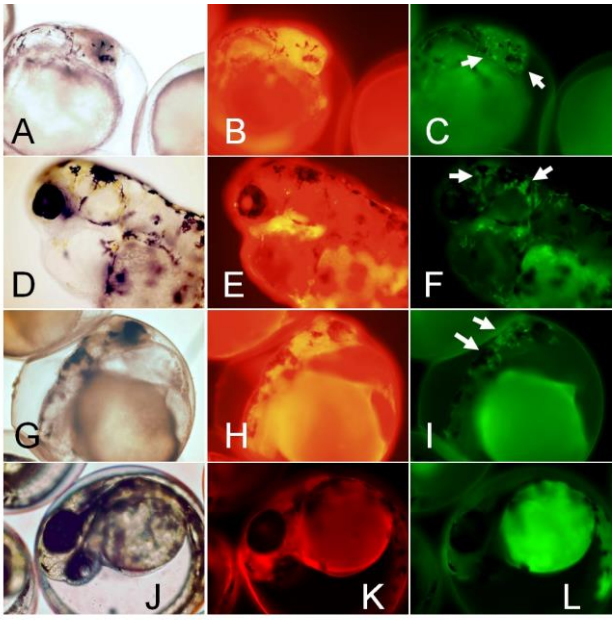

Fig. 1. Expression of mCherry and GFP in the transgenic zebrafish embryos 2 days after the irradiation with carbon ion beam (10 Gy, A, B, C), proton beam (10 Gy, D, E, F) and gamma-rays (30 Gy, G, H, I). White arrows in C, F and I indicate the cells expressing GFP which is the signal of occurence of reversion mutation. Bright field images: A, D, G, J. Red fluorescence images: B, E, H, K. Green fluorescence images: C, F, I, L. J, K and L are images of not-irradiated transgenic embryo. The zebrafish egg is approximately 0.7 mm in diameter.

References

[1] A. Noda *et al.*, PLOS ONE 10, e0136041 (2015). DOI:10.1371/journal.pone.0136041
[2] T. Watanabe-Asaka, *et al.*, Cytologia 83, 221 (2018). DOI:10.1508/cytologia.83.221

2 - 02 DNA damage foci formation after simulated-space radiation exposure

T. Oizumi[a)], T. Suzuki[a)], T. Funayama[b)] and AJ. Nakamura[a)]

[a)]College of Science, Ibaraki University
[b)]Department of Radiation-Applied Biology Research, TARRI, QST

Exposure to ionizing radiation is one of the critical concerns associated with human activities in space. Heavy ion beams with high linear energy transfer (LET) in space radiation are known to cause cluster DNA damage in which multiple DNA damage occurs within 1–2 helix turns of a DNA molecule [1]. Furthermore, radiation exposure would occur under the microgravity environment in space that might induce different responses for radiation exposure from that on the ground. Since the failure of DNA damage repair may induce genomic instability and increase the risk of developing cancer, it is important to understand the difference of DNA damage response after space radiation exposure. Therefore, in this study, we evaluate the DNA damage responses after radiation exposure by immunostaining for phosphorylated H2AX (γ-H2AX) and 53BP1 to assess the biological impact of those stresses in space.

Histone H2AX, which is a key protein in DNA repair, is rapidly phosphorylated at the site of DNA double-strand breaks (DSBs) following DNA damage induction [2-3]. Upon DNA DSB induction by ionizing radiation (IR), the accumulation of hundreds of molecules of various DNA repair proteins including γ-H2AX and 53BP1 can be visualized as a clear focus at the DNA DSB site which is known as Ionizing Radiation-Induced Foci (IRIF) [4]. The γ-H2AX foci serve as sites of accumulation of DNA repair proteins and may also induce chromatin remodeling possibly to aid access of repair proteins to the DSB sites. Therefore, the formation of γ-H2AX foci is critical for efficient DNA repair and the maintenance of genome stability.

In previous study, we analyzed the kinetics of γ-H2AX and 53BP1 foci formation after exposure of proton beam (20 MeV), helium ion beam (63 MeV) and carbon ion beam (190 MeV) that are considered as a component of cosmic rays. TIG-3 (normal human diploid skin fibroblast) were plated on chamber slides and exposed to radiation. Cells were fixed by 2% paraformaldehyde and immunostained for γ-H2AX and/or 53BP1. Carbon ion beam, which causes more complex DNA damage than the helium ion, induced a larger size of γ-H2AX foci than helium ion beam at one hour after exposure [5]. Not only one hour after the exposure, LET-dependent foci size expansion was clearly shown by four-hour post-irradiation, indicating more complex DNA damages were induced LET-dependent manner [5]. Consistent with γ-H2AX, the 53BP1 focus size at one hour after irradiation increased in a LET-dependent manner [5]. Interestingly, in the proton and helium irradiated groups, the mean 53BP1 focus size was slightly increased from 1–4 hour after irradiation [5]. It has been reported that the repair of DSBs, characterized by large 53BP1 foci, was a slow process within the biphasic kinetics of DSB repair, suggesting non-homologous end joining with error-prone end resection. Therefore, it is reasonable to assume that the LET-dependent specific DNA damage repair switching is occurred after radiation exposure.

However, the real situation of radiation exposure in the space environment would not be simple. For example, different types of radiation might expose simultaneously. Therefore, here, we evaluated whether DNA damage induction differed in the order of beams of exposure from C-ion to He-ion and He-ion to C-ion. DNA damage foci were investigated after the combination of helium ion beam and carbon ion beam exposure. TIG-3 cells were plated on chamber slides and exposed to mixed beam. As shown in Fig. 1, no difference of number of γ-H2AX foci were detected regardless the order of beam exposure. This result indicates the order of beam might not affect at least the induction of DNA damage and repair kinetics. Our data suggest that the biological effects of space radiation may be significantly influenced by the dose as well as the type of radiation exposure.

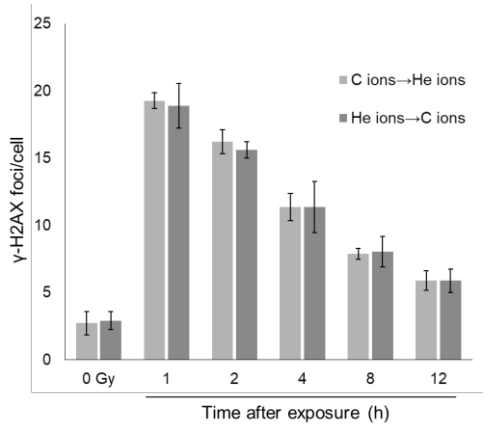

Fig. 1. Mean number of γ-H2AX foci per cell after radiation exposure.TIG-3 cells were exposed to either C-ion (0.5 Gy) to He-ion (0.5 Gy) and He-ion (0.5Gy) to C-ion (0.5Gy), and then fixed at 1hr to 12hr post irradiation. It took about 20min to switch beams. 100 cells were counted. (error bars signify SD, n=3)

References

[1] Y Lorat *et al.*, Radiother. Oncol. **121**, 154 (2016). DOI: 10.1016/j.radonc.2016.08.028
[2] E. Rogakou *et al.*, J. Cell Biol. **146**, 905 (1999). DOI: 10.1083/jcb.146.5.905
[3] E. Rogakou *et al.*, J. Biol Chem. **273**, 5858 (1998). DOI: 10.1074/jbc.273.10.5858
[4] T. T. Paull *et al.*, Curr Biol. **10**, 886 (2000). DOI: 10.1016/S0960-9822(00)00610-2
[5] T. Oizumi *et al.*, Life **10**, 341 (2020). DOI: 10.3390/life10120341

2 - 03 Precise localized irradiation of individual organisms using focused heavy ion microbeams

T. Funayama and M. Suzuki

Department of Radiation-Applied Biology Research, TARRI, QST

At QST-Takasaki, we have been developing heavy-ion microbeams for irradiating biological samples and studying the biological effects of heavy ions using these microbeams. QST-Takasaki has two microbeam devices with different microbeam formation methods: collimated microbeam and focused microbeam. The collimated microbeam has been used since 1994, and the focused microbeam was developed for precise irradiation that cannot be achieved with the collimated device [1].

Using this microbeams, we have been studying the effects of heavy-ion irradiation on a variety of organisms. One of these research categories is a research that analyzes individual functions by locally irradiating specific tissues or organs of individual model organisms with a microbeam and examining the subsequent effects.

In this research on irradiating model organisms, studies have been carried out using silkworm, Japanese medaka, and nematode worms as materials. These studies have been conducted using a collimated microbeam device that allows the change of target tissue size by changing the beam exit. However, the beam spot shape of collimated microbeam devices is circular because it uses a pinhole. Therefore, it is impossible to irradiate the entire tissue or area to be targeted with a uniform dose.

On the other hand, we have established a method of using focused microbeams to target a specific point on cultured cells or a specific cell in the central nervous system of the nematode *C. elegans* [2]. We considered that this focused microbeam could be used to irradiate a specific tissue or region of a model organism with a uniform dose over the entire target area, which is not possible with collimated microbeams. Thus, we started to develop a technology to provide such irradiation.

Irradiation that fits the shape of the area is possible with the use of a beam scanner. However, controlling the absorbed dose is complicated because the dose to the sample produced by a heavy ion hit is discrete and not continuous. For example, a single carbon ion hit with a LET of 80 kiloelectronvolts per micrometer (keV/μm) on a 2 μm square area, which is the same size as the beam spot, results in an average absorbed dose of 3.2 Gy for the area; two hits result in 6.4 Gy. No intermediate value can be taken. To achieve an intermediate value for the entire region, the area to be targeted can be divided into smaller matrices, and the number of ions irradiated in each matrix can be adjusted. Then, it becomes important to determine which matrix to exclude ions from the hits in order to provide a uniform ion hit.

To solve this problem, we developed a method for calculating hit positions in which a specified number of ions are randomly and uniformly distributed in a specified region. This method can calculate a more uniform ion distribution than the two other methods that use pseudo-random numbers, even though the distribution is random. We irradiated a CR-39 film to the ion distribution calculated by this method and confirmed that the ion hit become uniform and increased according to the specified absorbed dose.

Finally, we performed irradiation of specific organs of individual organisms. Gonads of the *C. elegans* observed under the microscope were designated and irradiated (Fig. 1A). The distribution of etch-pits on the CR-39 film that was overlapped on the irradiated sample showed the same shape as that of the gonads (Fig. 1B). From this result, it was confirmed that the developed irradiation method can be used to irradiate the targeted organs of *C. elegans* by uniformly irradiating them with the dose specified.

This technology is expected to make a significant contribution to future research using microbeams to elucidate the functions of living organisms.

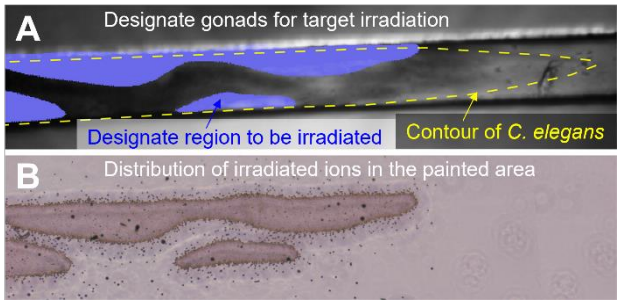

Fig. 1. Designated irradiation of *C. elegans* gonads with focused heavy-ion microbeam. (A) Observation of the anterior half-body of *C. elegans* enclosed in a straight microfluidic channel of a microfluidic chip (Worm Sheet) [3] to immobilize motion during irradiation. Gonads were designated for irradiation (painted in blue on the irradiation control software). (B) Etch-pits of carbon ions on a CR-39 film placed under the Worm Sheet.

Acknowledgments

This work was carried out in part with a JSPS KAKENHI (JP21K12247) to T.F. and the 61th research grant from the radiation effects association to M.S.

References

[1] T. Funayama, Quantum Beam Sci. **3**, 13 (2019). DOI: 10.3390/qubs3020013

[2] T. Funayama *et al.*, Nucl. Instrum. Methods. Phys. Res. B **465**, 101 (2020). DOI: 10.1016/j.nimb.2019.12.028

[3] M Suzuki *et al.*, J. Neurosci. Methods **306**, 32 (2018). DOI: 10.1016/j.jneumeth.2018.05.025

2 - 04 New trial toward the precise identification of fluorescence dots originated from oxidative damage in DNA thin sheet perpendicularly irradiated with heavy ions

A. Ito[a)], K. Urano[a,b)], A. Sudo[a)], B. Daisi[a)], S. Yoshida[a)], R. Hirayama[c)], Y. Furusawa[c)], Y. Yokota[d)] and T. Funayama[d)]

[a)]School of Engineering, Department of Nuclear Engineering, Tokai University
[b)]Nuclear Safety Research Center, JAEA
[c)]Department of Charged Particle Therapy Research, IQMS, QST
[d)]Department of Radiation-Applied Biology Research, TARRI, QST

Introduction

We have been developing the imaging method of penumbra area with low-LET nature produced by heavy ions, using an immunofluorescence method for 8-hydroxydeoxyguanosine (8-OHdG) as a representative species in OH radical induced DNA damages [1, 2, 3]. For this purpose, we adopted water insoluble DNA thin sheet made on coverglass in order to enable ion irradiation in water environment that is indispensable for the generation of OH radicals. In the previous report, for the whole fluorescence dots observed in irradiated DNA sheet, we tried to discriminate fluorescence dots produced by incident ions from background dots, by estimating the threshold level of fluorescence intensity between ion induced dots and background ones [2]. However, more precise identification of ion induced dots is definitely desired. In the present study, we made DNA sheet on CR39 plate generally used for the ion track detection, and tried to detect both 8-OHdG fluorescence dots and etch pits produced by passing ions simultaneously.

Materials and Methods

DNA thin sheet was made on CR-39 with 0.1mm thickness (HARZLAS TNF-1, Fukuvi Chemical Industry Co, Ltd., Japan) instead of cover glass as described previously [1]. After the irradiation of CR-39 with 50 MeV He ions having LET of 16.2 keV/μm at the dose of 0.135 Gy, the side opposed to that with attached DNA was put gently on the surface of etching solution (13.4 M KOH) at the temperature of 65 °C. The treatment time was surveyed from 10 min to 90 min to find the best etch pit size to observe with phase-contrast microscopy using 100 × oil immersed objective lens. Following etching, the DNA sheet was treated with the procedure of immunofluorescence method using 8-OHdG antibody (Santa Cruz Biotech. Inc., USA). The image of fluorescence dots was obtained with fluorescence microscope.

Results and Discussion

The etching time was determined as 60 min as shown in Fig. 1. The number of etch pits was counted as 0.3 dots per 5 μm square area, which is close to the estimated number of 1 dot per the same area. In addition, since the opposite side of CR-39 to beam incidence is subjected to etching, etch pits may not be formed in the case that beam is stopped in the middle of CR-39.

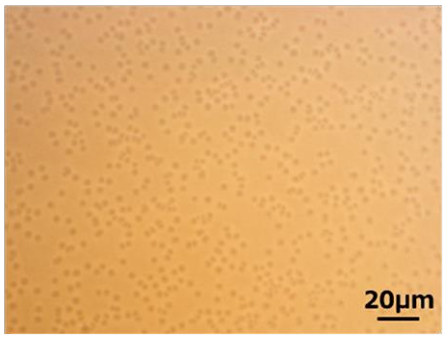

Fig. 1. Etch pits on CR-39 irradiated with He ions with an LET of 16.2 keV/μm at the dose of 0.135 Gy.

Figure 2 shows a preliminary result of a superimposed image of etch pits and fluorescence dots by the immunofluorescence treatment. Red circles indicate possible coincidence of etch pits and fluorescence dots. Unexpectedly a considerable number of fluorescence dots do not accord with the location of etch pits. Since the experimental assay condition has been established, further accumulation of data for different ion species and LETs is a next issue.

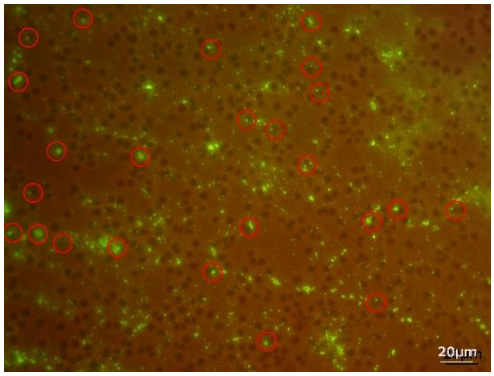

Fig. 2. Superimposed image of etch pits and fluorescence dots. Red circles show possible pair of the same position.

References

[1] A. Ito *et al*., QST Takasaki Annu. Rep. 2018 **QST-M-19**, 66 (2020).
[2] K. Urano *et al*., QST Takasaki Annu. Rep. 2019 **QST-M-23**, 84 (2021).
[3] K. Urano *et al*., QST Takasaki Annu. Rep. 2020 **QST-M-33**, 70 (2022).

2 - 05 Development of depth-controlled irradiation methods for silkworm eggs - Determination of shielding range -

N. Miyasaka[a)], Y. Soma[a)], T. Funayama[b)], M. Suzuki[b)] and K. Shirai[a)]

[a)] Faculity of Textile Science and Technology, Shinshu University
[b)] Department of Radiation-Applied Biology Research, TARRI, QST

In general, there are no (or incomplete) checkpoint systems in the early embryo of animals to carry out rapid cell (or nuclear) cleavage. However, we have reported a dose-dependent developmental delay of the silkworm (*Bombyx mori*) eggs at the early developmental stage after heavy ion irradiation. These results suggest that the silkworm egg in the early developmental stage has the developmental arrest mechanisms by checkpoints.

The maternally derived components control early embryonic development in the silkworm eggs. Moreover, the egg is a polynuclear cell (syncytium) at the cleavage stage. So, the radiation response of the eggs is quite complicated. The targeted irradiation experiments using the collimated heavy-ion microbeam of TIARA suggest that the developmental arrest of the egg is probably determined by the ratio of damaged and normal nuclei.

However, the targeted irradiation using the microbeam cannot process enough eggs, thus, we attempted to construct a new irradiation method last year. It enables expose only half of the nuclei of the egg by depth-controlled irradiation with broad field irradiation using stacked Mylar films. The irradiation using two-layer films had a significant delay in the development, but the irradiation using three-layer films did not. Nevertheless, optimal irradiation conditions have not yet been determined..

In this study, the effect of irradiation depth control was verified again with increasing the irradiation dose from 20 Gy to 100 Gy, and based on the results, the optimal thickness range of the Mylar film for depth control irradiation was determined.

Materials and Methods

The silkworm strain used in the experiments was the pigmented non-diapause strain, *pnd pS*. The silkworm eggs were collected and irradiated with 100 Gy of carbon ions (190 MeV) at broad field irradiation of HY1 port at 8 hours after oviposition. The irradiated eggs were incubated at 25°C until fixation with Carnoy's solution. Depth control of the irradiation was carried out using stacked Mylar films (100 μm/sheet). Two weeks after oviposition, unhatched eggs were fixed in hot water, and then the eggshells were removed for morphological observation.

Results and Discussion

The developmental stage of most eggs 8 hours after oviposition is cycle 7. Most of the non-irradiated control eggs fixed 4 hours after irradiation (12 hours after oviposition) reached cycle 11, and some eggs reached cycle 12 (Table 1).

On the other hand, irradiated eggs covered with two layers of Mylar film were significantly delayed in development, and many remained at cycle 7. This result is probably because the process of development stopped immediately after irradiation (Table 1). These eggs seems to be severely irradiated, and although incomplete serous membrane cells were formed, embryogenesis was not observed.

Table 1
Developmental delay of the irradiation (100 Gy of carbon ions)eggs shielding with maylar film

	developmental stage			
	cycle 5 or 6	cycle 7	cycle 11	cycle 12
control	2	8	33	10
2-layer				
3-layer			13	

On the other hand, no significant developmental delay was observed in eggs shielded with three-layer films (Table 1). However, the eggs did not hatch even after two weeks. Observation of the unhatched embryo revealed an existence of abnormalities. Most lethal embryos had the head capsule hypoplastic at either side (Fig. 1). In addition, some individuals showed the deletion of thoracic legs. These abnormalities can be seen only on one side, either left or right, so it is judged that they have been deleted by irradiation.

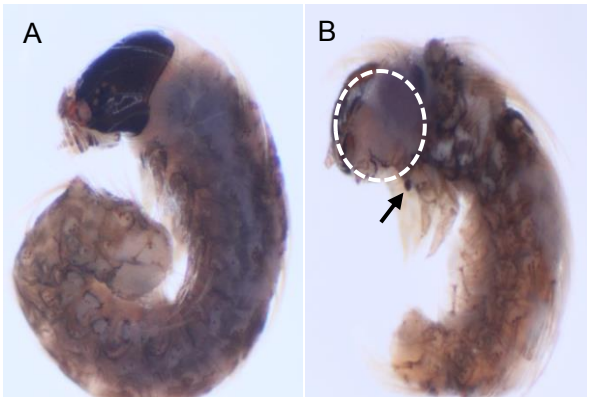

Fig. 1. Unhatched irradiated larvae (shieled with three-layer films)
A: non-irradiated larvae, B: irradiated larvae.

These studies revealed that depth-controlled irradiation for the silkworm eggs at the cleavage stage (8 hours after oviposition) was possible by shielding them with a Mylar film with a thickness of 200 μm to 300 μm. By investigating the conditions under which only the nucleus on the egg's left (or right) side can be irradiated, we will try to analyze the radiation response of the egg in which both the damaged nucleus and undamaged nucleus coexist in one cell.

2 - 06 Comparison between 190MeV $^{12}C^{6+}$ and 220MeV $^{12}C^{5+}$ ions in inducing *P-53* gene dependent bystander cell-killing effect in human tumor cell lines

M. Suzuki[a)], T. Funayama[b)] and M. Suzuki[b)]

[a)]Department of Charged Particle Therapy, IQMS, QST
[b)]Department of Radiation-Applied Biology Research, TARRI, QST

We have been studying the cellular bystander effects, such as cell killing and gene mutation, in normal human fibroblasts and tumor cell lines using the heavy-ion microbeams. In 2010 we reported the difference in bystander cell-killing effect between human tumor cell lines harboring with wild-type *P53* and mutated-type *P53* gene using 220MeV-$^{12}C^{5+}$-ion microbeams. The results clearly showed that the bystander cell-killing effect was induced in the cells harboring with wild-type *P53* gene, not mutated-type *P53* gene. Furthermore, observed bystander cell-killing effect was suppressed by treating with a specific inhibitor of gap-junction mediated cell-cell communication [1]. This year we examined the same bystander cell-killing effect in both cells with wild-type *P53* and mutated-type *P53* gene using 190MeV-$^{12}C^{6+}$-ion microbeams, and compared to the results of 220MeV-$^{12}C^{5+}$-ion microbeams.

Human adenocarcinoma cell line derived from lung cancer harboring with wild-type *P53* gene (Cell name, A549; Cell No., JCRB0076) distributed by the JCRB Cell Bank, National Institutes of Biomedical Innovation, Health and Nutrition in Japan and also human gliosarcoma cells harboring with mutated-type *P53* gene (Cell name, KNS-89; Cell No., IFO50360) distributed by the Institute for Fermentation in Japan were utilized in this study. Irradiations were carried out by the 256 (16 × 16)-cross-stripe method using C ions ($^{12}C^{6+}$, 190 MeV) at the HZ1 port [2]. The beam size was 20 μm in diameter and the irradiations in each point were performed to deliver 7 ions. Half of the sample dishes were treated with a specific inhibitor of gap-junction mediated cell-cell communication (40 μM of γ-isomer of hexachloro-cyclohexane) from 3 h before irradiation. After the irradiations, sample dishes were incubated for 3 h in a CO_2 incubator at 37 ºC, and assayed cell-killing effect, which was measured by a colony-forming assay as a reproductive cell death.

Figure 1 showed cell-killing effect in the 2 different human tumor cell lines with different *P53*-gene status irradiated with 190MeV-$^{12}C^{6+}$-ion microbeams, comparing to 220MeV-$^{12}C^{5+}$-ion microbeams. The surviving fraction in the cells harboring with wild-type *P53* gene (A549) in microbeam-irradiated dishes without the gap-junction inhibitor (IR) was approximately 0.90, while almost 1.0 was observed in microbeam-irradiated dishes with the gap-junction inhibitor (L+IR). On the other hand, the surviving fraction in the cells harboring with mutated-type *P53* gene (NKNS-89) was the same at 1.0 between IR and L+IR. Using the 256 (16 × 16)-cross-stripe method, the estimated percent of carbon-ion direct hit cells was approximately 0.032% of all cells in the dish. The surviving fraction were markedly less than expected, assuming that only carbon-ion direct hit cells (0.032%) were killed in the cells irradiated with both 220MeV-$^{12}C^{5+}$-ion and 190MeV-$^{12}C^{6+}$-ion microbeams. The obtained results showed that bystander cell-killing effect induced by 190MeV-$^{12}C^{6+}$-ion microbeams was observed in tumor cells harboring with wild-type *P53* gene, but not in *P53*-mutated tumor cells as well as 220MeV-$^{12}C^{5+}$-ion microbeams. Furthermore, observed bystander effect was suppressed by treating with the specific inhibitor of gap-junction mediated cell-cell communication. There is evidence that both *P53*-mediated cellular response and gap-junction-related bystander effect are an important role of carbon-ion induced bystander cell-killing effect. It is consistent with the data using 190MeV-$^{12}C^{6+}$-ion and 220 MeV $^{12}C^{5+}$-ion microbeams.

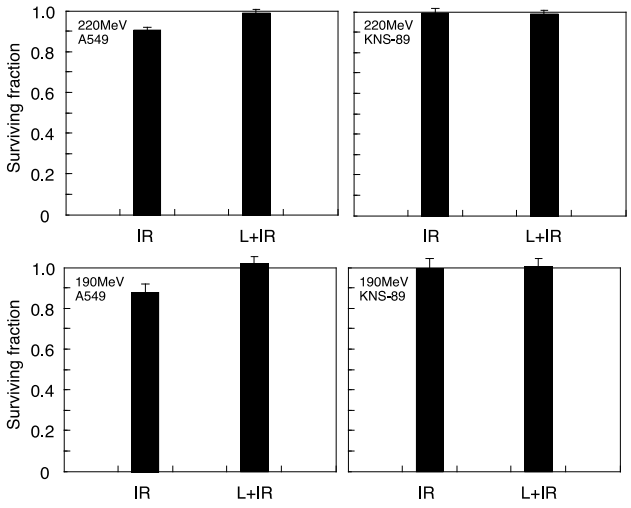

Fig. 1. Bystander cell-killing effect in the 2 different human tumor cell lines with different *P53*-gene status. Upper graphs showed with 220MeV-$^{12}C^{5+}$-ion microbeams taken from [1] and lower graphs were the result of the 2021 report. Cells were irradiated with carbon-ion microbeams treated with (L+IR) / without (IR) a specific inhibitor of gap-junction mediated cell-cell communication. The results were the means and standard errors from 6 independent beam times for 220MeV-$^{12}C^{5+}$ ions and the means and standard errors from 2 independent beam times for 190MeV-$^{12}C^{6+}$ ions.

References

[1] M. Suzuki *et al*., JAEA Takasaki Ann. Rep. 2009 **JAEA-Review 2010-065**,92 (2011).
[2] M. Suzuki *et al*., JAEA Takasaki Ann. Rep. 2006 **JAEA-Review 2007-060**,107 (2008).

2 - 07 Basic study of immunoradiation therapy using anti-PD-L1 antibody

T. Hara[a], T. Funayama[b], H. Sato[c], Y. Nakagami[d], Y. Suzuki[e] and T. Ohno[c]

[a]Department of Radiological Technology, Gunma Prefectural College of Health Sciences
[b]Department of Radiation-Applied Biology Research, TARRI, QST
[c]Department of Radiation Oncology, Gunma University Graduate School of Medicine
[d]Department of Radiology, Dokkyo Medical University
[e]Department of Radiation Oncology, Fukushima Medical University School of Medicine

Background and Objectives

The current development of immunotherapy has been remarkable; among them, treatment using immune checkpoint inhibitors has attracted attention. Among these immune checkpoint inhibitors, there is anti-PD-L1 antibody. It has been suggested that the expression of PD-L1 is related not only to the immune evasion mechanism of tumor cells, but also to the viability and proliferation of tumor cells themselves [1]. In addition, recent studies have shown that the PD-L1 pathway is associated with DNA repair pathways and radiosensitivity [2]. Therefore, we hypothesized that the PD-L1 pathway might be a target for radiosensitizing effects.

Material and Methods

A mouse melanoma cell line, B16, was used in the experiments. First, the cell killing effect of the drug alone was examined using the alamer blue assay. The concentration of the drug in combination with radiation was determined from the graph of the cell killing effect of the drug alone. The combined effect of radiation and drug was examined using the colony formation assay. The protocol for the combined use of radiation and drug was as follows: pre-treat, in which the drug was added 24 hours before irradiation, and post-treat, in which the drug was added 24 hours after irradiation (Fig.1).

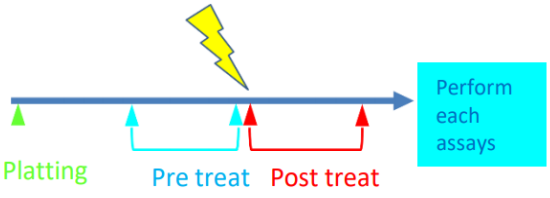

Pre treat : cell cultures treated with drug for 24 hours before irradiation
Post treat : cell cultures treated with drug for 24 hours after irradiation

Fig. 1. Protocol for irradiation procedure.

Irradiation was carried out using ^{60}Co gamma-ray facility of QST-Takasaki. Radiation dose irradiated was in range of 1-8 Gy.

Results

Treatment of B16 cells with anti PD-L1 antibody resulted in dose-dependent manner inhibition of cell survival. A drug concentration that resulted in approximately 20% inhibition of cell viability was 0.015 ㎎/ml for B16 cells. (Fig.2)

The influence of anti PD-L1 antibody on radiosensitivity was examined with three different drug treatment: pre-treat, post-treat and without treat (RT). Anti PD-L1 antibody increased the Increase of cytotoxic effects of radiation was observed only in pre-treat. (Fig.3)

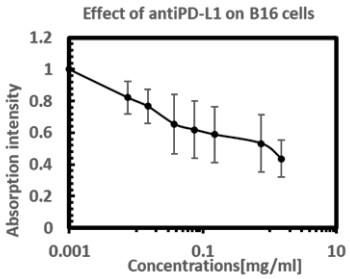

Fig. 2. Effect of anti PD-L1 antibody (Alamer Blue assay).

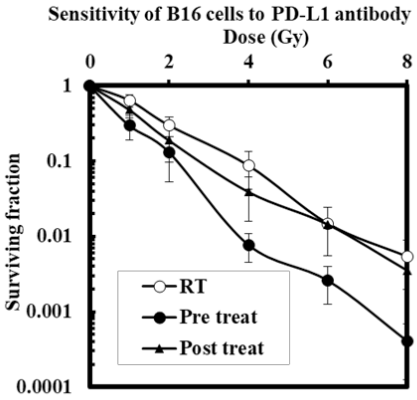

Fig. 3. Effect of anti PD-L1 antibody on radiosensitivity (colony formation assay).

Conclusion

The radiosensitizing effect observed in this study is considered to have been caused by suppressing PD-L1 expressing B16 with an anti-PD-L1 antibody. Our data suggest that targeting the PD-L1 pathway with an immune checkpoint inhibitor can produce a radiosensitizing effect.

Acknowledgments

This work was supported in part by JSPS KAKENHI Grant Number JP19K08182.

References

[1] J. Li *et al.* Cell Physiol Biochem. **41**, 907 (2017). DOI: 10.1159/000460504
[2] A. V. R. Kornepati *et al.* Cancer Res. **82**, 2156 (2022). DOI: 10.1158/0008-5472.CAN-21-2076

2 - 08 Efficient dose of carbon ion beam irradiation for azalea seeds

K. Ureshino[a], K. Satoh[b] and Y. Oono[b]

[a]Faculty of Agriculture, University of the Ryukyus
[b]Department of Radiation-Applied Biology Research, TARRI, QST

Introduction

Evergreen azaleas are one of the representative ornamental woody plants. The flower colors of cultivated varieties are mainly variations of white, pink, red, or purple. However, no yellow-flowered cultivar of evergreen azaleas has been produced till date.

R. japonicum f. *flavum* is a yellow-flowered deciduous species belonging to the subgenus Pentanthera [1]. The yellow petals contain carotenoid compounds such as β-carotene and lutein as the main pigments [2]. To create yellow-flowered evergreen azaleas, we have conducted intersubgeneric three-way crosses between an interspecific hybrid of white-flowered evergreen azaleas ('Miyamasatsuki') and *R. japonicum* f. *flavum* (a yellow-flowered deciduous species belonging to the subgenus Pentanthera). The petal color of the buds on the progenies was light yellow just before anthesis, and these petals contained carotenoid pigments [3]. However, the light-yellow color of the petals was not stable, and it faded as the flower developed. Carotenoid degradation in the petals of the progeny was mediated by a high *CCD4* gene expression inherited from white-flowered evergreen azalea [2]. Inactivation of *CCD4* gene during petal development is useful to avoid discoloration of petals in the progenies.

Heavy-ion beam irradiation is one of the useful methods for inactivation of target genes. We previously investigated seed germination test with seeds irradiated with various doses (8.3, 25, 50 and 83 Gy) of carbon ion beam [4]. Germination rate of seeds and frequency of green plant appearance were not significantly different among treatments. On the other hands, survival rates of seedlings significantly decreased at 83 Gy. The present study was conducted to clarify an efficient dose of carbon ion beam irradiation for azalea seeds in more detail.

Materials and methods

Seeds from the three-way crosses between a white-flowered evergreen hybrid from *R. kiusianum* × *R. eriocarpum* ('Miyamasatsuki') and yellow flowered deciduous species, *R. japonicum* f. *flavum* were used. They were irradiated with various doses (0, 5, 15, 30 and 50 Gy) of the 320 MeV carbon ion ($^{12}C^{6+}$) accelerated by a TIARA AVF cyclotron. After irradiation, seeds were sterilized in 5 % sodium hypochlorite solution for 15 min followed by three washes in sterile distilled water. After sterilizing, about 100 seeds were sown on the petri-dish (ø 9.0 cm) filled with 25 mL of Anderson's rhododendron medium [5] supplemented with 30 g·l^{-1} sucrose having pH 5.0 and solidified with 3.5 g·l^{-1} gellangum. Three replicates were conducted per each treatment. The cultures were incubated at 25 °C in a growth chamber in the light (ca. 44.73 μmol·sec^{-1}·m^{-2}) of 16 h daylength. After one month, the germination rate and leaf color of progenies were observed. The seedlings were then, transplanted into the medium with 10 mg·l^{-1} of N6-(2-isopentenyl) adenine (2ip) to induce multiple shoots. After one month, survival rate of seedlings was observed.

Derived shoots were cut into a sphagnum moss to induce roots at the same environmental conditions. Rooted plants were planted in pots containing Kanuma soil, and cultured at non heated glass house.

Results

Germination rate of seeds, frequency of green plant appearance and survival rates of seedlings were not significantly different among treatments from 0 to 30 Gy (Table 1). On the other hands, germination rate and survival rates significantly decreased at 50 Gy. From this, the efficient dose was considered to be 30Gy.

Seedlings from previous investigation were cultured in a non-heated glass house. Their plant height was about 20cm, but differentiation of floral organ has not been yet (Fig. 1). In future, we will check the flower color and carotenoid content of them.

Table 1
Effect of carbon ion beam irradiation on seed germination, leaf color and survival rate of seedlings.

Dose (Gy)	% of germination	% of green plant appearance	% of seedlings survived
0	45.3[a]	52.2[a]	86.2[a]
5	48.1[a]	57.4[a]	78.9[a]
15	53.1[a]	57.9[a]	85.5[a]
30	49.4[a]	45.1[a]	63.9[a]
50	33.7[b]	44.1[a]	53.6[b]

Values marked with different letters indicate statistically significant difference (Tukey's test, 1 % significance).

Fig. 1. Seedlings which were irradiated with various doses of ion beam.

References

[1] T. Yamazaki, A revision of the genus Rhododendron in Japan, Taiwan, Korea and Sakhalin. Kokusai Bunken Insatsusha, Tokyo. (1996).
[2] K. Ureshino *et al.*, Euphytica. **207**, 401 (2016). DOI 10.1007/s10681-015-1557-2
[3] I. Miyajima *et al.*, J. Jpn. Soc. Hort. Sci. **69**, 280 (2000). DOI: 10.2503/jjshs.69.280
[4] K. Ureshino *et al.*, QST-Takasaki Annu. Rep. 2020 **QST-M-33**, (2021).
[5] W.C. Anderson, J. Amer. Soc. Hort. Sci. **109**, 343 (1984). DOI: 10.21273/JASHS.109.3.343

2 - 09 Effect of carbon ion-beam irradiation on growth and mutation spectra of *Physcomitrium patens*

Y. Yokota, K. Satoh and A. N. Sakamoto

Department of Radiation-Applied Biology Research, TARRI, QST

Introduction

We have previously shown that the moss (*Physcomitrium patens*) cells are 200-fold more resistant to γ-rays than mammalian cells [1], and suggested that *P. patens* has an efficient repair mechanism for DNA double strand breaks (DSBs). In mammal, DSB can be repaired by non-homologous end-joining (NHEJ), alternative end-joining (Alt-EJ), or homologous recombination (HR). To examine if any of these pathways contribute to the radioresistance of *P. patens*, we have created the knock-out (KO) plants for *LIG4*, *POLQ*, *RAD51B*, which respectively play major roles in NHEJ, Alt-EJ, and HR.

In our previous growth analysis of γ-ray irradiated *P. patens*, no difference was detected among wildtype (WT), *LIG4*-KO and *POLQ*-KO plants [2]. However, a drastic reduction of growth was shown in *RAD51B*-KO plants. Moreover, γ-irradiation to *RAD51B*-KO plants frequently induced complex mutations at adenine phosphotransferase (*APRT*) allele [2].

To analyze the responses of these mutants to DSB, further, here we irradiated WT, *LIG4*-, *POLQ*-, and *RAD51B*-KO plants with carbon ion-beams and analyzed the effect on the growth and mutation spectra.

Materials and methods

WT, *lig4-1*, *polq-1*, and *rad51b-1* were provided by F. Nogué. Six-day-old tissues grown on BCDAT [3] plates were irradiated with 220 MeV carbon ions (LET = 108 keV/μm). To measure the radioresistance, the irradiated tissue was grown for another 6 days, then dried and weighted. For mutation analysis, the irradiated tissue was further grown on 2-fluoriadenine (2-FA)-containing BCDAT plates for 3-4 weeks. DNA was extracted from 2-FA resistant colonies to detect mutation at *APRT* allele. Statistical significance was assessed by Poisson test.

Results and discussion

While *LIG4*-KO and *POLQ*-KO lines showed no or little reduction of dry weights as compared to WT, *RAD51B-KO* line showed drastic reduction of the dry weight (Fig. 1). This result implies that the *P. patens* mostly depends on HR to repair DSBs induced by carbon ions. The slight reduction of the growth of *polq-1* with high dose may suggest that the alt-EJ pathway is used in part when excess DSBs are present.

For mutation analysis the doses that reduce the dry weight by half (100 Gy for WT and *lig4-1*, 70 Gy for *polq-1*, and 3.5 Gy for the *rad51b-1*) were used. Mutations in each line were classified into transition, transversion, insertion or deletion (In/Del) or complex mutation, and mutation frequencies were calculated by dividing the 2-FA resistant cell number with the total cell number (Fig.2). Total mutation frequencies in WT, *lig4-1*, and *rad51b-1* were comparable, but slightly lower in *polq-1* ($p<0.05$). In addition, *rad51b-1* showed no transition ($p<0.05$). It may imply that different DNA polymerases are employed in HR and other repair pathways.

Further analyses using double or triple KO lines will unveil the secret of radioresistance of *P. patens*.

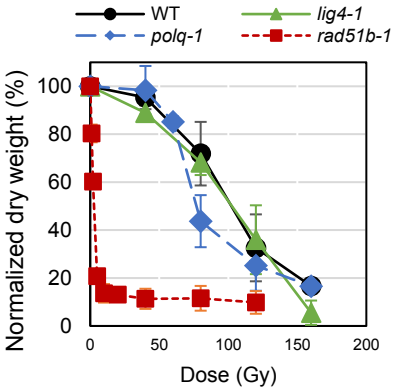

Fig. 1. Effect of carbon ion-beam irradiation on growth of WT and DSB-repair deficient plants. Data represent the mean ± SD of more than three independent experiments.

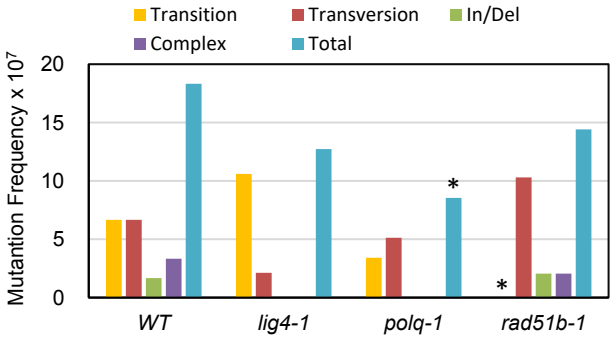

Fig. 2. Summary of mutations induced by carbon ions in WT and DSB repair deficient mutants. * $p < 0.05$ compared with WT

Acknowledgments

We thank F. Nogué for providing materials. We also thank N. Maeda, Y. Yanagawa for their technical support.

References

[1] Y. Yokota and A.N. Sakamoto, Genes **9**, 76 (2018). DOI: 10.3390/genes9020076

[2] A. N. Sakamoto *et al.*, JRRS 65, Abstracts, 146 (2022).

[3] https://moss.nibb.ac.jp/

2 - 10 Mutagenesis of the oil-producing algae by heavy ion irradiation

H. Araie[a)], Y. Hase[b)], Y. Iwata[c)], Y. Oono[b)] and I. Suzuki[d)]

[a)]Department of Biosciences, Kanto Gakuin University College of Science and Engineering
[b)]Department of Radiation-Applied Biology Research, TARRI, QST
[c)]Research Institute for Advanced Electronics and Photonics, AIST
[d)]Faculty of Life and Environmental Sciences, University of Tsukuba

There are high expectations for Carbon dioxide Capture, Utilization, or Storage (CCUS) technology development toward the realization of a carbon-neutral and decarbonized society in 2050. Among them, regarding the effective utilization of CO_2, the practical application of biofuels produced by photosynthetic organisms, especially microalgae, is attracting attention because it does not compete with food production. However, it is necessary to improve and create useful strains, which have high oil content or high growth rate and are more suitable for oil production. In this study, we focused on very-long-alkyl ketones so-called alkenones (Fig. 1), which are thought to be good candidates for biofuels [1]. There are 5 haptophyte species known to produce alkenones. Among them, we selected *Tisochrysis lutea* (Strain T-Iso), because some molecular biotechnological methods and information are available [2, 3]. In sake yeasts, it is reported that mutants with enhanced fatty acid synthesis were obtained by adding cerulenin to the medium after heavy ion beam irradiation [4]. Therefore, we added cerulenin to the samples during heavy ion beam irradiation to get mutants with enhanced alkenone synthesis. Previously, we reported the screening results of high oil-producing mutants by monitoring the lipid fluorescence intensity for mutants obtained above experiments [5].

Here, we analyzed alkenone amounts of 61 high oil-producing mutants obtained from previous screening [5]. As the result, 5 mutants with high-alkenone productivity and 2 mutants with a high-alkenone amount per cell were picked up. These mutants will be candidates for the analysis of alkenone biosynthesis and production.

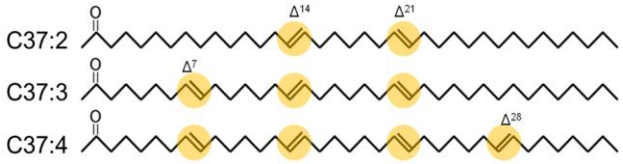

Fig. 1. Alkenone structures. The carbon number of these alkenones is 37 and they have two to four *trans*-type double bonds and a keto group at a C2 position.

In this experiment, 61 high oil-producing mutants obtained from previous screening were grown in 50 mL plastic flasks containing the 20 mL MA-ESM medium. All cultures were maintained for 2 weeks in the algal growth chamber where continuously illuminated at the intensity of 100 µmol photons m^{-2} s^{-1} and temperature was controlled at 22 °C. The total lipid content of cells was extracted with methanol and dichloromethane and analyzed in alkenone amounts by GC-FID [6].

As the results, 2 mutants (red circles) showed 3.5 to 4.5 times higher alkenone amount per cell than the wild type (Fig. 2A). However, these 2 mutants showed almost the same alkenone productivity as the wild type (Fig. 2B). On the other hand, 5 mutants (orange circles) showed 1.5 to 2.2 times higher alkenone amount per cell than the wild type (Fig. 2A) and 1.3 times higher alkenone productivity than the wild type (Fig. 2B). Overall, many mutants showed a little bit higher alkenone amount per cell than wild type. But only a few mutants showed higher alkenone productivity. These results suggested that it is difficult to improve the balance between lipid accumulation and growth. However, the possibility was shown that the balance can be improved by heavy ion beam irradiation.

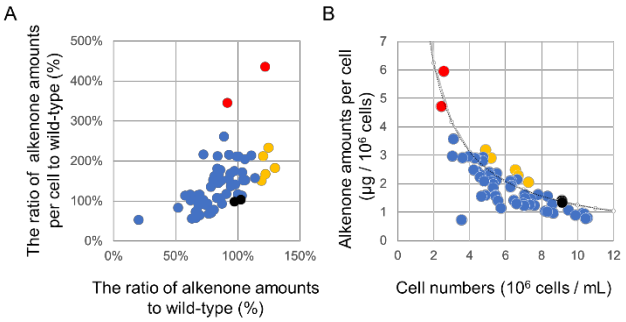

Fig. 2. The alkenone amounts and productivity of mutants to wild type. (A) The ratio of alkenone amounts per cell and alkenone amounts to wild type. (B) The relationship between alkenone amounts per cell and cell numbers. Black, orange and red circles indicate wild types, 5 mutants with high-alkenone productivity, and 2 mutants with a high-alkenone amount per cell, respectively. The dash line indicates alkenone productivity of wild type.

References

[1] G. W. O'Neil *et al.*, Energy Fuels **29**, 922 (2015). DOI: 10.1021/ef502617z
[2] H. Endo *et al.*, Sci. Rep. **8**, 11230 (2018). DOI: 10.1038/s41598-018-29482-8
[3] G. Carrier *et al.*, Algal Res. **29**, 1 (2018). DOI: 10.1016/j.algal.2017.10.017
[4] T. Masubuchi *et al.*, Bioindustry **30**(7), 65 (2013)
[5] H. Araie *et al.*, QST Takasaki Annu. Rep. 2020 **QST-M-33**, 81 (2020).
[6] H. Araie *et al.*, Org. Geochem. **121**, 89 (2018). DOI: 10.1016/j.orggeochem.2018.04.008

2 - 11 Genome analysis of the low cesium-accumulating mutants of *Rhodococcus qingshengii* CS98 generated by ion beam breeding

K. Satoh[a)], S. Ozawa[b)], H. Hayashi[b)] and Y. Oono[a)]

[a)]Department of Radiation-Applied Biology Research, TARRI, QST
[b)]Faculty of Engineering, Maebashi Institute of Technology

Bioremediation uses biological organisms to solve an environmental problem, which draws attention as a technology with a low environmental burden compared with physical and chemical technologies. Microorganisms were often used for developing a technology to remove and recover contaminated environments. *Rhodococcus erythropolis* CS98 was isolated from soil as a cesium (Cs)-accumulating bacteria [1]. *R. erythropolis* CS98 is expected to be useful for removing radioactive Cs from contaminated environments for bioremediation purposes. Recently, this strain was reclassified as *Rhodococcus qingshengii* CS98 based on the results of the average nucleotide identity analysis [2], and its complete genome sequence has been revealed [3]. However, the mechanisms of Cs-accumulation in *R. qingshengii* CS98 are still incompletely understood. In the previous study, we had generated low Cs-accumulating mutants by irradiation of carbon ion beams ($^{12}C^{5+}$, 220 MeV, 121.8 keV/μm) accelerated by an AVF cyclotron at TIARA [4]. In this study, we did comparative genome analysis to reveal the genes responsible for the Cs-accumulating mechanisms.

The whole genome sequence was performed using genomic DNA from two low Cs-accumulating mutants (named No.5 and 6) that showed below 20% lower the intracellular Cs concentration than that of the parental strain (CS98) [4]. Sequencing libraries were prepared using the KAPA HyperPlus Kit (Nippon Genetics) and IDT for Illumina TruSeq DNA UD Indexes (Illumina). The libraries were sequenced on an Illumina NextSeq500 platform and 150 bp paired-end reads were generated. The raw sequencing reads were cleaned using Illumiprocessor (ver. 2.0.9), and the cleaned data were mapped to the reference sequence of *R. qingshengii* CS98 using BWA (ver. 0.7.5), SAMtools (ver. 1.3.4), and Picard-tools (ver. 1.119). The candidate mutation sites were identified using GATK HaplotypeCaller (ver. 4.1.8), pindel (ver. 0.2.4), and BreakDancer (ver. 1.4.5) algorithms. The candidate mutations detected at the same position and mutation type in both samples were excluded as false positives. The candidate mutation sites were considered as unique and fixed mutations if allele frequencies (proportion of mutant reads at a site) were higher than 80%. All candidate mutations were confirmed with Integrative Genomics Viewer (ver. 2.4.10). The candidate mutations were confirmed by further Sanger sequencing of the PCR-amplified products.

The mutant No.5 genome had a G:C to T:A transversion at position 1,613,922 bp, a C:G to T:A transition at position 1,822,937 bp, and simple inversion between 1,79,110 and 3,616,436 bp (Table 1). The two point mutations caused missense mutations in permerase and elongation factor Tu genes. The junction of simple inversion caused frameshift mutations of hypothetical protein and TetR family transcriptional regulator genes. On the other hand, the mutant No.6 had a T:A to C:G transition at position 3,616,395 bp and a large structural variant (SV) contained an inversion with 2 deletions between 4,171,397 to 4,382,535 (Table 1). The point mutation caused missense mutations in TetR family transcriptional regulator gene. The large SV caused frameshift mutations of luciferase-like monooxygenase, MBL fold metallo-hydrolase and fructose-1,6-bisphosphatase genes. From the comparative genome analysis, the mutation of TetR family transcriptional regulator was detected in the two low Cs-accumulating mutants in common, indicating that this protein is involved in Cs-accumulating mechanisms of *R. qingshengii* CS98. The TetR-family transcriptional regulators are known as DNA binding factors that regulate gene expression in bacteria. Further analysis of the factors regulated by the TetR-family transcriptional regulators will be necessary to elucidate the molecular basis of Cs-accumulation mechanisms.

Table 1
Mutation sites in low Cs-accumulating mutants.

Mutant	Position	Type	REF	ALT	Gene description
No.5	1,613,922	SBS	G	T	Permerase
	1,822,937	SBS	C	T	Elongation factor Tu
	1,79,110 to 3,616,436	INV	–	–	Hypothetical protein & TetR family transcriptional regulator
No.6	3,616,395	SBS	T	C	TetR family transcriptional regulator
	4,171,397 to 4,382,535	DEL + INV	–	–	Luciferase-like monooxygenase & MBL fold metallo-hydrolase & Fructose-1,6-bisphosphatase

REL, reference nucleotide; ALT, altered nucleotide; SBS, single base substitution; DEL, deletion; INV, inversion.

References

[1] N. Tomioka *et al*., Appl. Environ. Microbiol. **58**, 1019 (1992). DOI: 10.1128/aem.58.3.1019-1023.1992.
[2] C. Raeburn *et al*., Biotechnol. Rep. **25**, e00415 (2020). DOI: 10.1016/j.btre.2019.e00415
[3] K. Satoh *et al*., Microbiol. Resour. Announc. **9**, e01188-20 (2020). DOI: 10.1128/MRA.01188-20.
[4] K. Satoh *et al*., QST Takasaki Annu. Rep. 2016 **QST-M-8**, 105 (2018).

2 - 12 Pilot-scale sake brewing tests using non-urea producing Gunma KAZE3 yeast bred by ion-beam mutagenesis

T. Watanabe[a)], M. Yanagisawa[a)], K. Satoh[b)] and Y. Oono[b)]

[a)]Gunma Industrial Technology Center
[b)]Department of Radiation-Applied Biology Research, TARRI, QST

Gunma KAZE yeasts, bred for ginjyo-sake brewing, are utilized in many sake-manufactures of Gunma prefecture. In Japanese sake, urea is a main precursor of ethyl carbamate which is classified in the group 2A "probably the cause of cancer" by International Agency for Research on Cancer. We previously bred non-urea producing Gunma KAZE1 yeast (KAZE1-Arg) by natural mutation and Gunma KAZE2 yeast (KAZE2-Arg) by ion-beam irradiation ($^{12}C^{5+}$, 220 MeV) accelerated by an AVF cyclotron at TIARA [1]. We also attempted to breed a non-urea producing yeast from Gunma KAZE3 yeast by ion-beam irradiation. By modifying the selecting condition, we succeeded to isolate six candidates that did not produce urea [2]. In this study, we tried select non-urea producing KAZE3 for practical use.

We first performed the laboratory scale sake brewing experiment using 1 kg of total rice, and sensory evaluation. From six candidates, KAZE3-2-2 and KAZE3-7-4 were selected as non-urea producing KAZE3 candidates (data not shown). Pilot-scale sake brewing tests were performed using 72 kg of total rice (40% polishing of Yamadanishiki). Koji making was performed using a seed koji, High-G (Higuchi Matsunosuke Shoten). Wild type KAZE3 and two candidates were pre-incubated in 18 mL of Koji-extracts at 23 °C for 4 d. Sokujyo seed mash was made using 1.2 kg of koji, 2.4 kg of steamed rice, 28.8 mL of lactic acid, 18 mL of pre-culture, and 4.8 L of tap water. Three-step preparation (soe, naka, and tome) for fermentation mash was performed. KAZE3 produced 10.7 mg/L of urea in sake brewing while two candidates did not. KAZE3-2-2 produced lower and higher amounts of isoamyl alcohol and ethyl caproate, respectively than KAZE3. Ethanol productivity of KAZE3-7-4 was lowest in the three strains (Table 1). Therefore, we will perform practical scale brewing tests using KAZE3-2-2.

Acknowledgments

This study was supported by Dr. Yoshifumi Jigami Memorial Fund, The Society of Yeast Scientists and the grant of Kenkyuukaihiatsu-suishinhi from Gunma prefecture.

References

[1] T. Watanabe *et al.*, QST Takasaki Annu. Rep. 2018 **QST-M-23**, 81 (2019).
[2] T. Watanabe *et al.*, QST Takasaki Annu. Rep. 2020 **QST-M-33**, 82 (2021).

Table 1
Fermentation profile of KAZE3 and two candidates with pilot-scale sake fermentation test.

KAZE3 (wild type)	Fermentation mash												Sake
	4d	6d	8d	11d	13d	15d	18d	20d	22d	25d	27d	28d	
Ethanol (%)	2.4	4.1	6.8	10.8	12.4	13.8	15.4	15.9	16.4	16.9	17.2	-	17.0
Acidity (mL)	0.8	0.7	1.1	1.2	1.2	1.4	1.5	1.5	1.5	1.5	1.6	-	1.4
Glucose (%)	6.7	5.3	3.6	1.9	1.1	0.9	0.4	0.4	0.3	0.3	0.3	-	0.5
Isoamyl acetate (ppm)	0.1	0.1	0.1	1.2	1.5	1.8	2.1	2.2	2.3	2.2	2.3	-	1.7
Ethyl caproate (ppm)	1.3	1.5	2.9	4.3	4.7	5.7	5.8	6.8	6.9	6.7	6.9	-	4.5

KAZE3-2-2	Fermentation mash												Sake
	4d	6d	8d	11d	13d	15d	18d	20d	22d	25d	27d	28d	
Ethanol (%)	2.6	4.7	7.3	11.2	13.0	14.4	15.7	16.5	17.0	17.5	-	-	16.8
Acidity (mL)	0.9	0.9	1.2	1.3	1.6	1.7	1.8	1.8	1.7	1.9	-	-	1.7
Glucose (%)	6.6	5.3	4.0	2.2	1.6	1.2	0.8	0.7	0.6	0.6	-	-	1.1
Isoamyl acetate (ppm)	0.1	0.1	0.1	0.9	1.0	1.2	1.4	1.6	1.6	1.7	-	-	1.3
Ethyl caproate (ppm)	0.1	0.8	2.9	7.8	9.3	10.3	11.2	12.5	12.2	12.5	-	-	7.7

KAZE3-7-4	Fermentation mash												Sake
	4d	6d	8d	11d	13d	15d	18d	20d	22d	25d	27d	28d	
Ethanol (%)	1.8	3.3	5.9	10.7	12.4	13.5	14.9	15.4	15.9	16.3	16.4	16.4	16.5
Acidity (mL)	0.7	0.7	0.7	1.0	1.2	1.2	1.3	1.2	1.2	1.3	1.4	1.4	1.2
Glucose (%)	7.1	6.7	4.2	1.0	0.6	0.4	0.3	0.3	0.3	0.3	0.3	0.3	0.4
Isoamyl acetate (ppm)	0.1	0.1	0.1	2.1	2.9	3.5	4.0	3.8	3.8	3.8	3.8	3.6	2.4
Ethyl caproate (ppm)	0.9	1.0	2.2	4.6	5.5	6.0	6.2	6.0	6.1	6.2	6.4	6.3	4.2

2 - 13 Growth curve analysis of *Bacillus subtilis* spores to evaluate damage and growth inhibition by ion-beam and gamma Irradiations

K. Tatsumoto[a)], R. Asada[a)], JJ. Sakamoto[b)], T. Tsuchido[b)],M. Furuta[a)], K. Satoh[b)] and Y. Oono[b)]

[a)]Quantum Radiation Engineering, Graduate School of Osaka Metropolitan University
[b)]Research Center of Microorganism Control, Organization for Research Promotion, Osaka Metropolitan University
[c)]Department of Radiation-Applied Biology Research, TARRI, QST

Introduction

Bacillus spores are more resistant to physical and chemical stress than their vegetative cells due to their unique layered structure with dehydrated interior, making spore control a critical issue in decontamination of foods and sterilization of medical products. In order to effectively use radiation sterilization for food and medical supplies, it is essential to clarify the radiation resistance of the spores and to clarify the characteristics of irradiation in comparison with other sterilization methods. In particular, it is still unclear whether damaged bacteria, i.e., cell populations that are damaged by sterilization but regain viability under certain conditions, may also emerge after various radiation treatment with different LET including high energy ion beams. The relationship between the level of damaged bacteria and the level of mutant emergence is also unknown.

To gain insight into the growth retardation and emerging injured cells among the survivors during developing process from *B. subtilis* spores to vegetative cells after γ-irradiation and ion beam irradiation with different LETs, we evaluated the presence of injured bacteria by the differential viability method (DiVSaL method) [1]. At the same time, the mutation rate was also examined.

Experimental methods

B. subtilis 168 *(trpC2)* spores were prepared with Schaeffer's medium and obtained according to the method of Koshikawa [2]. The spores were suspended in 50 mM potassium phosphate buffer (KPB) containing 0.1% Tween 80 and irradiated with ^{60}Co γ-rays (0-6 kGy) at the Radiation Research Center, Osaka Metropolitan University, and with $^{4}He^{2+}$ (50 MeV; 19.4 keV/μm) $^{12}C^{6+}$ (190 MeV; 148.7 keV/μm), and $^{20}Ne^{8+}$ (350 MeV; 440.8 keV/μm) ion beams were irradiated at TIARA, TARRI, QST. The number of surviving spores (CFU) was determined by the plate counting method, in which the spores were appropriately diluted in KPB, incubated on LB agar plates and the colonies generated were counted. The difference between irradiated and unirradiated was compared by the DiVSaL method [1] to estimate the quantity of the damaged bacteria, in which the number of viable spores (CFU) was determined by the colony counting method. The same spores were then suspended in liquid LB medium, and changes in turbidity were tracked over time using a microplate reader to monitor growth retardation. Converted viability (IV) was determined by the DiVSaL method [2], and the difference between IV and CFU determined by the colony coefficient method was used to enumerate injured bacteria. The detection and quantification of Rifampicin (50 μg/ml) resistant mutants were evaluated by the appearance of colonies after incubation on agar medium containing the drug.

Results and Discussions

The killing effect of ion beam irradiation of spores with different LETs showed a LET-dependent loss of colony forming ability as previously reported [3]. Analysis by DiVSaL method also showed the reproducible results (Fig. 1), in which injured cell population, enumerated by the difference between IV and CFU, tended to increase with increasing RBE according to the LET of ion species used for irradiation, suggesting that high-LET ion beams might cause more lethal damage to the genome DNA and DNA repair deficiency might be relating to the occurrence of the injured cell population. Mutation rate was not correlated with the LET although more investigations are needed.

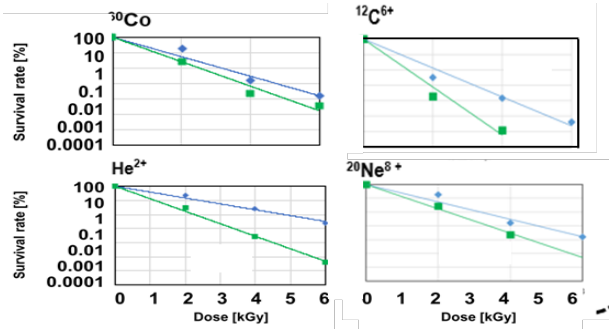

Fig. 1. Evaluation of injured fraction of survivors of *B. subtilis* following ^{60}Co- and high LET ion-beam irradiation by DiVSal method. Difference of survival rate values at each dose shows the injured cell fractions.
●:Survived and recovered cell fraction from injured state by culturing on the LB agar media obtained CFU.
■:Surviving cell fraction without injure determined by DivSal methods.

References

[1] T. Tsuchido, Biocontrol Sci. **22**, 131 (2017). DOI: 10.4265/bio.22.131
[2] F. Koshikawa, RADIOISOTOPES **43**, 710 (1994). DOI: 10.3769/radioisotopes.43.11_710
[3] H. Den, QST Takasakai Annu. Rep. 2019 **QST-M-29**, 100 (2021).

2 - 14 Gamma-ray resistance of the thermophilic *Rubrobacter* species

K. Katsumata[a)], K. Satoh[b)], Y. Oono[b)], K. Miyazaki[c)] and I. Narumi[a)]

[a)]Graduate School of Life Sciences, Toyo University
[b)]Department of Radiation-Applied Biology Research, TARRI, QST
[c)]International Center for Biotechnology, Osaka University

Introduction

The genus *Rubrobacter* belong to the phylum "Actinobacteria" while the genus *Deinococcus* belong to the distinct phylum "Deinococcus-Thermus", both members of which are well known as the radioresistant bacteria. Previously, we cultured several *Rubrobacter* species, including the strain AA3-22 isolated from Arima Onsen [1], at their optimal growth temperatures and media and showed survival curves after gamma irradiation [2]. To compare the gamma radiation resistance of *Rubrobacter* more accurately, several thermophilic strain, including AA3-22, were grown in the same medium at optimal growth temperatures and survival rates after gamma irradiation were determined in this study.

Materials and Methods

Strain AA3-22, *R. xylanophilus* (strain PRD-1), *R. calidifluminis* (strain RG-1) and *R. naiadicus* (strain RG-3) were cultivated in CYC medium (3.5% Difco Czapek Dox Broth, 0.2% Bacto Yeast Extract, 0.6% Difco Casamino Acids) at 60 °C, which is their optimal growth temperature, until late exponential growth phase. For gamma irradiation, cultured cells suspended in 10 mM sodium phosphate buffer (pH 7.0) were exposed to ^{60}Co gamma-rays at the gamma-ray irradiation facility, TARRI, QST, and the survived cells were counted using the serial dilution spotting method on CYC agar after incubating at 60 °C.

Results and Discussion

Rubrobacter species have been isolated from various environments. Until now, there are 11 validly published species in the genus *Rubrobacter* (https://lpsn.dsmz.de/genus/rubrobacter). Some *Rubrobacter* species inhabit geothermal areas, but some inhabit non-thermal areas such as ocean sediment, marine sponge, and church walls. Among them, *R. xylanophilus* (PRD-1) was isolated from thermally polluted industrial runoff at Wilton in England [3], while *R. calidifluminis* (RG-1) and *R. naiadicus* (RG-3) were isolated from a stream heated by several fumaroles near Ribeira Grande on the Island of São Miguel in the Azores [4]. The optimal growth temperature of these three species as well as strain AA3-22 is known to be 60 °C. The other known *Rubrobacter* species is shown to have lower optimal growth temperature. No bacteria of the genus *Rubrobacter* have been isolated with an optimal growth temperature exceeding 60 °C. Therefore, the strains used in this study are classified as a thermophilic *Rubrobacter* group.

Figure 1 show the survival curves of the four thermophilic *Rubrobacter* strains. Stains AA3-22 and PRD-1 were equally resistant to gamma radiation, while strains RG-1 and RG-3 were slightly more sensitive but showed similar survival curves. Figure 2 showed the Neighbor-joining tree based on 16S rRNA gene sequences of the four thermophilic Rubrobacter strains. The similarity of the survival curves was thought to reflect the similarity of the 16S rRNA gene sequences of the respective strains.

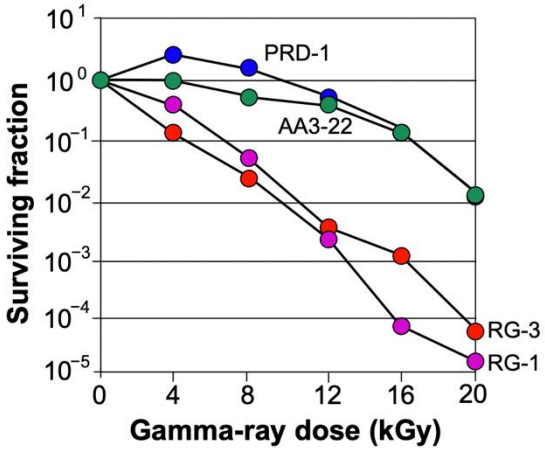

Fig. 1. Survival curves of the four thermophilic *Rubrobacter* strains following gamma irradiation.

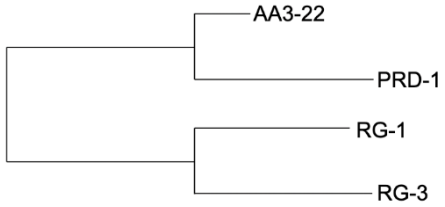

Fig. 2. Neighbor-joining tree based on 16S rRNA gene sequences of the four thermophilic *Rubrobacter* strains.

Acknowledgments

This research was conducted as part of the Toyo University Bio-Resilience Research Project and supported by the Toyo University Priority Research Program.

References

[1] N. Tomariguchi and K. Miyazaki, Microbiol. Resour. Announc. **8**, e00818-19 (2019). DOI: 10.1128/MRA.00818-19
[2] K. Izumi *et al.*, QST Takasaki Annual Report 2020 **QST-M-33**, 86 (2022).
[3] L. Carreto *et al.*, Int. Natl. J. Syst. Evol. Microbiol. **46**, 460 (1996). DOI: 10.1099/00207713-46-2-460
[4] L. Albuquerque *et al.*, Syst. Appl. Microbiol. **37**, 235 (2014). DOI: 10.1016/j.syapm.2014.03.001

2 - 15 Strategy for detecting genome-wide mutations in mutagenized Arabidopsis plants

S. Kitamura, K. Satoh and Y. Oono

Department of Radiation-Applied Biology Research, TARRI, QST

Until now it has been difficult to detect genome-wide mutations from a mutagenized plant (the first generation; M1), in which cells having different mutation patterns are present. Thus, current knowledge on the genome-wide mutations in plants depends solely on the analysis results using M2 or later generation of the mutagenized plants. In this report, we describe the method to enrich progenitors originated from a single mutated cell in the mutagenized plant by using loss of heterozygosity of genes for anthocyanin pigmentation in Arabidopsis and to detect genome-wide mutations occurred in the M1 tissue [1].

Arabidopsis triple mutants for anthocyanin pigmentation (*tt3 tt4 tt18*) were crossed with wild-type plants to obtain triple heterozygous plants (*TT3tt3 TT4tt4 TT18tt18*). Seeds of the tiple heterozygote were irradiated with 1,000 Gy of ^{60}Co gamma-rays. When a mutation does not occur in wild-type *TT* alleles at any of the three heterozygous loci, whole aerial part of the M1 seedlings will be anthocyanin-positive. On the other hand, when one of the wild-type *TT* alleles at the three heterozygous loci is disrupted by irradiation, the anthocyanin synthetic pathway will be abolished in the corresponding cell. Because loss of anthocyanins does not affect cell division, the cell harboring the *de novo TT* mutation forms an anthocyanin-less sector in an irradiated plant. This sector will be composed mainly of cells with the same mutation pattern, providing an opportunity to detect genome-wide mutations by whole-genome sequencing (WGS) from the irradiated plant tissue (Fig. 1). The cell

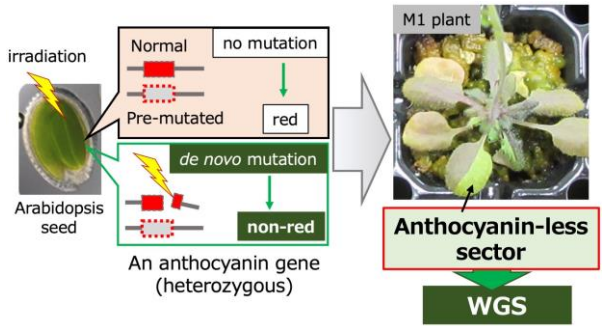

Fig. 1. Scheme for detecting genome-wide mutations in M1 plants.

responsible for anthocyanin-less phenotype is composed of pre-mutated allele and *de novo* mutated allele at a heterozygous locus. If the sector is derived absolutely from division of a single cell, allele frequency (AF) of the *de novo* mutation would be 0.5 in the sector DNA. If cells with other mutation patterns are included in the sector, the AF would be below 0.5, depending on the extent of the inclusion. This is contrastive to simple genome composition of the prevailing WGS using M2 plants, such as homozygous (AF = 1) or heterozygous (AF = 0.5) at any loci. Thus, to detect mutations with such the low AF, WGS using the anthocyanin-less sector in the M1 plants should be conducted with deep coverage (~100).

Seven anthocyanin-less sectors were isolated from gamma-irradiated triple heterozygous plants. Genomic DNA was extracted independently from the 7 sectors and was used for library preparation for short-read next-generation sequencing. Differences of the sequence from wild-type Arabidopsis reference sequence were detected by standard bioinformatics protocol and were called as mutations. We first examined the presence of *de novo* mutations at three heterozygous loci in the sector DNA. Out of 7 sectors, 5 were found to possess *de novo TT* mutations at one of the three heterozygous loci and their AF values were about 0.3 to 0.4. This implies that a single cell population with the same mutations including the *de novo TT* mutation was successfully enriched by our experimental system. Then we searched mutations beyond the three heterologous loci, and found 769 genome-wide mutations with various types such as single base substitution (SBS), deletion (DEL), insertion (INS), structural variation (SV) including inversion and translocation, and complex, from 7 sectors (Fig. 2A). The overall spectrum found in the M1 plants was similar to that in the M2 plants irradiated with the same dose of gamma-rays to Arabidopsis seeds (Fig. 2B [2]). However, the proportion of large DNA alterations such as ≥100 bp deletion (≥100 DEL) and SV was higher in M1 than M2, suggesting that M1 genome analysis is appropriate for detecting large DNA alteration more effectively than M2 genome analysis.

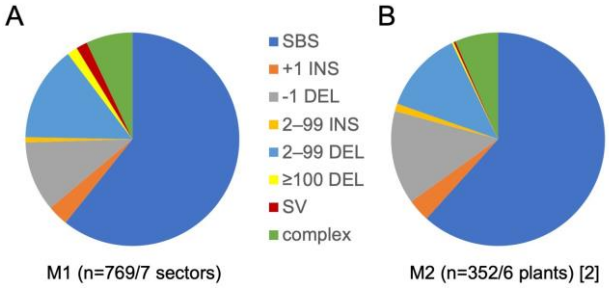

Fig. 2. Mutation spectrum in the DNA of the M1 sectors (A) and M2 plants (B) following the gamma-irradiation of seeds.

Acknowledgments

This work was partially supported by JSPS KAKENIH 19K12333.

References

[1] S. Kitamura *et al.*, PLoS Genet. **18**, e1009979 (2022). DOI:10.1371/journal.pgen.1009979

[2] Y. Hase *et al.*, Front. Plant Sci. **11**, 336 (2020). DOI:10.3389/fpls.2020.00336

2 - 16 Elucidation of genes involved in camptothecin biosynthesis of *Ophiorrhiza pumila*

A. Takamatsu[a)], N. Tsujimoto[a)], S. Kitamura[b)], Y. Oono[b)] and M. Yamazaki[a)]

[a)]Graduate School of Pharmaceutical Sciences, Chiba University
[b)]Department of Radiation-Applied Biology Research, TARRI, QST

We applied random mutagenesis by ion beam irradiation to elucidate gene functions in *Ophiorrhiza pumila* (Fig. 1) producing camptothecin, anti-cancer mono-terpenoid indole alkaloid. Camptothecin is one of the strongest inhibitors of topoisomerase I, and its derivatives e.g. Irinotecan and Topotecan are frequently used in clinical cancer treatments. This toxic alkaloid is produced in several plant species of separate families as the result of convergent evolution. The elucidation of biosynthetic pathway is important subject for sustainable usage of natural medicinal resources. *O. pumila* belonging Rubiaceae is a perennial herb growing naturally in Nansei islands in Japan. So far, we established *in vitro* culture systems of hairy roots and hydroponics system of this species. Recently, chromosome-level genome assembly of this species had been completed [1] and transcriptome and metabolome data are available.

Effect of ion beam irradiation on germination rate

The seeds of *O. pumila* were irradiated by various doses (0, 5, 10, 15, 20, 30, 40, 50 Gy) of 17.3 MeV/u carbon ion beams. The 50 seeds/dish were put on filter paper moistened in petri dishes for two weeks and the germinated plants were counted and germination rate was investigated. The results (Fig.2) showed that 5, 10,15, 20, 25 and 30 Gy irradiations do not affect so much on the germination rate besides the rate was reduced to 50-60% at 40 Gy and to 30-40% at 50 Gy.

Frequency of morphological abnormality

The germinated plants were transferred to hydroponics system and maintained. After 2-3 months, morphological changes were observed in plants grown from 15-50 Gy irradiated seeds. The frequency of morphological changes was increased according to the irradiation intensity (Fig. 3). The morphological changes were found roughly 10% plants at 15Gy, 30% plants at 30 Gy and 50% plants at 50 Gy.

Seed setting of hydroponic plants

The progeny seeds were obtained in some plants. The camptothecin producibility was tentatively measured by fluorescence induced by UV-illumination of germinated plants in microtiter plates. The variation of the producibility could be evaluated by using this system, becoming effective for screening the camptothecin-related mutants in this large-scale irradiation study.

Fig. 1. Plant of *O. pumila* grown hydroponically.

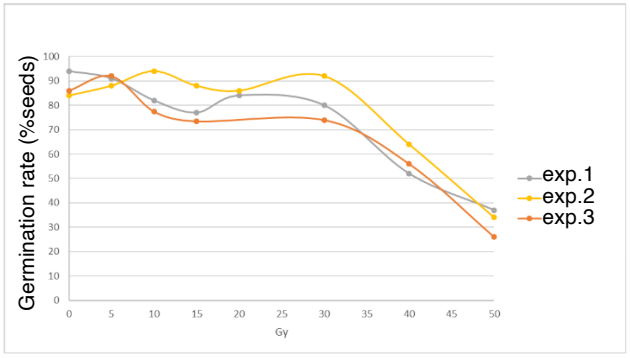

Fig. 2. Germination rate of irradiated seeds.

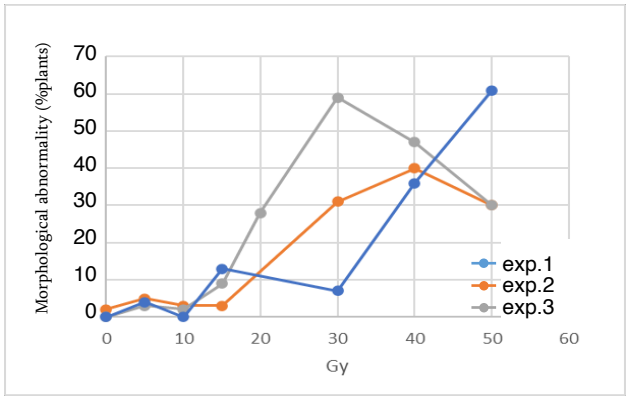

Fig. 3. Frequency of morphological changes.

Reference

[1] A. Rai *et al*., Nat. Commun. **12**, 405 (2021).
DOI: 10.1038/s41467-020-20508-2

2 - 17 Enhancing the therapeutic effect of 2-^{211}At-astato-α-methyl-L-phenylalanine with probenecid loading

H. Hanaoka[a,b], Y. Ohshima[c], H. Suzuki[d], I. Sasaki[c], T. Watabe[e], K. Ooe[e], S. Watanabe[c] and N.S. Ishioka[c]

[a]Faculty of Medicine, Kansai Medical University
[b]Gunma University Graduate School of Medicine
[c]Department of Radiation-Applied Biology Research, TARRI, QST
[d]Graduate School of Pharmaceutical Science, Chiba University
[e]Graduate School of Medicine, Osaka University

Targeted alpha therapy (TAT), a cancer treatment with a specifically delivered α-emitter, is an attractive potential therapy because of its high therapeutic effect without significant toxicity. We previously developed α-methyl-L-phenylalanine derivatives labeled with ^{211}At, an attractive α-emitter of halogen (2-[^{211}At]astato-α-methyl-L-phenylalanine [2-AAMP]) [1]. 2-AAMP showed tumor-specific uptake via L-type amino acid transporter 1 (LAT1) highly expressed in various types of human cancers and had a beneficial effect on survival in tumor-bearing mice. However, its therapeutic effect was insufficient, likely due to its low tumor retention. Its therapeutic effect could be improved by increasing its accumulation and retention in tumors. A previous study demonstrated that preloading of probenecid, an organic anion transporter (OAT) inhibitor, markedly delayed the clearance of radioiodine-labeled α-methyltyrosine (IMT) from the blood and increased its accumulation in tumors by reducing renal uptake [2]. Considering the target molecule (LAT1) and structural similarity between 2-AAMP and IMT, we speculated that the probenecid loading strategy should work on 2-AAMP. In this study, we evaluated the effect of probenecid loading on the biodistribution and therapeutic effect of 2-AAMP in mice [3].

In tumor-bearing mice, probenecid (400 mg/kg) preloading delayed the clearance of 2-AAMP from the blood. The accumulation of 2-AAMP in tumors in the probenecid loading group was significantly higher than that in the control group at 1 h and 3 h after injection (Fig.1, $p < 0.01$ and $p < 0.05$, respectively). Thereafter, in the probenecid loading group, radioactivity was rapidly eliminated from the tumors, and the accumulation level was similar to that in the control group at 6 h after injection. Probenecid preloading also increased the accumulation of 2-AAMP in other organs at 1 h and 3 h after injection and then the accumulation became very low at 6 h after injection. These results indicate that probenecid preloading prevented the renal uptake of 2-AAMP, which delayed its clearance from the blood as expected. In the therapeutic study, tumor growth was suppressed by 2-AAMP treatment, whereas tumors treated with probenecid alone rapidly grew at the same rate as those in the control mice (Fig. 2a). The transient loss (< 10%) in body weight was similar between the 2-AAMP and probenecid-only groups, thus the loss in body weight was caused by probenecid injection and not 2-AAMP (Fig 2b). Kaplan–Meier survival analysis revealed that the survival of mice significantly improved with 2-AAMP treatment ($p < 0.05$; Fig. 2c). These results indicate that probenecid loading is useful to improve the therapeutic effect of 2-AAMP by increasing its accumulation in tumors.

Acknowledgments

The authors thank the staff in the cyclotron operation section for the cyclotron operation.

References

[1] Y. Ohshima *et al.*, Nucl. Med. Biol. **90-91**, 15 (2020). DOI:10.1016/j.nucmedbio.2020.08.003
[2] S. Nakajima *et al.*, Nucl. Med. Biol. **34**, 1003 (2007). DOI:10.1016/j.nucmedbio.2007.06.017
[3] H. Hanaoka *et al.*, Cancers. **13**, 5514 (2021). DOI:10.3390/cancers13215514

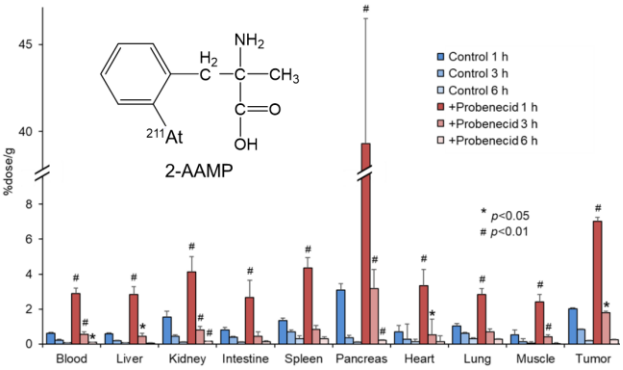

Fig. 1. Biodistribution of 2-AAMP in tumor-bearing mice (mean ± SD, n = 4). * $p<0.05$ and # $p<0.01$ compared with the control group.

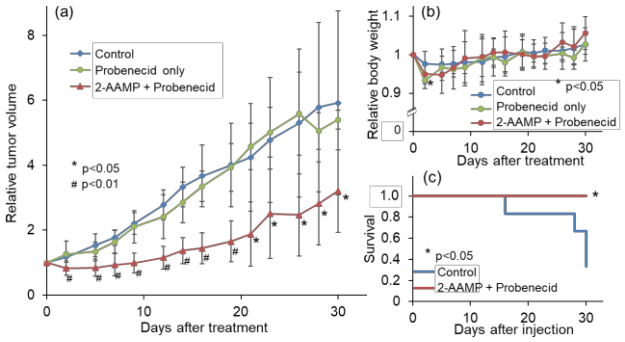

Fig. 2. The therapeutic effect of 2-AAMP (2 MBq) in tumor-bearing mice with or without intraperitoneal injection of probenecid (mean ± SD, n = 5–6). (a) average tumor volume, (b) average body weight change, (c) Kaplan–Meier survival curves after treatment. * p<0.05 and # p<0.01 compared with the control group.

2 - 18 Rapid flow-based system for separation of radioactive metals by selective complex formation

Y. Sugo[a], S. Obata[b], R. Miyachi[b], H. Manabe[c], M. Mori[c], S. Ohira[b] and N. S. Ishioka[a]

[a]Department of Radiation-Applied Biology Research, TARRI, QST
[b]Department of Chemistry, Kumamoto University
[c]Faculty of Science and Technology, Kochi University

Introduction

Short-lived radioactive metals, such as ^{64}Cu (half-life of 12.7 h), ^{66}Ga (9.5 h), and ^{68}Ga (1.1 h), are useful nuclides for positron emission tomography (PET) diagnosis. Recently ^{68}Ga is particularly in the limelight with increasing applicability of ^{68}Ga-labeled PSMA (prostate specific membrane antigen). Radioactive Ga can be produced from the source Zn by irradiation with proton beam using cyclotrons. For clinical usage, radioisotopes need to be rapidly and efficiently separated from a large amount of the source metals.

In this study [1], we developed a new flow-based system with a parallel plate cation-trapping device followed by UV irradiation. The principle of this separation is based on the difference in formation constants between Ga/Zn and ethylenediaminetetraacetic acid (EDTA) (log $K_{Ga\text{-}EDTA}$ = 20.3, log $K_{Zn\text{-}EDTA}$ = 16.5). The formation constant of the Ga–EDTA complex ([Ga-EDTA]$^{-}$) was 3.8 orders of magnitude higher than that of the Zn–EDTA complex ([Zn-EDTA]$^{2-}$), promoting the selective formation of Ga–EDTA complex under optimized conditions.

Experimental

A solid target ^{nat}ZnO was irradiated with an 18 MeV proton beam at a current of 5 μA using the AVF cyclotron of TIARA. Radioactive nuclides such as ^{67}Ga (3.26 d) and ^{65}Zn (243.7 d) were simultaneously produced by nuclear reactions of ^{68}Zn(p,2n)^{67}Ga and ^{66}Zn(p,pn)^{65}Zn, respectively. These nuclides were used as tracers for the evaluation of Ga/Zn separation performance. The irradiated target was dissolved in HNO_3. The solution matrices were adjusted to 1 mmol L^{-1} EDTA in 30 mmol L^{-1} HNO_3 (pH 1.5). This condition was pre-optimized in cold separation test. The prepared sample solution was passed through a cation exchange trap to selectively remove Zn (adsorption process). Subsequently, 1 mol L^{-1} HNO_3 solution was passed through the opposite side of the cation-trapping device to recover Zn (desorption process). The recovered Ga-EDTA complex was irradiated with UV light to decompose EDTA.

Results and Discussion

The sample containing ^{67}Ga and ^{65}Zn tracers with 100 mg L^{-1} ^{nat}Zn was passed through the cation-trapping device. The recovery of ^{67}Ga and ^{65}Zn in each fraction is illustrated in Fig. 1a. During the adsorption process, only ^{67}Ga was observed. The fraction collected at 1-2 min presented the highest concentration of Ga, and most Ga was collected within 8 min. Conversely, only Zn was recovered in the desorption process. The total recoveries of Ga and Zn were respectively 98.0% and 83.5% (Fig. 1b). Figure 1c shows the γ-ray spectra before and after separation. These results indicate that Zn was selectively and quantitatively trapped, and Ga was effectively separated from Zn as the Ga–EDTA complex in this system.

In addition, UV irradiation was treated to release the Ga^{3+} ions from the Ga–EDTA complex. The recovery of Ga^{3+} ions (98.9%) was achieved via UV irradiation for 10 min in the presence of 0.3% H_2O_2. Therefore, the obtained EDTA complex of Ga was converted to free Ga^{3+} by decomposition under UV irradiation.

It is concluded that our developed system was successfully applied to separate radioactive Ga from the source Zn.

Acknowledgments

This work was supported by JSPS KAKENHI Grant Number JP 21H02870, and 20H03632.

Reference

[1] Y. Sugo *et al*., Anal. Chem. **93**, 17069 (2021).
DOI: 10.1021/acs.analchem.1c03866

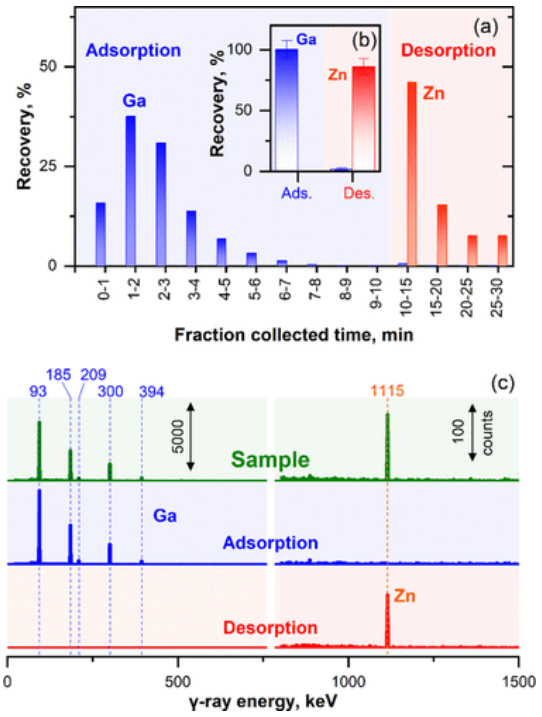

Fig. 1. Separation of ^{67}Ga from ^{65}Zn using the selective chelate formation method. (a) recovery of Ga and Zn in each fraction, (b) total recoveries of Ga and Zn, and (c) γ-ray spectra before and after separation.

2 - 19 Preparation for single-cell RNA-sequence assay of PC12 pheochromocytoma cells

T. Sakashita, Y. Ohshima, Y. Yokota and N. S. Ishioka

Department of Radiation-Applied Biology Research, TARRI, QST

Introduction

Pheochromocytomas (PCCs) are rare neuroendocrine tumors with malignant progression. Clinical improvement of malignant PCCs with β-emitting *meta*-^{131}I-iodo-benzylguanidine (^{131}I-MIBG) constitutes a stage of partial remission in metastatic PCC [1]. Recently, we reported strong anti-tumor effects of α-emitting *meta*-^{211}At-astato-benzylguanidine (^{211}At-MABG) in a PCC mouse model, suggesting a potential option for targeted α therapy (TAT) for patients with malignant PCC [2]. We also found that the gene expression profiles of cell cycle checkpoints displayed similar modes of cell death via the p53-p21 signaling pathway after ^{211}At-MABG treatment and γ-ray irradiation [3]. On the other hand, heterogeneous distribution of nuclear medicine within tumor tissue has been reported [4], and the same would go for cell-population. Our previous findings might not yet be sufficient to understand the cell-killing mechanism of TAT, because of not single-cell analysis but bulk RNA-sequence (RNA-seq) analysis. Therefore, we aimed to carry out a single-cell RNA-seq for TAT in future experiments. Here, we reported preparation for single-cell RNA-seq assay of PC12 cells.

Materials and methods

Cell culture. PC12 cells were cultured in RPMI1640 medium (Wako, Osaka, Japan) supplemented with 5% v/v fetal bovine serum (FBS), 10% horse serum (HS), 100 U/mL penicillin and 100 μg/mL streptomycin in a humidified 5% CO_2, 37 °C incubator.

Cell irradiation. PC12 cell suspension was irradiated by ^{60}Co γ-rays at the absorbed dose of 10 Gy.

Cell detachment. 6 h after γ-rays irradiation, PC12 cell suspension was centrifuged at 200 g for 3 min, and supernatant was removed. Cell pellet was gently resuspended in 1 mL accutase (Nacalai tasque, Kyoto, Japan), and incubated for 30-40 minutes in a humidified 5% CO_2, 37 °C incubator.

Cell wash and filtering. A vial containing detached cells was placed on ice and detached cells were counted by the cell-counting methods. Cell suspension was filtered using a Flowmi tip strainer (40 μm, Scienceware, Wayne, NJ, USA) to remove small aggregates from single cells. Filtered cell suspension was centrifuged at 200 g for 3 min at 4 °C. Cell pellet was washed by 1 mL of 1x PBS with 1.0% BSA (Bovine Serum Albumin solution). Washed cell suspension was centrifuged at 200 g for 3 min at 4 °C and washed by 1 mL of 1x PBS with 1.0% BSA again. Finally, cell suspension was filtered using a Flowmi tip strainer. Final prepared cells were counted by the cell-counting methods to check a loss of cells and determine mixing condition at the standard protocol of Chromium Next GEM single cell RNA-seq [5].

Cell count. To distinguish dead cells, 20 μl cells were aliquoted and mixed with 20 μl 0.4% trypan blue stain. Mixed cells were manually counted under microscope with a Burker-Turke hemocytometer equivalent to 10^4 cells/mL.

Preparation for single-cell RNA-seq. The Chromium Single Cell Gene Expression Solution upgrades short read sequencers to deliver a scalable microfluidic platform for 3' digital gene expression by profiling 500-10,000 individual cells per sample [5]. A pool of ~3,500,000 10x Barcodes are sampled separately to index each cell's transcriptome. It is done by partitioning thousands of cells into nanoliter-scale Gel Beads-in-emulsion (GEMs), where all generated cDNA shares a common 10x Barcode. Libraries are generated and sequenced from the cDNA and 10x Barcodes are used to associate individual reads back to the individual partitions.

Preliminary results

Cell viability. To achieve a single-cell RNA-seq, PC12 cells must be incorporated into the GEM while they are alive. Through cell wash and filtering processes, cells are required to have a viability of 80% or greater. Table 1 shows the over 80% viability of PC12 cells during these processes.

Table 1
Viability of PC12 cells at the time of counting during cell wash and filtering processes.

Dose (Gy)	First counting	Second counting
0	96.9±7.5%	96.5±11.4%
10	98.7±12.8%	99.0±8.6%

GEM. PC12 cells were incorporated into the GEM. Then, GEMs become a white suspended state. Our sample of GEMs showed white suspension (Fig. 1). Next, we carried out cDNA amplification and made 3' gene expression library construction in accordance with the standard protocol in the user guide of 10× Genomics [5].

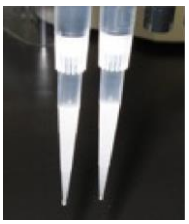

Fig. 1. GEM suspension.

References

[1] J.A. Carrasquillo *et al.*, Semin. Nucl. Med. **46**, 203 (2016). DOI: 10.1053/j.semnuclmed.2016.01.011
[2] Y. Ohshima *et al.*, Eur. J. Nucl. Med. Mol. Imaging **45**, 999 (2018). DOI: 10.1007/s00259-017-3919-6
[3] Y. Ohshima *et al.*, Theranostics **9**, 1538 (2019). DOI: 10.7150/thno.30353
[4] T. Beck and L. Jacobsson, J. Nucl. Med. **51**, 1616 (2010). DOI: 10.2967/jnumed.110.077578
[5] https://www.10xgenomics.com/support

2 - 20 Spatial distributions of cesium and strontium in tea leaves evaluated by micro-PIXE analysis

A. Terakawa[a)], K. Momokita[a)], Y. Hattori[a)], M. Sato[a)], K. Ishii[a)], M. Koka[b)], N. Yamada[c)], R. Yamagata[c)], Y. Ishii[c)], N. Suzui[b)], T. Satoh[c)] and N. Kawachi[b)]

[a)]Cyclotron and Radioisotope Center, Tohoku University
[b)]Department of Radiation-Applied Biology Research, TARRI, QST
[c)]Department of Advanced Radiation Technology, TARRI, QST

Introduction

After the nuclear power plant accidents in Chernobyl and Fukushima, extensive research focused on radioactive contamination of tea plants due to ^{134,137}Cs in tea-growing regions of Turkey [1] and Japan [2], respectively. However, few studies have examined ^{90}Sr in tea plants. In this study, we performed particle-induced x-ray emission (PIXE) analysis using a micrometer-sized beam (micro-PIXE) to explore similarities and differences in Cs and Sr accumulation on cell and tissue scales and the relationships between their homologous elements.

Materials and methods

To obtain tea leaf samples, we grew five tea trees [*Camellia sinensis* (L.) Kuntze] in pots with commercial garden soil. We transferred stable Cs and Sr into tea leaves via foliar absorption by partially soaking the leaves in mixed aqueous solutions of CsCl (43.6 g/L) and $SrCl_2$ (104.8 g/L) for 1 minute. Tea leaves were collected 3, 30, and 90 days after foliar absorption, washed in water for 1 minute, and freeze-dried. We cut away portions of the leaves subject to foliar and non-foliar absorption as samples for a micro-PIXE analysis. We performed the micro-PIXE analysis using a 3-MeV proton beam and an in-air micro-PIXE analysis system at TIARA.

Results and discussion

Figure 1 presents the two-dimensional spatial distributions (elemental maps) of K and Cs obtained by micro-PIXE analysis of the foliar-absorbed samples. We confirmed that K and Cs were distributed throughout the sample. No significant differences were basically observed in the distribution of K or Cs or in the days elapsed after leaf surface absorption.

Figure 2 presents elemental maps of Ca (red) and Sr (green) in the foliar absorbed potions of the leaf samples. When Ca and Sr accumulate in the same location, their distributions appear yellow in the overlaid images. Unlike the tendency of K and Cs accumulation, Ca and Sr accumulated mainly in extremely narrow areas of the tea leaves, seen as small dots. Furthermore, we confirmed that Sr accumulated in almost exactly the same narrow regions as Ca, except on day 3. In the Sr map for day 3, the accumulation was observed in narrow areas and also widely distributed. Based on the Sr maps from day 3 to 90, it appears that Sr absorbed from the leaf surface was translocated and accumulated in the same small areas as Ca as time passed. Additionally, clear Cs and Sr accumulation was observed in the non-foliar absorption portion at days 30 and 90 due to translocation from the foliar-absorption region.

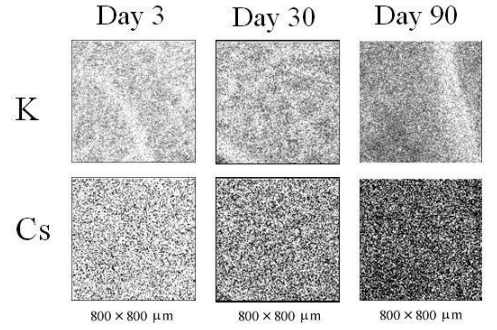

Fig. 1. Spatial distribution of Cs and K in the foliar-applied region of tea leaf samples collected 3, 30, and 90 days after foliar absorption.

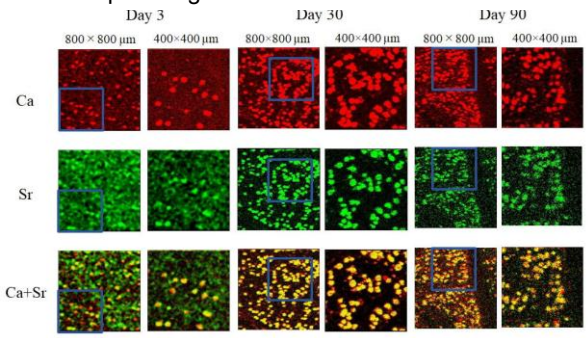

Fig. 2. Spatial distribution of Ca and Sr in the foliar-applied region of tea leaf samples collected 3, 30, and 90 days after foliar absorption. Blue open squares indicate the corresponding 400 × 400 μm areas to the right.

Conclusion

An almost uniform Cs concentration was observed throughout the leaf, in common with K. On day 3, the foliar-absorbed Sr was distributed in narrow areas as small dots, as well as in the entire leaf. On days 30 and 90, however, the Sr in the samples accumulated in almost exactly the same narrow areas as Ca, including the non-foliar absorption portion of the same leaf via elemental translocation.

References

[1] M. Scott *et al*., Health Phys. **57**, 205 (1989).
[2] A. Kamata *et al*., Soil Sci. Plant Nutr. **61**, 212 (2015). DOI: 10.1080/00380768.2014.1003191

2 - 21 Identification of multi-element accumulation mechanism in legume

J. Furukawa[a)], Y. Noda[b)], N. Suzui[b)], Y.-G. Yin[b)], M. Koka[b)], N. Yamada[c)], R. Yamagata[c)], Y. Ishii[c)], N. Kawachi[b)] and T. Satoh[c)]

[a)] Life and Environmental Sciences, University of Tsukuba
[b)] Department of Radiation-Applied Biology Research, TARRI, QST
[c)] Department of Advanced Radiation Technology, TARRI, QST

Plants need various elements for its growth. Not only major elements, such as nitrogen, phosphorous and potassium, but many essential trace elements are needed for plant development. The analysis of trace element content and localization in the focused organ or tissue is important to identify its functions. Especially, under some stress conditions, information about the localization of trace elements in the tissue level is highly valuable for investigating where the deficiency or toxicity of elements is detected and how to control the mechanisms for keeping metal homeostasis of plant body. Atmospheric Micro-PIXE (Particle Induced X-ray Emission) analysis can visualize multi-element localization with high-resolution images and is a promising method for understanding plant adaptation for the growth environment [1, 2].

Lotus japonicus is a model legume and its two experimental lines, MG-20 and B-129, have a diversity in some metal concentrations including iron (Fe) [3, 4]. Iron concentration in above ground shoot part was higher in MG-20, however, in root, Fe concentration was obviously higher in B-129. These Fe allocation pattern suggests the Fe translocation activity from root to shoot is low in B-129. Based on the Micro-PIXE analysis using 3 MeV H^+ beam, high Fe accumulation around the root stele was observed in B-129, suggesting the Fe ion transferred from root surface to the stele was loaded into the xylem vessels in MG-20 but might not in B-129 [5].

For investigating the adaptation strategy for low Fe concentration in B-129 shoot, Fe homeostasis regulating gene, *LjIMA1*, was focused on this study. Plant *IMA* is recently identified in Arabidopsis and the *IMA* homolog in *L. japonicus* was named *LjIMA1* [6]. *IMA* gene encodes a small peptide and its expression in shoot is thought to regulates Fe uptake and translocation related genes in root by the IMA transfer from shoot to root via sieve tubes.

After the 4-week-cultivation of MG-20 and B-129 with hydroponics using 1/10 Hoagland's solution, shoot and root were harvested and subjected to gene expression analysis. Although low concentration of Fe in shoot and Fe accumulation in root stele suggested the Fe deficiency in B-129 shoot, *LjIMA1* expression in B-129 shoot was lower than MG-20 (Fig. 1A).

For identifying Fe uptake and translocation activities in B-129 root, *LjIRT1*, *LjIRT3* and *LjNAS1* expression was investigated. *LjIRT1* and *LjIRT3* are involved in the Fe uptake from soil solution and *LjNAS1* expression is necessary for the intracellular Fe translocation. Comparing to MG-20, each gene expression was more than three-fold higher in B-129, suggesting the high activity of Fe uptake and translocation in B-129 root (Fig. 1B).

These results suggested that *LjIRT*s and *LjNAS1* expression was regulated by the shoot Fe status in *L. japonicus* and the existence of new systemic Fe homeostasis regulation except for *LjIMA1*. For identifying this long-distance interaction between shoot and root, further experiment including transcriptomic gene expression analysis under Fe deficiency and Fe excess conditions are scheduled.

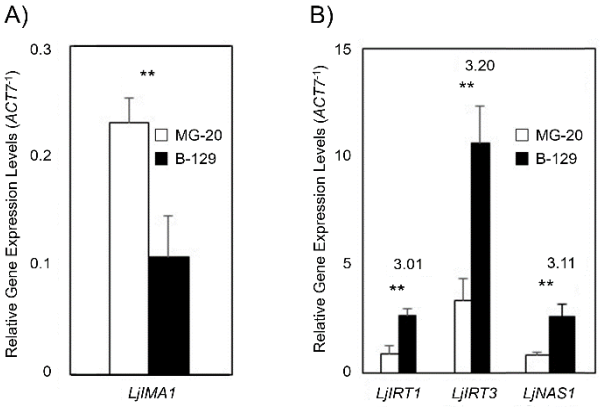

Fig. 1. Gene expression analysis using 4-week-old MG-20 and B-129 [4]. White and black bars indicate MG-20 and B-129, respectively. Expression levels are normalized by *ACT7* expression. A) *LjIMA1* expression in shoot. B) *LjIRT1*, *LjIRT3* and *LjNAS1* expressions in root. Fold change in B-129 comparing to MG-20 were indicated by the value. ** $p < 0.01$.

Acknowledgments

This study was supported in part by the Grant-in-Aid for Scientific Research (no. 20780046, 24780054) to J.F.

References

[1] T. Yamamoto *et al.*, JAEA Takasaki Annu. Rep. 2014 **JAEA-Review 2015-022**, 88 (2016).
[2] Y. Noda *et al.*, QST Takasaki Annu. Rep. 2015. **QST-M-2**, 151 (2017).
[3] M.A. Klein and M.A. Grusak, Genome **52**, 677 (2009). DOI: 10.1139/G09-039
[4] Y. Noda *et al.,* Ann. Bot. in press (2022). DOI: 10.1093/aob/mcac101
[5] J. Furukawa *et al.*, QST Takasaki Annu. Rep. 2017. **QST-M-16**, 111 (2019).
[6] L. Grillet *et al.*, Nat. Plants **4**, 953 (2018). DOI: 10.1038/s41477-018-0266-y

2 - 22 Visualization of zinc distribution in the root of oilseed rape plants by atmospheric micro-PIXE (Particle Induced X-ray Emission) analysis

S. Nakamura[a)], Y. Imaizumi[a)], K. Suda[a)], A. Shinozawa[a)], K. Sato-Izawa[a)], N. Yamada[b)], R. Yamagata[b)], Y. Ishii[b)], T. Satoh[b)], Y.-G. Yin[c)], N. Suzui[c)] and N. Kawachi[c)]

a) Department of Bioscience, Faculty of Life Sciences, Tokyo University of Agriculture
b) Department of Advanced Radiation Technology, TARRI, QST
c) Department of Radiation-Applied Biology Research, TARRI, QST

Zinc is one of our essential elements with various physiological functions [1]. Inadequate intake of zinc for us leads to a loss of our health. Therefore, we need to obtain the proper amount of zinc in our daily diet. However, not many foods contain enough zinc to meet the intake target. Biofortification" is an effort to make plants (the edible parts of plants) accumulate certain target components that we need, such as zinc [2]. In order to put "zinc biofortification" into practical use, it is necessary to elucidate zinc behaviors in plants and control them.

Our previous research revealed glutathione, applied to leaves site-specifically, activates zinc translocation from roots to shoots in oilseed rape plants [3]. Glutathione, applied to leaves, affected zinc behaviors in their roots and activated zinc loading into xylem vessels [3]. Elucidating the molecular mechanisms of these phenomenon will lead to practical applications of zinc biofortification in cruciferous plants. To that end, it is necessary to investigate zinc behaviors in the roots of oilseed rape plants in more detail.

In-air micro-PIXE (Particle Induced X-ray Emission) analysis allows us to visualize the two-dimensional distribution of the element of interest in samples [4]. This analysis method also demonstrated two-dimensional distributions of a target element in plant samples [5]. Therefore, we attempted to visualize two-dimensional distribution of zinc in plant roots by using this analytical method. We expect that the experimental results obtained in this study will provide an insight for understanding the molecular mechanisms which is triggered by glutathione, applied to leaves, and control zinc behaviors in plant roots.

Oilseed rape plants (*Brassica napus* L. var. Nourin No.16) were grown using hydroponic solutions under fully controlled conditions [3]. In this study, 30 μM $ZnCl_2$ were given to test plants for 10 days prior to harvest. At harvest, plant roots were embedded in a clear resin (Cryomatrix, Epredia) for frozen section preparation and stored at -30°C. Sections for analysis were prepared using a sectioning device (CM1520, Leica Biosystems). Sections were prepared at a thickness of 60 μm. After slicing, the sections were freeze-dried briefly using a lyophilizer (FDU-1200, Tokyo Rikakikai) and further heated on a hot plate (NHP-45N, NISSIN) to remove moisture from the sections. After microscopic confirmation that sections of root cross sections had been prepared, micro-PIXE analysis was performed at TIARA (Takasaki Ion Accelerators for Advanced Radiation Application). Prepared section samples were analyzed for 15 minutes using a 3 MeV proton beam. The characteristic X-rays generated by proton beam were detected by a Si(L) X-ray detector.

Figure 1A indicated the root cross section from oilseed rape plants prepared in aforementioned method. Results of the micro-PIXE analysis are shown in Fig. 1B. Distribution of zinc (cyan color) was seen in Fig 1B. Zinc distribution in roots of oilseed rape plants was visualized. Distribution of potassium (red color) were also indicated. Unevenness exists in potassium distribution (Fig.1B). In our preliminary experiments, potassium was observed to be distributed throughout the cell. These experimental results indicate that there is room for improvement in the method of cross section preparation. The optimization of the sectioning method and ion beam irradiation time will lead to the observation of more detailed distribution of zinc in plant roots by micro-PIXE.

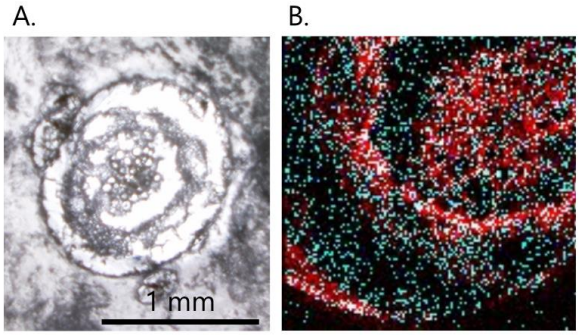

Fig. 1. A: Photo of root cross section from oilseed rape plants grown with 30 μM zinc. B: Micro-PIXE analysis of root cross sections, cyan; zinc, red; potassium

Acknowledgments

This study was supported in part by the Grant-in-Aid for Scientific Research (no. 17H03952, 22H02480) to S.N.

References

[1] C.V. Buturi *et al*., Foods. **10**, 223 (2021). DOI:10.3390/foods10020223
[2] C. Stanton et al., Mol. Plant. **15**, 65-85 (2022). DOI: 10.1016/j.molp.2021.12.008
[3] S. Nakamura et al., Plant Sci. **283**, 424-434 (2019). DOI: 10.1016/j.plantsci.2018.10.018
[4] T. Sakai et al., Nucl. Instrum. Methods Phys. Res. B. 190, 271-275 (2002). DOI:10.1016/S0168-583X(02)00469-X
[5] P.M. Kopittke *et al*., Plant Physiol. **182**, 1869-1882 (2020). DOI:10.1104/pp.19.01306

2 - 23 Evaluation of photosynthate translocation dynamics to strawberry fruits in response to increasing daylight integrals at leaf surface

Y. Miyoshi [a], K. Hidaka [b], Y.-G. Yin [a], N. Suzui [a], K. Kurita [c] and N. Kawachi [a]

[a] Department of Radiation-Applied Biology Research, TARRI, QST
[b] Kyushu Okinawa Agricultural Research Center, NARO
[c] Materials Sciences Research Center, JAEA

The translocation of photosynthates from source leaves to sink fruits is an important physiological function in protected cultivation, which directly affects dry matter accumulation in fruits and promotes auxetic growth of the sink tissues. Therefore, controlling dynamics of photosynthate translocation is critical for high-yield and high-quality fruits production. This requires a more detailed understanding of the ever-changing photosynthates translocation, which must be based on measurement data with higher temporal and spatial resolution than the conventional techniques. The positron-emitting tracer imaging system (PETIS) is an advanced imaging technique to visualize and quantitatively analyze the dynamics of photosynthetic translocation from leaves to sink organs (roots, fruits, etc.) in intact plant bodies [1,2]. In this study, ^{11}C-photosynthates translocation into fruits of strawberry (*Fragaria* × *ananassa* Duch.) was visualized non-invasively and repeatedly using PETIS and ^{11}C tracer (half-life: 20.4 min) to assess the spatiotemporal variability in the translocation dynamics in response to increasing daylight integrals.

Strawberry plants were cultivated for two weeks in the growth chamber with 12 h photoperiod, photosynthetically active radiation of 400 μmol m^{-2} s^{-1}, air temperature of 20°C, and subsequently analyzed by PETIS. The $^{11}CO_2$ gas was fed to a fourth leaf just below the inflorescence of test plants and PETIS imaging for 180 min was immediately started. Three consecutive experiments of PETIS imaging were performed on the same plant. The first imaging started 0.5 h after the change from dark period to light period which is referred to as “0.5 h lighting”. The second imaging started 4.5 h and the third imaging started 9 h after the change to light period which are referred to as “4.5 h lighting” and “9 h lighting”, respectively. At the end of the third imaging experiment, inside the growth chamber was change to dark period again. These treatments were performed by irradiating the assimilated leaves with LED. Diurnal changes of photosynthetic rates of leaves were measured from an hour before to an hour after the 12 h light period, under the same environmental conditions as in the PETIS experiment.

Serial images obtained from PETIS confirmed that ^{11}C-photosynthates were translocated heterogeneously into each fruit on the same inflorescence (Fig. 1). In addition, the fruits in which translocation was observed did not change with the elapsed time of the light period. These results indicate that the correspondence between source leaves and sink fruits is unaffected by changes in the light environment but is mediated by the individual vascular connections between a source leaf and each sink fruit as reported in Hidaka *et al*. 2019 [1]. The translocation rate of ^{11}C-photosynthates into each fruit significantly increased as the integrated light intensity at the leaf surface increased (Fig. 2). The cumulated photosynthesis in leaves increased almost linearly with during the light period (data not shown), suggesting that an increase in the amount of photosynthates in leaves promotes the export of photosynthates from leaves, resulting in an increase in the photosynthate translocation rate into fruits. This is the first study to use ^{11}C-radioisotopes to clarify the spatiotemporal variability in photosynthate translocation from source leaves to individual sink fruits *in vivo* in response to increasing daylight integrals at a high spatiotemporal resolution [3].

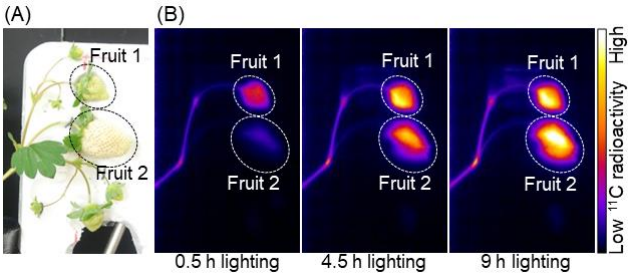

Fig. 1. (A) Strawberry fruits in the PETIS field of view. (B) Integrated PETIS images of ^{11}C-photosynthate translocation into fruits for the 0.5 h, 4.5 h, and 9 h lighting treatments.

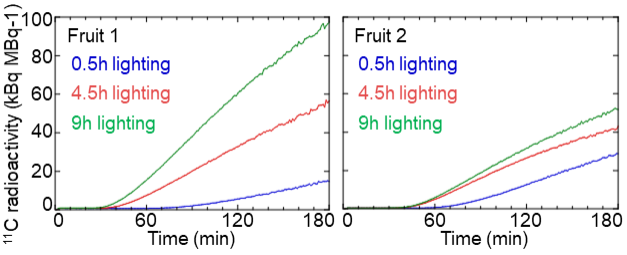

Fig. 2. Time-course analysis of ^{11}C radioactivity in fruits 1 and 2 shown in Fig. 1 in response to the 0.5 h, 4.5 h, and 9 h lighting treatments. The data were normalized against the ^{11}C-radioactivity assimilated by the leaf during PETIS imaging experiment.

References

[1] K. Hidaka *et al*., Front. Plant Sci. **9**, 1946 (2019). DOI: 10.3389/fpls.2018.01946
[2] Y.-G. Yin *et al*., Sci. Rep. **10**, 8446 (2020). DOI: 10.1038/s41598-020-65668-9
[3] Y. Miyoshi *et al*., Front. Plant Sci. **12**, 688887 (2021). DOI: 10.3389/fpls.2021.688887

2 - 24 Elemental distribution into root dentin from pilot materials incorporating with titanium fluoride

K. Okuyama[a)], Y. Matsuda[b)], H. Yamamoto[c)], M. Sakurai[b)], K. Naito[c)], H. Kanda[c)], T. Saito[b)], M. Hayashi[c)], Y. Tamaki[a)], T. Satoh[d)], N. Yamada[d)], R. Yamagata[d)] and Y. Ishii[d)]

[a)]Asahi University School of Dentistry
[b)]School of Dentistry, Health Sciences University of Hokkaido
[c)]Graduate School of Dentistry, Osaka University
[d)]Department of Advanced Radiation Technology, TARRI, QST

Introduction

We reported the effect of titanium fluoride (TiF_4) on the inhibition of demineralization in a previous report [1]. The purpose of this study is to evaluate the elemental distribution of root dentin from materials incorporating TiF_4.

Materials and Methods

Extracted bovine teeth were used as specimens. Each tooth was exposed to a flat root dentin surface and made a cavity at the center of the flat surface (2 × 5 × 1 mm^3). Titanium fluoride was added to the power of glass ionomer cement (Fuji IX Extra) for 0.1%(01T), 1% (1T), or 10% (10T) of its weight, respectively. The powder with TiF_4 was mixed with liquid for Fuji IX by a standard ratio of powder/liquid, and then the mixed cement was filled into the cavity. Bovine artificial caries-affected dentin were prepared by pH cycling (pH 4.5 and 7.0, 6 cycles/day) for 8 weeks. Then these specimens were sliced perpendicular to the tooth axis (thickness: 500 μm) while keeping the tooth structure. Calcium, fluorine(F), and titanium (Ti) distribution were analyzed by an in-air micro-PIXE/PIGE system with a 1.7-MeV $^1H^+$ microbeam at TIARA. Then the cumulative concentration of F or contents of Ti in each specimen was calculated as an area of 100 μm from the superficial surface. The obtained data were analyzed by a Games-Howell test (α = 0.05). Fuji IX without TiF_4(GI), and resin composite (Dentcraft fineflow) (CR) were used in this study also. Six specimens were tested on each group.

Results

Figure 1 shows the mapping images of each group. 1T and 10T indicate both clear distributions of F and Ti. Ti on CR might show barium in the material. Figs. 2 and 3 show the distribution of F and Ti, respectively. For F, 10T indicated a higher value than 0.1T, GI, and CR. There were no significant differences among groups of 1T, 01T, and GI. CR shows the lowest F distribution in all groups. For Ti, there were no significant differences between 10T and 1T, or 1T and 01T. 10T shows a higher Ti distribution than that of 01T. GI and CR indicate lower distribution than the 1T and 10T groups.

Discussion

The F or Ti distribution depended on the concentration of the solution, especially for Ti. 01T did not significantly indicate F and Ti distribution than GI, because this F and Ti distributions from the materials show lower values compared with those by treat by TiF_4 solution [1]. These elements release from the material through a solution to dentin. Lower elements were detected than when teeth were treated by solution, because F or Ti could not go into the tooth directly. Although the number of specimens is small, those fluorine and titanium distributions from the material incorporating titanium fluoride including the powder between 1% and 10% of TiF_4 might show preventive effect.

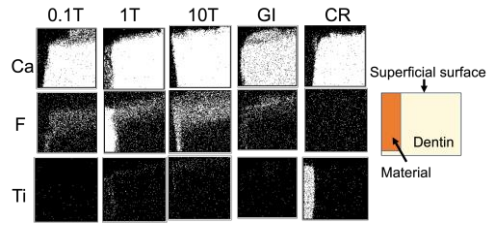

Fig. 1. Representative elemental PIXE/PIGE mapping images of specimen and schematic drawing these images. Upper images show calcium by PIXE. Middle images show fluorine by PIGE. Lower images show titanium by PIXE. White dots in the map represent each element.

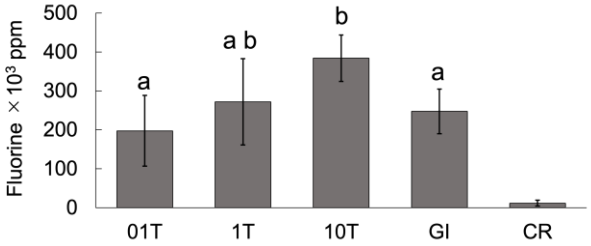

Fig. 2. Concentration of distributed F into dentin at 100μm depth area from superficial surface. Same letters indicate no significant differences ($p > 0.05$).

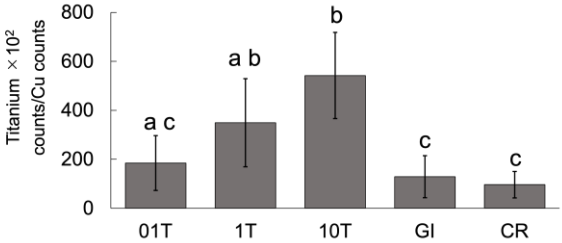

Fig. 3. Ti distribution into dentin at 100μm depth area from superficial surface. Same letters indicate no significant differences ($p > 0.05$).

Reference

[1] K. Okuyama *et al.*, Dent. Mater. J. **40**, 736 (2021). DOI: 10.4012/dmj.2020-193

2 - 25 Ion penetration of zinc-containing fluoride material into sound and demineralized dentin

H. Yamamoto[a)], K. Okuyama[b)], Y. Matsuda[c)], K. Naito[a)], H. Kanda[a)], M. Sakurai[c)], M. Hayashi[a)], T. Satoh[d)], N. Yamada[d)], R. Yamagata[d)] and Y. Ishii[d)]

[a)]Graduate School of Dentistry, Osaka University
[b)]Asahi University School of Dentistry
[c)]School of Dentistry, Health Sciences University of Hokkaido
[d)]Department of Advanced Radiation Technology, TARRI, QST

Introduction

It is widely known that fluoride is effective in inhibiting dental caries, and many reports have recently been published on the caries inhibiting effects of other trace elements. We have also reported the caries-inhibiting effects of zinc-containing material [1], and in this study, we examined the uptake of zinc into sound and demineralized dentin (abbreviated as S- and Dem- Dentin).

Materials and Methods

Specimens were prepared as previously reported [1]. The S-dentin of six human molars was exposed, and three were immersed in demineralized solution for 3 days, to create Dem-dentin. Three fluoride-containing materials {ZIF-10 (zinc-containing), FRC-02 and MI Varnish (all from GC)} were applied to the S- and Dem-Dentin and immersed in saline solution for 3 months. Then, 500-μm-thick sections were prepared, and dentin cross sections were measured for calcium, zinc, and fluoride concentration from the surface layer into the dentin using an in-air micro-PIXE/PIGE system with a 1.7-MeV $^{1}H^{+}$ microbeam at TIARA [1].

Ionic penetration from the surface to 200-μm depth was compared in S- and Dem-Dentin, and statistical processing was performed by Kruskal-Wallis and Mann-Whitney ($p < 0.05$).

Results

There was a tendency for more penetration into Dem-dentin, only ZIF-10 showed a significant difference in the amount of penetration in both S- and Dem-Dentin. There was no significant difference in the amount of penetration between the materials in both S- and Dem-Dentin, and in ZIF-10, the amount of penetration of zinc was significantly higher than fluoride in both S- and Dem-Dentin (Figs. 1 and 2).

Discussion

Although there was no difference in the amount of fluoride penetration between materials in both S- and Dem-Dentin, only the material containing zinc showed significant penetration of fluoride into Dem-dentin. Therefore, it is considered that zinc has an influence on this result. It has been reported that the addition of zinc ions may increase the biological activity of dentin tissue [2]. It is possible that this may have facilitated the penetration of fluoride.

Acknowledgments

We thank the staff of the National Institutes for Quantum Science and Technology (QST). This study was supported by Grants-in-Aid for Scientific Research (17H04382, 17K11705, and 20H00552) from the Japan Society for the Promotion of Science.

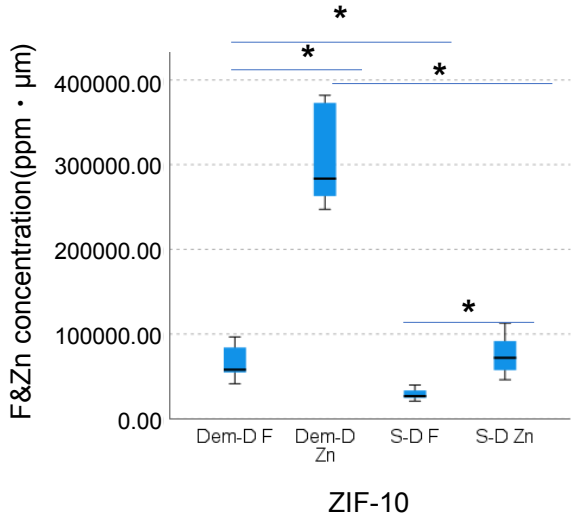

Fig. 1. Cumulative fluoride and zinc concentrations in Zif-10 from the surface to 200-μm depth of demineralized and sound dentin. Asterisked bars indicate significant differences.

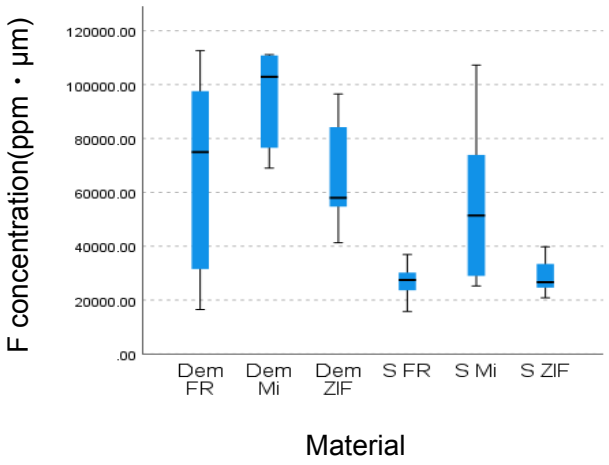

Fig. 2. Cumulative fluoride concentration in each material from the surface to 200-μm depth of demineralized dentin and sound dentin.

References

[1] K. Naito *et al.*, Materials & Design **215**, 110412 (2022) DOI: 10.1016/j.matdes.2022.110412
[2] R. Osorio *et al.*, Caries res. **48**, 276 (2014). DOI: 10.1159/000356873

2 – 26 Estimation of damage localization of ion beam-irradiated DNA in water by means of fluorescence anisotropy

K. Akamatsu, N. Shikazono and K. Satoh

Institute for Quantum Life Science, QST

Introduction

Ionizing radiation-induced DNA damage can cause mutation and carcinogenesis. In particular, “clustered damage”, that is a DNA region with two or more lesions within a few helical turns, is believed to be hardly repaired. This damage would be induced around high-LET ionizing radiation tracks. However, detail of the damage is unknown. We have already developed a method for estimating localization of apurinic/apyrimidinic sites (APs) on DNA using fluorescence resonance energy transfer (FRET) occurring between different fluorescent dyes (Alexa350 and Alexa 488) (*hetero*-FRET). The FRET efficiency (*E*) was calculated from Alexa350 fluorescence intensities before/after enzymatic digestion of the labeled DNA with APs [1]. We succeeded in estimating qualities of clustered APs produced in $^{4}He^{2+}$-, $^{12}C^{5+}$-, and ^{60}Co γ-irradiated dry DNA film to study “direct” radiation effects using the method [2]. We also applied the method to aqueous DNA solution to study “indirect” radiation effects. However, there are some problems of the complex protocol and of the sensitivity due to the low extinction coefficient of Alexa350. We have, therefore, developed “*homo*-FRET” occurred between two or more Alexa488 molecules. We will obtain magnitude of FRET also from “fluorescence anisotropy” of *homo*-FRET between Alexa488 molecules [3]. The new protocol using *homo*-FRET enables us to estimate DNA damage localization without any enzymes and improves sensitivity to detect a clustered damage.

Experiments

●Sample preparation and irradiation

PUC19 digested by Sma I was used (linear formed) for DNA samples to be irradiated. The DNA was dissolved in pure water, to be ~10 g/L. Eight microliters of the DNA solution was mounted on a 10 mmϕ glass plate (thickness: ~0.1 mm), and was irradiated with $^{4}He^{2+}$ (LET: 17 keV/μm), $^{12}C^{6+}$ (LET: 78), and with $^{20}Ne^{8+}$ (LET: 511) at several doses up to 30kGy. Moreover, X-rays (70kVp, tungsten target; LET: ~1) were also used as a standard radiation source.

●Preparation of fluorophore-labeled irradiated DNA and FRET observation [3]

The irradiated DNA (10 μL in water) and 10 μL of 100 mM Tris-HCl (pH 7.5) were mixed in a microtube. Two microliters of Alexa488/DMSO were added to the DNA solution, followed by incubation for 24 h at 37 °C. The fluorophore-labeled DNA was purified by ethanol-precipitation and solid phase extraction.

The fluorescence anisotropy was measured at 525 nm (ex. 470 nm). The anisotropy, $< r >$, is defined as follows:

$$< r > = (I_{VV} - G \cdot I_{VH}) / (I_{VV} + 2 \cdot G \cdot I_{VH})$$

where I_{VV} is the fluorescence intensity when the excitation and emission polarizers are both vertically oriented. I_{VH} is one when the excitation/emission polarizers are vertically/horizontally oriented. G is the grating factor defined as I_{HV}/I_{HH}.

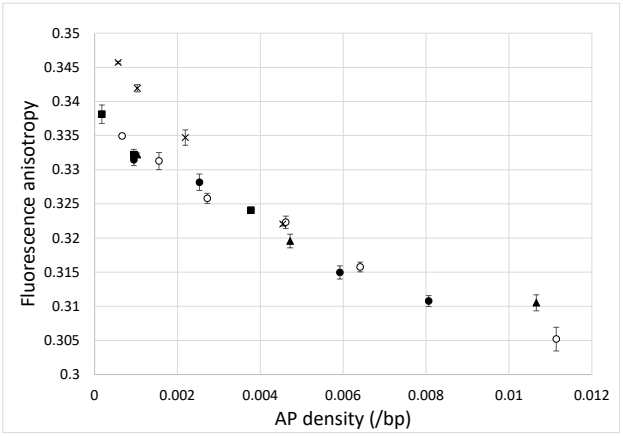

Fig.1. Fluorescence anisotropy of DNA irradiated with 70kVp X-rays (○), $^{4}He^{2+}$ (LET:17 keV/μm) (●), $^{12}C^{6+}$ (78) (▲), and $^{20}Ne^{8+}$ (511) (■) as a function of averaged AP density. Each of the cross marks (×) indicates the value of DNA with random AP-sites produced by incubation in the acidic buffer (~pH 5) at 70°C.

Results and discussion

Figure 1 shows relationships between averaged AP density and fluorescence anisotropy, $<r>$, for He-, C-, Ne-, and X-irradiated DNA in water (without any radical scavenger). This indicates that all the radiation sources tested are likely to produce clustered lesions compared with the case of randomly distributed lesions. Moreover, the degree of damage localization does not depend on radiation quality. Contrary to the results, in the solid state (using dry DNA sample) AP distribution clearly depended on linear energy transfer (LET) [4] (data not shown), that is, the higher LET radiation produces more clustered damaged sites by the “direct” effects. These findings suggest that “indirect” effect (e.g., by OH radical) would not be responsible for DNA damage clustering.

References

[1] K. Akamatsu *et al.*, Anal. Biochem. **433**, 171 (2013). DOI: 10.1016/j.ab.2012.10.004

[2] K. Akamatsu *et al.*, Radiat. Res. **183**, 105 (2015). DOI: 10.1667/RR13780.1

[3] K. Akamatsu *et al.*, Anal. Biochem. **536**, 78 (2017). DOI: 10.1016/j.ab.2017.08.007

[4] K. Akamatsu *et al.*, Anal. Bioanal. Chem. **413**, 1185 (2021). DOI: 10.1007/s00216-020-03082-w

2 – 27 Development of drug delivery system (DDS), through two repetitions of radiation

S. Harada[a] and T. Satoh[b]

[a]Department of Radiology, School of Medicine, Iwate Medical University
[b]Department of Advanced Radiation Technology, TARRI, QST

We innovated P-selectin antibody-labelled nanoparticles, which accumulate to P-selectin antigen and releases anticancer drug with response to radiation (radiosensitive nanoparticles) [1]. Using intravenously injected those radiosensitive particles, we developed new anticancer drug delivery system with two repetitions of radiations, following four steps: 1) the first radiation to tumors induces P-selectin antigen in the endothelium of tumor vessels; 2) the radiosensitive particles were intravenously injected; 3) injected radiosensitive circulate in the body and trapped to the first irradiated tumor vessels, via antigen-antibody reaction of P-selectin; 4) those trapped radiosensitive particles received the second radiation and released anticancer drug. In this study, we tested the efficacy of our anticancer drug delivery system, using micro PIXE camera.

Preparation of particles

The nanoparticles were prepared by spraying a mixture of hyaluronic acid and alginate; supplemented with carboplatin, into a solution of $CaCl_2$ supplemented with P-selectin antibody and $FeCl_2$ through a 0.8 μm pore stainless mesh filter. The generated particles by micro PIXE camera (TARRI, QST) was shown in Fig. 1. The mean diameter was 457±24 nm.

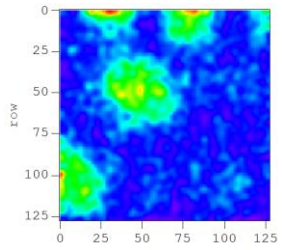

Fig. 1. Generated particles.

Tumor models, first radiation, induction of P-selectin antigen, and accumulation of P-selectin antibody -labelled particles through P-selectin's antigen (Ag)-antibody (Ab) reaction

MM 46 tumors (breast cancer cell lines), which were inoculated in the left hind legs of C3He/N mice, received single 10 or 20 Gy of 100 KeV X-ray irradiation (first irradiation). The P-selectin Ag was proximally induced, dependently on radiation doses. Their peaks were observed on 72 hours after radiation. Subsequently, the P-selectin Ab -labelled particles were injected through tail vein of mice. The P-selectin Ab-labelled particles was accumulated to tumors via P-selectin Ag-Ab reaction. The accumulation was increased over time and was completed on 9 hours after first irradiation.

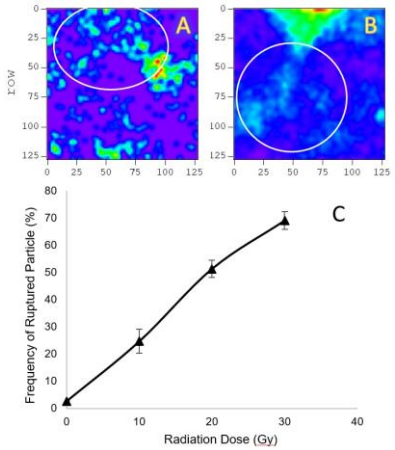

Fig. 2. Ruptured particles by Pt- imaging , observed using micro PIXE camera (A, B), and their frequency vs radiation dose (C) .

Second irradiation and releasing of carboplatin from particles

To those accumulated particles the second radiation was given. The rupturing of particles by irradiation was determined, basing on the two morphological changes, observed by Pt-images of micro PIXE camera: 1) releasing of Pt from particles (Fig. 2 A); 2) particle obfuscation (Fig. 2 B). The frequency of rupturing was expressed as the mean percentage of ruptured particles within 10 views of micro PIXE camera at 12×12 μm scan. The frequency of ruptured particles was increased, dependently on radiation dose (Fig. 2 C).

Antitumor effect

Antitumor effect was measured by alteration of tumor diameter days after treatment. In the combination of radiation with carboplatin that was encapsulated in P-selectin labelled particles, antitumor effect was elongated and enhanced than any other treatments in each radiation dose (Fig. 3 A-C ●). The strongest antitumor effect was observed in the combined treatment of 30 Gy radiation with carboplatin, encapsulated in P-selectin labelled particles (Fig. 3 C ●).

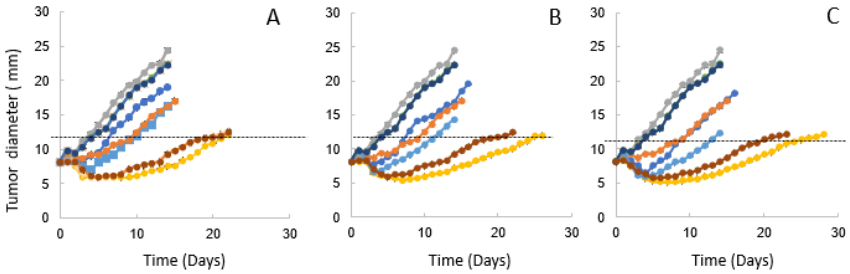

Fig. 3. Antigumor effect. A: 10 Gy, B; 20Gy, C: 30 Gy. ●: No treatment, ●: Unirradiated particle (P-selectin unlabelled) ●: Unirradiated particle (P-selectin labelled), ●: Unencapsulated carboplatin only, ●: Radiation only, ●: Radiation + unencapsulated carboplatin, ●: Radiation + particle (P-selectin unlabelled), ●: Radiation + particle (P-selectin labelled).

Reference

[1] T. Segawa *et. al.* Radiat. Res. **193**, 263 (2020). DOI: 10.1667/RR15357.1

Part Ⅱ

3. Advanced Quantum-Beam Technology

3-01 Measurement test of beam energy and position monitor system in the beam transport line for RI production ····· 100
N. Miyawaki, H. Kashiwagi, S. Kurashima, S. Watanabe and N. S. Ishioka

3-02 Cyclotron development study for the beam formation using the nonlinear magnetic field ····· 101
T. Yuyama, H. Kashiwagi, T. Ishizaka and Y. Yuri

3-03 Fabrication of mold for stamp by proton beam writing and transfer characteristics of printed a-IGZO TFT ····· 102
K. Kawamura, H. Seki, Y. Ishii and H. Nishikawa

3-04 Lithium concentration measurement in lithium-ion battery materials by nuclear reaction ····· 103
T. Satoh, N. Yamada, R. Yamagata, Y. Ishii, B. Tsuchiya, K. Suzuki, T. Kamiya and K. Mima

3-05 Elemental analysis of silica/silicates accumulation in scleroderma lungs by in-air micro PIXE ····· 104
Y. Koga,T. Satoh, N. Yamada, R. Yamagata, T. Hisada and K. Dobashi

3-06 Dentin remineralization enhances by trace-element ····· 105
Y. Matsuda, K. Okuyama, H. Yamamoto, M. Sakurai, K. Naito, H. Kanda, T. Saito, M. Hayashi, Y. Tamaki, T. Satoh, N. Yamada, R. Yamagata and Y. Ishii

3-07 Au sputtering yield by C_{60-} and C_{70}-ion bombardment ····· 106
K. Narumi, K. Yamada, Y. Hirano, A. Chiba, Y. Yuri and Y. Saitoh

3 - 01 Measurement test of beam energy and position monitor system in the beam transport line for RI production

N. Miyawaki[a)], H. Kashiwagi[a)], S. Kurashima[a)], S. Watanabe[b)] and N. S. Ishioka[b)]

[a)]Department of Advanced Radiation Technology, TARRI, QST
[b)]Department of Radiation-Applied Biology Research, TARRI, QST

A beam energy and position monitor (BEPM) [1] is installed to measure beam energy precisely in real time at the beam transport line for the RI production, which is in the straight line with the exit of the TIARA AVF cyclotron. To measure the energy of the beam accelerated by the cyclotron, a precision bending magnet (TAM) on the way of this beamline is usually used, as shown in Fig.1. However, during the more than 30 minutes required for this measurement and the excitation and degaussing of the TAM, the accelerated beam cannot be transported to the target at the end of this beamline and the RI production experiment have to be interrupted.

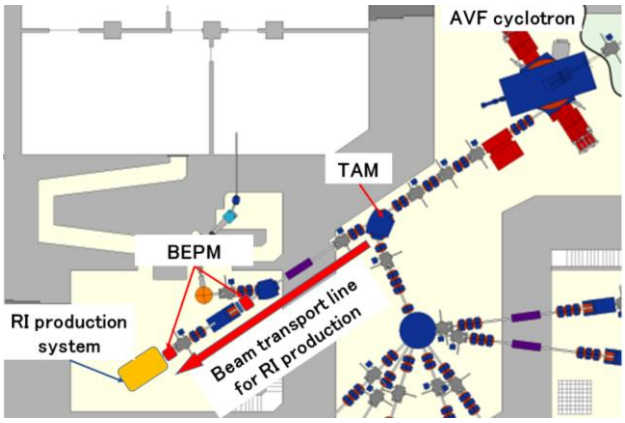

Fig. 1. Schematic layout of the AVF cyclotron and beam transport line for RI production.

The BEPM consists of two cylindrical electrostatic pickup electrodes. The beam energy is calculated from the distance between the electrodes divided by the time difference (time of flight) of each signal produced by the beam passing through the electrodes. It is possible to acquire beam energy in real-time while irradiating the target with a straight beamline, since the beam is not stopped or deflected by the BEPM. The measurement test of a beam energy using the BEPM have been performed by a 50 MeV $^4He^{2+}$ beam. The results of beam energy measurements with the BEPM were compared with the results using the TAM.

The energy measurement results using the BEPM and the TAM on each experimental day are shown in Fig. 2. Due to the tight operating schedule of the cyclotron, there were a few opportunities to measure the beam energy using the TAM. Both measurement methods show that the beam energy often change at each experiment day. The difference of the beam energy is caused by conditions and setting parameters at the time of starting up the cyclotron and the fine adjustment of parameters for the beam. The beam energy measurements using the BEPM are always about 0.4 MeV lower than those of using the TAM. In the beam energy measurement using the TAM, measurement errors are large because the beam position is visually adjusted to the center of the beam duct using an alumina fluorescent plate before entering and after exiting the TAM. In addition, since there is no limit to the angle of the beam injection into the TAM, the beam energy cannot be measured accurately when the beam is obliquely injected into the TAM, and the measured value of the beam energy of the TAM differ from that of the BEPM. On the other hand, since the BEPM can monitor the beam energy in real time, the fluctuation of the beam energy within the same experiment day is also obtained, and the fluctuation is less than about 0.1%. This result shows that the beam energy is almost constant after starting up the cyclotron and the change of parameters due to beam adjustment. Therefore, the beam energy measurement using the BEPM has the advantage of accuracy and real time measurement compared to that using the TAM. Consequently, the use of the BEPM allows us to precisely measurement of the beam energy used for RI production in real time.

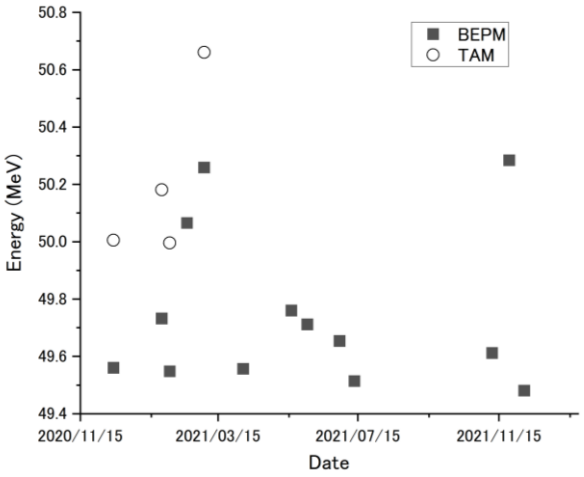

Fig. 2. Measured $^4He^{2+}$ beam energy by the BEPM and the TAM at each experiment.

Acknowledgments

This work was supported by JSPS KAKENHI Grant Number JP20K08014.

Reference

[1] T. Watanabe *et al*., Proc. 14th Annual Meeting of Particle Accelerator Society of Japan, 1114 (2017).

3 - 02 Cyclotron development study for the beam formation using the nonlinear magnetic field

T. Yuyama, H. Kashiwagi, T. Ishizaka and Y. Yuri

Department of Advanced Radiation Technology, TARRI, QST

The technique on nonlinear focusing of charged-particle beams has the potential to form various beam profiles. So far, we have developed the formation techniques of a large-area uniform beam that enables constant-fluence-rate irradiation and a hollow beam that has a high intensity in the radial edge of the beam using multipole magnets [1]. We have conducted some experimental studies mainly with 10-MeV proton beams at the LB line of the TIARA cyclotron for the advanced beam formation [2].

Extraction of a Gaussian-like beam for the large-area uniform beam formation

A beam with a Gaussian transverse distribution is initially required for large-area uniform irradiation with the multipole magnets, so as to fold its outer tail with a nonlinear magnetic field. This initial distribution has been achieved by multiple scattering using a thin foil at the beam line after the beam extraction from the cyclotron. However, there are some problems on the beam loss due to the charge exchange for heavy-ion beams and an increase in the beam emittance. To solve these problems, we tried to obtain a Gaussian-like beam directly using the single-turn extraction from the cyclotron. For this purpose, optimizing the isochronous magnetic field, acceleration phase, and beam extraction adjustment was performed. The measurement result is summarized in Fig. 1. The turn separation of the beam in the cyclotron became more distinct. The extracted beam actually had a Gaussian-like distribution in the horizontal direction at the first diagnostic port (TS1) of the cyclotron beam line.

With this beam tuning in the cyclotron, we will try the large-area uniform beam formation for high-intensity beams and cocktail acceleration of heavy-ion beams.

Measurement of the beam transmission distribution for beam loss reduction in the hollow beam formation

A hollow beam with different cross-sectional shapes can be formed by the horizontal-vertical coupling effect of nonlinear focusing force. However, particles with larger oscillation amplitude can be a source of beam halo, which results in beam loss. Toward reducing the generation of the beam halo, we explored the beam measurement to identify the beam halo using a phase-space collimator [3] installed at the injection section in the cyclotron. Using the phase-space collimator, it is possible to scan an arbitrarily transverse phase-space region and, thus, measure which part of the phase-space region of the injected beam reaches the beam halo or hollow beam. The injection beam regions that form the beam halo and hollow beam can be measured separately by the current in the slits cutting the beam halos and the current in the Faraday cup stopping the hollow beam. The measurement setup and result are shown in Fig. 2. Comparing the graphs in Fig. 2(c), it can be confirmed that the region in which the beam halo is formed is obviously different from the region in which a hollow beam is formed.

Thus, we showed the possibility of increasing the intensity of a hollow beam and reducing the beam halo by optimizing the beam control at the injection section.

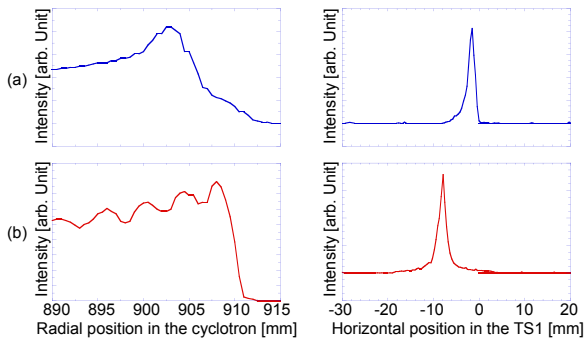

Fig. 1. Measured beam intensity distributions for (a) multi-turn extraction and (b) single-turn extraction. The horizontal intensity distributions (left) before the extraction from the cyclotron and (right) after the extraction.

Acknowledgments

This work was supported in part by JSPS KAKENHI JP18K11934.

References

[1] Y. Yuri *et al.*, Prog. Theor. Exp. Phys. **2019**, 053G01 (2019). DOI:10.1093/ptep/ptz024

[2] H. Kashiwagi *et al.*, Proc. 18th Annual Meeting of Particle Accelerator Society of Japan, 88 (2021).

[3] H. Kashiwagi *et al.*, Rev. Sci. Instrum. **85**, 02A735 (2014). DOI:10.1063/1.4858175

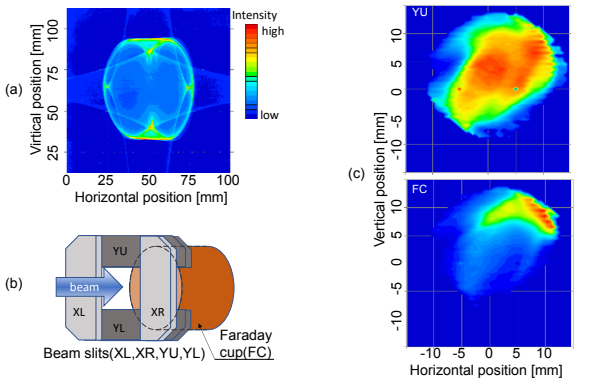

Fig. 2. (a) 2D intensity distribution of a hollow beam with beam halo. (b) The beam measurement configuration. The beam halo and the hollow beam are separated by the slits (XL, XR, YU, YL) and the hollow beam is stopped by a Faraday cup (FC) behind the slits. The real-space transmission distributions of the injected beam reaching YU and FC are shown in (c).

3 - 03 Fabrication of mold for stamp by proton beam writing and transfer characteristics of printed a-IGZO TFT

K. Kawamura[a)], H. Seki[a)], Y. Ishii[b)] and H. Nishikawa[a)]

[a)]Department of Electrical Engineering, Shibaura Institute of Technology
[b)]Department of Advanced Radiation Technology, TARRI, QST

With increasing demand for IoT devices to ensure the safety and security of our society, we need to develop low-cost electronic devices with low-power consumption. Amorphous Indium-Gallium-Zinc-Oxide (a-IGZO) is an oxide semiconductor with superior characteristics such as a high electron mobility and low leakage current [1]. Therefore, these characteristics make a-IGZO TFT as a highly functional switching device with low-power consumption. Since the a-IGZO can be synthesized by a solution process, printing methods using stamps have been proposed as a low-cost and easy to fabricate process [1].

In this report, we studied the application of proton beam writing (PBW) to fabricate molds for the printing process of a-IGZO TFT.

PMMA (Kayaku Microchem, 950A) was spin-coated on Si wafer (400 rpm for 30 secs, 1000 rpm for 2 sec) to make a 10 μm-thick PMMA layer. The PBW was performed using scanning focused beam of 1.0 μm from proton beam facilities at beam energy of 1.0 or 1.7 MeV at Shibaura Institute of Technology or TIARA Takasaki, QST.

The patterning was successfully made with fluence of 100 to 200 nC/mm^2. After development for 20 min. with a solution of isopropyl alcohol (IPA) and water (IPA: water=7:3) and rinse in water, we obtained a mold for PDMS stamps. PDMS solution (Dow Corning, Sylgard184) prepared as specified in the recipe was casted onto the mold of PMMA and cured at 150 °C for 11 min. in air. We confirmed successful pattern transfer from the PMMA mold to 50-200 μm squared PDMS stamps.

We studied the effect of plasma treatments (Harrick Plasma, PDC-32G) on the wettability of IGZO solution (In:Ga:Zn = 6:1:3 [2]). The contact angle on the surface of the PDMS by a measuring system (Dataphysics Instruments, OCA15EC). Figure 1 shows the results of the contact angle measurements of the IGZO solution with PDMS surface. The wettability of the stamp was ensured with increasing plasma treatment time [3].

We used the configuration of a bottom-gate transistor with 300-nm-thick silicon oxide as a gate insulator on silicon wafer, where the Si substrate works as a gate as shown in Fig. 2 (a). A preliminary large area (10 mm-square) pattern transfer was made by an IGZO-spin-coated (2000 rpm for 15 sec) PDMS block. After transfer of the IGZO solution to the oxide from PDMS and baking at 300 °C for 1h in air, we patterned source and drain electrodes by Al evaporation. The dimension of the channel area is 5.0 mm in width and 500 μm in length.

We characterized the transfer characteristics (I_{DS}-V_{GS}) of the a-IGZO TFT with a semiconductor parameter analyzer (HP 4145B). As shown in Fig. 2 (b), the switching characteristics was observed for the stamped IGZO. A comparison with a standard solution process sample by spin coating shows that the onset voltage of V_{GS} shifts to higher region and the on-current I_{DS} is smaller by one-to-two orders of magnitudes.

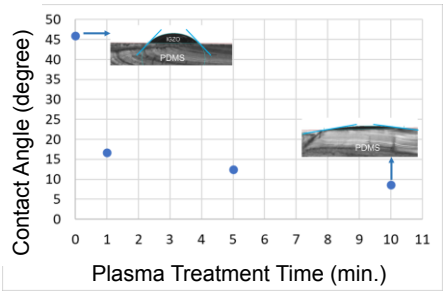

Fig. 1. Contact angles of the IGZO solution to the PDMS stamp as a function of plasma treatment time.

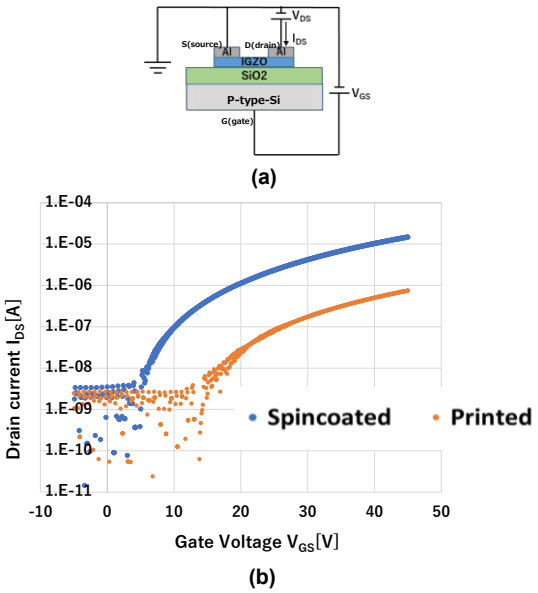

Fig. 2. (a) Schematics of the a-IGZO-TFT characterization and (b) transfer characteristics of the printed a-IGZO TFT compared with spin-coated a-IGZO TFT.

References

[1] S. K. Garlapati, *et al.*, Adv. Mater. **30**, 1707600 (2018). DOI: 10.1002/adma.201707600
[2] Y. Takamori, *et al.*, AIP Adv. **8**, 115304 (2018). DOI: 10.1063/1.5049618
[3] D. Qin, *et al.*, Nat. Protoc. **5**, 493 (2010). DOI:10.1038/nprot.2009.234

3 - 04 Lithium concentration measurement in lithium-ion battery materials by nuclear reaction

T. Satoh[a)], N. Yamada[a)], R. Yamagata[a)], Y. Ishii[a)], B. Tsuchiya[b)], K. Suzuki[c)], T. Kamiya[d)] and K. Mima[e)]

[a)]Department of Advanced Radiation Technology, TARRI, QST
[b)]Faculty of Science and Technology, Meijo University
[c)]Institute of Innovative Research, Tokyo Institute of Technology
[d)]Graduate School of Science and Technology, Gunma University
[e)]Institute of Laser Engineering, Osaka University

Introduction

The practical application of all-solid-state lithium-ion batteries (ASS-LIB) using solid electrolytes requires a significant improvement in output performance, and how to reduce the interfacial resistance between the electrodes and the solid electrolyte is an issue. Therefore, it is essential to develop a method to visualize the movement of lithium.

So far, the two-dimensional distributions of lithium in the ASS-LIBs were successfully measured by detecting prompt 478-keV gamma-rays from the nuclear reaction of ^{7}Li(p, p'γ)^{7}Li induced by a 3.0-MeV proton microbeam.

In contrast, the cathode of an actual ASS-LIB consists of particulate cathode material with a size of approximately 10 μm and a solid electrolyte with a size of 1 μm or less. Therefore, to obtain clues for reducing the interfacial resistance, it is necessary to visualize the dynamics of lithium ions at the interface three-dimensionally with micron-level spatial resolution.

Therefore, in this study, we performed nuclear reaction analysis (NRA) using a MeV-class proton microbeam. Since approximately 10-MeV energy of α-particles from the nuclear reaction ^{7}Li(p, α)^{4}He are attenuated in the sample, it is expected that energy spectra of the α-particles provide information on depth profiles of lithium in a target. As a first step, we built an NRA measurement system and confirmed the quantification using standard samples with different lithium concentrations.

Experiment

Using pulsed laser deposition, standard targets of lithium cobalt oxide, which is commonly used as a positive electrode material, were prepared with different lithium concentrations such as Li_xCoO_2, where $x = 0.2$, 0.4, 0.6, 0.8, 1.0 and 1.4.

A surface barrier detector having sensitive volume of 50 mm^2 × 100 μm was placed at 101 mm from the target and at 140 degrees to the beam axis. At the same time, in order to standardize the dose of the proton beam with yield of characteristic X-rays of cobalt, a Si(Li) detector having sensitive volume of 30 mm^2 × 500 μm was placed at 72 mm from the target and at 140 degrees to the beam axis.

A 3-MeV proton beam from the single-ended machine in TIARA was used. The beam current was approximately 50 pA. To obtain sufficient statistical accuracy, the NRA measurement were made for approximately two hours per target.

Results

Figure 1 shows one of the energy spectra from the surface barrier detector. The large number of counts in channel range bellow 1200 were Rutherford back scattering (RBS) protons. The right shoulder and the peak in the RBS region are due to cobalt and oxygen in the target, respectively. On the other hand, the precious α-particle counts in channel range above 1200 show the concentration of lithium in the target.

Figure 2 shows the total count in channel range above 1200 standardized by the X-ray counts from cobalt, where the horizontal axis represents the lithium concentration. It is confirmed from this result that the quantitative performance for lithium is kept up to $x = 1.0$. That may be related to the lack of crystallographic sites with $x > 1$ in Li_xCoO_2.

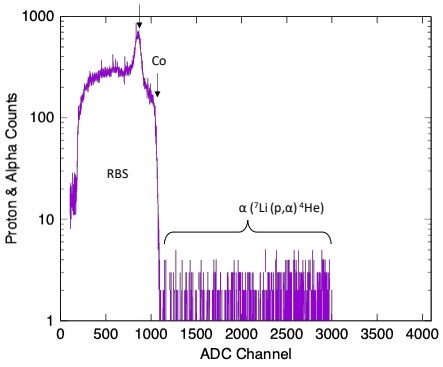

Fig. 1. Energy spectrum from the surface barrier detector.

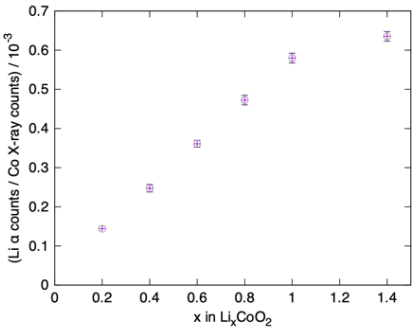

Fig. 2. α counts standardized by cobalt X-ray counts.

Reference

[1] A. Yamazaki *et al.*, Nucl. Instrum. Methods Phys. Res. B **371**, 298 (2016). DOI: 10.1016/j.nimb.2015.10.042

3 - 05 Elemental analysis of silica/silicates accumulation in scleroderma lungs by in-air micro PIXE

Y. Koga[a],T. Satoh[b], N. Yamada[b], R. Yamagata[b], T. Hisada[c] and K. Dobashi[d]

[a]Department of Respiratory Medicine, Gunma University Graduate School of Medicine
[b]Department of Advanced Radiation Technology, TARRI, QST
[c]Gunma University Graduate School of Health Sciences
[d]Jobu Hospital for Respiratory Diseases

Introduction

Collagen disease is a systemic disease that causes connective tissue abnormalities in systemic organs such as the skin, kidneys, lungs, and lymph nodes due to dysfunction of the immune system. Although the causes of connective tissue diseases have not yet been elucidated, it has been suggested that exposure to heavy metals and silica may cause systemic scleroderma, a typical connective tissue disease. Recently we identified the accumulation of silica/silicates in the lungs in patients with idiopathic pulmonary fibrosis by in-air microparticle-induced X-ray emission (micro-PIXE) [1]. Therefore, we performed the elemental analysis of scleroderma lungs by in-air micro-PIXE and compared them with control lungs.

Materials and methods

From 2001 to 2019, elemental analysis of aluminum, magnesium, silica, sulfur, phosphorus, iron, calcium, and zinc in lung tissue specimens of 18 cases of control and systemic sclerosis was performed. The relative concentrations normalized by sulfur concentration were compared each other. Elemental analysis of the normal lung part of 18 cases of early-stage lung cancer was also performed for a control. The elemental distributions of scleroderma and control lungs were statistically compared using Graphpad Prism software.

Results

Elemental analysis of 18 scleroderma lungs by in-air micro-PIXE showed significantly higher relative concentrations of silica and magnesium compared with control lungs (Fig. 1). Aluminum also tended to be higher in scleroderma lungs, however it was not significant. Other elements such as phosphorus, iron, zinc, and calcium did not show significant differences between the two groups.

High-magnification elemental analysis revealed that the silica particles accumulated in the lungs were a few μm in size and could reach the alveolar space (Fig. 2). Furthermore, co-localization of silica with other elements such as iron was shown in part.

Discussion

In-air micro-PIXE analysis of scleroderma lungs suggested that inhalation of silica/silicates into the lungs may be a cause of the development of systemic sclerosis.

References

[1] Y. Koga *et al.*, Environ. Health Prev. Med. **21**, 492 (2016). DOI: 10.1007/s12199-016-0576-5
[2] Y. Koga *et al.*, Environ. Sci. Technol. Lett. **8**, 903 (2021). DOI: 10.1021/acs.estlett.1c00659

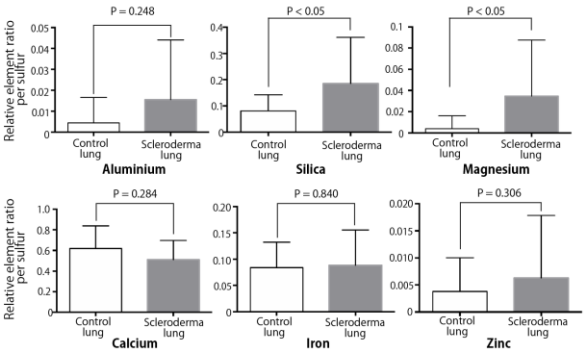

Fig. 1. Elemental comparison between control and scleroderma lungs by in-air micro PIXE. Significant difference between control (n = 18) and scleroderma lungs (n = 18) of silica and magnesium accumulation. Aluminium also tended to be increased in scleroderma lungs.

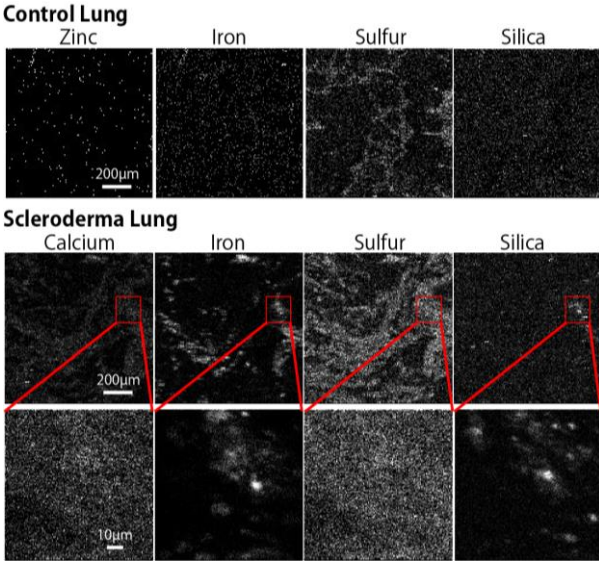

Fig. 2. Representative elemental images of control and scleroderma lungs by in-air micro PIXE. High magnification analysis of in-air micro PIXE showed the aggregation of a few μm particles containing silica/silicates in the scleroderma lungs. No apparent aggregation of silica particles was seen in the control lungs.

3 - 06 Dentin remineralization enhances by trace-element

Y. Matsuda[a)], K. Okuyama[b)], H. Yamamoto[c)], M. Sakurai[b)], K. Naito[c)], H. Kanda[c)], T. Saito[a)], M. Hayashi[c)], Y. Tamaki[b)], T. Satoh[d)], N. Yamada[d)], R. Yamagata[d)] , Y. Ishii[d)]

[a)]School of Dentistry, Health Sciences University of Hokkaido,
[b)]Asahi University School of Dentistry,
[c)]Graduate School of Dentistry, Osaka University,
[d)]Department of Advanced Radiation Technology, TARRI, QST

We have previously reported that the ZnO/CuO nanocomposite has antibacterial effects [1]. In addition, zinc and copper are known to enhance remineralization and inhibit demineralization. Therefore, this study aimed to evaluate the remineralization effects of trace elements.

Materials and Methods

Three extracted bovine teeth were used in the present study. The teeth were cut horizontally to obtain specimens with approximately 500 μm thickness. The sliced specimens were immersed in a 10% lactic acid solution for 72 hours. Additionally, 1% solutions of $ZnCl_2$, $CuSO_4$, $MgCl_2$, and NaF were prepared. The demineralized specimens were immersed in these material solutions 48 hours. The control group was immersed in distilled water.

After immersing the material solutions, the specimens were remineralized in the remineralized solution (pH 6.8, 0.02 M HEPES, 3.0 mM $CaCl_2$, and 1.8 mM KH_2PO_4) at 37 °C one week. The analytical techniques in this study were the same as those reported previously [1]. In -air micro-PIXE/PIGE analysis was carried out using a 1.7-MeV proton beam from the single-ended accelerator at TARRI. One of the specimens was attached directly to a window at the end of the microbeam line. The beam spot size was approximately 1 μm in diameter with a beam current of approximately 100 pA.

The Ca and trace element concentrations were measured at a 270 μm × 270 μm area. The measured data were opened using the analysis application package program, which converted the data into 128 × 128 pixels. After those measurement, one-way ANOVA and Tukey's test were used for the analysis ($p < 0.05$).

Results

Figure 1 shows the volume of calcium in the dentin. The number of material groups was significantly different from that of the control group. However, there were no significant differences among the material groups. These results suggested that trace-elements in the collagen of dentin will enhance the remineralization. The trace-elements. The elements uptake showed the significant differences among the element types.

Discussion

Although the trace element solutions concentrations were the same, there were significant differences in the amounts taken up to the dentin.

Fluorine was the smallest element used in this study and therefore was considered to have penetrated more.

However, despite being larger than zinc, copper penetrated the dentin more predominantly than zinc, possibly because copper is involved in the cross-linking structure of collagen fibers and has a higher affinity for collagen than zinc. In the future, we would like to further investigate the role of trace elements in dentin remineralization in more detail.

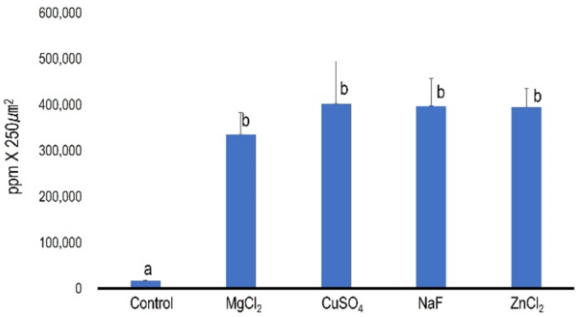

Fig. 1. Volume of calcium in the remineralized dentin. The same letters indicate no significant differences ($p > 0.05$).

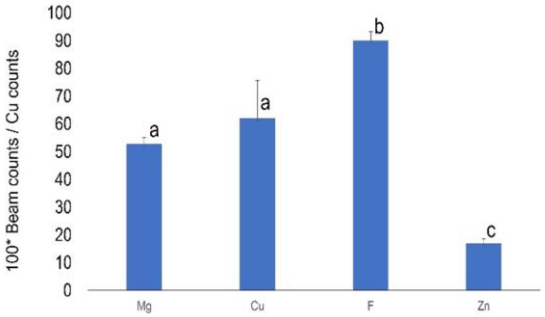

Fig. 2. Trace-element beam counts / Cu counts in the remineralized dentin.

Acknowledgments

We thank the staff of the National Institutes for Quantum Science and Technology (QST) This study was supported in part by a Grant-in-Aid for Scientific Research from the Japan Society for the Promotion of Science, Scientific Research (No.C- 20K09962, A- 20H00552, C- 19K10136, B- 18H02979, C- 17K11712).

Reference

[1] Altankhishig B. *et al.*, Nanomaterials 1291 (2022). DOI: 10.3390/nano12081291

3 - 07 Au sputtering yield by C_{60}- and C_{70}-ion bombardment

K. Narumi, K. Yamada, Y. Hirano, A. Chiba, Y. Yuri and Y. Saitoh

Department of Advanced Radiation Technology, TARRI, QST

When an energetic molecular or cluster ion is incident on condensed matter, its constituent ions or atoms simultaneously collide with many target atoms in a small space. This leads to highly dense energy deposition. A large molecule or cluster such as fullerenes should induce such an effect significantly, which can make fullerene-ion beams a promising tool for highly dense energy deposition. For application use of fullerene-ion beams, two factors are indispensable: One is stable and intense beams. We succeeded in supplying stable 0.03-to-1-MeV C_{60}- and C_{70}-ion beams with enough flux from a 400-kV ion implanter of TIARA. In addition, we have recently developed a highly intense negative fullerene-ion source for a tandem accelerator [1]. The other factor is practical data on fundamental processes relating to ion stopping in matter; as known well, ion-beam applications at present are based on such huge practical data. There are not enough data on fullerene ions up to the present. Sputtering is one of the most important subjects, because it is not only a characteristic of cluster-ion bombardment but also closely related to fullerene-ion stopping in condensed matter and secondary-ion emissions by fullerene ions. In the present study, we have measured Au sputtering yields by 0.03-to-9-MeV C_{60}- and C_{70}-ion bombardment.

Au sputtering yields were measured with a quartz-crystal microbalance technique. A Au thin film, which was one of the electrodes on a quartz crystal, was used as a target as it is and was bombarded with C_{60} and C_{70} ions. These ions were accelerated to 0.03 to 1.08 MeV and to 1.08 to 9 MeV with the 400-kV ion implanter and a 3-MV tandem accelerator of TIARA, respectively. Sputtering yields by 18-to-150-keV C^+ ions were also measured.

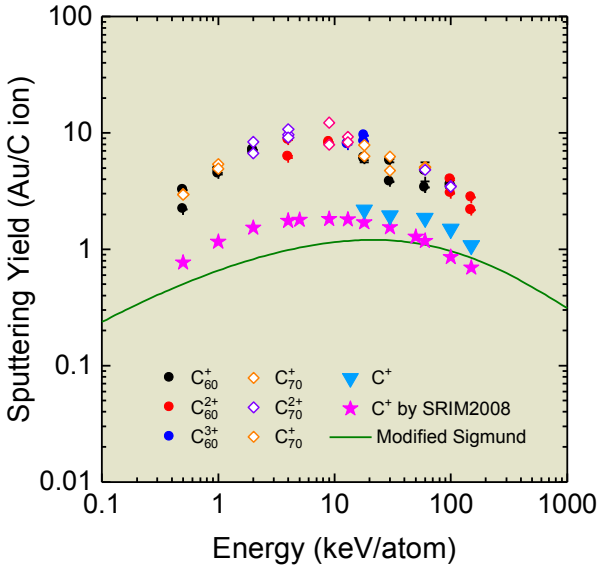

Fig. 1. Energy dependence of the sputtering yield per constituent atom of an incident ion. The results of Monte Carlo simulations using the SRIM2008 code and calculations by modified Sigmund theory are represented by stars and a solid curve, respectively.

Figure 1 shows the experimental results, the dependence of the sputtering yield per constituent atom of an incident ion on the energy per atom. The sputtering yields by C monatomic ions are also plotted. As shown in the figure, the sputtering yields per atom are nearly equal for C_{60} and C_{70} ions. Both the sputtering yields per atom rise to the peak of approximately 10 around 10 keV/atom. The sputtering yields by C monatomic ions are compared with SRIM simulation [2] as well as the linear-collision-cascade theory by Sigmund [3]. In the Monte Carlo simulation using the SRIM2008 code, the lattice binding energy, the surface binding energy and the displacement energy were 3.0 eV, 3.8 eV and 25.0 eV, respectively. The nuclear stopping power for a C monatomic ion in the calculation of Sigmund's theory was calculated using the SRIM2008 code. The agreement between the experiments and the calculations for C monatomic ions is not so bad. The sputtering yields per atom by C_{60} and C_{70} ions are 2~4 times larger than those by C monatomic ions, which means that the nonlinear effect was observed.

Acknowledgments

This work was supported in part by JSPS KAKENHI Grant Number JP18K05005, and partially supported by the Inter-organizational Atomic Energy Research Program in an academic collaborative agreement among JAEA, QST and the Univ. of Tokyo.

References

[1] A. Chiba *et al.*, Quantum Beam Sci. **4**, 13 (2020). DOI: 10.3390/qubs4010013
[2] Available online: http://www.srim.org.
[3] P. Sigmund, Phys.l Rev. **184**, 383 (1969). DOI: 10.1103/PhysRev.184.383

Part Ⅱ

4. Status of Quantum-Beam Facilities

4-01 Utilization status at the TIARA facility ····· 108
H. Hanaya, I. Ishibori, H. Takizawa, S. Watanabe, N. Kubota, T. Shimizu and S. Kaneya

4-02 Operation of the AVF cyclotron ····· 109
K. Yoshida, T. Yuyama, T. Ishizaka, S. Hosoya, I. Ishibori, N. Miyawaki, H. Kashiwagi, T. Nara, S. Ishiro, K. Takano and S. Kurashima

4-03 Operation of electrostatic accelerators in TIARA ····· 110
K. Yamada, A. Chiba, Y. Hirano, S. Kanai, Y. Aoki, M. Hashizume and S. Kurashima

4-04 Operation status of the electron accelerator and the gamma-ray irradiation facilities ····· 111
H. Seito, Y. Nagao, S. Yamasaki, E. Yokozuka, T. Agematsu, M. Hosono, N. Yagi, M. Takagi, K. Imai, K. Akaiwa, S. Uno and N. Nagasawa

4-05 Utilization status of the electron accelerator and the gamma-ray irradiation facilities ····· 112
H. Seito, Y. Nagao, S. Yamasaki, E. Yokozuka, T. Agematsu, M. Hosono, N. Yagi, M. Takagi, K. Imai, K. Akaiwa, S. Uno and N. Nagasawa

4-06 Radiation monitoring in TIARA ····· 113
Safety Management Section

4-07 Radioactive waste management in TIARA ····· 114
N. Higuchi

4-08 Facility Use Program in Takasaki Advanced Radiation Research Institute ····· 115
S. Nozawa, H. Hanaya and A. Shimada

4 - 01 Utilization status at the TIARA facility

H. Hanaya[a)], I. Ishibori[a)], H. Takizawa[a)], S. Watanabe[a)],
N. Kubota[a)], T. Shimizu[b)] and S. Kaneya[c)]

[a)]Department of Advanced Radiation Technology, TARRI, QST
[b)]Takasaki Establishment, Radiation Application Development Association
[c)]Beam Operation Co., Ltd.

Research & industrial use

Four kinds of accelerators, a cyclotron and three electrostatic accelerators (tandem accelerator, single-ended accelerator and an ion implanter), are used at the TIARA facility to meet various researchers' needs. The activities of research fields that the cyclotron was used for the past 5 fiscal years are shown in Fig. 1. Total utilization time of each fiscal year (FY) was in the range of 1,090 to 1,380 hours except for FY 2018 and FY 2021. The utilization time of FY 2018 was reduced to about 500 hours because of repairing of the main coil of the cyclotron. And also, the utilization time of FY 2021 was reduced to about 800 hours because of changing of the cyclotron operating time from 24 hours to 14 hours. The utilization time of "Material Science" and "Life Science" accounted for more than about 60% of the total time.

On the other hand, for the three electrostatic accelerators, as shown in Fig. 2, the utilization time of "Material Science" and "Basic Technology of Quantum Beam" accounted for more than about 60% of the total time. Total utilization time amounted to about 430 days per year until FY 2019. However, in FY 2020 and FY 2021, total utilization time was reduced due to the cancel of experiments under the influence of COVID-19 and to the renewal of control systems of the three electrostatic accelerators.

The trend of the number of project category (Internal use, Joint research, Cooperation priority research, Funded research and Facility use program) for the past 5 years is shown in Fig. 3. The total number of projects was in the range of 59 to 73 per year.

The trend of the number of users in the past 5 years is shown in Fig. 4. The total number of users was in the range of 460 to 770 per year.

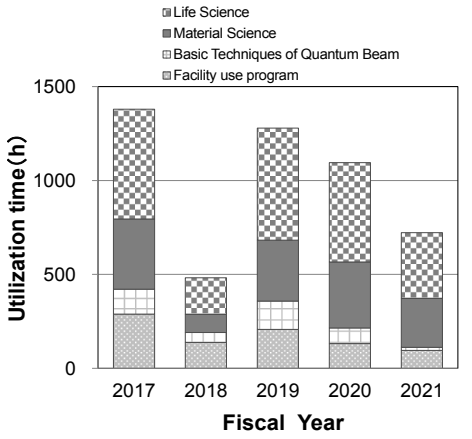

Fig. 1. Research activities for the cyclotron for the past 5 years.

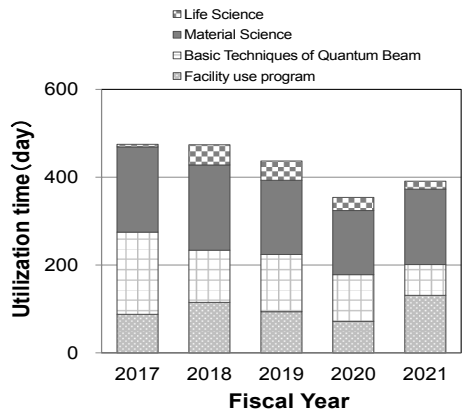

Fig. 2. Research activities for the three electrostatic accelerators for the past 5 years.

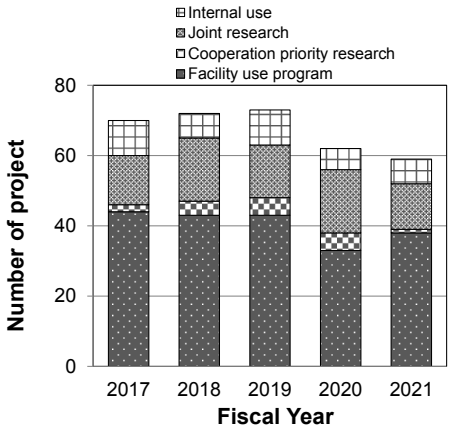

Fig. 3. The number of projects for the past 5 years.

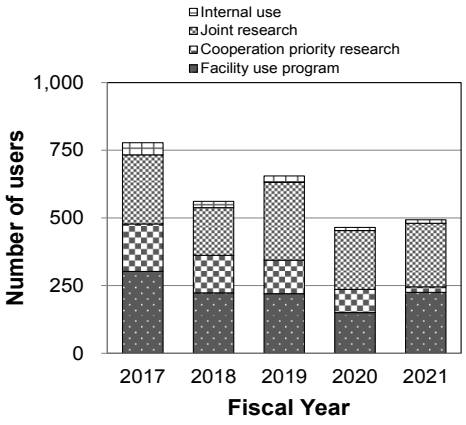

Fig. 4. The number of users for the past 5 years.

4 - 02 Operation of the AVF cyclotron

K. Yoshida, T. Yuyama, T. Ishizaka, S. Hosoya, I. Ishibori, N. Miyawaki,
H. Kashiwagi, T. Nara, S. Ishiro, K. Takano and S. Kurashima

Department of Advanced Radiation Technology, TARRI, QST

Operation

Since the continuous operation of the cyclotron from Monday to Friday was abolished, operation time of the AVF cyclotron in fiscal year of 2021 was remarkably reduced. After checking the water-cooling system and changing the acceleration harmonics, the operation of the cyclotron starts every day by 11 am. After careful beam tuning, the experiment starts at 2 pm. or 3 pm. and ends at 10 pm. The total operation time of the AVF cyclotron eventually amounted to 1338 h, and the number of experiments of the year was 189. The accumulative operation time was 88762 h and the total number of experiments was 12679 from the first beam extraction in 1991 to March, 2022.

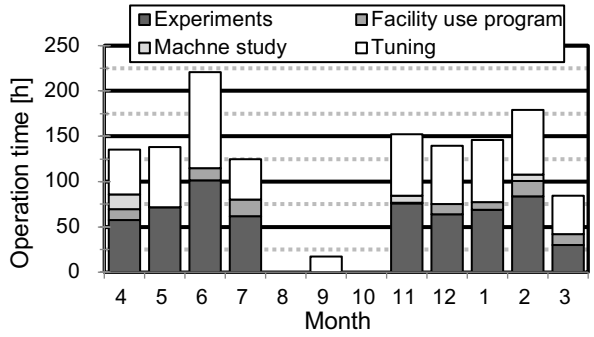

Fig. 1. Monthly operation times in fiscal 2021.

Table 1
Statistics for cyclotron operation.

Fiscal year	2020	2021
Beam service time	1035 h	708 h
Beam tuning	722 h	598h
Machine study	123 h	32 h
Total operation time	1880 h	1338 h
Change of particle and/or energy	152 times	143 times
Change of beam course	135 times	141 times
Change of harmonic number	67 times	61 times
The number of experiments	194	189
Cancellation due to machine trouble	0	0

Monthly operation times are shown in Fig. 1. The scheduled maintenances were carried out from the middle of July to October and in March. Table 1 shows the statistics of the cyclotron operation of fiscal 2021, with the data of fiscal 2020 for comparison. The percentages of operation time of the year used for regular experiments, facility use program and promotion of shared use program, beam tuning, and beam development are 46.0%, 6.9%, 44.7%, and 2.4%, respectively. Table 2 shows the operation time of each ion source. NANOGAN ion source is used to produce H, D, and He ions. For production of ions heavier than He, HYPERNANOGAN ion source is used. OCTOPUS ion source is mainly used for the cocktail beam of M/Q = 5. The operation times of OCTOPUS and HYPERNANOGAN ion source were reduced by the abolishment of 24 hours operation. Fractional distribution of major ions used for experiments is shown in Fig. 2. The tendencies of the statistics are similar to those of the past years.

Table 2
Operation times of ion sources.

ECR Ion source	2020	2021
NANOGAN	530 h (26.0%)	504 h (33.3%)
OCTOPUS	365 h (17.9%)	159 h (10.5%)
HYPERNANOGAN	1143 h (56.1%)	852 h (56.2%)

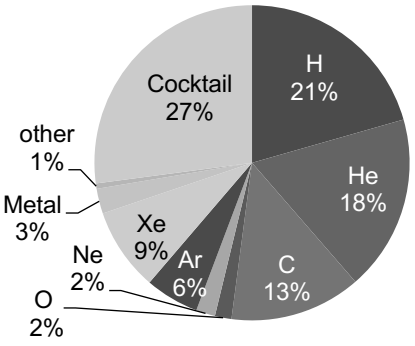

Fig. 2. Ion species used for experiments in fiscal 2021.

Machine trouble and maintenance

The number of machine troubles and maintenances of the year were 64 and 69, respectively. The rubber hoses of the main coils for cooling water between the valve and the main coil were replaced in summer. The beam detector of the magnetic channel probe was replaced to improve water cooling efficiency. The P501 water pump for ion sources and injection line was overhauled due to water leakage from the mechanical seal.

The other major items of the maintenance were as follows: 1) Inspection of all power supply for magnet coils. 2) Replacement of the consumable parts of the cryopumps of the beam injection line. 3) Replacement of the fast-closing vacuum valve controller of the HC line. 4) Replacements of the gas leakage detector in the ion-source room. 5) Inspection of the power supplies and the main RF system. 6) Change of lubricating oil for 47 vacuum pumps. 7) Replacements of internal power supply and cooling fan in the control systems.

4 - 03 Operation of electrostatic accelerators in TIARA

K. Yamada, A. Chiba, Y. Hirano, S. Kanai,
Y. Aoki, M. Hashizume and S. Kurashima

Depaertment of Advanced Radiation Technology, TARRI, QST

Operation

The transitions of the annual operation time since the start of operation for each electrostatic accelerator are shown in Fig. 1. The annual operation times of the tandem accelerator, the single-ended accelerator and the ion implanter in FY 2021 were 1,021 h, 1,227 h and 918 h, respectively. With the revision of the management structure of the electrostatic accelerators, the daily operation time of the accelerators has been shortened about 5 h from FY 2021. Therefore, the annual operation times of all accelerators were significantly lower than last fiscal year. The monthly operation times of FY 2021 for each electrostatic accelerator are shown in Fig. 2. The significant decrease in operating times from February to March is due to the upgrade of the control systems of each electrostatic accelerator. There were no serious problems with the tandem accelerator and the ion implanter that the experiment had to be stopped. On the other hand, the experiments with the single-ended accelerator were cancelled for four days due to the damage of voltage measurement resistor and the vacuum tube of the RF oscillator circuit caused by the discharge of acceleration voltage. In the regular maintenance, the pellet-chain of the tandem accelerator was cleaned, and the alignment of the extraction electrode of the single-ended accelerator was done and each ion source of accelerators was overhauled.

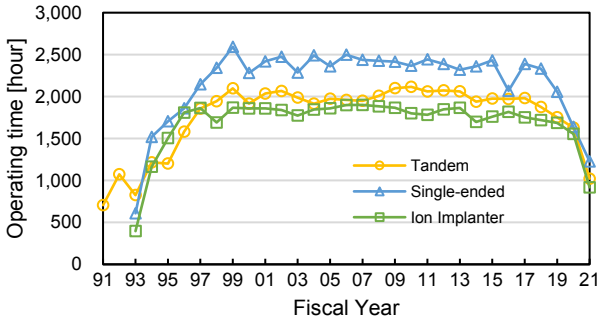

Fig. 1. Transitions of annual operation time.

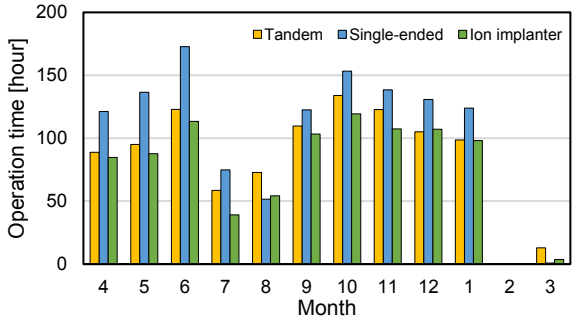

Fig. 2. Monthly operation time.

Upgrade of accelerator control systems

The deterioration of control PCs and remote I/O controllers of the accelerator control system was a common problem for all three electrostatic accelerators. In recent years, the control PCs have often hung up, requiring a reboot each time, which lost time of experiments using the electrostatic accelerators [1]. Therefore, the control PC and software for each electrostatic accelerator have been updated to be compatible with the current Linux OS. For the tandem accelerator, in addition to the control PC, the remote I/O controllers and three analyzing magnet power supplies for the beam transport line, which had been used for about 30 years, were upgraded shown in Fig. 3. The type of remote I/O controller was changed from the CAMAC to the ACT system made by National Electrostatics Corporation. As a result of these upgrades, control of the analyzing magnetic field became more precise and the ion beam stability has been improved. Around the same time, focusing magnet and control systems of the light- and heavy-ion-micro-beamline were upgraded. Using these upgraded accelerator control systems and micro-beamlines, we plan to develop more advanced irradiation technique in the future.

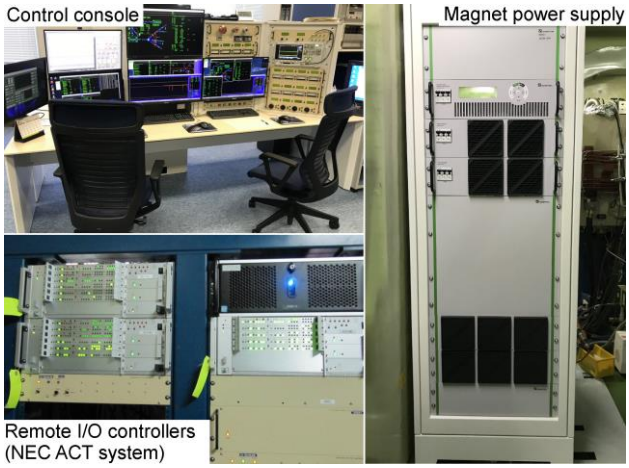

Fig. 3. Upgraded control system and magnet power supply of the tandem accelerator.

Reference

[1] A. Chiba *et al.*, QST Takasaki Annu. Rep. 2017 **QST-M-16**, 150 (2019).

4 - 04 Operation status of the electron accelerator and the gamma-rays irradiation facilities

H. Seito[a)], Y. Nagao[a)], S. Yamasaki[a)], E. Yokozuka[a)], T. Agematsu[a)], M. Hosono[a)], N. Yagi[b)], M. Takagi[b)], K. Imai[b)], K. Akaiwa[b)], S. Uno[a)] and N. Nagasawa[a)]

[a)]Department of Advanced Radiation Technology, TARRI, QST
[b)]Takasaki Establishment, Radiation Application Development Association

Operation

The electron accelerator and the ^{60}Co gamma-ray irradiation facilities in Takasaki Advanced Radiation Research Institute (TARRI) were operated almost smoothly in fiscal year 2021 (FY2021).

The operation of the electron accelerator, and the first and the second ^{60}Co gamma-ray irradiation facilities was suspended in FY2021 due to the seismic reinforcement work of their buildings.

The annual operation time of the electron accelerator in FY 2021 was 312 h, including 45 h of conditioning operation to keep the accelerator in good condition. The annual operation time decreased due to the seismic reinforcement work. The operation time in recent years is shown in Fig. 1. Although there was a trouble about the high frequency power supply unit of the accelerator, the annual operation time shows an increasing tendency from FY2017 to FY2021 because the number of long-time irradiation experiment increased. Despite the influence of COVID-19, the annual operation time in FY 2020 did not decrease due to long-time irradiation experiments conducted by the in-house users.

The ^{60}Co gamma-ray irradiation facilities consisting of three buildings with eight irradiation rooms cover a wide dose-rate range from 2×10^{-1} Gy/h to 0.9×10^{4} Gy/h as of March 2021. The annual operation times of the first and the second ^{60}Co gamma-ray irradiation facilities and the food irradiation facility were 14,008 h, 11,806 h and 13,419 h, respectively, as shown in Fig. 2. The annual operation time until FY 2017 increased because long-time irradiation increased. However, the annual operation time decreased from FY 2018 because long-time irradiation experiments by the in-house users decreased. Due to the influence of COVID-19, the number of irradiation experiments by in-house and outside users decreased, but the long-time irradition experiments didn't lead decrease of the operating time in FY2020. Except for the food irradiation building, which did not undergo seismic reinforcement work, the annual operation time in FY2021 also decreased due to the seismic reinforcement work.

Maintenance

In the seismic reinforcement works of the electron accelerator building, the first and the second ^{60}Co gamma-rays irradiation facilities, reinforce of the structural steel frame of the facility was carried out, as well as replacement of the mercury lamps in the ceiling with LEDs, and update of the shutters and emergency exit doors.

・*Electron accelerator*

The trouble of the horizontal beam line occurred at the beginning of December 2017, and generation of the horizontal beam came to a halt. We found in the maintenance in 2018 that this trouble was due to failure of a certain capacitor of the power supply circuit for the electron gun, not to failure of a filament. Replacement of this capacitor was performed during the maintenance inspection conducted in 2019, 2020 and 2021, and the electron beams of the horizontal beamline were generated with good stability. Since the opening and closing problem of shield door of the horizontal irradiation room occurred and human assistance was required under unsafe condition, a shield door hinge which were the causes of the problem was updated in FY 2021.

・*Gamma-ray irradiation facilities*

The periodical maintenance check mainly on mechanical systems for radiation source transportation is performed every year at one of the three gamma-rays irradiation facilities in turn. The maintenance check of the first ^{60}Co gamma-rays irradiation facility was done in October and November 2021 with suspension of operation for 21 days. The food irradiation facility closed at the end of February 2022.

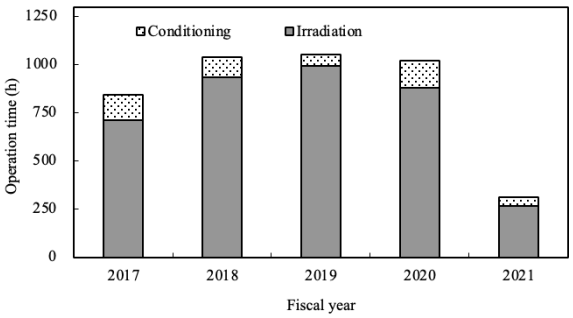

Fig. 1. Annual operation time of the electron accelerator.

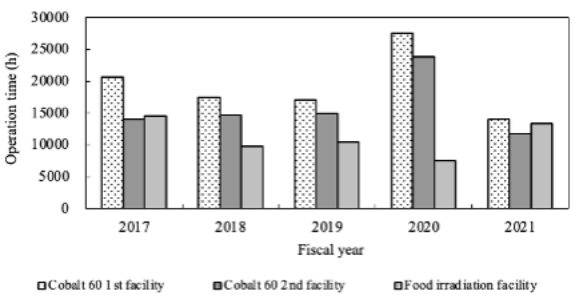

Fig. 2. Annual operation time of the ^{60}Co gamma-rays irradiation facilities.

4 - 05 Utilization status of the electron accelerator and the gamma-ray irradiation facilities

H. Seito[a)], Y. Nagao[a)], S. Yamasaki[a)], E. Yokozuka[a)], T. Agematsu[a)], M. Hosono[a)], N. Yagi[b)], M. Takagi[b)], K. Imai[b)], K. Akaiwa[b)], S. Uno[a)] and N. Nagasawa[a)]

[a)]Department of Advanced Radiation Technology, TARRI, QST
[b)]Takasaki Establishment, Radiation Application Development Association

The electron accelerator and the three ^{60}Co gamma-ray irradiation facilities were operated for various research subjects according to the operation plans of the fiscal year (FY) 2021. Their research fields were classified to 'Materials science', 'Life science', and 'Quantum beam science'.

Figure 1 shows the time and the number of electron beam (EB) irradiation experiments in each research field in FYs 2017-2021. The accelerator was mainly used for materials science such as NV-center process in diamonds, novel catalyst materials, graft-polymerization for new absorbent material and so on. The EB-irradiation time increased in FYs 2017 - 2020 due to smoother operation than in FY 2016. The irradiation time in FYs 2018-2020 increased because of increase in long-term irradiation for research in material science such as developing techniques of NV-center process in diamonds and novel catalyst. But the irradiation time for 'Facility Use Program' in FY 2020 was dramatically reduced under the influence of the rise of irradiation fee and COVID-19. In FY 2021, the irradiation time was shortened to about 20% of the usual year due to the seismic reinforcement work for the building. Therefore, the time and the number of electron beam irradiation dramatically reduced.

Figure 2 shows the time and the number of gamma-ray irradiation experiments in each research field in FYs 2017-2021. The gamma-rays irradiation time decreases year by year except FY2019. This is because of a reduction of a research subject on the radiation resistance test of materials and equipment that required long-term irradiation. Furthermore, research on the creation of novel functional materials synthesized in a short time using high dose rates of gamma-rays also decreased since the sources of ^{60}Co could not be supplied enough to increase the radiation intensity in gamma-rays irradiation facilities. In FY 2021, the irradiation time of each facility was also shortened to about 30% of the usual year due to the seismic reinforcement work for the first and second ^{60}Co gamma-rays irradiation facilities. As a result, the time and the number of the gamma-ray irradiation experiment also decreased dramatically.

The first ^{60}Co gamma-rays irradiation facility was employed mainly for long-term-radiation-resistant tests, such as polymeric materials used for accelerators, cables used in nuclear power plants and nuclear reactor facilities. The second ^{60}Co gamma-rays irradiation facility, including the irradiation room No.6 operated according to hourly schedule, was used for development of new functional polymeric materials such as biocompatible protein hydrogels, fuel cell separator membrane and hydrogen fuel tube, as well as radiation-resistant tests of materials and parts for International Thermonuclear Experimental Reactor (ITER), and other research subjects. The food irradiation facility of a lower-dose-rate field was used for radiation-resistant tests of electric devices and Li battery at wide dose-rate ranges to simulate the space environment and radiation effects of organisms such as microorganisms and plants.

Especially in the ^{60}Co gamma-rays irradiation facilities, several irradiation-resistance experiments of various devices used in the accident of the Fukushima Daiichi Nuclear Power Station of Tokyo Electric Power Company were carried out largely using 'Facility Use Program'.

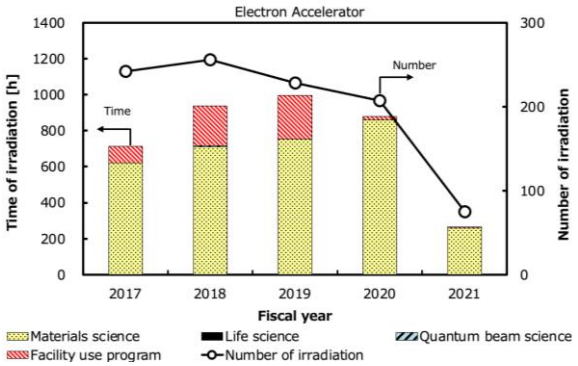

Fig. 1. The time and the number of irradiation experiments in the electron accelerator.

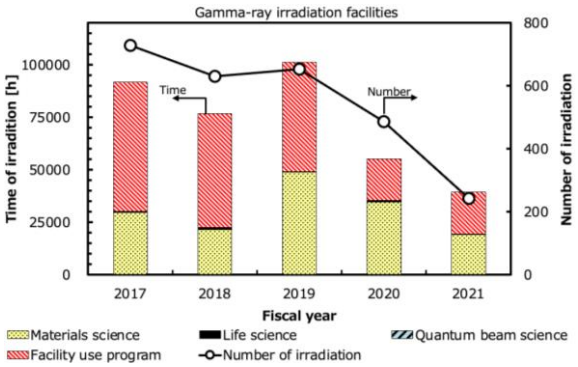

Fig. 2. The time and the number of irradiation experiments in the ^{60}Co gamma-rays irradiation facilities.

4 - 06 Radiation Monitoring in TIARA

Safety Management Section

Department of Administrative Services, TARRI, QST

Individual monitoring

(1) Individual monitoring for the radiation workers

Table 1 shows a distribution of effective dose of the radiation workers in FY 2021. The effective dose values of almost all radiation workers were below the detection limit of 0.1 mSv.

The maximum dose of the radiation worker was 0.2 mSv/y, which was due to experiments with positron-emitting radionuclide.

Table 1
Distributions of the effective dose of the radiation workers in FY 2021.

Items		Number of persons in each periods				
		1st quarter	2nd quarter	3rd quarter	4th quarter	Annual
Distribution range of effective dose HE:Effective dose *1 (mSv)	HE ＜ 0.1	562	630	655	604	864
	0.1 ≦ HE ≦ 1.0	1	1	2	1	4
	1.0 ＜ HE ≦ 5.0	0	0	0	0	0
	5.0 ＜ HE ≦ 15.0	0	0	0	0	0
	15.0 ＜ HE	0	0	0	0	0
Total number of persons (A)		563	631	657	605	868
Exposure above 1mSv	Number of persons (B)	0	0	0	0	0
	(B)/(A)×100(%)	0	0	0	0	0
Mass effective dose (Person･mSv)		0.1	0.1	0.2	0.1	0.5
Mean dose (mSv)		0.00	0.00	0.00	0.00	0.00
Maximum dose (mSv)		0.1	0.1	0.1	0.1	0.2

*1 The dose by the internal exposure was not detected.

(2) Individual monitoring for the visitors and others

Table 2 shows the number of people who temporarily entered the radiation controlled areas. The effective doses of all people were less than 0.1 mSv.

Table 2
The number of people who temporarily entered the radiation controlled areas in FY 2021.

Periods	1st quarter	2nd quarter	3rd quarter	4th quarter	Total
Number of persons	209	247	313	408	1,177

Monitoring of radioactive gases and dusts

Table 3 shows the maximum radioactive concentrations and total activities for radioactive gases released from the stack of TIARA in each quarter of FY 2021.

Small amounts of ^{11}C and ^{77}Br were detected occasionally during the operation of the cyclotron or experiments, but the particulate substances (^{65}Zn, etc.) were not detected.

Table 3
Monitoring results of released radioactive gases and dust in FY 2021.

Nuclide	Periods / Items	1st quarter	2nd quarter	3rd quarter	4th quarter	Total
^{41}Ar	Maximum concentration	$<1.2\times10^{-4}$	$<1.2\times10^{-4}$	$<1.2\times10^{-4}$	$<1.2\times10^{-4}$	
	Activity	0	0	0	0	0
^{11}C	Maximum concentration	$<1.2\times10^{-4}$	$<1.2\times10^{-4}$	$<1.2\times10^{-4}$	$<1.2\times10^{-4}$	
	Activity	2.0×10^{8}	1.1×10^{8}	2.8×10^{8}	2.7×10^{8}	8.6×10^{8}
^{77}Br	Maximum concentration	—	—	—	3.1×10^{-9}	
	Activity	—	—	—	5.2×10^{4}	5.2×10^{4}
^{65}Zn	Maximum concentration	$<5.8\times10^{-10}$	$<1.2\times10^{-9}$	$<6.9\times10^{-10}$	$<7.9\times10^{-10}$	
	Activity	0	0	0	0	0

Unit : Bq/cm^3 for Maximum concentration, Bq for Activity.

Monitoring for external radiation and surface contamination

The monitoring for external radiation and surface contamination was routinely performed in/around the radiation controlled areas. Neither anomalous value of dose equivalent rate nor surface contamination was detected.

Figure 1 shows a typical example of distribution of the dose equivalent rate in the radiation controlled area of the cyclotron building.

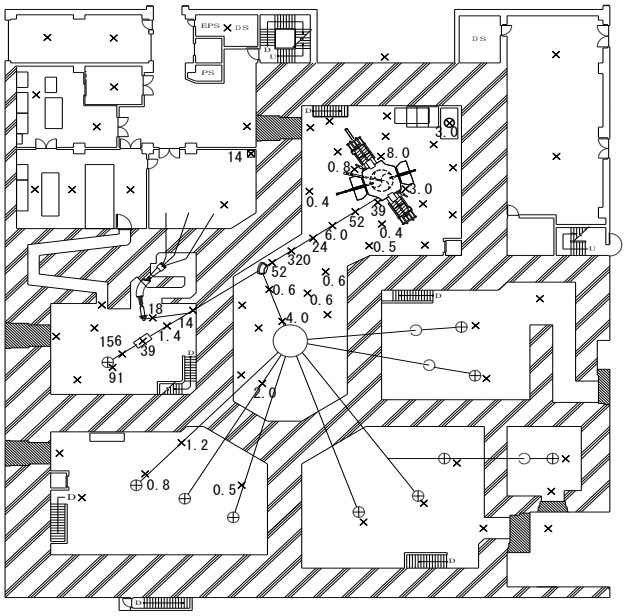

Fig. 1. Dose equivalent rate distribution in the radiation controlled area of the cyclotron building.
Measurement date : 9th, 24th and 25th March 2022,
Measuring position : Indicated with × (1 m above floor),
Unit : μSv/h.(The values are not indicated if less than 0.2 μSv/h.)

4 - 07 Radioactive waste management in TIARA

N. Higuchi

Department of Administrative Services, TARRI, QST

Radioactive waste management

The radioactive waste generated in TIARA is managed by Utilities and Maintenance Section. The main radioactive waste is the solid waste generated from research experiments and the maintenance of the cyclotron. Other radioactive waste is the liquid waste such as inorganic waste fluids generated from research experiments and the air-conditioning machines in the radiation controlled area. These wastes are managed according to their properties. Radioactive waste is stored in a storage facility and handed over to the Japan Radioisotope Association for disposal.

Solid radioactive waste

Table 1 shows the amounts of various types of solid waste generated in each quarter of FY 2021. Combustible waste consists of papers and clothes, and so on. Flame-retardant waste consists of rubber gloves, plastic articles, and polyethylene articles. Incombustible waste consists of metal pieces, the glasses, and contaminated parts. Solid waste emitting α, β, and γ is classified according to the properties.

Liquid radioactive waste

Table 2 shows the amounts of liquid waste generated in each quarter of FY 2021. Most of liquid waste was inorganic waste water generated from chemical experiments and others were condensed water going out of the air-conditioner installed in the radiation controlled area. The largest amount of waste water in summer season (2nd quarter) was the condensed water. After the treatment of evaporation of the waste water, inorganic water is reused in the radiation controlled area. Only small amounts of concentrated liquid were generated by the treatment.

Table 1
Radioactive solid waste generated in FY 2021.

Amounts / Items	Amounts of generation in each period (m^3)					Number of package /drum
	1st quarter	2nd quarter	3rd quarter	4th quarter	Total	
Category β, γ*	0.86	0	0.10	0.40	1.36	32 **
Combustible	0.02	0	0	0.12	0.14	3 **
Flame-retardant	0.04	0	0.04	0.18	0.26	10 **
Incombustible(Compressible)	0	0	0.04	0.10	0.14	3 **
〃 (Incompressible)	0.80	0	0	0	0.80	16
Laboratory animal	0	0	0.02	0	0.02	0
Filters	0	0	0	0	0	-
Category α*	0	0	0	0.14	0.14	4
Combustible	0	0	0	0	0	0
Flame-retardant	0	0	0	0.10	0.10	4
Incombustible(Compressible)	0	0	0	0.02	0.02	0
〃 (Incompressible)	0	0	0	0	0	0
Laboratory animal	0	0	0	0.02	0.02	0
Filters	0	0	0	0	0	-

* defined by amount in Bq (β, γ): < 2 GBq , (α) : < 37 MBq,
** 50-liter drum.

Table 2
Radioactive liquid waste generated in FY 2021.

Amounts / Items	Amounts of generation in each period (m^3)					Number of package /drum
	1st quarter	2nd quarter	3rd quarter	4th quarter	Total	
Category β, γ*	13.91	19.32	4.54	5.03	42.80	-
1) Inorganic	13.91	19.32	4.54	5.03	42.80	-
Inorganic	13.91	19.32	4.54	5.03	42.80	treatment
Sludge, Evaporation residue	0.00	0.00	0.00	0.00	0.00	0
2) Organic	0.00	0.00	0.00	0.00	0.00	0
Organic	0.00	0.00	0.00	0.00	0.00	0
Oil	0.00	0.00	0.00	0.00	0.00	0
Category α*	0.00	0.00	0.00	0.00	0.00	0

* defined by concentrations in Bq/mL (β, γ Inorganic) : < 200 kBq, (Organic) : < 2 kBq, (α) : ≤ 1.85 kBq,

4 - 08 Facility Use Program in Takasaki Advanced Radiation Research Institute

S. Nozawa, H. Hanaya and A. Shimada

Department of Research Planning and Promotion, QuBS, QST

Irradiation facilities in Takasaki Advanced Radiation Research Institute (TARRI) have been opened to many researchers in universities, public institutes, R&D divisions of private companies (hereafter 'external users'), under Facility Use Program.

In this program, external users can use gamma-rays, electron beams, and ion beams, these were provided from irradiation facilities of Co-60 gamma-ray, electron accelerator, TIARA's four ion accelerators, and off-line analytical instruments. When using these facilities, external users are required to bear the operating costs of irradiation equipment.

Facility Use Program in FY2021

In Pricing system of Facility Use Program, experimental costs have been calculated from the total amount of service charge, irradiation charge, and extra-costs (ex. additional consumable goods and human support).

Research-and-development's users, who disclose the results of studies by publication, have been partially discounted for the experimental costs. To receive this discount, users were required to submit a research proposal to Research Planning and Promotion Office in TARRI. The proposals were reviewed by expert committee members in terms of the effectiveness of experimental designs. The approved proposals were implemented under Facility Use Program with the partially discounted cost. This discount was not applied at gamma-ray irradiation facilities and electron accelerator.

Number of irradiation experiments under Facility Use Program

Number of irradiation experiments under Facility Use Program in FY2021 were shown in Table 1. The number of experiments in Co-60 gamma-ray irradiation facilities was much higher than other facilities. Number of experiments classified by user's affiliation were shown in Table 2. AVF cyclotron and 3 MV tandem accelerator were mainly used by researchers who belonging to universities. On the other hand, many users of Co-60 gamma ray irradiation facilities were belonging to private companies.

Due to suspension of electron accelerator for the renovation of building, the number of experiments in FY2021 were decreased.

Additional information about this program is available at the following QST website:

https://www.qst.go.jp/site/qubs/1954.html

Table 1
Number of irradiation experiments under the Facility Use program in FY2021

Irradiation facility \ Pricing system		Public disclosure	Non-disclosure	Total
TIARA	AVF cyclotron	13	11	24
	3 MV tandem accelerator	22	19	41
	3 MV single-ended accelerator	15	7	22
	400 kV ion implanter	12	16	28
Co-60 gamma-ray irradiation facilities		-*	152	152
Electron accelerator		-*	4	4
Total		62	209	271

*: Discounting was not applied

Table 2
Number of irradiation experiments classified by user's affiliations

Irradiation Facility \ User's affiliation		University	Public institute	Private company	Total
TIARA	AVF cyclotron	13	6	5	24
	3 MV tandem accelerator	28	9	4	41
	3 MV single-ended accelerator	9	13	0	22
	400 kV ion implanter	16	12	0	28
Co-60 gamma-ray irradiation facilities		27	21	104	152
Electron accelerator		1	1	2	4
Total		94	62	115	271

blank page

Appendices

Appendix 1 Publication List ····· 118

Appendix 2 Type of Research Collaboration and Facilities Used for Research ····· 134

Appendix 3 Abbreviated Name for National Organizations ····· 136

Appendix 1 Publication List

Bold letters at the last of each item mean accelerators or irradiation facilities used for the work as follows:
C : Cyclotron, **T** : Tandem accelerator, **S** : Single-ended accelerator, **I** : Ion implanter,
E : Electron accelerator, **G** : Gamma-ray irradiation facilities, **N** : Not used.
Items in gray show the works in collaboration with other projects of QST.

P1-1 Project "Functional Polymer "

Papers

1) S. Sawada and Y. Maekawa, "Radiation-Induced Asymmetric Grafting of Different Monomers into Base Films to Prepare Novel Bipolar Membranes", Molecules, **26**, 2028 (2021). **G**

2) T. Motegi, K. Takiguchi, Y. Tanaka-Takiguchi, T. Itoh, and R. Tero, "Physical Properties and Reactivity of Microdomains in Phosphatidylinositol-Containing Supported Lipid Bilayer", Membranes, **11**, 339 (2021). **N**

3) Y. Zhao, K. Yoshimura, T. Motegi, A. Hiroki, and Y. Maekawa, "Three-Component Domains in the Fully Hydrated Nafion Membrane Characterized by Partial Scattering Function Analysis", Macromolecules, **54,** 4128-4135 (2021). **N**

4) S. Okushima, S. Hasegawa, T. Kawakatsu, and Y. Maekawa, "Coarse-grained Molecular Dynamics Simulation to Reproduce Phase-separated Structures in Graft-type Polymer Electrolyte Membranes", Polymer **230**, 124036 (2021). **G**

5) T. Hamada, K. Yoshimura, K. Takeuchi, S. Watanabe, Y. Zhao, A. Hiroki, T. Hagiwara, H. Shishitani, S. Yamaguchi, H. Tanaka, A. Radulescu, K. Ohwada and Y. Maekawa, "Synthesis and Characterization of 4-Vinylimidazolium/Styrene-Cografted Anion-Conducting Electrolyte Membranes", Macromol. Chem. Phys. **222,** 2100028 (2021). **G**

6) T. Hamada, Y. Zhao, K. Yoshimura, A. Radulescu, K. Ohwada and Y. Maekawa, "Hydrophobic Effect on Alkaline Stability of Graft Chains in Ammonium-type Anion Exchange Membranes Prepared by Radiation-Induced Graft Polymerization", ChemistrySelect **6**, 8879-8888 (2021). **G**

7) M. Schiavone, Y. Zhao, H. Iwase, H. Arima-Osonoi, S. Takata, A. Radulescu, "On the Proton Conduction Pathways in Polyelectrolyte Membranes Based on Syndiotactic-polystyrene", Membranes **12**, 143 (2022). **G**

8) L. H. Hao, T. D. Tap, D. T. T. Hieu, E. Korneeva, N. V. Tiep, K. Yoshimura, S. Hasegawa, S. Sawada, T. V. Man, N. Q. Hung, L. A. Tuyen, V. P. Dinh, L. Q. Luan, and Y. Maekawa, "Morphological Characterization of Grafted Polymer Electrolyte Membranes at a Surface Layer for Fuel Cell Application", J. Appl. Polym. Sci., **139**, 51901 (2022). **G**

9) Y. Ueki, N. Seko, and Y. Maekawa, "Machine learning approach for prediction of the grafting yield in radiation-induced graft polymerization", Appl. Mater. Today **25**, 101158 (2021). **G**

10) Y. Hosaka, H. Yamamoto, M. Ishino, T. H. Dinh, M. Nishikino, A. Kon, S. Owada, Y. Inubushi, Y. Kubota, Y. Maekawa, "Study on Irradiation Effects by Femtosecond-pulsed Extreme Ultraviolet in Resist Materials", J. Photopolym. Sci. Technol. **34**, 95-98 (2021). **N**

11) A. Hiroki and M. Taguchi, "Development of Environmentally Friendly Cellulose Derivative-Based Hydrogels for Contact Lenses Using a Radiation Crosslinking Technique", Appl. Sci. **11**, 9168 (2021). **E**

Proceedings

1) 茂木俊憲, 吉村公男, ザオユエ, 廣木章博, 前川康成, "構造機能相関解明に向けた放射線グラフト重合高分子膜のナノイメージング", 第 18 回放射線プロセスシンポジウム 要旨集, 67, オンライン (2021). **G**

2) 澤田真一, 前川康成, 坂本有希子, 船津公人, "機械学習法による放射線グラフト電解質膜に適した高分子基材の特性評価", 第 18 回放射線プロセスシンポジウム 要旨集, 68 , オンライン (2021). **G**

3) 坂本有希子, 澤田真一, 廣木章博, 前川康成, "放射線グラフト重合法による全固体二次電池用高分子電解質材料の創製研究", 令和 3 年度日本化学会関東支部群馬地区研究交流発表会 要旨集, P025, オンライン (2021). **G**

4) 阿部聖賢, 茂木俊憲, 吉村公男, 廣木章博, 前川康成, "散逸粒子動力学法によるグラフト型高分子電解質膜の構造最適化", 令和 3 年度日本化学会関東支部群馬地区研究交流発表会 要旨集, P038, オンライン (2021). **G**

5) 出崎亮, 廣木章博, 長谷川伸, 藤原広匡, 澁谷光夫, 竹下宏樹, 前川康成, 徳満勝久, 西村伸, "耐高圧水素材料の開発を目指した放射線架橋によるポリエチレンの改質", 第 70 回高分子討論会 要旨集, 2N01, オンライン (2021). **E, G**

6) 藤原広匡, 澁谷光夫, 西村伸, 出崎亮, 廣木章博, 長谷川伸, 前川康成,竹下宏樹, 徳満勝久, "放射線架橋ポリエチレンの高圧水素特性", 第 70 回高分子討論会 要旨集, 2N02, オンライン (2021). **E, G**

7) 藤原広匡, 澁谷光夫, 西村伸, 出崎亮, 廣木章博, 長谷川伸, 前川康成,竹下宏樹, 徳満勝久, "燃料電池用水素貯蔵タンク開発に向けたモデル材料としての放射線架橋ポリエチレンの高圧水素耐性評価", 第 62 回高圧討論会 要旨集, 3A09, 姫路・アクリエひめじ (2021). **E, G**

Patent

1) 吉村 公男, アーメドハンマド アーメド マフムード, ユハンチュル, ザオ ユエ, 廣木 章博, 前川 康成, "樹脂組成物、樹脂組成物の製造方法及び電気化学デバイス", 特願2021-088830 (2021.05.26). **E, G**

P1-2 Project “Advanced Catalyst”

Papers

1) T. Mori, K. Tong, S. Yamamoto, S. Chauhan, T. Kobayashi, N. Isaka, G. Auchterlonie, R. Wepf, A. Suzuki, S. Ito, Fei Ye, “Active Pt nano-coated layer with Pt-O-Ce bond on CeOx nanowire cathode formed by electron beam irradiation”, ACS Omega **7**, 25822-25836 (2022). **E**
2) S. Entani, S. Sato, M. Honda, C. Suzuki, T. Taguchi, S. Yamamoto, T. Ohshima, “Structural analysis of high-energy implanted Ni atoms into Si(100) by X-ray absorption fine structure spectroscopy”, Radiat. Phys. Chem. **199**, 110369 (2022). **C**
3) T. Kimata, K. Kakitani, S. Yamamoto, I. Shimoyama, D. Matsumura, A. Iwase, W. Mao, T. Kobayashi, T. Yamaki, T. Terai, “Activity enhancement of platinum oxygen-reduction electrocatalysts using ion-beam induced defects”, Phys. Rev. Mater. **6**, 035801 (2022). **C**
4) Y. Shimizu, M. Imbe, K. Godo, N. Sasajima, H. Koshikawa, T. Yamaki, K. Amemiya, “High-precision flat-plate reference infrared radiator using perfect blackbody composite with a microcavity structure”, Appl. Opt. **61**, 517-522 (2022). **C**
5) Y. Sato, H. Koshikawa, S. Yamamoto, M. Sugimoto, S. Sawada, T. Yamaki, “Fabrication of size- and shape-controlled platinum cones by ion-track etching and electrodeposition techniques for electrocatalytic applications”, Quantum Beam Sci. **5**, 21 (2021). **C**
6) A. Miyashita, M. Maekawa, C. Suzuki, S. Yamamoto, A. Kawasuso, J. Wang, T. Seki, R.Y. Umetsu, K. Takanashi, “Effect of disorder and vacancy defects on electrical transport properties of Co2MnGa thin films grown by magnetron sputtering”, J. Appl. Phys. **130**, 225301 (2021). **N**
7) Y. Shimizu, H. Koshikawa, M. Imbe, T. Yamaki, K. Godo, N. Sasajima, K. Amemiya, “ Micro-cavity perfect blackbody composite with good heat transfer towards a flat-plate reference radiation source for thermal imagers”, Opt. Lett. **46**, 4871-4874 (2021). **C**
8) M. Yoshimoto, T. Nakanoya, Y. Yamazaki, P. Saha, M. Kinsho, S. Yamamoto, H. Okazaki, T Taguchi, N. Yamada, R. Yamagata, “Analysis of J-HBC stripper foil for the J-PARC RCS”, J. Phys. Soc. Conf. Proc. **33**, 011019 (2021). **C, S**
9) H. Ishitobi, S Yamamoto, T. Ishii, K. Oba, H. Doki, R. Obata, A. Miyashita, H. Okazaki, N. Nakagawa, “Activity enhancement of a carbon electrode material for vanadium redox flow battery by electron-beam irradiation”, J. Chem. Eng. Jpn. **54**, 219-225 (2021). **E**
10) S. Chauhan, T. Mori, T. Kobayashi, S. Yamamoto, S. Ito, G. Auchterlonie, R. Wepf, S. Ueda, F. Ye, “Surface layer of Pt-O-Ce bonds on CeOx nanowire with high ORR activity converted by proton beam irradiation”, J. Am. Ceram. Soc. **104**, 1945-1952 (2021). **T, I**
11) T. Taguchi, S. Yamamoto, H. Oba, “Synthesis and formation mechanism of novel double-thick-walled silicon carbide nanotubes from multiwalled carbon nanotubes”, Appl. Surf. Sci. **551**, 149421 (2021). **C**
12) H. Amekra, M. Toulemonde, K. Narumi, R. Li, A. Chiba, Y. Hirano, K. Yamada, S. Yamamoto, N. Ishikawa, N. Okubo, Yuichi Saitoh, “Ion tracks in silicon formed by much lower energy deposition than the track formation threshold”, Sci. Rep. **11**, 185 (2021). **T**

Proceedings

1) 岡崎 宏之, 出崎 亮, 越川 博, 松村 大樹, 池田 隆司, 山本 春也, 八巻 徹也, “担体へのイオン照射による炭素担持 Pt 触媒の酸素吸着状態変化”, 電気化学会第 89 回大会, 3H01, オンライン (2022.03). **I**
2) 河裾 厚男, 宮下 敦巳, 前川 雅樹, 鈴木 智広, 山本 春也, 関 剛斎, J. Wang, 梅津 理恵, 高梨 弘毅, “Co2MnGa 中の不規則性と点欠陥が電気伝導特性に与える影響”, 日本物理学会第 77 回年次大会, 17pT31-9, オンライン (2022.03). **N**
3) 恩田 拓実, 山本 春也, 出崎 亮, 中村 将志, 星 永宏, “Pd ドープ TiO_2 単結晶電極上における ORR 活性化因子”, 電気化学会第 89 回大会, 2H08, オンライン (2022.03). **I**
4) 渡辺 友理, 松澤 幸一, 永井 崇昭, 池上 芳, 門田 隆二, 今西 哲士, 山本 春也, 石原 顕光, “4 族酸化物薄膜の物性が酸性溶液中での酸素還元反応に与える影響”, 電気化学会第 89 回大会, 1H28, オンライン (2022.03) **N**
5) 越川 博, 澤田 真一, 八巻 徹也, “イオンビーム照射によるポリスチレン多孔膜の作製”, 日本膜学会第 44 年会, 1C-1, オンライン (2022.06) **C**
6) H. Okazaki, A. Idesaki, H. Koshikawa, D. Matsumura, S. Yamamoto, T. Yamaki, “Oxygen adsorption state of Pt nanoparticles deposited on the ion-irradiated carbon support”, MRM2021, H5-O10-02, Online (2021.12). **I**
7) T. Taguchi, S. Yamamoto, H. Oba, “Synthesis of Polycrystalline and Amorphous Double-Thick-Walled Silicon Carbide Nanotubes”, MRM2021, H5-PR17-04, Online (2021.12). **T, I**
8) S. Yamamoto, H. Koshikawa, T. Taguchi, A. Idesaki, H. Okazaki, T. Yamaki, “Formation of Metal Nanoparticles inside Ion-Track-Etched Polyimide Capillaries”, MRM2021, H5-PR17-01, Online (2021.12). **I**
9) N. Tanaka, S. Sawada, C. Sugimoto, T. Yamaki, “Development of proton exchange membranes for hydriodic acid concentration by ion-track grafting technique”, MRM2021, H5-PR17-05, Online (2021.12). **I**
10) H. Koshikawa, S. Yamamoto, M. Sugimoto, S. Sawada, T. Yamaki, “Fabrication of metal oxide nanocones using ion-tracks of polymer membranes”, MRM2021, B2B3-PR15-16, Online (2021.12). **C**
11) T. Taguchi, S. Yamamoto, H. Oba, “Ion irradiation induced synthesis of novel amorphous double-thick-walled silicon carbide nanotubes”, The 9th International Symposium on Surface Science (ISSS9), 30PS-33, Online, (2021.11). **T, I**
12) 牛木 知彦, 今澤 良太, 村上 英利, 清水 宏祐, 杉江 達夫, 岡崎 宏之, 北澤 真一, 石川 正男, 波多江 仰紀, “ITER ダイバータ赤外サーモグラフィのレンズ材料のガンマ線及び中性子照射による中赤外光学特性の影響評価”, 第 38 回プラズマ核融合学会・年会, 23P-4F-15, オンライン (2021.11). **G**
13) 岡崎 宏之, 出崎 亮, 越川 博, 山本 春也, 八巻 徹也, “炭素担体へのイオン照射による Pt ナノ粒子触媒の ORR 活性向上”, 第 18 回放射線プロセスシンポジウム, P3-3, オンライン (2021.11) **I**
14) 藤原 広匡, 澁谷 光夫, 西村 伸, 出崎 亮, 廣木 章博, 長谷川 伸, 前川 康成, 竹下 宏樹, 徳満 勝久, “燃料電池用水素貯蔵タンク開発に向けたモデル材料としての放射線架橋ポリエ

チレンの高圧水素耐性評価", 第 62 回高圧討論会, 3A09, アクリエひめじ (2021.10) **G**

15) 齋藤 寛之, 佐藤 豊人, 谷上 真惟, 池田 一貴, 町田 晃彦, 綿貫 徹, 田口 富嗣, 山本 春也, 八巻 徹也, 高木 成幸, 大友 季哉, 折茂 慎一, "Al-Fe 合金の高温高圧水素化反応", 第 62 回高圧討論会, 1S05, アクリエひめじ (2021.10). **I**

16) H. Okazaki, A. Idesaki, H. Koshikawa, D. Matsumura, S. Yamamoto, T. Yamaki, "Changes of oxygen adsorption state of Pt nanoparticle catalyst on the carbon support by the ion irradiation." 240th ECS Meeting, I01D-1175, Online (2021.10). **I**

17) 山本 春也, 齋藤 寛之, 田口 富嗣, 内海 伶那, 綿貫 徹, 八巻 徹也, "スパッタリング法により成膜した Al-Fe 薄膜中の水素", 日本金属学会 2021 年秋期講演大会, S7.17, オンライン (2021.09). **I**

18) 齋藤 寛之, 内海 伶那, 町田 晃彦, 綿貫 徹, 山本 春也, 田口 富嗣, 八巻 徹也, 佐藤 豊人, 高木 成幸, 折茂 慎一, 池田 一貴, 大友 季哉, "アルミニウム-遷移金属合金水素化物の合成", 日本金属学会 2021 年秋期講演大会, S7.16, オンライン (2021.09). **I**

19) 出崎 亮, 藤原 広匡, 廣木 章博, 長谷川 伸, 澁谷 光夫, 竹下 宏樹, 前川 康成, 徳満 勝久, 西村 伸, "耐高圧水素材料の開発を目指した放射線架橋によるポリエチレンの改質", 第 70 回高分子討論会, 2N01, オンライン (2021.09). **G**

20) 藤原 広匡, 澁谷 光夫, 西村 伸, 出崎 亮, 廣木 章博, 長谷川 伸, 前川 康成, 竹下 宏樹, 徳満 勝久, "放射線架橋ポリエチレンの高圧水素特性", 第 70 回高分子討論会, 2N01, オンライン (2021.09.07). **G**

21) 田口 富嗣, 山本 春也, 大場 弘則, "イオン照射によるアモルファス二層厚壁 SiC ナノチューブの合成とその形状変化", 日本顕微鏡学会第 77 回学術講演会, P-M_14, オンライン (2021.06). **T, I**

22) 雨倉 宏, 鳴海 一雅, 千葉 敦也, 平野 貴美, 山田 圭介, 山本 春也, 齋藤 勇一, "MeV C_{60} イオン照射による媒質に埋め込まれた金属ナノ粒子の楕円変形と Si 中でのイオントラック形成", 2020 年度連携重点研究成果報告書, H30-4 (2021.06). **T**

Books

1) T. Kimata, K. Nakamura, T. Yamaki, "Chapter 16: Electrocatalysts developed from ion-implanted carbon materials", High-Energy Chemistry and Processing in Liquids, Springer Nature, 311-330 (2022).

2) 八巻 徹也, "18.2 単一の潜在飛跡を用いた加工技術:ナノ構造制御機能膜の創製", 電子・イオンビームハンドブック（第4版）, 日本学術振興会第 132 委員会, 480-498 (2021).

Press・TV

1) "燃料電池触媒の酸素還元反応活性を 2 倍以上向上させることに成功 －触媒性能 10 倍に向け前進 燃料電池のコスト低減に期待－", 2022.03.29, プレス発表： TechEyesOnline, EE Times Japan, YAHOO! JAPAN ニュース, ニュースイッチ, 日本経済新聞, MIT テクノロジーレビュー, ASCII.jp×ビジネス, マイナビニュース, 日刊工業新聞（電子版）, Mapion ニュース, BIGLOBE ニュース, dmenu, エキサイトニュース, マイナビニュース TECH+, fabcross for エンジニに掲載. **I**

P1-3 Project "Positron Nanoscience"

Papers

1) A Kawasuso, K. Wada A. Miyashita M. Maekawa H. Iwamori, S. Iida and Y Nagashima, "Positronium formation at 4H SiC(0001) surfaces", J. Phys. Condens. Matter **33** 035006 (2021). **N**

2) M. Maekawa , A. Miyashita , S. Sakai , S. Li , S. Entani , and A. Kawasuso and Y. Sakuraba, "Spin-Polarized Positronium Time-of-Flight Spectroscopy for Probing Spin-Polarized Surface Electronic States", Phys. Rev. Lett. **126,** 186401 (2021). **N**

3) A. Kawasuso, M. Maekawa, A. Miyashita, K. Wada, Y. Nagashima and A Ishida, "Positronium emission from GaN(0001) and AlN(0001) surfaces", J. Phys. B-At. Mol. Opt. Phys. **54**, 205202-1-6 (2021). **N**

4) A. Miyashita, M. Maekawa, Y. Shimoyama, N. Seko, A. Kawasuso and R. Y. Umetsu, "High-density magnetic-vacancy inclusion in Co_2MnGa single crystal probed by spin-polarized positron annihilation spectroscopy", J. Phys. Condens. Matter **34**, 045701-1-9 (2022). **N**

5) A. Miyashita, M. Maekawa, C. Suzuki, S. Yamamoto, A. Kawasuso, J. Wang, T. Seki, R. Y. Umetsu, and K. Takanashi, "Effect of disorder and vacancy defects on electrical transport properties of Co_2MnGa thin films grown by magnetron sputtering", J. Appl. Phys. **130**, 225301-1-7 (2021). **N**

6) 半導体からのポジトロニウム放出、河裾 厚男、和田 健、宮下 敦巳、前川 雅樹、陽電子科学 第 **18** 号, 3-17 (2022). **N**

Proceedings

1) M. Maekawa, A. Miyshita and A. Kawasuso, "Evaluation of energy-resolved spin polarization of surface electrons by spin-polarized positronium time-of-flight method", 12.5th International Workshop on Positron and Positronium Chemistry, Online, (2021.08-09). **N**

2) A. Kawasuso, K. Wada, A. Miyashita, Y. Nagashima and A. Ishida, "Positronium emission from semiconductor surfaces", 12.5th International Workshop on Positron and Positronium Chemistry, Online, (2021.08- 09). **N**

3) A. Kawasuso, "Spin-polarized positron beam: Application to spintronics", **【Invited talk】**, Materials Research Meeting 2021, Yokohama, Japan (2021.12). **I**

4) 河裾 厚男, 和田 健, 前川 雅樹, 宮下 敦巳, 石田 明, 長嶋 泰之, "GaN(0001)表面におけるポジトロニウム生成", 第 58 回アイソトープ・放射線研究発表会， オンライン (2021.07) **N**

5) 前川 雅樹, 宮下 敦己, 河裾 厚男, "スピン偏極ポジトロニウム放出エネルギー分光測定による磁性体最表面スピン評価", 第 58 回アイソトープ・放射線研究発表会, オンライン (2021.07). **N**

6) 宮下 敦巳, 前川 雅樹, 河裾 厚男, "第一原理バンド計算によるポジトロニウム分光スペクトルの解析～放出角制限における k 空間選択", 第 58 回アイソトープ・放射線研究発表会, オンライン (2021.07). **N**

7) 河裾 厚男, 宮下 敦巳, 前川 雅樹, 下山 陽子, 瀬古 典明, 梅津 理恵, "ワイル半金属候補物質 Co_2MnGa が内包する多量

の磁性空孔－スピン偏極陽電子による観測－", 日本物理学会 2021 年秋季大会, オンライン (2021.09). **N**

8) 前川 雅樹, 宮下 敦巳, 河裾 厚男, "スピン偏極ポジトロニウム分光による物質最表面電子状態評価", 日本物理学会 2021 年秋季大会, オンライン (2021.09). **N**

9) 山田 智子, 岩瀬 彰宏, 松井 利之, 前川 雅樹, 河裾 厚男, 堀 史説, "二重イオン照射による SiO_2 内 Ag-Ni 複合粒子合成における微細構造の照射順序効果", 日本金属学会 2021 年秋期講演大会, オンライン (2021.09). **T, I**

10) 大林 浩也, 岩瀬 彰宏, 金野 泰幸, 和田 武, 加藤 秀実, 前川 雅樹, 河裾 厚男, 石川 法人, 堀 史説, "重イオン照射による Ni-Zr 金属間化合物の微細構造と硬度変化", 日本金属学会 2021 年秋期講演大会, オンライン (2021.09). **T, S, I**

11) 河裾 厚男, 宮下 敦巳, 前川 雅樹, 梅津 理恵, "ワイル半金属候補物質 Co_2MnGa の多量原子空孔内包―原子空孔の規則化における役割―", 京都大学複合原子力科学研究所専門研究会「陽電子科学とその理工学への応用」, オンライン (2021.12.10). **N**

12) 宮下 敦巳, 河裾 厚男, 前川 雅樹, 梅津 理恵, "ワイル半金属候補物質 Co_2MnGa の多量原子空孔内包 原子空孔に付随する電子状態", 京都大学複合原子力科学研究所専門研究会「陽電子科学とその理工学への応用」, オンライン (2021.12.10). **N**

13) 前川 雅樹, 宮下敦 巳, 河裾 厚男, "スピン偏極ポジトロニウム分光法の開発", 京都大学複合原子力科学研究所専門研究会「陽電子科学とその理工学への応用」, オンライン (2021.12.10). **N**

P1-4 Project "Semiconductor Radiation Effects"

Papers

1) R. Nagy, D. B. R. Dasari, C. Babin, D. Liu, V. Vorobyov, M. Niethammer, M. Widmann, T. Linkewitz, I. Gediz, R. Stohr, H. B. Weber, T. Ohshima, M. Ghezellou, N. T. Son, J. U. Hassan, F. Kaiser and J. Wrachtrup, "Narrow inhomogeneous distribution of spin-active emitters in silicon carbide", Appl. Phys. Lett. **118**, 144003-1-7 (2021). **E**

2) S. Yanagimoto, N. Yamamoto, T. Sannomiya and K. Akiba "Purcell effect of nitrogen-vacancy centers in nanodiamond coupled to propagating and localized surface plasmons revealed by photon-correlation cathodoluminescence", Phys. Rev. B **103**, 205418-1-9 (2021). **N**

3) M. Imaizumi, T. Ohshima, Y. Yuri, K. Suzuki and Y. Ito, "Effects of Beam Conditions in Ground Irradiation Tests on Degradation of Photovoltaic Characteristics of Space Solar Cells", Quantum Beam Sci. **5**, 15-1-12 (2021). **E, S, C**

4) Y. Hijikata, S. Komori, S. Otojima, Y. Matsushita and T. Ohshima, "Impact of formation process on the radiation properties of single-photon sources generated on SiC crystal surfaces", Appl. Phys. Lett. **118**, 204005-1-6 (2021). **N**

5) J. Coutinho, J. D. Gouveia, T. Makino, T. Ohshima, Z. Pastuovic, L. Bakrac, T. Brodar and I. Capan, "M center in 4H-SiC is a carbon self-interstitial", Phys. Rev. B **103**, L180102-1-5 (2021). **E**

6) H. Takashima, A. Fukuda, K. Shimazaki, Y. Iwabata, H. Kawaguchi, A. W. Schell, T. Tashima, H. Abe, S. Onoda, T. Ohshima and S. Takeuchi, "Creation of silicon vacancy color centers with a narrow emission line in nanodiamonds by ion implantation", Opt. Mater. Express **11**, 1978-1988 (2021). **I**

7) Y. Miyazawa, G. M. Kim, A. Ishii, M. Ikegami, T. Miyasaka, Y. Suzuki, T. Yamamoto, T. Ohshima, S. Kanaya, H. Toyota and K. Hirose, "Evaluation of Damage Coefficient for Minority-Carrier Diffusion Length of Triple-Cation Perovskite Solar Cells under 1 MeV Electron Irradiation for Space Applications", J. Phys. Chem. C **125**, 13131-13137 (2021). **E**

8) H. Kubota, H. Ogawa, M. Miyazaki, S. Ishii, K. Ohyama, Y. Kawamura, S. Ishiwata and M. Suzuki, "Microscopic Temperature Control Reveals Cooperative Regulation of Actin–Myosin Interaction by Drebrin E", Nano Lett. **21**, 9526-9533 (2021). **N**

9) K. Shimazaki, H. Kawaguchi, H. Takashima, T. F. Segawa, F. T.-K. So, D. Terada, S. Onoda, T. Ohshima, M. Shirakawa and S. Takeuchi, "Fabrication of Detonation Nanodiamonds Containing Silicon-Vacancy Color Centers by High Temperature Annealing", Phys. Status Solidi A **218**, 2100144-1-9 (2021). **I**

10) K. Oyama, S. Ishii and M. Suzuki, "Opto-thermal technologies for microscopic analysis of cellular temperature-sensing systems", Biophys. Rev. **14**, 41-54 (2021). **N**

11) M. O. D. Vries, S. -I. Sato, T. Ohshima, B. C. Gibson, J. -M. Bluet, S. Castelletto, B. C. Johnson and P. Reineck, "Fluorescent Silicon Carbide Nanoparticles", Adv. Opt. Mater. **9**, 2100311 (2021). **I, T**

12) H. Nakane, M. Kato, Y. Ohkouchi, X. T. Trinh, I. G. Ivanov, T. Ohshima and N. T. Son, "Deep levels related to the carbon antisite–vacancy pair in 4H-SiC", J. Appl. Phys. **130**, 65703-1-8 (2021). **E**

13) R. Bernat, L. Bakrac, V. Radulovic, L. Snoj, T. Makino, T. Ohshima, Z. Pastuovic and I. Capan, "4H-SiC Schottky Barrier Diodes for Efficient Thermal Neutron Detection", Materials **14**, 5105-1-10 (2021). **N**

14) K. Sakamoto, S. Baba, D. Kobayashi, S. Okamoto, H. Shindou, O. Kawasaki, T. Makino, Y. Mori, D. Matuura, M. Kusano, T. Narita, S. Ishii and K. Hirose, "Investigation of Buried-Well Potential Perturbation Effects on SEU in SOI DICE-Based Flip-Flop Under Proton Irradiation", IEEE Trans. Nucl. Sci. **68**, 1222-1227 (2021). **C**

15) T. Tatsuishi, K. Kanehisa, T. Kageura, T. Sonoda, Y. Hata, K. Kawakatsu, T. Tanii, S. Onoda, A. Stacey, S. Kono and H. Kawarada, "Highly aligned 2D NV ensemble fabrication from nitrogen-terminated (111) surface", Carbon **180**, 127-134 (2021). **N**

16) C. Zhang, F. Shagieva, M. Widmann, M. Kübler, V. Vorobyov,P. Kapitanova, E. Nenasheva, R. Corkill, O. Rhrle, K. Nakamura, H. Sumiya, S. Onoda, J. Isoya and J. Wrachtrup, "Diamond Magnetometry and Gradiometry Towards Subpicotesla dc Field Measurement", Phys. Rev. Appl. **15**, 64075-1-11 (2021). **E**

17) R. A. Parker, N. Dontschuk, S. -I. Sato, C. T.-K. Lew, P. Reineck, A. Nadarajah, Ohshima Takeshi, B. C. Gibson, S. Castelletto, J. C. McCallum and B. C. Johnson, "Infrared

erbium photoluminescence enhancement in silicon carbide nano-pillars", J. Appl. Phys. **130**, 145101-1-8 (2021). **N**

18) X. Wu, S. Kondo, H. Yu, Y. Okuno, M. Ando, H. Kurotaki, S. Tanaka, K. Hokamoto, R. Ochiai, S. Konishi and R. Kasada, "Bonding strength evaluation of explosive welding joint of tungsten to ferritic steel using ultra-small testing technologies", Mater. Sci. Eng. A **826**, 141995 (2021). **N**

19) S. Ishii, S. Saiki, S. Onoda, Y. Masuyama, H. Abe and T. Ohshima, "Ensemble Negatively-Charged Nitrogen-Vacancy Centers in type-Ib Diamond Created by High Fluence Electron Beam Irradiation", Quantum Beam Sci. **6**, 2-1-10 (2021). **E**

20) C. Shinei, M. Miyakawa, S. Ishii, S. Saiki, S. Onoda, T. Taniguchi, T. Ohshima and T. Teraji, "Equilibrium charge state of NV centers in diamond", Appl. Phys. Lett. **119**, 254001-1-5 (2021). **E**

21) J. Ieda, S. Okayasu, K. Harii, M. Kobata, K. Yoshii, T. Fukuda, M. Ishida and E. Saitoh, "The damage analysis for irradiation tolerant spin-driven thermoelectric device based on single-crystalline $Y_3Fe_5O_{12}$/Pt heterostructures", IEEE Trans. Magn. **58**, 1301106 (2022). **N**

22) Y. Abe, A. Chaen, M. Sometani, S. Harada, Y. Yamazaki, T. Ohshima and T. Umeda, "Electrical detection of T_{V2a}-type silicon vacancy spin defect in 4H-SiC MOSFETs, Appl. Phys. Lett. **120**, 064001-1-6 (2022). **I**

23) C. P. Anderson, E. O. Glen, C. Zeledon, A. Bourassa, Y. Jin, Y. Zhu, C. Vorwerk, A. L. Crook, H. Abe, J. U. Hassan, T. Ohshima, N. T. Son, G. Galli and D. D. Awschalom, "Five-second coherence of a single spin with single-shot readout in silicon carbide", Sci. Adv. **8**, eabm5912-1-9 (2022). **E**

24) K. Yamane, R. Futamura, S. Genjo, D. Hamamoto, Y. Maki, E. M. Pavelescu, T. Ohshima, T. Sumita, M. Imaizumi and A. Wakahara, "Improved crystallinity of GaP-based dilute nitride alloys by proton/electron irradiation and rapid thermal annealing", Jpn. J. Appl. Phys. **61**, 020907-1-5 (2022). **E, I**

25) F. So, A. I. Shames, D. Terada, T. Genjo, H. Morishita, I. Ohki, T. Ohshima, S. Onoda, H. Takashima, S. Takeuchi, N. Mizuochi, R. Igarashi, M. Shirakawa and T. F. Segawa, "The Anomalous Formation of Irradiation Induced Nitrogen-Vacancy Centers in 5-Nanometer-Sized Detonation Nanodiamonds", J. Phys. Chem. C **126**, 5206-5217 (2022). **E**

26) M. Imaizumi, Y. Okuno , T. Takamoto, S. -I. Sato and T. Ohshima, "Displacement damage dose analysis of the output characteristics of $In_{0.5}Ga_{0.5}P$ and $Cu(In,Ga)(S,Se)_2$ solar cells irradiated with alpha ray simulated helium ions", Jpn. J. Appl. Phys. **61**, 044002-1-7 (2022). **I, T**

27) T. Luo, L. Lindner, J. Langer, V. Cimalla, X. Vidal, F. Hahl, C. Schreyvogel, S. Onoda, S. Ishii, T. Ohshima, D. Wang, D. A. Simpson, B. C. Johnson, M. Capelli, R. Blinder and J. Jeske, "Creation of nitrogen-vacancy centers in chemical vapor deposition diamond for sensing applications", New J. Phys. **24**, 0033030-1-16 (2022). **E**

28) M. Capelli, L. Lindner, T. Luo, J. Jaske, H. A, S. Onoda, Onoda, T. Ohshima, B. Johnson, D. A. Simpson, A. Stacey, P. Reineck, B. C. Gibson and A. D. Greentree, "Proximal nitrogen reduces the fluorescence quantum yield of nitrogen-vacancy centres in diamond", New J. Phys. **24**, 033053-1-10 (2022). **E**

29) I. Capan, T. Brodar, R. Bernat, Ž. Pastuović, T. Makino, T. Ohshima, J. D. Gouveia and J. Coutinho, "M-center in 4H-SiC: Isothermal DLTS and first principles modeling studies", J. Appl. Phys. **130**, 125703-1-10 (2021). **E**

30) J. Meinel, V. Vorobyov, B. Yavkin, D. Dasari, H. Sumiya, S. Onoda, J. Isoya and J. Wrachtrup, "Heterodyne sensing of microwaves with a quantum sensor", Nat. Commun. **12**, 1-8 (2021). **E**

31) D. Kobayashi, K. Hirose, K. Sakamoto, Y. Tsuchiya, S. Okamoto, S. Baba, H. Shindou, O. Kawasaki, T. Makino and T. Ohshima, "An SRAM SEU Cross Section Curve Physics Model, IEEE Trans. Nucl. Sci. **69**, 232-240 (2022). **C**

32) T. Umeda, K. Watanabe, H. Hara, H. Sumiya, Onoda Shinobu, A. Uedono, I. Chuprina, P. Siyushev, F. Jelezko, J. Wrachtrup and J. Isoya, "Negatively charged boron vacancy center in diamond", Phys. Rev. B **105**, 165201-1-13 (2022). **I**

33) T. Kageura, Y. Sasama, C. Shinei, T. Teraji, K. Yamada, S. Onoda and T. Yamaguchi, "Charge stability of shallow single nitrogen-vacancy centers in lightly boron-doped diamond", Carbon **192**, 473-481 (2022). **N**

34) O. V. Zwier, T. Bosma, C. M. Gilardoni, X. Yang, A. R. Onur, T. Ohshima, N. T. Son and C. H. Wal, "Electromagnetically induced transparency in inhomogeneously broadened divacancy defect ensembles in SiC", J. Appl. Phys. **131**, 094401-1-8 (2022). **E**

35) M. G. Fard, Z. Khabir, P. Reineck, N. M. Cordina, H. Abe, T. Ohshima, S. Dalal, B. C. Gibson, N. H. Packer and L. M. Parker, "Targeting cell surface glycans with lectin-coated fluorescent nanodiamonds", Nanoscale Adv. **4**, 1551-1564 (2022). **E**

36) T. Yanagi, K. Kaminaga, M. Suzuki, H. Abe, H. Yamamoto, T. Ohshima, A. Kuwahata, M. Sekino, T. Imaoka, S. Kakinuma, T. Sugi, W. Kada, O. Hanaizumi and R. Igarashi, "All-Optical Wide-Field Selective Imaging of Fluorescent Nanodiamonds in Cells, In Vivo and Ex Vivo", ACS Nano **15**, 12869-12879 (2021). **E**

37) K. Kaminaga, H. Yanagihara, T. Genjo, T. Morioka, H. Abe, M. Shirakawa, T. Ohshima, S. Kakinuma and R. Igarashi, "Non-contact Measurement of Internal Body Temperature Using Subcutaneously Implanted Diamond Microparticles", Biomater. Sci. **9**, 7049-7053 (2021). **E**

38) A. Akther, E. P. Walsh, P. Reineck, B. C. Gibson, T. Ohshima, H. Abe, G. McColl, N. L. Jenkins, L. T. Hall, D. A. Simpson, A. R. Rezk and L. Y. Yeo, "Acoustomicrofluidic Concentration and Signal Enhancement of Fluorescent Nanodiamond Sensors", Anal. Chem. **93**, 16133-16141 (2022). **E**

39) H. Ikegami, K. Akiba and H. Minoda, "Evaluation of electron radiation damage to green fluorescent protein", Ultramicroscopy **225**, 113272-1-5 (2021). **N**

Proceedings

1) M. Imaizumi, Y. Okuno, S. -I. Sato and T. Ohshima, "Displacement Damage Dose Analysis of Alpha-ray Degradation of Output of a CIGS Solar Cell", Proc. 48th IEEE Photovoltaic Specialists Conference (48th PVSC), Online (2021.06). **T, I, E**

Books

1) 小野田 忍、谷井 孝至、寺地 徳之、渡邊 幸志、磯谷 順一、"量子センシング NMR による超微量試料の化学構造同定", 第 2 章 第 3 節、"NMRによる有機材料分析とその試料前処理、データ解釈", 技術情報協会, 72-109 (2021).

2) 小野田 忍、山崎 雄一、大島 武、"ダイヤモンド中への負に

帯電した窒素-空孔(NV-)センタの形成技術”、第 1 章 第 3 節、“量子センシングハンドブック”、監修 根来 誠、株式会社エヌ・ティー・エス, 43-56 (2021).

Patents

1) 山崎 雄一, 増山 雄太, 大島 武, “物理量検出装置、物理量検出方法、および物理量検出プログラム” 特願 2022-005281 (2022.01.17). **S**

2) 佐藤 真一郎, 出来 真斗, 西村 智朗, “温度検出装置、温度センサ、温度検出方法、および温度検出プログラム” 特願 2021-032894 (2021.03.02). **I**

3) 佐藤 真一郎, 出来 真斗, 西村 智朗, “温度センサ、温度検出装置、温度検出方法、温度検出プログラム、および温度センサの製造方法”, 特願 2021-032895 (2021.03.02). **I**

P1-5 Project “Environmental Polymer”

Papers

1) Y. Ueki, N. Seko, “Synthesis of Fibrous Metal Adsorbent with a Piperazinyl-Dithiocarbamate Group by Radiation-Induced Grafting and Its Performance”, ACS Omega **5**, 2947–2956 (2020). **E**

2) N. A. F. Othman, S. Selambakkannu, T. T. Ming, N. H. Mohamed, T. Yamanobe, N Seko, “Application of Response Surface Modelling to Economically Maximize Thorium (IV) Adsorption”, Desalination Water Treat. **179**, 172–182 (2020). **E,G**

3) N. A. F. Othman, S. Selambakkannu, T. Yamanobe, H. Hoshina, N. Seko, T. A. T. Abdullah, “Radiation grafting of DMAEMA and DEAEMA based adsorbents for thorium adsorption”, J. Radioanal. Nucl. Chem. **324**, 429–440 (2020). **E,G**

4) N. A. F. Othman, S. Selambakkannu, H. Azian, C.T.Ratnam, T. Yamanobe, H. Hoshina, N. Seko, “Synthesis of surface ion imprinted polymer for specific detection of thorium under acidic conditions”, Polym. Bull. **78**, 165–183, (2021). **E, G**

5) Y. Ueki, N. Seko, Y. Maekawa, “Machine learning approach for prediction of the grafting yield in radiation-induced graft polymerization”, Appl. Mater. Today **25**, 101158 (2021). **E**

6) A. Miyashita, M. Maekawa, Y. Shimoyama, N. Seko, A. Kawasuso, R. Y. Umetsu, “High-density magnetic-vacancy inclusion in Co_2MnGa single crystal probed by spin-polarized positron annihilation spectroscopy”, J. Phys. Condens. Matter. **34**, 045701 (2021). **N**

7) N. Hayashi, D. Matsumura, H. Hoshina, Y. Ueki, T. Tsuji, J. Chen, N. Seko, “Chromium(VI) adsorption–reduction using a fibrous amidoxime-grafted adsorbent”, Sep. Purif. Technol. **277**, 119536 (2021). **E**

8) R. Kakuchi, R. Tsuji, K. Fukasawa, S. Yamashita, M. Omichi, N. Seko, “Polymers of lignin-sourced components as a facile chemical integrant for the Passerini three-component reaction”, Polym. J. **53**, 523–531 (2021). **E**

9) H. Hoshina, J. Chen, H. Amada, N. Seko, “Chelating fabrics prepared by an organic solvent-free process for boron removal from water”, Polymers **13**, 1163 (2021). **E, G**

10) B. J. D. Barba, D. P. Peñaloza Jr., N. Seko, J. F. Madrid, “RAFT-mediated radiation grafting on natural fibers in aqueous emulsion”, Mater. Proc. **7**(1), 4 (2021). **E**

11) T. Hamada, H. Hoshina, N. Seko, “Poly(vinyl diglycolic acid ester)-grafted polyethylene/polypropylene fiber adsorbent for selective recovery of samarium”, ACS Appl. Polym. Mater. **4**, 1846–1854 (2022). **E**

12) P. J. E. Cabalar, T. Hamada, J. F. Madrid, N Seko, “Synthesis of anion electrolyte membrane through radiation-induced graft polymerization of poly(4-vinylbenzyl chloride) onto isotactic polypropylene film”, Mindanao J. Sci. Technol. **20**, 189–210 (2022). **E**

13) Y. Ueki, M. Oshida, H. Sando, N. Seko, “Bleed-out suppression of silicone rubber by electron beam crosslinking”, Radiat. Phys. Chem. **193**, 110002 (2022). **E**

14) M. Omichi, N. Seko, Y. Maekawa, “Synergizing radiation-induced emulsion graft polymerization of glycidyl methacrylate on polyethylene-coated polypropylene nonwoven fabric by addition of hydrophobic alcohols”, Radiat. Phys. Chem. **191**, 109867 (2022). **E**

Proceedings

1) 瀬古 典明, “量子ビームを用いた高分子材料の創製と評価”【招待講演】, 第 63 回放射線化学討論会 (2020.12).

2) 瀬古 典明, “量子ビームを活用した機能性高分子材料の開発”【招待講演】, 群馬大学 S メンブレン・プロジェクト／複合材料懇話会 (2021.03).

3) 瀬古典明, “量子ビームを活用した材料創製と評価”【招待講演】日本原子力学会 2022 年春の年会 (2022.03).

Book

1) 瀬古 典明, 植木 悠二, “電子線・放射線による加工・改質”, 2020 版 薄膜作製応用ハンドブック, 660–665 (2020). **E**

Patents

1) 保科宏行, 瀬古典明, 高橋牧克, “金属担持材料の製造方法、及びその利用”, 特願 2021-078062 (2021.04.30). **E**

2) 物部 長順, 物部 長智, 内村 泰造, 瀬古 典明, 保科宏行, “セシウム及びストロンチウム吸着ろ過剤 及びこれを用いたセシウム及びストロンチウム除去システム”, 特願 2022-013799 (2022.01.31). **E, G**

3) 植木 悠二, 瀬古 典明, 渡邉 朗, 赤井 日出子, 齊藤 貴宏, 澤田 幸子, “セルロースナノファイバーグラフト重合体の製造方法”, 特願 2022-031941 (2022.03.02). **E, G**

4) 植木 悠二, 瀬古 典明, 岩曽 一恭, “セルロースグラフト重合体の製造方法”, 特願 2022-031942 (2022.03.02). **E, G**

Press・TV

1) “素材から「銀」が剥がれない、効果長持ち！抗ウイルスグラフト材料の開発に成功～マスクに付着した COVID-19 ウイルスの 99.9%以上を 1 時間で不活化 ～”, 2021.07.15, プレス発表：FM ぐんま、上毛新聞、日刊工業新聞、東京新聞に掲載. **E, G**

2) “どの原料モノマーを使えば、どんな高分子材料を作れるか分かる！？ 人工知能（AI）で重合反応率を簡単に予測”, 2021.09.29, プレス発表：上毛新聞に掲載. **E**

P1-6 Project “Biocompatible Materials”

Papers

1) M. Koshimizu, N. Kawano, A. Kimura, S. Kurashima, M. Taguchi, Y. Fujimoto and K. Asai, “Effects of Excitation Density on the Scintillation Properties of Organic-Inorganic Layered Perovskite-type Compounds”, Sens. Mater. **33**, 2137-2145 (2021). **C**

2) T. G. Oyama, K. Oyama, A. Kimura, F. Yoshida, R. Ishida, M. Yamazaki, H. Miyoshi and M. Taguchi, “Collagen hydrogels with controllable combined cues of elasticity and topography to regulate cellular processes”, Biomed. Mater. **16**, 045037 (2021). **G**

3) B. J. D. Barba, T. G. Oyama and M. Taguchi, “Simple fabrication of gelatin-polyvinyl alcohol bilayer hydrogel with wound dressing and nonadhesive duality”, Polym. Adv. Technol. **32**, 4406-4414 (2021). **G**

4) T. G. Oyama, K. Oyama, H. Miyoshi and M. Taguchi, “3D cell sheets formed via cell-driven buckling-delamination of patterned thin films”, Mater. Des. **208**, 109975 (2021). **S**

5) S. Matsuura, T. Takayama, T. G. Oyama, K. Oyama, M. Taguchi, T. Endo, T. Akai, T. Isaji and K. Hoshina, “Radiation-crosslinked gelatin hydrogel that promotes tissue incorporation of an expanded polytetrafluoroethylene vascular graft in rats”, Biomolecules **11**, 1105 (2021). **G**

6) T. Tachibana, T. G. Oyama, Y. Yoshii, F. Hihara, C. Igarashi, A. B. Tsuji, T. Higashi and M. Taguchi, “A novel in vivo xenograft mouse model of a subcutaneous submillimeter tumor formed from a single spheroid transplanted using radiation-crosslinked gelatin hydrogel microwell”, Appl. Sci. **11**, 7031 (2021). **G**

7) Y. Kawahara, T. Sekiguchi, Y. Shinahara, N. Nagasawa, Y. Nishikawa, T. Yoshioka and Y. Tamada, “Structure of the gamma ray irradiation-curable liquid silk 3D scaffold with cell-adhesive property”, J. Macromol. Sci. **B** 61, 10-25 (2021). **G**

8) A. Hiroki and M. Taguchi, “Development of environmentally friendly cellulose derivative-based hydrogels for contact lenses using a radiation crosslinking technique”, Appl. Sci. **11**, 9168 (2021). **E**

9) F. Kobirumaki-Shimozawa, T. Shimozawa, K. Oyama, S. Baba, J. Li, T. Nakanishi, T. Terui, W. E. Louch, S. Ishiwata and N. Fukuda, “Synchrony of sarcomeric movement regulates left ventricular pump function in the in vivo beating mouse heart”, J. Gen. Physiol. **153**, e202012860 (2021). **N**

10) Y. Kumagai, A. Kimura, M. Taguchi and M. Watanabe, “Zeolite-assisted radiolysis of aromatic chlorides mitigating influence of coexisting ions in water matrix”, Radiat. Phys. Chem., in press. **G**

11) E. H. Kubota, H. Ogawa, M. Miyazaki, S. Ishii, K. Oyama, Y. Kawamura, S. Ishiwata and M. Suzuki, “Microscopic temperature control reveals cooperative regulation of actin-myosin interaction by drebrin”, Nano Lett., in press. **E**

12) M. Koshimizu, S. Kurashima, A. Kimura, M. Taguchi, T. Yanagida, Y. Fujimoto and K. Asai, “Excitation density effects on scintillation dynamics of CdWO4”, Sensors and Materials 33, 2137-2145 (2921). **C**

13) K. Oyama, S. Ishii and M. Suzuki, “Opto-thermal technologies for microscopic analysis of cellular temperature-sensing systems”, Biophys. Rev. **14**, 41-54 (2022). **N**

14) Q. Yun, A. Kimura, M. Taguchi and E. Miyako, “Sonication- and γ-ray-mediated biomolecule-liquid metal nanoparticlization in cancer optotheranostics”, Appl. Mater. Today **26**, 101302 (2022). **G**

15) A. Omori, S. Ajito, H. Abe, K. Hata, T. Sato, Y. Kaji, H. Inoue, M. Taguchi, H. Seito, E. Tada, S. Suzuki and E. Akiyama, “Corrosion monitoring of carbon steel in non-irradiated, humidity-controlled environments simulating gamma-ray irradiation”, Mater. Trans. **63**, 555-561 (2022). **G**

16) A. E. Swilem, T. G. Oyama, K. Oyama, A. Kimura and M. Taguchi, “Development of carboxymethyl cellulose/gelatin hybrid hydrogels via radiation-induced cross-linking as novel anti-adhesion barriers”, Polym. Degrad. Stab. **197**, 109856 (2022). **G**

17) N. Natori, Y. Shibano, A. Hiroki, M. Taguchi, A. Miyajima, K. Yoshizawa, Y. Kawano and T. Hanawa, “Preparation and evaluation of hydrogel film containing tramadol for reduction of peripheral neuropathic pain”, J. Pharm. Sci., in press. **E**

Press・TV

1) “平面状の細胞シートが立体的に！細胞が自分の力でシートを3次元化 ― 臓器表面にフィットする移植治療用細胞シートへの応用に期待 ―”, 2021.07.14, プレス発表：上毛新聞, 日刊工業新聞,科学新聞, 雑誌「医薬経済」に掲載.

P1-7 Project “Spintronics in Two-dimensional Materials”

Papers

1) F. Zheng, Z. Han, S. Li, Z. Ma, H. Gao, ‘Improvement of soft magnetic properties and in-plane uniaxial magnetic anisotropy in FeCoAlO films fabricated by asymmetric targets’ Appl. Phys. A **128**, 253 (2022). **N**

2) 三井 隆也, 境 誠司, 瀬戸 誠, 赤井 久純, ‘鉄の表面近傍の特異な磁性を発見 - 原子一層毎に磁気モーメントの大きさが増減する’ 日本物理学会誌 **77**, 23 (2022). **N**

3) J. Okabayashi, S. Li, S. Sakai, Y. Kobayashi, T. Mitsui, K. Tanaka, Y. Miura, S. Mitani, ‘Perpendicular magnetic anisotropy at Fe/Au(111) interface studied by Mössbauer, x-ray absorption, and photoemission spectroscopies’, Phys. Rev. B **103**, 104435 (2021). **N**

4) H. Yokota, Y. Kobori, S. Jitsukawa, S. Sakai, Y. Takeda, T. Mitsui, Y. Kobayashi, S. Kitao, ‘Element-specific agnetic hysteresis loops observed in hexagaonal $ErFeO_3$ thin films’ Mater. Res. Express **8**, 086402 (2021). **N**

5) M. Maekawa, A. Miyashita, S. Sakai, S. Li, S. Entani, A. Kawasuso, Y. Sakuraba, ‘Spin-polarized positronium time-of-flight spectroscopy for probing spin-polarized surface electronic states’ Phys. Rev. Lett. **126**, 186401 (2021). **N**

6) S. Entani, M. Honda, H. Naramoto, S. Li, S. Sakai, ‘Synchrotron X-ray standing wave characterization of atomic

arrangement at interface between transferred graphene and alpha-Al_2O_3(0001)' Surf. Sci. **704**, 121749 (2021). **N**

7) T. Mitsui, S.Sakai, S. Li, T. Ueno, T. Watanuki, Y. Kobayashi, R. Masuda, M. Seto, H. Akai, 'Direct observation of magnetic Friedel oscillation at Fe(001) surface' Hyperfine Interact. **242**, 37 (2021). **N**

8) J. Okabayashi, S. Li, S. Sakai, Y. Kobayashi, K. fujiwara, T. Mitsui, S. Mitani, 'Mossbauer spectroscopy with polarized synchrotron beams at Fe/Au (111) interface' Hyperfine Interact. **242**, 59 (2021). **N**

P1-9 Project "Element Separation and Analysis"

Papers

1) K. Tamura, R. Nakanishi, H. Ohba, T. Taira, I. Wakaida "Recovery of the laser-induced breakdown spectroscopy system using a ceramic microchip deteriorated by radiation", J. Nucl. Sci. Technol., Published online: 14 Jul 2022, **G**

2) M. Saeki, D. Matsumura, R. Nakanishi, T. Yomogida, T. Tsuji, H. Saitoh, and H. Ohba "Dispersive XAFS study on the laser-induced reduction of a Rh3+ ion complex: Presence of a Rh+ intermediate in direct photoreduction", J. Phys. Chem. C **126**, 5607 (2022). **N**

3) S. Entani, S. Sato, M. Honda, C. Suzuki, T. Taguchi, S. Yamamoto, T. Ohshima "Structural analysis of high-energy implanted Ni atoms into Si(100) by X-ray absorption fine structure spectroscopy", Radiat. Phys. Chem. **199**, 110369 (2022). **N**

4) N. Ishikawa, Y. Fujimura, K. Kondo, G. L. Szabo, R.A. Wilhelm, H. Ogawa, T. Taguchi "Surface nanostructures on Nb-doped SrTiO3 irradiated with swift heavy ions at grazing incidence," Nanotechnology **33**, 235303 (2022). **N**

5) T. Suzuki, J. Ishihara, T. Taguchi, K. Miyajima "Effect of anionic surfactant on dispersibility and luminescence of SiC nanotubes," Journal of Luminescence, 245, 118771 (2022). **N**

6) K. Tamura, R. Nakanishi, H. Ohba, T. Taira, I. Wakaida "Radiation robustness of laser ceramics and single crystal for microchip laser remote analysis," Jpn. J. Appl. Phys. **61**, 032003 (2022). **G**

7) Y. Kurosaki, K. Yokoyama, and Y. Ohtsuki "Quantum Control of Isotope-Selective Molecular Orientation," AIP conf. proc. ICCMSE 2022, in press. **N**

8) T. Yomogida, M. Saeki, S. Morii, H. Ohba, Y. Kitatuji, "Selective Pd separation from a simulated radioactive liquid waste by precipitation using a xenon lamp irradiation for simplified procedure," Anal. Sci. **37**, 1843-1846 (2021). **N**

9) R. Nakanishi, H. Ohba, M. Saeki, I. Wakaida, R. Tanabe-Yamagishi, Y. Ito, "Highly sensitive detection of sodium in aqueous solutions using laser-induced breakdown spectroscopy with liquid sheet jets," Opt. Express **29**, 5205-5212 (2021). **N**

10) H. Saitoh, T. Sato, M. Tanikami, K. Ikeda, A. Machida, T. Watanuki, T. Taguchi, S. Yamamoto, T. Yamaki, S. Takagi, T. Otomo, S. Orimo "Hydrogen storage by earth-abundant metals, synthesis and characterization of Al3FeH3.9", Mater. Des. **208**, 109953 (2021). **N**

11) M. Yoshimoto, T. Nakanoya, Y. Yamazaki, P. Saha, M. Kinsho, S. Yamamoto, H. Okazaki, T. Taguchi, N. Yamada, R. Yamagata "Analysis of J-HBC stripper foil for the J-PARC RCS", J. Phys. Soc. Conf. Proc. **33**, 011019 (2021). **N**

12) T. Taguchi, S. Yamamoto, H. Ohba "Synthesis and formation mechanism of double-thick-walled silicon carbide nanotubes from multiwalled carbon nanotubes", Appl. Surf. Sci. **551**, 149421 (2021). **N**

13) R. Nakanishi, M. Saeki, I. Wakaida, H. Ohba, "Detection of Gadolinium in Surrogate Nuclear Fuel Debris Using Fiber-Optic Laser-Induced Breakdown Spectroscopy under Gamma Irradiation", Appl. Sci. **10**, 8985 (2020). **G**

14) Y. Kurosaki, R. Nakanishi, M. Saeki, H. Ohba, "Ab initio MRCI study on potential energy surfaces for double Cl loss from the palladium tetrachloride anion $PdCl_4^{2-}$", Chem. Phys. Lett. **764**, 138247 (2020). **N**

15) Y. Kurosaki, K. Yokoyama, "Quantum Optimal Control of Isotope-Selective Rovibrational Transitions," AIP Conf. Proc. **2343**, 020005 (2021). **N**

16) K. Tamura, H. Ohba, M. Saeki, T. Taguchi, H. H. Lim, T. Taira, I. Wakaida, "Radiation dose rate effects on the properties of a laser-induced breakdown spectroscopy system developed using a ceramics micro-laser for fiber-optic remote analysis," J. Nucl. Sci. Technol. **58**, 405-415 (2021). . **G**

17) S. Yamamoto, H. Koshikawa, T. Taguchi, T. Yamaki, "Precipitation of Pt nanoparticles inside ion-track-etched capillaries," Quantum Beam Sci. **4**, 8 (2020). **N**

18) N. Ishikawa, T. Taguchi, A. Kitamura, G. Szenes, M. E. Toimil-Molares, C. Trautmann, "TEM analysis of ion-tracks and hillocks produced by swift heavy ions of different velocities in $Y_3Fe_5O_{12}$," J. Appl. Phys. **127**, 055902 (2020). **N**

19) M. Saeki, T. Yomogida, D. Matsumura, T. Saito, R. Nakanishi, T. Tsuji, H Ohba, "Application of augmentation method to MCR-ALS analysis for XAFS and Raman data matrices in structural change of isopolymolybdates", Analytical Sci. **36**, 1371 (2020). **N**

20) K. Tamura, H. Ohba, M. Saeki, T. Taguchi, H.H. Lim, T. Taira, I. Wakaida, "Development of a laser-induced breakdown spectroscopy system using a ceramic micro-laser for fiber-optic remote analysis", J. Nucl. Sci. Technol. **57**, 1189 (2020). **G**

21) 大場弘則, 若井田育夫, 平等拓範, "原子炉廃炉措置に向けた遠隔レーザ分析技術" , 電気学会誌 **142**(2), 77-80, (2022). **G**

22) 石川法人, 田口富嗣, 大久保成彰, "高速重イオン照射したセラミックスにおける照射損傷メカニズム" , 原子衝突学会学会誌「しょうとつ」, **18**(3) , 43-55 (2021). **N**

23) 中西 隆造, 佐伯 盛久, 大場 弘則, "パルスレーザー照射による希少金属を回収する", レーザ加工学会誌 **27**(3), 159 161 (2020). **N**

24) Y. Kurosaki, R. Nakanishi, M. Saeki, H. Ohba, "Ab initio MRCI study on potential energy curves for a single Cl loss from the palladium tetrachloride anion $PdCl_4^{2-}$", Chem. Phys. Lett. **746**, 137288 (2020). **N**

25) 大場 弘則, 佐伯 盛久, 中西 隆造, ”廃液にレーザーを照射して希少金属を回収する”, ケミカルエンジニヤリング **65**(6), 347-352 (2020). **N**

26) 田村 浩司, 遠山 伸一, “レーザー法による原子炉厚板鋼材切断技術の開発”, 日本原子力学会誌 **62**(5), 268-271 (2020). **N**

27) 大場 弘則, 若井田 育夫, 平等 拓範, “過酷環境下での遠隔レーザー分析技術”, 日本原子力学会誌 **62**(5), 263-267 (2020). **G**

P1-10 Advanced Functional Polymer Materials Research Group

Papers

1) S. Sawada and Y. Maekawa, “Radiation-Induced Asymmetric Grafting of Different Monomers into Base Films to Prepare Novel Bipolar Membranes”, Molecules **26**, 2028 (2021). **G**

2) T. Motegi, K. Takiguchi, Y. Tanaka-Takiguchi, T. Itoh, and R. Tero, “Physical Properties and Reactivity of Microdomains in Phosphatidylinositol-Containing Supported Lipid Bilayer”, Membranes **11**, 339 (2021). **N**

3) Y. Zhao, K. Yoshimura, T. Motegi, A. Hiroki, and Y. Maekawa, “Three-Component Domains in the Fully Hydrated Nafion Membrane Characterized by Partial Scattering Function Analysis”, Macromolecules **54**, 4128-4135 (2021). **N**

4) S. Okushima, S. Hasegawa, T. Kawakatsu, and Y. Maekawa, “Coarse-grained Molecular Dynamics Simulation to Reproduce Phase-separated Structures in Graft-type Polymer Electrolyte Membranes”, Polymer **230**, 124036 (2021). **G**

5) T. Hamada, K. Yoshimura, K. Takeuchi, S. Watanabe, Y. Zhao, A. Hiroki, T. Hagiwara, H. Shishitani, S. Yamaguchi, H. Tanaka, A. Radulescu, K. Ohwada and Y. Maekawa, “Synthesis and Characterization of 4-Vinylimidazolium/Styrene-Cografted Anion-Conducting Electrolyte Membranes”, Macromol. Chem. Phys. **222**, 2100028 (2021). **G**

6) T. Hamada, Y. Zhao, K. Yoshimura, A. Radulescu, K. Ohwada and Y. Maekawa, “Hydrophobic Effect on Alkaline Stability of Graft Chains in Ammonium-type Anion Exchange Membranes Prepared by Radiation-Induced Graft Polymerization”, ChemistrySelect **6**, 8879-8888 (2021). **G**

7) M. Schiavone, Y. Zhao, H. Iwase, H. Arima-Osonoi, S. Takata, A. Radulescu, “On the Proton Conduction Pathways in Polyelectrolyte Membranes Based on Syndiotactic-polystyrene”, Membranes **12**, 143 (2022). **G**

8) L. H. Hao, T. D. Tap, D. T. T. Hieu, E. Korneeva, N. V. Tiep, K. Yoshimura, S. Hasegawa, S. Sawada, T. V. Man, N. Q. Hung, L. A. Tuyen, V. P. Dinh, L. Q. Luan and Y. Maekawa, “Morphological Characterization of Grafted Polymer Electrolyte Membranes at a Surface Layer for Fuel Cell Application”, J. Appl. Polym. Sci. **139**, 51901 (2022). **G**

9) Y. Ueki and N. Seko, “Synthesis of Fibrous Metal Adsorbent with a Piperazinyl-Dithiocarbamate Group by Radiation-Induced Grafting and Its Performance”, ACS Omega **5**, 2947-2956 (2020). **E**

10) N. A. F. Othman, S. Selambakkannu, T. T. Ming, N. H. Mohamed, T. Yamanobe, N Seko, “Application of Response Surface Modelling to Economically Maximize Thorium (IV) Adsorption”, Desalination Water Treat. **179**, 172-182 (2020). **E, G**

11) N. A. F. Othman, S. Selambakkannu, T. Yamanobe, H. Hoshina, N. Seko, T. A. T. Abdullah, “Radiation grafting of DMAEMA and DEAEMA based adsorbents for thorium adsorption”, J. Radioanal. Nucl. Chem. **324**, 429-440 (2020). **E, G**

12) N. A. F. Othman, S. Selambakkannu, H. Azian, C.T.Ratnam, T. Yamanobe, H. Hoshina, N. Seko, “Synthesis of surface ion imprinted polymer for specific detection of thorium under acidic conditions”, Polym. Bull. **78**, 165-183, (2021). **E, G**

13) Y. Ueki, N. Seko, Y. Maekawa, “Machine learning approach for prediction of the grafting yield in radiation-induced graft polymerization”, Appl. Mater. Today **25**, 101158 (2021). **E**

14) A. Miyashita, M. Maekawa, Y. Shimoyama, N. Seko, A. Kawasuso, R. Y. Umetsu, “High-density magnetic-vacancy inclusion in Co2MnGa single crystal probed by spin-polarized positron annihilation spectroscopy”, J. Phys. Condens. Matter. **34**, 045701 (2021). **N**

15) N. Hayashi, D. Matsumura, H. Hoshina, Y. Ueki, T. Tsuji, J. Chen, N. Seko, “Chromium(VI) adsorption-reduction using a fibrous amidoxime-grafted adsorbent”, Sep. Purif. Technol. **277**, 119536 (2021). **E**

16) R. Kakuchi, R. Tsuji, K. Fukasawa, S. Yamashita, M. Omichi, N. Seko, “Polymers of lignin-sourced components as a facile chemical integrant for the Passerini three-component reaction”, Polym. J. **53**, 523-531 (2021). **E**

17) H. Hoshina, J. Chen, H. Amada, N. Seko, “Chelating fabrics prepared by an organic solvent-free process for boron removal from water”, Polymers **13**, 1163 (2021). **E, G**

18) B. J. D. Barba, D. P. Peñaloza Jr., N. Seko, J. F. Madrid, “RAFT-mediated radiation grafting on natural fibers in aqueous emulsion”, Mater. Proc. **7**, 4 (2021). **E**

19) T. Hamada, H. Hoshina, N. Seko, “Poly(vinyl diglycolic acid ester)-grafted polyethylene/polypropylene fiber adsorbent for selective recovery of samarium”, ACS Appl. Polym. Mater. **4**, 1846-1854 (2022). **E**

20) P. J. E. Cabalar, T. Hamada, J. F. Madrid, N Seko, “Synthesis of anion electrolyte membrane through radiation-induced graft polymerization of poly(4-vinylbenzyl chloride) onto isotactic polypropylene film”, Mindanao J. Sci. Technol. **20**, 189-210 (2022). **E**

21) Y. Ueki, M. Oshida, H. Sando, N. Seko, “Bleed-out suppression of silicone rubber by electron beam crosslinking”, Radiat. Phys. Chem. **193**, 110002 (2022). **E**

22) M. Omichi, N. Seko, Y. Maekawa, “Synergizing radiation-induced emulsion graft polymerization of glycidyl methacrylate on polyethylene-coated polypropylene nonwoven fabric by addition of hydrophobic alcohols”, Radiat. Phys. Chem. **191**, 109867 (2022). **E**

Proceedings

1) 茂木 俊憲, 吉村 公男, ザオ ユエ, 廣木 章博, 前川 康成, “構造機能相関解明に向けた放射線グラフト重合高分子膜のナ

ノイメージング”, 第 18 回放射線プロセスシンポジウム 要旨集, 67, オンライン (2021). **G**

2) 澤田 真一, 前川 康成, 坂本 有希子, 船津 公人, “機械学習法による放射線グラフト電解質膜に適した高分子基材の特性評価”, 第 18 回放射線プロセスシンポジウム 要旨集, オンライン 68 (2021). **G**

3) 坂本 有希子, 澤田 真一, 廣木 章博, 前川 康成, “放射線グラフト重合法による全固体二次電池用高分子電解質材料の創製研究”, 令和 3 年度日本化学会関東支部群馬地区研究交流発表会 要旨集, オンライン P025 (2021). **G**

4) 阿部聖賢, 茂木俊憲, 吉村公男, 廣木章博, 前川康成, “散逸粒子動力学法によるグラフト型高分子電解質膜の構造最適化”, 令和 3 年度日本化学会関東支部群馬地区研究交流発表会 要旨集, P038, オンライン (2021). **G**

5) 出崎亮, 廣木章博, 長谷川伸, 藤原広匡, 澁谷光夫, 竹下宏樹, 前川康成, 徳満勝久, 西村伸, “耐高圧水素材料の開発を目指した放射線架橋によるポリエチレンの改質”, 第 70 回高分子討論会 要旨集, 2N01, オンライン(2021). **E, G**

6) 藤原広匡, 澁谷光夫, 西村伸, 出崎亮, 廣木章博, 長谷川伸, 前川康成,竹下宏樹, 徳満勝久, “放射線架橋ポリエチレンの高圧水素特性”, 第 70 回高分子討論会 要旨集, 2N02, オンライン (2021). **E, G**

7) 藤原広匡, 澁谷光夫, 西村伸, 出崎亮, 廣木章博, 長谷川伸, 前川康成,竹下宏樹, 徳満勝久, “燃料電池用水素貯蔵タンク開発に向けたモデル材料としての放射線架橋ポリエチレンの高圧水素耐性評価”, 第 62 回高圧討論会 要旨集, 3A09 , 姫路・アクリエひめじ (2021). **E, G**

8) 瀬古典明, “量子ビームを活用した機能性高分子材料の開発”,【招待講演】, 群馬大学Ｓメンブレン・プロジェクト／複合材料懇話会 要旨集, オンライン (2021). **E, G**

9) 瀬古典明, “量子ビームを活用した材料創製と評価”,【招待講演】, 日本原子力学会 2022 年春の年会 要旨集, オンライン (2022). **E, G**

Patents

1) 吉村 公男, アーメドハンマド アーメド マフムード, ユ ハンチュル, ザオ ユエ, 廣木 章博, 前川 康成, “樹脂組成物、樹脂組成物の製造方法及び電気化学デバイス”, 特願 2021-088830 (2021.05.26). **E, G**

2) 保科 宏行, 瀬古 典明, 高橋 牧克, “金属担持材料の製造方法、及びその利用”, 特願 2021-078062 (2021.04.30). **E**

3) 物部 長順, 物部 長智, 内村 泰造, 瀬古 典明, 保科 宏行, “セシウム及びストロンチウム吸着ろ過剤 及びこれを用いたセシウム及びストロンチウム除去システム”, 特願 2022-013799 (2022.01.31) **E, G**

4) 植木 悠二, 瀬古 典明, 渡邉 朗, 赤井 日出子, 齊藤 貴宏, 澤田 幸子, “セルロースナノファイバーグラフト重合体の製造方法”, 特願 2022-031941 (2022.03.02). **E, G**

5) 植木 悠二, 瀬古 典明, 岩曽 一恭, “セルロースグラフト重合体の製造方法”, 特願 2022-031942 (2022.03.02). **E, G**

Press・TV

1) “素材から「銀」が剥がれない、効果長持ち！抗ウイルスグラフト材料の開発に成功～マスクに付着した COVID-19 ウイルスの 99.9%以上を 1 時間で不活化 ～”, 2021.07.15, プレス発表：FM ぐんま、上毛新聞、日刊工業新聞、東京新聞に掲載. **E, G**

2) “どの原料モノマーを使えば、どんな高分子材料を作れるか分かる！？ 人工知能（AI）で重合反応率を簡単に予測”, 2021.09.29, プレス発表：上毛新聞に掲載. **E**

P1-11 Quantum Sensing and Information Materials Research Group

Papers

1) R. Nagy, D. B. R. Dasari, C. Babin, D. Liu, V. Vorobyov, M. Niethammer, M. Widmann, T. Linkewitz, I. Gediz, R. Stohr, H. B. Weber, T. Ohshima, M. Ghezellou, N. T. Son, J. U. Hassan, F. Kaiser and J. Wrachtrup, “Narrow inhomogeneous distribution of spin-active emitters in silicon carbide”, Appl. Phys. Lett. **118**, 144003-1-7 (2021). **E**

2) S. Yanagimoto, N. Yamamoto, T. Sannomiya and K. Akiba “Purcell effect of nitrogen-vacancy centers in nanodiamond coupled to propagating and localized surface plasmons revealed by photon-correlation cathodoluminescence”, Phys. Rev. B **103**, 205418-1-9 (2021). **N**

3) M. Imaizumi, T. Ohshima, Y. Yuri, K. Suzuki and Y. Ito, “Effects of Beam Conditions in Ground Irradiation Tests on Degradation of Photovoltaic Characteristics of Space Solar Cells”, Quantum Beam Sci. **5**, 15-1-12 (2021). **E, S, C**

4) Y. Hijikata, S. Komori, S. Otojima, Y. Matsushita and T. Ohshima, “Impact of formation process on the radiation properties of single-photon sources generated on SiC crystal surfaces”, Appl. Phys. Lett. **118**, 204005-1-6 (2021). **N**

5) J. Coutinho, J. D. Gouveia, T. Makino, T. Ohshima, Z. Pastuovic, L. Bakrac, T. Brodar and I. Capan, “M center in 4H-SiC is a carbon self-interstitial”, Phys. Rev. B **103**, L180102-1-5 (2021). **E**

6) H. Takashima, A. Fukuda, K. Shimazaki, Y. Iwabata, H. Kawaguchi, A. W. Schell, T. Tashima, H. Abe, S. Onoda, T. Ohshima and S. Takeuchi, “Creation of silicon vacancy color centers with a narrow emission line in nanodiamonds by ion implantation”, Opt. Mater. Express **11**, 1978-1988 (2021). **I**

7) Y. Miyazawa, G. M. Kim, A. Ishii, M. Ikegami, T. Miyasaka, Y. Suzuki, T. Yamamoto, T. Ohshima, S. Kanaya, H. Toyota and K. Hirose, “Evaluation of Damage Coefficient for Minority-Carrier Diffusion Length of Triple-Cation Perovskite Solar Cells under 1 MeV Electron Irradiation for Space Applications”, J. Phys. Chem. C **125**, 13131-13137 (2021). **E**

8) H. Kubota, H. Ogawa, M. Miyazaki, S. Ishii, K. Ohyama, Y. Kawamura, S. Ishiwata and M. Suzuki, “Microscopic Temperature Control Reveals Cooperative Regulation of Actin–Myosin Interaction by Drebrin E”, Nano Lett. **21**, 9526-9533 (2021). **N**

9) K. Shimazaki, H. Kawaguchi, H. Takashima, T. F. Segawa, F. T.-K. So, D. Terada, S. Onoda, T. Ohshima, M. Shirakawa, and S. Takeuchi, “Fabrication of Detonation Nanodiamonds Containing Silicon-Vacancy Color Centers by High Temperature Annealing”, Phys. Status Solidi A **218**, 2100144-1-9 (2021). **I**

10) K. Oyama, S. Ishii and M. Suzuki, “Opto-thermal technologies for microscopic analysis of cellular temperature-sensing systems”, Biophys. Rev. **14**, 41-54 (2021). **N**

11) M. O. D. Vries, S. -I. Sato, T. Ohshima, B. C. Gibson, J. -M. Bluet, S. Castelletto, B. C. Johnson and P. Reineck, “Fluorescent Silicon Carbide Nanoparticles”, Adv. Opt. Mater.

9, 2100311 (2021). **I, T**

12) H. Nakane, M. Kato, Y. Ohkouchi, X. T. Trinh, I. G. Ivanov, T. Ohshima and N. T. Son, "Deep levels related to the carbon antisite–vacancy pair in 4H-SiC", J. Appl. Phys. **130**, 65703-1-8 (2021). **E**

13) R. Bernat, L. Bakrac, V. Radulovic, L. Snoj, T. Makino, T. Ohshima, Z. Pastuovic and I. Capan, "4H-SiC Schottky Barrier Diodes for Efficient Thermal Neutron Detection", Materials **14**, 5105-1-10 (2021). **N**

14) K. Sakamoto, S. Baba, D. Kobayashi, S. Okamoto, H. Shindou, O. Kawasaki, T. Makino, Y. Mori, D. Matuura, M. Kusano, T. Narita, S. Ishii and K. Hirose, "Investigation of Buried-Well Potential Perturbation Effects on SEU in SOI DICE-Based Flip-Flop Under Proton Irradiation", IEEE Trans. Nucl. Sci. **68**, 1222-1227 (2021). **C**

15) T. Tatsuishi, K. Kanehisa, T. Kageura, T. Sonoda, Y. Hata, K. Kawakatsu, T. Tanii, S. Onoda, A. Stacey, S. Kono and H. Kawarada, "Highly aligned 2D NV ensemble fabrication from nitrogen-terminated (111) surface", Carbon **180**, 127-134 (2021). **N**

16) C. Zhang, F. Shagieva, M. Widmann, M. Kübler, V. Vorobyov,P. Kapitanova, E. Nenasheva, R. Corkill, O. Rhrle, K. Nakamura, H. Sumiya, S. Onoda, J. Isoya and J. Wrachtrup, "Diamond Magnetometry and Gradiometry Towards Subpicotesla dc Field Measurement", Phys. Rev. Appl. **15**, 64075-1-11 (2021). **E**

17) R. A. Parker, N. Dontschuk, S. -I. Sato, C. T.-K. Lew, P. Reineck, A. Nadarajah, Ohshima Takeshi, B. C. Gibson, S. Castelletto, J. C. McCallum and B. C. Johnson, "Infrared erbium photoluminescence enhancement in silicon carbide nano-pillars", J. Appl. Phys. **130**, 145101-1-8 (2021). **N**

18) X. Wu, S. Kondo, H. Yu, Y. Okuno, M. Ando, H. Kurotaki, S. Tanaka, K. Hokamoto, R. Ochiai, S. Konishi and R. Kasada, "Bonding strength evaluation of explosive welding joint of tungsten to ferritic steel using ultra-small testing technologies", Mater. Sci. Eng. A **826**, 141995 (2021). **N**

19) S. Ishii, S. Saiki, S. Onoda, Y. Masuyama, H. Abe and T. Ohshima, "Ensemble Negatively-Charged Nitrogen-Vacancy Centers in type-Ib Diamond Created by High Fluence Electron Beam Irradiation", Quantum Beam Sci. **6**, 2-1-10 (2021). **E**

20) C. Shinei, M. Miyakawa, S. Ishii, S. Saiki, S. Onoda, T. Taniguchi, T. Ohshima and T. Teraji, "Equilibrium charge state of NV centers in diamond", Appl. Phys. Lett. **119**, 254001-1-5 (2021). **E**

21) J. Ieda, S. Okayasu, K. Harii, M. Kobata, K. Yoshii, T. Fukuda, M. Ishida and E. Saitoh, "The damage analysis for irradiation tolerant spin-driven thermoelectric device based on single-crystalline $Y_3Fe_5O_{12}$/Pt heterostructures", IEEE Trans. Magn. **58**,1301106 (2022). **N**

22) Y. Abe A. Chaen, M. Sometani, S. Harada, Y. Yamazaki, T. Ohshima, and T. Umeda, "Electrical detection of T_{V2a}-type silicon vacancy spin defect in 4H-SiC MOSFETs, Appl. Phys. Lett. **120**, 064001-1-6 (2022). **I**

23) C. P. Anderson, E. O. Glen, C. Zeledon, A. Bourassa, Y. Jin, Y. Zhu, C. Vorwerk, A. L. Crook, H. Abe, J. U. Hassan, T. Ohshima, N. T. Son, G. Galli and D. D. Awschalom, "Five-second coherence of a single spin with single-shot readout in silicon carbide", Sci. Adv. **8**, eabm5912-1-9 (2022). **E**

24) K. Yamane, R. Futamura, S. Genjo, D. Hamamoto, Y. Maki, E. M. Pavelescu, T. Ohshima, T. Sumita, M. Imaizumi and A. Wakahara, "Improved crystallinity of GaP-based dilute nitride alloys by proton/electron irradiation and rapid thermal annealing", J. J. Appl. Phys. **61**, 020907-1-5 (2022). **E, I**

25) F. So, A. I. Shames, D. Terada, T. Genjo, H. Morishita, I. Ohki, T. Ohshima, S. Onoda, H. Takashima, S. Takeuchi, N. Mizuochi, R. Igarashi, M. Shirakawa and T. F. Segawa, "The Anomalous Formation of Irradiation Induced Nitrogen-Vacancy Centers in 5-Nanometer-Sized Detonation Nanodiamonds", J. Phys. Chem. C **126**, 5206-5217 (2022). **E**

26) M. Imaizumi, Y. Okuno , T. Takamoto, S. -I. Sato and T. Ohshima, "Displacement damage dose analysis of the output characteristics of $In_{0.5}Ga_{0.5}P$ and $Cu(In,Ga)(S,Se)_2$ solar cells irradiated with alpha ray simulated helium ions", J. J. Appl. Phys. **61**, 044002-1-7 (2022). **I, T**

27) T. Luo, L. Lindner, J. Langer, V. Cimalla, X. Vidal, F. Hahl, C. Schreyvogel, S. Onoda, S. Ishii, T. Ohshima, D. Wang, D. A. Simpson, B. C. Johnson, M. Capelli, R. Blinder and J. Jeske, "Creation of nitrogen-vacancy centers in chemical vapor deposition diamond for sensing applications", New J. Phys. **24**, 0033030-1-16 (2022). **E**

28) M. Capelli, L. Lindner, T. Luo, J. Jaske, H. A, S. Onoda, Onoda, T. Ohshima, B. Johnson, D. A. Simpson, A. Stacey, P. Reineck, B. C. Gibson and A. D. Greentree, "Proximal nitrogen reduces the fluorescence quantum yield of nitrogen-vacancy centres in diamond", New J. Phys. **24**, 033053-1-10 (2022). **E**

29) I. Capan, T. Brodar, R. Bernat, Ž. Pastuović, T. Makino, T. Ohshima, J. D. Gouveia and J. Coutinho, "M-center in 4H-SiC: Isothermal DLTS and first principles modeling studies", J. Appl. Phys. **130**, 125703-1-10 (2021). **E**

30) J. Meinel, V. Vorobyov, B. Yavkin, D. Dasari, H. Sumiya, S. Onoda, J. Isoya and J. Wrachtrup, "Heterodyne sensing of microwaves with a quantum sensor", Nat. Commun. **12**, 1-8 (2021). **E**

31) D. Kobayashi, K. Hirose, K. Sakamoto, Y. Tsuchiya, S. Okamoto, S. Baba, H. Shindou, O. Kawasaki, T. Makino and T. Ohshima, "An SRAM SEU Cross Section Curve Physics Model, IEEE Trans. Nucl. Sci. **69**, 232-240 (2022). **C**

32) T. Umeda, K. Watanabe, H. Hara, H. Sumiya, Onoda Shinobu, A. Uedono, I. Chuprina, P. Siyushev, F. Jelezko, J. Wrachtrup and J. Isoya, "Negatively charged boron vacancy center in diamond", Phys. Rev. B **105**, 165201-1-13 (2022). **I**

33) T. Kageura, Y. Sasama, C. Shinei, T. Teraji, K. Yamada, S. Onoda and T. Yamaguchi, "Charge stability of shallow single nitrogen-vacancy centers in lightly boron-doped diamond", Carbon **192**, 473-481 (2022). **N**

34) O. V. Zwier, T. Bosma, C. M. Gilardoni, X. Yang, A. R. Onur, T. Ohshima, N. T. Son and C. H. Wal, "Electromagnetically induced transparency in inhomogeneously broadened divacancy defect ensembles in SiC", J. Appl. Phys. **131**, 094401-1-8 (2022). **E**

35) M. G. Fard, Z. Khabir, P. Reineck, N. M. Cordina, H. Abe, T. Ohshima, S. Dalal, B. C. Gibson, N. H. Packer and L. M. Parker, "Targeting cell surface glycans with lectin-coated fluorescent nanodiamonds", Nanoscale Adv. **4**, 1551-1564 (2022). **E**

36) T. Yanagi, K. Kaminaga, M. Suzuki, H. Abe, H. Yamamoto, T. Ohshima, A. Kuwahata, M. Sekino, T. Imaoka, S. Kakinuma, T. Sugi, W. Kada, O. Hanaizumi and R. Igarashi, "All-Optical Wide-Field Selective Imaging of Fluorescent Nanodiamonds

in Cells, In Vivo and Ex Vivo", ACS Nano **15**, 12869-12879 (2021). **E**

37) K. Kaminaga, H. Yanagihara, T. Genjo, T. Morioka, H. Abe, M. Shirakawa, T. Ohshima, S. Kakinuma and R. Igarashi, "Non-contact Measurement of Internal Body Temperature Using Subcutaneously Implanted Diamond Microparticles", Biomater. Sci. **9**, 7049-7053 (2021). **E**

38) A. Akther, E. P. Walsh, P. Reineck, B. C. Gibson, T. Ohshima, H. Abe, G. McColl, N. L. Jenkins, L. T. Hall, D. A. Simpson, A. R. Rezk and L. Y. Yeo, "Acoustomicrofluidic Concentration and Signal Enhancement of Fluorescent Nanodiamond Sensors", Anal. Chem. **93**, 16133-16141 (2022). **E**

39) H. Ikegami, K. Akiba and H. Minoda, "Evaluation of electron radiation damage to green fluorescent protein", Ultramicroscopy 225, 113272-1-5 (2021). **N**

Proceedings

1) M. Imaizumi, Y. Okuno, S. -I. Sato and T. Ohshima, "Displacement Damage Dose Analysis of Alpha-rayDegradation of Output of a CIGS Solar Cell", Proc. 48th IEEE Photovoltaic Specialists Conference (48th PVSC), Online (2021.06). **T, I, E**

Books

1) 小野田 忍, 谷井 孝 至, 寺地 徳之, 渡邊 幸志, 磯谷 順一, "量子センシング NMR による超微量試料の化学構造同定", 第 2 章 第 3 節, "NMRによる有機材料分析とその試料前処理、データ解釈", 技術情報協会, 72-109 (2021).

2) 小野田 忍, 山崎 雄一, 大島 武, "ダイヤモンド中への負に帯電した窒素-空孔(NV-)センタの形成技術", 第 1 章 第 3 節, "量子センシングハンドブック", 監修 根来 誠, 株式会社エヌ・ティー・エス, 43-56 (2021).

Patents

1) 山崎 雄一、増山 雄太、大島 武、"物理量検出装置、物理量検出方法、および物理量検出プログラム" 特願 2022-005281 (2022.01.17). **S**

2) 佐藤 真一郎, 出来 真斗, 西村 智朗, "温度検出装置、温度センサ、温度検出方法、および温度検出プログラム", 特願 2021-032894 (2021.03.02). **I**

3) 佐藤 真一郎, 出来 真斗, 西村 智朗, "温度センサ、温度検出装置、温度検出方法、温度検出プログラム、および温度センサの製造方法", 特願 2021-032895 (2021.03.02). **I**

P2-1 Project "Microbeam Radiation Biology"

Papers

1) K. Sakamoto, Z. Soh, M. Suzuki, Y. Iino and T. Tsuji, "Forward and backward locomotion patterns in *C. elegans* generated by a connectome-based model simulation", Sci. Rep. **11**, 13737 (2021). **C**

2) T. Yanagi, K. Kaminaga, M. Suzuki, H. Abe, H. Yamamoto, T. Ohshima, A. Kuwahata, M. Sekino, T. Imaoka, S. Kakinuma, T. Sugi, W. Kada, O. Hanaizumi and R. Igarashi, "All-Optical Wide-Field Selective Imaging of Fluorescent Nanodiamonds in Cells, In Vivo and Ex Vivo", ACS Nano **15**, 12869 (2021). **N**

3) A. Yamasaki, M. Suzuki, T. Funayama, T. Moriwaki, T. Sakashita, Y. Kobayashi and Q. M. Zhang-Akiyama, "High-Dose Irradiation Inhibits Motility and Induces Autophagy in *Caenorhabditis elegans*", Int. J. Mol. Sci. **22**, 9810 (2021). **C**

4) K. Nagata, T. Yasuda, M. Suzuki, T. Funayama, H. Mitani and S. Oda, "Testis-ova Induction by Microbeam Irradiation in P53-Deficient Medaka Testis", Cytologia **87**, 1 (2022). **C**

5) T. D. Ta, T. Umedachi, M. Suzuki and Y. Kawahara, "A Printable Soft-bodied Wriggle Robot with Frictional 2D-anisotropy Surface", J. Inform. Proc. **30**, 201 (2022). **N**

6) M. Suzuki, Y .Hattori, T. Saito and Y. Harada, "Pond Assay for the Sensory Systems of *Caenorhabditis elegans*: A Novel Anesthesia-Free Method Enabling Detection of Responses to Extremely Low Chemical Concentrations", Biology **11**, 335 (2022). **N**

7) 鈴木 芳代, 舟山 知夫, "重イオンマイクロビームを用いた個体機能解析研究", 放射線生物研究 **57**, 114 (2022). **C**

Patents

1) 鈴木 芳代, "試験方法および線虫試験用プレート", 国際出願 PCT/JP2021/039211 (2021.10.25). **N**

2) 鈴木 芳代, 服部 佑哉, 齋藤 俊行, 原田 良信, "線虫トラップ用プレート、およびその利用", 特願 2021-516257 (2021.10.21). **N**

3) 鈴木 芳代, 服部 佑哉, 齋藤 俊行, 原田 良信, "NEMATODE TRAP PLATE AND USE THEREFOR", アメリカ 17/605,337 (2021.10.21). **N**

4) 鈴木 芳代, "線虫封入カプセル、線虫封入カプセルの製造方法、および、線虫封入 カプセルの用途", 特願 2021-199634 (2021.12.08). **N**

5) 鈴木 芳代, "試験方法および線虫試験用プレート", 特願 2022-514816 (2022.03.04). **N**

6) 森 慎一郎, 鈴木 芳代, 原田 良信, 立花 泰彦, 服部 佑哉, "画像認識プログラム、これを用いた画像認識装置、検出対象個体数計数方法、およびこれらに使用する画像認識学習用モデル画像作成装置", 特願 2022-042659 (2022.03.17). **N**

P2-2 Project "Ion Beam Mutagenesis"

Papers

1) S. Kitamura, K. Satoh and Y. Oono, "Detection and characterization of genome-wide mutations in M1 vegetative cells of gamma-irradiated *Arabidopsis*", PLOS Genet. **18**, e1009979 (2022). **G**

2) A. N. Sakamoto, T. Sakamoto, Y. Yokota, M. Teranishi, K. O. Yoshiyama and S. Kimura, "SOG1, a plant-specific master regulator of DNA damage responses, originated from nonvascular land plants", Plant Direct, **5**, e370 (2021). **G**

3) Y. Hase, K. Satoh, A. Chiba, Y. Hirano, K. Moribayashi and K. Narumi, Proton-Cluster-Beam lethality and mutagenicity in *Bacillus subtilis* spores, Quantum Beam Science **5**, 25 (2021). **T**

4) Y. Kato, T. Oyama, K. Inokuma, C. J. Vavricka, M. Matsuda, R. Hidese, K. Satoh, Y. Oono, J.-S. Chang, T. Hasunuma and A. Kondo, "Enhancing carbohydrate repartitioning into lipid and carotenoid by disruption of microalgae starch debranching enzyme", Commun. Biol. **4**, 450 (2021). **C**

5) T. Oyama, Y. Kato, K. Satoh, Y. Oono, M. Matsuda, T. Hasunuma and A. Kondo, "Development of mutant microalgae that accumulate lipids under nitrate-replete conditions", Algal Res. **60**, 102544 (2021). **C**

6) T. Koretsune, Y. Ishida, Y. Kaneda, E. Ishiuchi, M. Teshima, N. Marubashi, K. Satoh and M. Ito, Novel cesium resistance mechanism of alkaliphilic bacterium isolated from jumping spider ground extract, Frontiers in Microbiology **13**, 841821 (2022). **N**

R. Yokoyama, T. Yokoyama, Y. Kaga, Y. Oono and K. Nishitani, "Characterization of *Cuscuta campestris* cell wall genes responsible for the haustorial invasion of host plants", Sci. J. Kanagawa Univ. **32**, 21-26 (2021). **N**

Book

1) 大野 豊, 長谷 純宏, 佐藤 勝也, "18.1 植物・微生物へのイオンビーム照射", 電子・イオンビームハンドブック(第4版), 日本学術振興会第 132 委員会, 466-479 (2021).

Patent

1) 北村 智, 佐藤 勝也, 大野 豊, "同一細胞を起源とする生物組織又は生物細胞を選抜する方法、及びその利用" , 特願 2022-006756, (2022.01.19). **G**

Press・TV

1) 神戸大学・量研機構, "微細藻類バイオ燃料:炭水化物を油脂に変換", 2021.04.09, プレス発表:毎日新聞, 東京新聞, 上毛新聞, 科学新聞, Tii 技術情報 web に掲載、エフエム群馬ニュースで放送. **C**

2) "世界初！変異処理した植物から、直接、DNA に生じた突然変異を全検出", 2022.01.21, プレス発表:毎日新聞, 日経新聞, 上毛新聞に掲載. **G**

3) "量子ビームで新酵母", 2022.01.08, 新聞連載記事, 毎日新聞. **C**

P2-3 Project "Medical Radioisotope Application"

Papers

1) A. Kanai, H. Hanaoka, A. Yamaguchi, I. Mahendra, C. Palangka, Y. Ohshima, T. Higuchi and Y. Tsushima, "Enhancing the accumulation level of 3-[^{18}F]fluoro-L-α-methyltyrosine in tumors by preloading probenecid", Nucl. Med. Biol. **104-105**, 47-52 (2022). **C**

2) Y. Nagao, M. Yamaguchi, S. Watanabe, N. S. Ishioka, N. Kawachi and H. Watabe, "Performance improvement of Compton imaging of astatine-211 by optimising coincidence time windows", J. Instrum. **16**, C12031, (2021). **C**

3) Y. Sugo, R. Miyachi, S. Obata, Y. Maruyama, H. Manabe, M. Mori, N. S. Ishioka, K. Toda and S. Ohira, "Rapid Flow-Based System for Separation of Radioactive Metals by Selective Complex Formation", Anal. Chem. **93**, 17069-17075, (2021). **C**

4) T. Sakashita, S. Matsumoto, S. Watanabe, H. Hanaoka, Y. Ohshima, Y. Ikoma, N. Ukon, I. Sasaki, T. Higashi, T. Higuchi, Y. Tsushima and N. S. Ishioka, "Nonclinical study and applicability of the absorbed dose conversion method with a single biodistribution measurement for targeted alpha-nuclide therapy", EJNMMI Phys. **8**, 80 (2021). **C**

5) H. Hanaoka, Y. Ohshima, H. Suzuki, I. Sasaki, T. Watabe, K. Ooe, S. Watanabe and N. S. Ishioka, "Enhancing the therapeutic effect of 2-^{211}At-astato-α-methyl-L-phenylalanine with probenecid loading", Cancers, **13(21)**, 5514, (2021). **C**

6) H. Suzuki, Y. Kaizuka, M. Tatsuta, H. Tanaka, N. Washiya, Y. Shirakami, K. Ooe, A. Toyoshima, T. Watabe, T. Teramoto, I. Sasaki, S. Watanabe, N. S. Ishioka, J. Hatazawa, T. Uehara and Y. Arano, "Neopentyl glycol as a scaffold to provide radiohalogenated theranostic pairs of high in vivo stability", J. Med. Chem. **64**, 15846-15857 (2021). **C**

7) R. Imura, H. Ida, I. Sasaki, N. S. Ishioka and S. Watanabe, "Re-evaluations of Zr-DFO Complex Coordination Chemistry for the Estimation of Radiochemical Yields and Chelator-to-Antibody Ratios of ^{89}Zr Immune-PET Tracers", Molecules **26**, 4977 (2021). **C**

Proceedings

1) 宮脇信正, 渡辺茂樹, 柏木啓次, 石岡典子, 倉島俊, 福田光宏, "TIARA AVF サイクロトロンにおける RI 製造用ビームラインのビームエネルギー・位置モニターの開発", Proc. 18th Annual Meeting of Particle Accelerator Society of Japan, 302-305, オンライン (2021.08). **C**

Patents

1) Noriko S. Ishioka, Hiroo Kondo and Shigeki Watanabe, "Producing Method of Radioisotopes and Radioisotope Producing Apparatus", US 11,276,506 B2, (2022.03.15). **C**

2) 大平 慎一, 戸田 敬, 須郷 由美, 森 勝伸, "分離方法、分離精製方法及び放射性同位体の製造方法、並びに分離装置及び分離精製システム", 特願 2021-128299, (2021.08.04). **C**

3) 坂下 哲哉, 渡辺 茂樹, 宮脇 信正, 石岡 典子, "放射性同位体の製造装置, 製造システム", 及び製造方法, 特願 2022-75333 (2022.04.28).

Press・TV

1) 千葉大学・東京工業大学・大阪大学放射線科学基盤機構・量子科学技術研究開発機構, "生体内で安定して機能するアスタチン-211 標識法を開発 より有効で安全な核医学治療への応用に期待", 2021.10.28 プレス発表:日経バイオテク Web 版、医療 NEWS QLifePro, 上毛新聞 Web 版に掲載, エフエム群馬ニュースで放送. **C**

P2-4 Project "Radiotracer Imaging"

Papers

1) K. Higuchi, K. Kurita, T. Sakai, N. Suzui, M. Sasaki, M. Katori, Y. Wakabayashi, Y. Majima, A. Saito, T. Ohyama and N. Kawachi, ""Live-Autoradiography" Technique Reveals Genetic Variation in the Rate of Fe Uptake by Barley Cultivars", Plants **11**, 817 (2022). **N**
2) M. Yamaguchi, N. Suzui, Y. Nagao and N. Kawachi, "Simulation evaluation on a compact monitor for gamma-emitting tracers in plant stems", Jpn. J. Appl. Phys. **61**, 027001 (2022). **N**
3) Y. Nagao, M. Yamaguchi, S. Watanabe, N. S. Ishioka and N. Kawachi, H. Watabe, "Performance improvement of Compton imaging of astatine-211 by optimising coincidence time windows", J. Instrum. **16**, C12031 (2021). **C**
4) Y. Miyoshi, Y. Nagao, M. Yamaguchi, N. Suzui, Y. G. Yin, N. Kawachi, E. Yoshida, S. Takyu, H. Tashima, T. Yamaya, N. Kuya, S. Teramoto and Y. Uga, "Plant root PET: visualization of photosynthate translocation to roots in rice plant", J. Instrum. **16**, C12018 (2021). **C**
5) K. Kurita, T. Sakai, N. Suzui, Y.-G. Yin, R. Sugita, N. I. Kobayashi, K. Tanoi and N. Kawachi, "Autoradiography system with phosphor powder (ZnS:Ag) for imaging radioisotope dynamics in a living plant", Jpn. J. Appl. Phys. **60**, 116501 (2021). **N**
6) Y.-G. Yin, Y. Mori, N. Suzui, K. Kurita, M. Yamaguchi, Y. Miyoshi, Y. Nagao, M. Ashikari, K. Nagai and N. Kawachi, "Non-invasive imaging of hollow structures and gas movement revealed the gas partial pressure gradient-driven long-distance gas movement in the aerenchyma along the leaf blade to submerged organs in rice", New Phytol. **232**, 1974-1984 (2021). **C**
7) M. Kitano, S. Yamamoto, T. Yabe, T. Akagi, T. Toshito, M. Yamaguchi, N. Kawachi, "Imaging and range estimations of prompt X-rays using YAP(Ce) camera during particle-ion irradiation to phantoms with air cavities", J. Instrum. **16**, P08064 (2021). **N**
8) Y. Miyoshi, K. Hidaka, Y.-G. Yin, N. Suzui, K. Kurita and N. Kawachi, "Non-invasive ^{11}C-Imaging Revealed the Spatiotemporal Variability in the Translocation of Photosynthates Into Strawberry Fruits in Response to Increasing Daylight Integrals at Leaf Surface", Front. Plant Sci. **12**, 688887 (2021). **C**
9) Y. H.-T. Kohda, Z. Qian, M.-F. Chien, K. Miyauchi, G. Endo, N. Suzui, Y.-G. Yin, N. Kawachi, H. Ikeda, H. Watabe, H. Kikunaga, N. Kitajima and C. Inoue, "New evidence of arsenic translocation and accumulation in *Pteris vittata* from real-time imaging using positron-emitting ^{74}As tracer", Sci. Rep. **11**, 12149 (2021). **C**

Patent

1) 三好悠太, 尹永根, 鈴井伸郎, 河地有木, "植物の育成管理システム, 植物の育成管理方法, 師管転流速の測定方法及び師管転流速の算出プログラム, 植物の生産方法", 特願 2021-130988 (2021.8.10).

Press・TV

1) "モエジマシダが猛毒のヒ素に耐えるしくみが見えてきた！～世界初, ヒ素高蓄積植物の根茎の役割をイメージング技術で解明～", 2021.7.8, プレス発表: 科学新聞, 大学ジャーナルオンライン, Science Japan に掲載. **C**

P2-5 Project "Generation of Radioisotopes with Accelerator Neutrons"

Papers

1) I. Nishinaka, K. Washiyama and K. Hashimoto, "Adsorption temperature of volatile astatine species formed via dry distillation in a glass tube", J. Radioanal. Nucl. Chem. **329**, 1459-1465 (2021). **N**
2) M. Kawabata, S. Motoishi, A. Ohta, A. Motomura, H. Saeki, K. Tsukada, S. Hashimoto, N. Iwamoto, Y. Nagai and K. Hashimoto, "Large scale production of ^{64}Cu and ^{67}Cu via the ^{64}Zn(n, p)^{64}Cu and ^{68}Zn(n, np/d)^{67}Cu reactions using accelerator neutrons", J Radioanal. Nucl Chem **330,** 913–922 (2021). **N**
3) Y. Nagai, "Production scheme for diagnostic-therapeutic radioisotopes by accelerator neutrons", Proc. Jpn. Acad. Ser. B **97,** 292-323(2021)**.** **N**
4) 4) Y. Nagai, M. Kawabata, S. Hashimoto, K. Tsukada, K. Hashimoto, S. Motoishi, H. Saeki, A. Motomura, F. Minato and M. Itoh, "Estimated Isotopic Compositions of Yb in Enriched ^{176}Yb for Producing ^{177}Lu with High Radionuclide Purity by ^{176}Yb(d,x)^{177}Lu", J. Phys. Soc. Jpn. **91**, 044201-1-10 (2022). **N**

Proceedings

1) 西中 一朗, 橋本 和幸, 鷲山 幸信, "医療用 α 放射性 ^{211}At 利用のための基礎研究－乾式蒸留法における熱分離特性－", 第 58 回アイソトープ・放射線研究発表会 要旨集, 29009-10-02, オンライン (2021.07). **N**
2) 本村 新, 川端 方子, 太田 朗生, 本石 章司, 佐伯 秀也, 塚田 和明, 初川 雄一, 永井 泰樹, 橋本 和幸, "低比放射能 ^{99}Mo を用いた小型ジェネレーターの開発", 第 58 回アイソトープ・放射線研究発表会 要旨集, 29004-04-01, オンライン, (2021.07). **N**
3) 3) 西中 一朗, 鷲山 幸信, 橋本 和幸, "乾式蒸留分離におけるアスタチンの熱分離特性", 日本放射化学会第 65 回討論会 要旨集, 3K04, オンライン, (2021.09). **N**
4) 永井 雄太, 青井 景都, 丸山 俊平, 西中 一朗, 鷲山 幸信, 羽場 宏光, 横山 明彦, "核医学用アスタチン抽出に利用できるイオン液体の研究", 日本放射化学会第 65 回討論会 要旨集, 2P10, オンライン, (2021.09). **N**
5) 塚田 和明, 橋本 和幸, 橋本 慎太郎, 浅井 雅人, 初川 雄一, 佐伯 秀也, 川端 方子, 太田 朗生, 本村 新, "加速器中性子によるがん治療用 Sc-47 の製造に関する研究", 日本放射化学会第 65 回討論会 要旨集, 3P10 オンライン, (2021.9). **N**

P3-2 Project " LCS Gamma-ray"

Papers

1) R. Hajima, “Bandwidth of a Compton radiation source with an electron beam of asymmetric emittance”, Nucl. Instrum. Methods Phys. Res. A **985**, 164655 (2021). **N**

2) T. Shizuma, F. Minato, M. Omer, T. Hayakawa, H. Ohgaki, and S. Miyamoto, “Low-lying electric and magnetic dipole strengths in ^{207}Pb”, Physical Review C, 103 (2021). 024309. **N**

3) R. Hajima, “Few-Cycle Infrared Pulse Evolving in FEL Oscillators and Its Application to High-Harmonic Generation for Attosecond Ultraviolet and X-ray Pulses”, Atoms **9**(1), **15** (2021). **N**

4) T. Hayakawa, Y. Toh, A. Kimura, S. Nakamura, T. Shizuma, N. Iwamoto, S. Chiba and T. Kajino, “Isomer production ratio of the ^{112}Cd(n,γ)^{113}Cd reaction in an s-process branching point”, Phys. Rev. C **103**, 045801 (2021). **N**

5) K. Ali, H. Zen, H. Ohgaki, T. Kii, T. Hayakawa, T. Shizuma, H. Toyokawa, M. Fujimoto, Y. Taira and M. Katoh, “Three-Dimensional Nondestructive Isotope-Selective Tomographic Imaging of ^{208}Pb Distribution via Nuclear Resonance Fluorescence”, Appl. Sci. **11**(8), 3415 (2021). **N**

6) T. Mori, A. Yogo, T. Hayakawa, S. R. Mirfayzi, Z. Lan, Y. Abe, Y. Arikawa, D. Golovin, T. Wei, Y. Honoki, M. Nakai, K. Mima, H. Nishimura, S. Fujioka and R. Kodama, “Direct evaluation of high neutron density environment using (n,2n) reaction induced by laser-driven neutron source”, Phys. Rev. C **104**, 015808 (2021). **N**

7) A. Yogo, S. R. Mirfayzi, Y. Arikawa, Y. Abe, T. Wei, T. Mori, Z. Lan, Y. Hoonoki, D. O. Golovin, K. Koga, Y. Suzuki, M. Kanasaki, S. Fujioka, M. Nakai, T. Hayakawa, K. Mima, H. Nishimura, S. Kar and R. Kodama, “Single shot radiography by a bright source of laser-driven thermal neutrons and x-rays”, Appl. Phys. Express **14**, 106001 (2021). **N**

8) R. Hajima, T. Hayakawa, T. Shizuma, S. Miyamoto and S. Matsuba, “Reconstruction of the laser Compton scattered gamma-ray distribution in the energy-angle phase space from crystal diffraction data”, Appl. Phys. Express **14**, 104004 (2021). **N**

9) K. Inaba, Y. Sasamoto, T. Kawabata, M. Fujiwara, Y. Funaki, K. Hatanaka, K. Itoh, M. Itoh, K. Kawase, H. Matsubara, Y. Maeda, K. Suda, S. Sakaguchi, Y. Shimizu, A. Tamii, Y. Tameshige, M. Uchida, T. Uesaka, T. Yamada and H. P. Yoshida, “Search for α condensed states in ^{13}C using α inelastic scattering”, Prog. Theor. Exp. Phys. **2021**, Issue 9, 093D01 (2021). **N**

10) Y. Honda, M. Adachi, S. Eguchi, M. Fukuda, N. Higashi, R. Kato, T. Miura, T. Miyajima, S. Nagahashi, N. Nakamura, K. Nigorikawa, T. Nogami, T. Obina, H. Sagehashi, H. Sakai, M. Shimada, T. Shioya, R. Takai, O. Tanaka, Y. Tanimoto, K. Tsuchiya, T. Uchiyama, A. Ueda, M. Yamamoto, D. Zhou, M. Kakehata, T. Sato, H. Yashiro and R. Hajima, “Construction and commissioning of mid-infrared self-amplified spontaneous emission free-electron laser at compact energy recovery linac”, Rev. Sci. Instrum. **92** (11), 113101 (2021). **N**

11) T. Maruyama, T. Hayakawa, T. Kajino and M.-K. Cheoun, “Generation of photon vortex by synchrotron radiation from electrons in Landau states under astrophysical magnetic fields”, Phys. Lett. B **826**, 136779 (2022). **N**

12) C. R. Howell, M. W. Ahmed, A. Afanasev, D. Alesini, J. R. M. Annand, A. Aprahamian, D. L. Balabanski, S. V. Benson, A. Bernstein, C. R. Brune, J. Byrd, B. E. Carlsten, A. E. Champagne, S. Chattopadhyay, D. Davis, E. J. Downie, M. J. Durham, G. Feldman, H. Gao, C. G. R. Geddes, H. W. Griesshammer, R. Hajima, H. Hao, D. Hornidge, J. Isaak, R. V. F. Janssens, D. P. Kendellen, M. A. Kovash, P. P. Martel, Ulf-G. Meissner, R. Miskimen, B. Pasquini, D. R. Phillips, N. Pietralla, D. Savran, M. R. Schindler, M. H. Sikora, W. M. Snow, R. P. Springer, C. Sun, C. Tang, B. Tiburzi, A. P. Tonchev, W. Tornow, C. A. Ur, D. Wang, H. R. Weller, V. Werner, Y. K. Wu, J. Yan, Z. Zhao, A. Zilges and F. Zomer, “International workshop on next generation gamma-ray source”, Journal of Physics G: Nuclear and Particle Physics J. Phys. G: Nucl. Part. Phys. **49**, 010502 (2022). **N**

13) M. Oshima, J. Goto, T. Kin, T. Hayakawa, Y. Ohta, H. Shinohara, K. Kitamura, H. Seto and K. Isogai, “Spectral determination method and its application to γ-ray determination”, J. Nucl. Sci. Technol. **59**, 472 (2022). **N**

Proceedings

1) R. Hajima, R. Nagai, K. Kawase, H. Ohgaki, H. Zen, Y. Hayakawa, T. Sakai, Y. Sumitomo, M. Shimada and T. Miyajima, "Research and Development of Attosecond VUV and X-ray Sources Driven by Mid-Infrared FEL Oscillators”, OSA High-brightness Sources and Light-driven Interactions Congress 2020, paper EF1A.4, Washington D.C., USA (2020.11). **N**

2) 沢村 勝, 羽島 良一, 佐伯 学行, 岩下 芳久, 頓宮 拓, 中村 哲朗, 渡邉 直久, “電子ビーム溶接したスポークの形状測定”, Proc. 18th Annual Meeting of Particle Accelerator Society of Japan, 330-331, Online (2021.08). **N**

3) 宮島 司, 全 炳俊, 高富 俊和, 福田 将史, 梶田 駿汰, 島田 美帆, 大垣 英明, 羽島 良一, “高効率極短 FEL パルス生成のための 1.6 セル高周波電子銃の開発”, Proc. 18th Annual Meeting of Particle Accelerator Society of Japan, 610-613, Online (2021.08). **N**

4) 羽島 良一, “共振器型自由電子レーザーにおける超放射”, Proc. 18th Annual Meeting of Particle Accelerator Society of Japan, 748-751, Online (2021.08) . **N**

5) 川瀬 啓悟, 羽島 良一, 森 道昭, 永井 良治, “差周波発生のための高非線形性フォトニック結晶ファイバーによる波長シフト”, Proc. 18th Annual Meeting of Particle Accelerator Society of Japan, 756-759, Online (2021.08). **N**

6) 住友 洋介, 境 武志, 早川 恭史, 川瀬 啓悟, 羽島 良一, 中赤外自由電子レーザーパルス高強度化のための外部蓄積実験に向けて, Proc. 18th Annual Meeting of Particle Accelerator Society of Japan, 942-945, Online (2021.08). **N**

Press・TV

1) “量子論で解く, ブラックホールでのガンマ線渦生成”, 2021.11.25, プレス発表: アストロアーツ, BIGLOBE ニュース, マイナビニュースに掲載.

2) “レーザー中性子・X 線による同時瞬間撮影－10 万分の 1 秒の短いパルスで可視光や X 線で見えなかった高速現象を撮る”, 2021.9.16, プレス発表: 中日新聞, 日刊工業新聞に掲載.

P3-3 Beam Engineering Section

Papers

1) A. Terakawa, K. Monokita, Y. Hattori, M. Sato, K. Ishii, M. Koka, N. Yamada, R. Yamagata, Y. Ishii, N. Suzui, T. Satoh and N. Kawachi, "Spatial distributions of cesium and strontium in tea [Camellia sinensis (L.) Kuntze] leaves evaluated by micro-PIXE analysis", Int. J. PIXE **30**, 41-47, (2022). **S**

2) H. Seki, K. Kawamura, H. Hayashi, Y. Ishi, N. Puttaraksa and H. Nishikawa, "Utilizing a photosensitive dry film resist in proton beam writing", Jpn. J. Appl. Phys. **61**, SD1006, (2022). **S**

3) Y. Koga, T. Satoh, K. Kaira, Y. Hachisu, Y. Ishii , T. Yajima, T. Hisada, H.,Yokoo and K. Dobashi, "Progression of idiopathic pulmonary fibrosis is associated with silica/silicate inhalation", Environ. Sci. Technol. Lett. 8, 903-910, (2021). **S**

4) S. Möller, T. Satoh, Y.Ishii, B. Teßmer, R. Guerdelli, T. Kamiya, K. Fujita, K. Suzuk, Y.Kato, H.-D. Wiemhöfer, K. Mima and M. Finsterbusch, "Absolute local quantification of Li as function of state-of-charge in all-solid-state Li batteries via 2D MeV ion-beam analysis", Batteries 7, 41 (2021). **S**

5) K. Motohashi, N. Miyawaki, K Narumi and Y. Saitoh, "Fluence enhancement of a 4 MeV-C4+ ion beam transmitted through a cylindrical glass channel after charging", Jpn. J. Appl. Phys. 60, 096003 (2021). **T**

6) K. Narumi, H. Naramoto, K. Yamada, A. Chiba and Y. Saitoh, "Sputtering Yields of Si Bombarded with 10–540-keV C_{60} Ions", Quantum Beam Sci. **6**, 12 (2022). **I, S**

Proceedings

1) 宮脇信正, 渡辺茂樹, 柏木啓次, 石岡典子, 倉島俊, 福田光宏, "TIARA AVF サイクロトロンにおける RI 製造用ビームラインのビームエネルギー・位置モニターの開発", Proc. 18th Annual Meeting of Particle Accelerator Society of Japan, 302-305, オンライン (2021.08). **C**

2) 倉島 俊, 千葉 敦也, 吉田 健一, 石坂 知久, 山田 圭介, 湯山 貴裕, 平野 貴美, 細谷 青児, 宮脇 信正, 柏木 啓次, 百合 庸介, 石堀 郁夫, 奥村 進, 奈良 孝幸, "QST 高崎イオン照射施設(TIARA)の現状報告", Proc. 18th Annual Meeting of Particle Accelerator Society of Japan, 771-773, オンライン (2021.08). **C, T, S, I**

External Research Groups Except for Takasaki Advanced Radiation Research Institute

Paper

1) J. H. Yu, H. Kurotaki, M. Ando and T. Nozawa, "Mechanical properties of self-ion irradiated pure tungsten using nano-indentation test and micro-tensile test", Nucl. Mater. Energy **30**, 101145 (2022). **T**

Appendix 2 Type of Research Collaboration and Facilities Used for Research

Paper No.	Type of Research Collaboration*1					Utilization of Irradiation Facility*2					
	Joint Res.	Entr. Res.	Coop. Res.	Inter. Use	Ext. Use	C	T	S	I	E	G
1-01	○									○	○
1-02	○										○
1-03				○		○					○
1-04				○						○	
1-05	○							○			
1-06		○								○	
1-07		○								○	○
1-08				○						○	○
1-09	○					○					
1-10	○					○					
1-11	○					○					
1-12	○						○				
1-13	○								○		
1-14	○								○		
1-15	○								○		
1-16	○										○
1-17				○					○		
1-18	○									○	
1-19				○			○				
1-20	○					○	○		○	○	
1-21	○					○					
1-22	○					○	○	○	○		
1-23				○						○	○
1-24				○						○	
1-25	○			○						○	○
1-26				○						○	○
1-27	○								○		
1-28		○									○
1-29				○			○		○		
1-30				○							○
1-31				○							○
1-32				○							○
1-33	○						○				
1-34					○			○			
1-35					○	○		○			
1-36					○		○	○	○		
1-37					○	○					
1-38					○				○		

Paper No.	Type of Research Collaboration*1					Utilization of Irradiation Facility*2					
	Joint Res.	Entr. Res.	Coop. Res.	Inter. Use	Ext. Use	C	T	S	I	E	G
1-39					○	○					
1-40					○						○
2-01	○					○					
2-02	○					○					
2-03	○					○					
2-04	○					○					
2-05	○					○					
2-06	○					○					
2-07	○										○
2-08	○					○					
2-09	○					○					
2-10	○					○					
2-11	○					○					
2-12	○					○					
2-13	○					○					
2-14	○										○
2-15	○										○
2-16	○					○					
2-17	○					○					
2-18	○					○					
2-19				○							○
2-20	○							○			
2-21	○					○		○			
2-22			○					○			
2-23	○					○					
2-24	○							○			
2-25	○							○			
2-26				○		○					
2-27					○			○			
3-01				○		○					
3-02				○		○					
3-03	○							○			
3-04	○							○			
3-05	○							○			
3-06	○							○			
3-07				○			○	○	○		
Total	**45**	**3**	**1**	**18**	**8**	**30**	**8**	**16**	**11**	**11**	**18**

Paper No.	Type of Research Collaboration*1					Management of Irradiation Facility*2					
	Joint Res.	Entr. Res.	Coop. Res.	Inter. Use	Ext. Use	C	T	S	I	E	G
4-01	–	–	–	–	–	O	O	O	O		
4-02	–	–	–	–	–	O					
4-03	–	–	–	–	–		O	O	O		
4-04	–	–	–	–	–					O	O
4-05	–	–	–	–	–					O	O
4-06	–	–	–	–	–	O	O	O	O		
4-07	–	–	–	–	–	O	O	O	O		
4-08	–	–	–	–	–	O	O	O	O	O	O

***1 Type of Research Collaboration**

Joint Res. : Joint research with external users

Entr. Res. : Research entrusted to QST

Coop. Res. : Cooperative research with plural universities through the University of Tokyo (Paper submission is voluntary.)

Inter. Use : Internal use

Ext. Use : Facility use program for external users (Paper submission is voluntary.)

***2 Irradiation Facility**

C : AVF Cyclotron

T : 3 MV Tandem Electrostatic Accelerator

S : 3 MV Single-ended Electrostatic Accelerator

I : 400 kV Ion Implanter

E : 2 MV Electron Accelerator

G : Co-60 Gamma-ray Irradiation Facilities

Appendix 3　Abbreviated Name for National Organizations

【National Institutes for Quantum Science and Technology: **QST**】
（量子科学技術研究開発機構）

◆Directorate and Institutes of QST appearing in this report

QuBS	量子ビーム科学部門	:	Quantum Beam Science Research Directorate
TARRI	高崎量子応用研究所	:	Takasaki Advanced Radiation Research Institute
KPSI	関西光科学研究所	:	Kansai Photon Science Institute
NFI	那珂研究所	:	Naka Fusion Institute
RFI	六ヶ所研究所	:	Rokkasho Fusion Institute
IQMS	量子医科学研究所	:	Institute for Quantum Medical Science
IASLS	次世代放射光施設整備開発センター	:	Institute for Advanced Synchrotron Light Source

◆Department and Center of QST appearing in this report

・量子ビーム科学部門、研究企画部
　Department of Research Planning and Promotion, QuBS, QST
・量子ビーム科学部門、高崎量子応用研究所、量子機能創製研究センター
　Quantum Materials and Applications Research Center, TARRI, QST
・量子ビーム科学部門、高崎量子応用研究所、先端機能材料研究部
　Department of Advanced Functional Materials Research, TARRI, QST
・量子ビーム科学部門、高崎量子応用研究所、放射線生物応用研究部
　Department of Radiation-Applied Biology Research, TARRI, QST
・量子ビーム科学部門、高崎量子応用研究所、放射線高度利用施設部
　Department of Advanced Radiation Technology, TARRI, QST
・量子ビーム科学部門、高崎量子応用研究所、東海量子ビーム応用研究センター
　Tokai Quantum Beam Science Center, TARRI, QST
・量子ビーム科学部門、高崎量子応用研究所、管理部
　Department of Administrative Services, TARRI, QST
・量子ビーム科学部門、関西光科学研究所、放射光科学研究センター
　Synchrotron Radiation Research Center, KPSI, QST
・量子ビーム科学部門、次世代放射光施設整備開発センター、高輝度放射光研究開発部
　Department of Advanced Synchrotron Radiation Research and Development, IASLS, QST
・量子エネルギー部門、那珂研究所、ITERプロジェクト部
　Department of ITER Project, NFI, QST
・量子エネルギー部門、六ヶ所研究所、核融合炉材料研究開発部
　Department of Fusion Reactor Materials Research, RFI, QST
・量子生命・医学部門、量子医科学研究所、重粒子線治療研究部
　Department of Charged Particle Therapy Research, IQMS, QST
・QST未来ラボ
　QST Advanced Study Laboratory, QST

【Other national organizations appearing in this report】

AIST	産業技術総合研究所	:	National Institute of Advanced Industrial Science and Technology
JAEA	日本原子力研究開発機構	:	Japan Atomic Energy Agency
JAXA	宇宙航空研究開発機構	:	Japan Aerospace Exploration Agency
NARO	農業・食品産業技術総合研究機構	:	National Agriculture and Food Research Organization
NIMS	物質・材料研究機構	:	National Institute for Materials Science
NINS	自然科学研究機構	:	National Institutes of Natural Sciences

QST Takasaki Annual Report 2021
(Ed) YAMAMOTO Hiroyuki

Date of Publishing : February 2023
Editorial committee : YAMAMOTO Hiroyuki, OHSHIMA Takeshi, ISHIOKA Noriko S.,
SAITOH Yuichi and TAGUCHI Mitsumasa

Publication : Takasaki Advanced Radiation Research Institute
National Institutes for Quantum Science and Technology
1233 Watanuki, Takasaki, Gunma 370-1292, Japan

Tel : +81-27-346-9232
E-mail : taka-annualrep@qst.go.jp
Homepage : https://www.qst.go.jp/site/taka/

QST-M-39

https://www.qst.go.jp